STATISTICAL BEHAVIOR OF POLARIMETRIC RADAR RESPONSE OF TERRAIN WITH EMPHASIS ON THE MILLIMETER-WAVE REGION

FINAL REPORT

K. Sarabandi and F.T. Ulaby
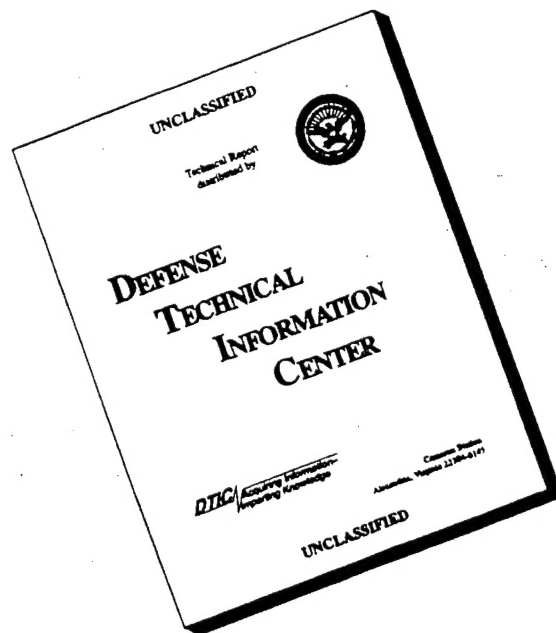
THE UNIVERSITY OF MICHIGAN

Radiation Laboratory
Department of Electrical Engineering
  and Computer Science
Ann Arbor, Michigan 48109-2122
USA

19960209 134
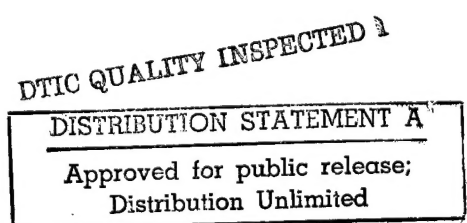
DISCLAIMER NOTICE

UNCLASSIFIED

Technical Report
distributed by

**DEFENSE
TECHNICAL
INFORMATION
CENTER**

DTIC Acquiring Information-
Imparting Knowledge

Cameron Station
Alexandria, Virginia 22304-6145

UNCLASSIFIED

THIS DOCUMENT IS BEST QUALITY AVAILABLE. THE COPY FURNISHED TO DTIC CONTAINED A SIGNIFICANT NUMBER OF PAGES WHICH DO NOT REPRODUCE LEGIBLY.

REPORT DOCUMENTATION PAGE

Public reporting burden for this collection of information is estimated to average 1 hour per response, including the time for reviewing instructions, searching existing data sources, gathering and maintaining the data needed, and completing and reviewing the collection of information. Send comments regarding this burden estimate or any other aspect of this collection of information, including suggestions for reducing this burden, to Washington Headquarters Services, Directorate for Information Operations and Reports, 1215 Jefferson Davis Highway, Suite 1204, Arlington, VA 22202-4302, and to the Office of Management and Budget, Paperwork Reduction Project (0704-0188), Washington, DC 20503.

1. AGENCY USE ONLY (Leave blank)	2. REPORT DATE 12/30/95	3. REPORT TYPE AND DATES COVERED Final 6/15/92–12/30/95

4. TITLE AND SUBTITLE	5. FUNDING NUMBERS
Statistical Behavior of Polarimetric Radar Response of Terrain with Emphasis on the Millimeter-Wave Region	$DAAL03-92-G-0269$

6. AUTHOR(S)

Kamal Sarabandi and Fawwaz T. Ulaby

7. PERFORMING ORGANIZATION NAME(S) AND ADDRESS(ES)	8. PERFORMING ORGANIZATION REPORT NUMBER
Radiation Laboratory, University of Michigan Ann Arbor, MI 48109-2122	029721-F

9. SPONSORING/MONITORING AGENCY NAME(S) AND ADDRESS(ES)	10. SPONSORING/MONITORING AGENCY REPORT NUMBER
U. S. Army Research Office P. O. Box 12211 Research Triangle Park, NC 27709-2211	ARO 30387.8-GS

11. SUPPLEMENTARY NOTES

The view, opinions and/or findings contained in this report are those of the author(s) and should not be construed as an official Department of the Army position, policy, or decision, unless so designated by other documentation.

12a. DISTRIBUTION/AVAILABILITY STATEMENT	12b. DISTRIBUTION CODE
Approved for public release; distribution unlimited.	

13. ABSTRACT (Maximum 200 words)

This final report provides a summary of the results we realized over the past three years in the field of polarimetric radar scattering from terrain. The contributions include: (a) The development of techniques for accurate calibration and measurement of the polarimetric scattering response of distributed targets, (b) The development of detection algorithms using polarimetric data, (c) The development of theoretical models for characterizing scattering by and propagation through dense random media, and (d) The development of semi-empirical models for millimeter-wave scattering from bare-soil surfaces and snow-covered terrain.

14. SUBJECT TERMS	15. NUMBER OF PAGES
Millimeter Waves, radar scattering, terrain clutter	228
	16. PRICE CODE

17. SECURITY CLASSIFICATION OF REPORT	18. SECURITY CLASSIFICATION	19. SECURITY CLASSIFICATION OF ABSTRACT	20. LIMITATION OF ABSTRACT
UNCLASSIFIED	UNCLASSIFIED	UNCLASSIFIED	UL

STATISTICAL BEHAVIOR OF POLARIMETRIC RADAR RESPONSE OF TERRAIN WITH EMPHASIS ON THE MILLIMETER-WAVE REGION

Final Report
U.S. Army Research Office
Contract DAAL03-92-G-0269
July 1995

K. Sarabandi and F.T. Ulaby

Contents

1 INTRODUCTION

Over the past three years, extensive theoretical, numerical, and experimental efforts have been devoted to the understanding of the polarimetric response of terrain at millimeter wavelengths. Our experimental efforts were directed at: (1) enhancement of the capabilities of our millimeter-wave scatterometer systems, (2) development of algorithms for accurate measurement of the polarimetric response of terrain, (3) development of sensors for "ground-truth" measurements, and (4) measurements and the development of semi-empirical models for various types of terrain types. We also have been able to advance our understanding of electromagnetic scattering by random media and rough surfaces through theoretical and numerical analyses. Much of our theoretical developments pertain to the statistical analysis of the Mueller matrices of distributed targets. Detection algorithms were also developed to demonstrate the feasibility and applicability of the developed theories. A considerable amount of time and effort were devoted to the development of numerical techniques for characterizing propagation through and scattering by random media and bistatic scattering by rough surfaces.

This report provides a summary of the significant results that were realized in the past three years under this program. The details of the procedures and algorithms are provided in the form of reprints in Appendix A. Apart from the reprints provided in this report, a rather lengthy two-volume polarimetric data handbook [24, 25] was published in collaboration with The University of Massachusetts. The references cited in the body of this report refer to the publication list given in Section 3.

2 SUMMARY OF RESULTS

2.1 Hardware Development and Measurement Algorithms

2.1.1 U-M Millimeter-Wave Measurement System

This section provides a summary of the capabilities and characteristics of the University of Michigan millimeter wave scatterometer systems. These systems consist of four operational scatterometers with center frequencies at 35, 94, 140, and 215 GHz. The first three are fully polarimetric, and the 215-GHz channel is capable of measuring only the magnitudes of the scattering matrix elements. A simplified block diagram of the radar system is shown in Fig. 1, and a more detailed
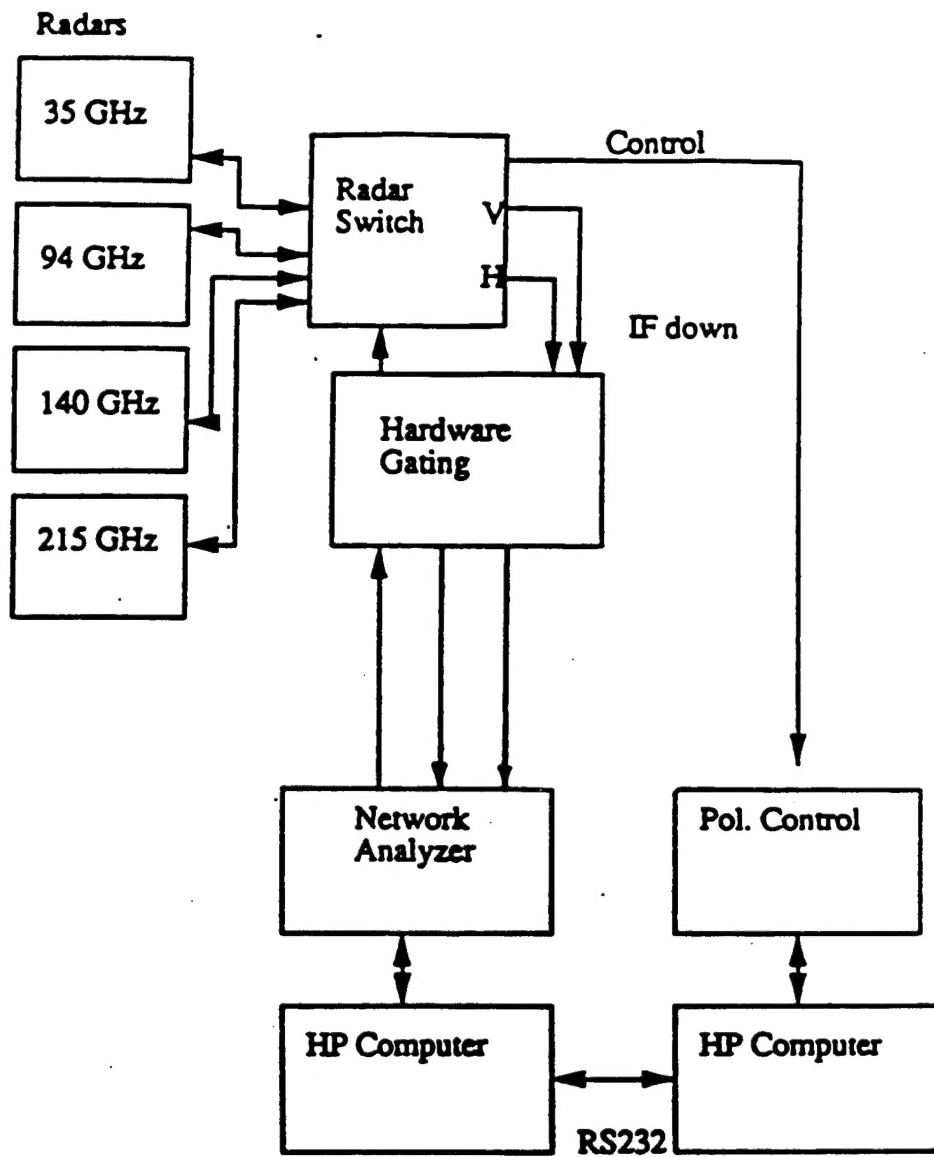
Figure 1: Millimeter-wave polarimetric radar system.

block diagram of one of the radar channels is shown in Fig. 2. The core of this system is the vector network analyzer where most of the signal processing takes place. An HP 8753C network analyzer was chosen for this purpose, and it includes a microwave synthesizer that covers the range from 0.3–3 GHz. The network analyzer is the base transmit and receive unit with up- and down-conversion used to provide the desired center frequencies.

The antennas and other RF equipment are mounted on a platform atop an articulating boom, and the control and processing equipment is housed in a control room on the truck bed. The scatterometers operate in high PRF chirped pulse mode to permit rejection of short range returns using the hardware gating unit. The PRF is chosen to be higher than the network-analyzer receiver's bandwidth and therefore the network analyzer operation is not affected by pulsing the chirped signal. An HP 3488 Switch/Control System with HP-Basic Language Processor was purchased and integrated with the radar system to provide control and feedback for many parts of the four frequency radar system, including polarization control and antenna pointing. The HP-Basic Language Processor provides control for numerous HP-IB instruments in an IBM compatible computer. The truck is a Ford F-800, and the boom can lift the antenna platform to a height of 56 feet.

Each of the radar units in the MMW scatterometer system can be operated in a number of measurement modes as indicated in Table 1. In this table the term "power only" refers to the capability of the radar unit for measuring the magnitudes of the scattering matrix elements. The term "coherent" indicates that the radar unit can measure the scattering matrix of a target by operating in single- or dual-antenna mode. Coherent-on-receive mode is a configuration wherein instead of measuring the scattering matrix of a target and then converting it into the Mueller matrix, the Mueller matrix is measured directly. This mode of operation is necessary in measurements of targets under field conditions when the fluctuation of the radar platform or the target does not permit phase-coherent measurements of all scattering matrix elements. In the bistatic mode, the radar unit operates in a dual-antenna mode, and depending on the capability of the radar unit the measurement can be performed in coherent, coherent-on-receive, or both modes.

2.1.2 Calibration Algorithm

A convenient and accurate polarimetric calibration technique was developed for coherent-on-receive radar systems [15]. In this algorithm, only the combination
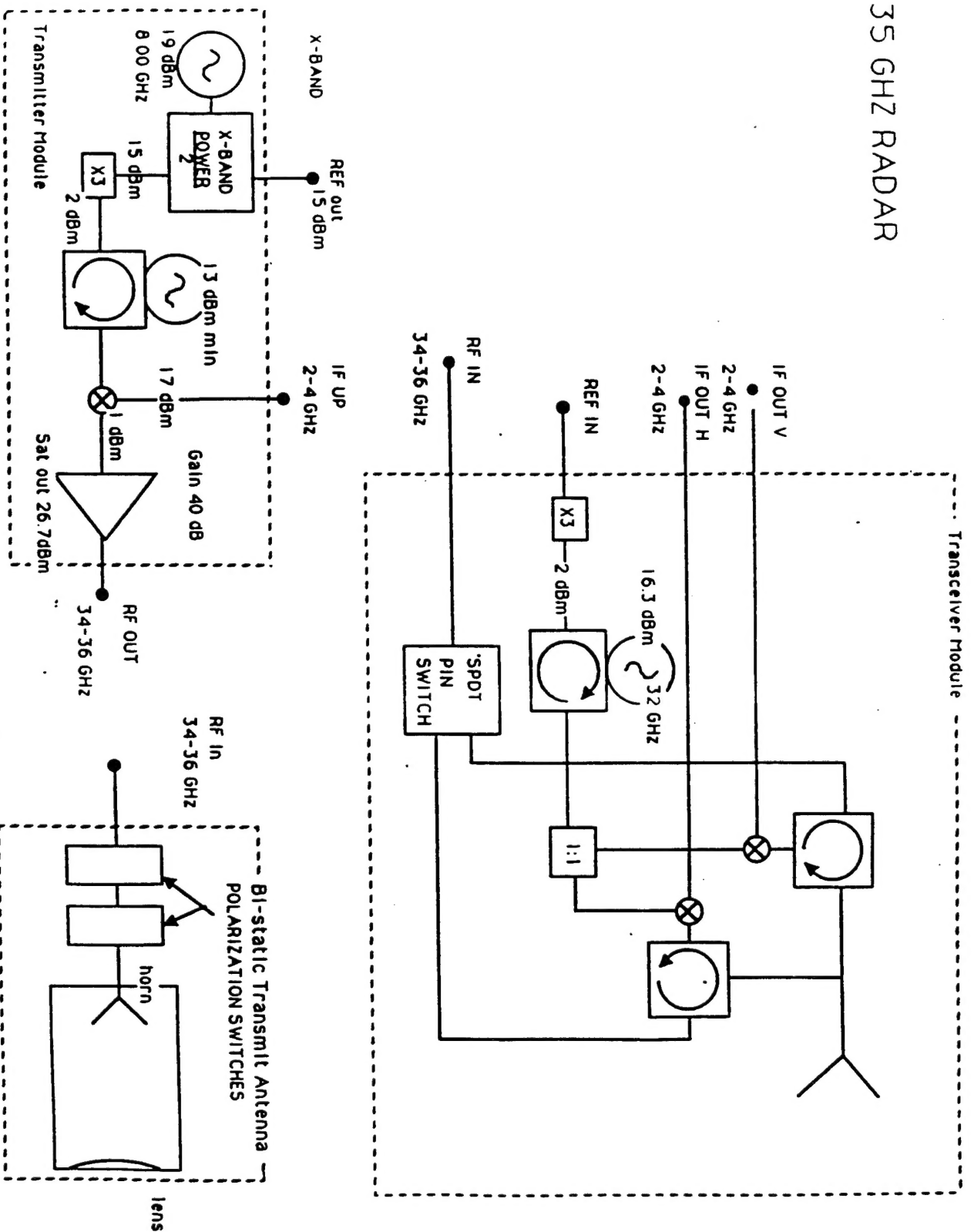
4

Figure 2: Block diagram of University of Michigan 35 GHz polarimetric scatterometer system.

5

	Power Only	Coherent		Coherent-on-Receive	Bistatic
		1-Antenna	2-Antenna		
35	✓	✓	✓	✓	✓
94	✓	✓	✓	✓	✓
140	✓			✓	✓
215	✓				

Table 1: MMW Scatterometer System modes of operation for each frequency.

of a metallic sphere and any depolarizing target (whose scattering matrix need not be known) are required as external calibration targets. With this technique, the difficulties and uncertainties associated with the standard calibration method based on wire-grid polarizers are completely circumvented.

2.1.3 Measurement Algorithm for Distributed Targets

An accurate algorithm was developed for measuring the differential Mueller matrix of distributed targets [1]. The distortion parameters of a polarimetric radar have significant variations over the antenna radiation pattern. In this algorithm the polarimetric distortion parameters of a scatterometer system are characterized over the entire mainlobe of its antenna using a metallic sphere. Then the calibrated differential Mueller matrix of the distributed target is obtained by removing the systematic errors.

2.1.4 Waveguide Polarizer

A new millimeter-wave waveguide polarizer was invented. This waveguide polarizer does not require rotary joints and its operation frequency can easily be adjusted using a number of set screws. The principle of operation of this device is based on separating the degenerate modes of a circular waveguide by deforming the circular cross section. The theoretical and experimental analysis of the device is given in reference [12, 20].

2.1.5 Snow Probe

We developed a snow probe capable of characterizing the liquid water content and density of a snowpack with high spatial resolution. The probe is basically an air-filled transmission line resonator that can be inserted into a snow medium. By measuring the change in the resonant frequency and the quality factor of the resonator, the complex permittivity of the snow medium can be measured. The theory of operation and measurement procedure are described in reference [11]. This device is used to gather ground-truth data fast and accurately.

2.2 Modeling Backscatter From Terrain

A hybrid surface/volume scattering model was developed for bare soil surfaces at millimeter wave frequencies [2]. The scattering model was constructed on the basis of an extensive set of backscatter measurements of bare soil surfaces with different rms heights and moisture contents. Simple empirical expressions for the backscattering coefficients were developed and their accuracies were tested using independent backscatter measurements. For dry soil surfaces at 94 GHz, volume scattering becomes important. For these cases radiative transfer theory is used to calculate the volume scattering contribution.

2.3 Radar Polarimetry And Detection Algorithms

A number of fundamental contributions were made in the field of radar polarimetry. In particlar, a technique was developed for extracting the polarization phase difference statistics from measurements of the Mueller matrix [4, 5]. The technique assumes that the matrix elements have Gaussian joint distribution functions. In another study, the enhancement provided by polarimetric radar in detecting hard targets was demonstrated by an algorithm developed for detecting power lines in a SAR image [6]. The technique relies on the property that the co-polarized and cross-polarized components of the scattering matrix are uncorrelated for a distributed target, such as terrain, but are at least partially correlated for a power line. In a third study, a hybrid electromagnetic/statistical scattering model was developed for MMW scattering by terrain [23].

2.4   Millimeter-Wave Polarimetric Data Base

A two-volume handbook containing a comprehensive set of polarimetric backscatter data for terrain was assembled and published in collaboration with the University of Massachusetts [24, 25]. This handbook contains a compilation of the polarimetric radar response for various types of terrain, together with the pertinent ground-truth data measured at 35, 94, 140, and 225 GHz. For each terrain surface and condition considered in these reports, the presented data contains (a) the measured values of the elements of the Mueller matrix and (b) values of certain attributes derived from the Mueller matrix such as the degree of polarization and the depolarization ratios.

2.5   Numerical Analysis For Characterization Of Volume Scattering In Dense Random Media

Propagation and scattering in dense random media at millimeter wavelengths are important for a number practical applications such as the evaluation of detectability of a hard target in a snow background. Existing analytical theories are not capable of accurately predicting the scattering and propagation of electromagnetic waves in dense random media, especially when the size of the constituent particles becomes comparable with the wavelength. Numerical techniques such as the T-matrix approach or the method of moments, in conjunction with Monte Carlo simulation, provide an alternative method for the study of electromagnetic waves and dense random media interactions. For this purpose, we developed packing algorithms [7] and numerical methods to characterize the extinction and phase function of dense random media [8, 9].

Scattering from random rough surfaces are often encountered in the study of radar backscatter from terrain. Theoretical scattering formulations for rough surfaces are limited to surfaces with homogeneous dielectrics and when the surface roughness is either very small or very large compared with the wavelength. Soil surfaces are usually inhomogeneous both laterally and vertically. To analyze the scattering behavior of soil surfaces, a numerical scattering algorithm was developed for inhomogeneous random surfaces [10].

8

3 LIST OF PUBLICATIONS

This section contains a list of papers published in scientific journals and symposia proceedings, or presented at technical meetings and workshops. The technical contributions described in these publications were generated in support of this project.

3.1 Journal Publications

[1] Sarabandi, K., Y. Oh, and F.T. Ulaby, "Measurement and calibration of differential Mueller matrix of distributed targets," *IEEE Trans. Antennas Propagat.,* vol. 40, no. 12, 1524–1532, Dec. 1992.

[2] Nashashibi, A., F.T. Ulaby, and K. Sarabandi, "Measurement and modeling the millimeter-wave backscatter response of soil surfaces," *IEEE Trans. Antennas Propagat.,* accepted for publication (April 1995).

[3] DeRoo, R. and F.T. Ulaby, "Bistatic spectral scattering from rough dielectric surfaces," *IEEE Trans. Antennas Propagat.,* vol. 42, no. 2, pp. 220–231, Feb. 1994.

[4] Sarabandi, K., "Derivation of phase statistics of distributed targets from the Mueller matrix," *Radio Sci.,* vol. 27, no. 5, pp 553–560, 1992.

[5] Ulaby, F.T., K. Sarabandi, and A. Nashashibi,"Statistical properties of the Mueller matrix of distributed targets," *IEE Proceedings-F: "Remote Sensing Radars",* vol. 139, no. 2, 136–146, 1992.

[6] Sarabandi, K., L. Pierce, Y. Oh, and F.T. Ulaby, "Power lines: Radar measurements and detection algorithm for polarimetric SAR images," *IEEE Trans. Aerospace and Electronic Sys.,* vol. 30, no. 2, 632–648, April 1994.

[7] Siqueira, P., K. Sarabandi, and F.T. Ulaby, "Numerical simulation of scatterer positions in a very dense medium with an application to the two-dimensional Born approximation," *Radio Sci.,* accepted for publication.

[8] Sarabandi, K. and P. Siqueira, "Numerical scattering analysis for two dimensional dense random media: characterization of effective permittivity," *IEEE Trans. Antennas Propagat.,* submitted for publication (March 95).

[9] Siqueira, P.R. and K. Sarabandi, "Numerical evaluation of the two-dimensional quasi-crystalline approximation," *IEEE Trans. Antennas Propagat.*, submitted for publication (June 1995).

[10] Sarabandi, K., Y. Oh, and F.T. Ulaby, "A numerical simulation of scattering from inhomogeneous dielectric random surfaces," *IEEE Trans. Geosci. Remote Sensing*, accepted for publication (June 95).

[11] Kendra, J.R., F.T. Ulaby, and K. Sarabandi, "Snow Probe for In-Situ Determination of Wetness and Density," *IEEE Trans. on Geosci. and Remote Sensing*, Vol. 32, pp. 1152–1159, Nov. 1994.

[12] Sarabandi, K., "A waveguide polarization controller," *IEEE Trans. MTT*, vol. 42, no. 11, 2171–2174, Nov. 1994.

3.2 Symposia Papers

[13] Ulaby, F.T., P. Siqueira, A. Nashashibi, and K. Sarabandi, "Semi-empirical model for radar backscatter from snow at 35 and 94 GHz," *Proc. IEEE Trans. Geosci. Remote Sensing Symp.*, Firenze, Italy, July 1995.

[14] Nashashibi, A., K. Sarabandi, and F.T. Ulaby, "Estimation of penetration depth in a random media using frequency decorrelation of backscattered field," *Proc. IEEE Trans. Geosci. Remote Sensing Symp.*, Pasadena, California, Aug. 1994.

[15] Nashashibi, A., K. Sarabandi, and F.T. Ulaby, "A new technique for calibration of polarimetric coherent-on-receive scatterometers," presented at AP/URSI symposium, Seattle, June 1994.

[16] Oh, Y. and K. Sarabandi, "An improved numerical simulation of electromagnetic scattering from perfectly conducting random surfaces," *Proc. IEEE Antennas Propagat. Symp.*, Seattle, June 1994.

[17] Kendra, J.R., K. Sarabandi, and F.T. Ulaby, "An innovative hybrid experimental/theoretical technique for modeling radar scatter from random media," Presented at AP/URSI symposium, Seattle, June 1994.

[18] DeRoo, R.D. and F.T. Ulaby, "Experimental observations of the forward scattering of microwaves from a rough dielectric surface," IGARSS'93, Aug. 1993, Tokyo, Japan.

[19] Nashashibi, A., K. Sarabandi, S. Ciccarelli, F.T. Ulaby, and P. Siqueira, "Backscatter measurements of soil surfaces at millimeter wave frequencies," *Proc. IEEE Trans. Antennas Propagat. Symp.*, Ann Arbor, 1993.

[20] Sarabandi, K., "A waveguide polarization controller," *Digest URSI Meeting,* Ann Arbor, 1993.

[21] Polatin, P.F., K. Sarabandi, and F.T. Ulaby, "Monte-Carlo Simulation of Electromagnetic Scattering from an heterogeneous two-component medium," presented at PIERS'93, Pasadena, July 1993.

[22] Sarabandi, K., L. Pierce, Y. Oh, and F.T. Ulaby, "Power lines: Radar measurements and detection algorithm for polarimetric SAR images," presented at PIERS'93, Pasadena, July 1993.

[23] Ulaby, F.T., P. Siqueira, and K. Sarabandi, "A hybrid electromagnetic - statistical approach for characterizing MMW scattering by terrain," *Proc. AGARD, Electromag. Wave Propag. Panel 48 Symp.*, Spain, May 1993.

3.3 Technical Reports

[24] Hartikka, R., A. Nashashibi, K. Sarabandi, P. Siqueira, F. Ulaby, P. Chang, S. Lohmeier, R. McIntosh, J. Mead, "Handbook of Millimeter-Wave Polarimetric Response of Terrain," Editors: F.T. Ulaby, R. McIntosh, and W. Flood, Vol. I, March 95.

[25] Hartikka, R., A. Nashashibi, K. Sarabandi, P. Siqueira, F. Ulaby, P. Chang, S. Lohmeier, R. McIntosh, J. Mead, "Handbook of Millimeter-Wave Polarimetric Response of Terrain," Editors: F.T. Ulaby, R. McIntosh, and W. Flood, Vol. II, March 95.

4 PARTICIPATING SCIENTIFIC PERSONNEL

The research conducted under this project was directed by Professor Fawwaz T. Ulaby. The participating team included Professor Kamal Sarabandi, who played

a key role in all aspects of the project; Mr. Craig Dobson, who supervised the activities related to ground data acquisition; Mr. Ron Hartikka, who served as the hardware engineer in charge of system construction; and three graduate students. The names, dissertation topics and status of the graduate students are given below.

Graduate Students

(a) **Name:** Mr. John Kendra

Degrees: M.S. (Electrical Engineering), December 1991; Ph.D. (Electrical Engineering), August 1995.

Dissertation Title: Remote Sensing of Snow: An Empirical/Theoretical Scattering Model for Dense Random Media

Dissertation Abstract:

It is generally recognized that microwaves, due to their penetrating ability, represent the best tool for inferring snowpack properties remotely. The challenge is how to unravel the information that the microwave radar or radiometric response carries regarding snowpack properties. Such properties can be used for such diverse applications as hydrology-related modeling, climate modeling, flood and avalanche prediction and missile guidance system design. The study of microwave interaction with snow is in itself very important for the fact that snow occurs in many remote sensing problems even when it is not the principal target. This dissertation focuses on assessing current capability with respect to modeling the active radar backscatter response of snow at microwave frequencies. A field experiment is described in which backscatter data was collected on artificial snowpacks of varying depths. In this carefully controlled experiment the ground truth effort was aided by the use of a device,the Snow Probe, which was developed to measure snow density and liquid water content quickly and accurately. The results of this experiment raise serious questions about the accuracy of existing theoretical techniques for representing volume scatter. An effort to address this problem and to provide a practical recourse for modeling dense media is introduced. This hybrid experimental/theoretical approach uses the framework of radiative transfer but empirically determines the defining quantities of that framework (the extinction and the scattering phase function) through an inversion involving controlled polarimetric backscatter measurements on

12

the test material. Results of the application of this technique to two different test materials indicate that (1) a simple hybrid model can provide a comprehensive polarimetric description of dense media scattering, and (2) material characterization required for parameterizing the hybrid model can be accomplished with a limited number of backscatter measurents.

(b) **Name:** Mr. Adib Nashashibi

Degree: Ph.D. (Electrical Engineering), August 1995.

Dissertation Title: Wave Propagation and Scattering in Dense Random Media with Application to Bare Soil Surfaces at Millimeter-Wave Frequencies

Dissertation Abstract:

Millimeter-wave (MMW) radars possess the inherent advantages of high resolution, large bandwidth, and small antenna size over microwave radars. Hence, millimeter-wave systems are, in general, more suitable for the applications of hard target detection and for search of buried bodies. To successfully design millimeter-wave systems tailored to these applications, the radar response of natural terrain must be known. In recent years, significant effort has been directed towards modeling the polarimetric radar response from natural terrain at MMW frequencies. For dry bare soils, the backscatter response is, in general, the sum of two scattering contributions: one is due to surface roughness and the other is due to dielectric inhomogeneity within the volume. At MMW frequencies, the volume scattering contribution is significant and must be included in any modeling effort. Two problems have thus far limited the successful modeling of the MMW response from soils, namely, the incapability of existing theoretical surface scattering models in predicting the backscatter response consistently and the lack of proven models that predict the effective propagation constant in dense random medium.

In this thesis, a semi-empirical surface scattering model is developed based on backscatter measurements of wet soil surfaces using two polarimetric coherent-on-receive radars operating at 35 and 94 GHz. Towards this end, a new calibration technique for polarimetric coherent-on-receive radars is developed. The new calibration technique overcomes the difficulties associated with the traditional technique and require the polarimetric measurement of only a sphere and any depolarizing target with unknown scattering matrix. Volume scattering contribution is modeled using the radiative transfer

13

theory and the combined contribution of the surface and volume scattering models agrees well with measured backscatter response from dry soil surfaces. The effective propagation constant of dense random media, such as soil, is an essential ingredient in both surface and volume scattering models. To determine which of the existing models are capable of predicting the effective propagation constant, a set of controlled indoor experiments where conducted on a dense collection of dielectric spheres over a wide range of volume fractions and compared to theoretical predictions. Towards this end, a novel technique for measuring the effective propagation constant of dense random media is developed. In this technique, the mean bistatic scattered fields of a cluster of the random medium confined in a spherical boundary is measured using only a monostatic radar and a rotatable ground plane. The effective propagation constant of the random medium is determined by fitting the mean bistatic scattered fields to the theoretically computed bistatic scattered fields of a homogeneous dielectric sphere. With this technique, the difficulties associated with the traditional free space transmission measurement technique are circumvented. In addition, the accuracy of this new technique is verified experimentally.

(c) **Name:** Mr. Paul Siqueira

Degree: Ph.D. (Electrical Engineering), December 1995.

Dissertation Title: Determination of Effective Permittivity for Very Dense Random Media

Dissertation Abstract:

The purpose of this dissertation is to address the physical problem of how electromagnetic waves propagate through very dense random media when the inhomogeneities may be considered as being neither tenous nor at one extreme of the frequency spectrum. The embodiment of how coherent fields travel through random media is found in the complex constant of effective permittivity. The real part of this constant characterizes the phase velocity of the field while the incoherent part results from the power losses of the coherent field into a combination of dielectric losses (absorption) and scattering losses. To deal with this problem, a number of theoretical methods exist, the application of which is dependent on the assumptions made. The theoretical methods however may become very complicated and difficult to test in regions where individual inhomogeneities (particles or grains for

14

instance) begin to interact with one another. Often, the existence of a theoretical model for a problem will guarantee its use because there simply is no other way to characterize this constant which is of such physical importance. Notable theories in this area are the Effective Field Approximation, the Quasi-Crystalline Approximation and the Quasi-Crystalline Approximation with Coherent Potential.

In this dissertation we develop an alternate, rigorous numerical solution to the problem of determining the effective permittivity for dense random media. Utilization of numerical methods (T-Matrix and the Method of Moments) allows for the direct solution of Maxwell's equations, thus shifting the burden of theoretical approximation to one of numerical complexity and computational resources. In this manner it is possible to provide detailed analysis of the effective permittivity as a function of particle size, particle permittivity, particle distribution and incident field polarization where no previous analysis was available before. Thus, independent comparisons may be made between commonly used theoretical methods and the numerical methods presented here. From this analysis, we may demarcate the regions of validity for the theoretical methods or develop empirical models and hybrid theoretical/numerical models for determining effective permittivity. The impact of this treatment will be to provide insight about the interaction of electromagnetic waves with natural media such as snow, sand and soils, the uses of which can be directly applied to the field of remote sensing of the environment.

In the development of this work, a number of new tools were implemented to achieve the modeling of dense natural media. Central to this problem was the creation of a packing algorithm which is capable of simulating arrangements of arbitrarily shaped particles in a two- or three-dimensional volume. This simulation is used to mimick natural media such as snow, sand and soils, from which it is possible to determine the aggregate pair distribution function and the correlation function. It is also possible to use the packing algorithm as the first step in the numerical solution of Maxwell's equations. To this end, in two dimensions, we have developed a unique method of determining permittivity for a fixed geometry bosed on an eigenvector docomposition of the impedance matrix for use with the Method of Moments. The more complicated three-dimensional problem is currently being studied with the aid of a recursive T-matrix algorithm. The well developed two-dimensional

analysis studied thus far will be used as a guide in finalizing the work of this dissertation on the three-dimensional problem.

APPENDIX A

Reprints of Journal Publications

MEASUREMENT AND MODELING OF THE MILLIMETER-WAVE BACKSCATTER RESPONSE OF SOIL SURFACES

A. Nashashibi, F. T. Ulaby, and K. Sarabandi
The Radiation Laboratory
Department of Electrical Engineering and Computer Science
University of Michigan, Ann Arbor, MI
Ann Arbor, MI 48109-2122

ABSTRACT

The millimeter-wave (MMW) backscatter response of bare-soil was examined by conducting experimental measurements at 35 and 94 GHz using a truck-mounted polarimetric scatterometer and by developing appropriate models to relate the backscattering coefficient to the soil's surface and volume properties. The experimental measurements were conducted for three soil surfaces with different roughnesses under both dry and wet conditions. The experimental measurements indicate that in general the backscattering coefficient is comprised of a surface scattering component σ^s and a volume scattering component σ^v. For wet soil conditions, the backscatter is dominated by surface scattering, while for dry conditions both surface and volume scattering are significant, particularly at 94 GHz. Because theoretical surface scattering models were found incapable of predicting the measured backscatter, a semi-empirical surface scattering model was developed that relates the surface scattering component of the total backscatter to the roughness parameter ks, where $k = 2\pi/\lambda$ and s is the rms height, and the dielectric constant of the soil surface. Volume scattering was modeled using radiative transfer theory with the packed soil particles acting as the host material and the air voids as the scattering particles. The combined contribution of surface and volume scattering was found to provide good agreement between the model calculations and the experimental observations.

1   INTRODUCTION

An extensive experimental investigation was conducted over the past three years to examine the polarimetric backscatter behavior of bare soil surfaces in the 1-10 GHz frequency range [1]. Using

a set of truck mounted coherent polarimetric scatterometers with center frequencies at 1.25, 4.75 and 9.5 GHz, measurements were made of the Mueller matrix as a function of incidence angle for soil surfaces covering wide ranges of surface roughness and moisture content. Using the relations outlined in [1] and [2], the measured Mueller matrices were then used to compute the co-polarized backscattering coefficients σ^o_{vv} and σ^o_{hh}, the cross-polarized backscattering coefficient σ^o_{hv}, and the probability density functions of the co-polarized and cross-polarized phase differences. Comparison of the measured data with calculations based on the physical optics model, the geometric optics model, and the small perturbation method revealed that all three models are incapable of correctly predicting the backscatter response of random rough surfaces, even when applied within their presumed ranges of validity. This realization led Oh *et al.* [1] to develop a semi-empirical model that relates σ^o_{ij}, for $i, j = h$ *or* v, to the incidence angle θ and the surface parameters ks and ϵ_r, where $k = 2\pi/\lambda$, s is the rms height and ϵ_r is the complex relative dielectric constant. The semi-empirical model, which was developed on the basis of measurements made during one season of experimental observations, was found to provide excellent agreement not only with observations made during two succeeding years for different sets of soil surfaces and conditions, but it also provided a reasonable match to experimental observations reported by Yamasaki *et al.* [3] for wet soil surfaces at 60 GHz.

This paper extends the preceding work by examining the backscatter response of soil surfaces at millimeter wavelengths (MMW); specifically 35 and 94 GHz. One of the major lessons learned from the present study is that at centimeter wavelengths it is reasonable to assume that the backscatter from a half-space soil medium is due to scatter by the soil surface alone, but at millimeter wavelengths the backscatter may consist of both surface and volume scattering contributions. Furthermore, for dry soils the volume-scattering component may be comparable to or greater than the surface-scattering component, but for wet soil the volume scattering component becomes negligibly small in comparison with the surface-scattering component. This behavior is consistent with calculations based on radiative transfer theory.

The next section contains detailed descriptions of the 35 and 94 GHz radar systems, the measurement procedure, and the measured properties of the soil surfaces. Section 3 provides an overview of the observed angular variation of σ^o for various surface roughnesses and introduces a scattering model composed of two terms, corresponding to surface and volume scattering contributions. The surface-scattering term is a semi-empirical expression that provides a better fit to the data than the expression previously derived by Oh *et al.* [1] for surface scattering at centimeter wavelengths. Section 4 examines the evidence for volume scattering and introduces a method for evaluating the volume-scattering term based on a numerical solution of the radiative transfer equation for a medium in which the soil particles are considered to be the host material and the air voids are the scatterers.

2   EXPERIMENTAL SETUP

The first part of this section provides a brief discription of the polarimetric scatterometers used in support of the present study. It is then followed with discussions of the techniques employed in preparing the surfaces and the methods used in characterizing the physical properties of the

observed surfaces.

2.1   Polarimetric Scatterometer System

Two fully polarimetric truck-mounted scatterometer systems operating at 35 GHz and 94 GHz were used to conduct the experiments reported in this paper. A block diagram of the overall system, as well as the RF front-end circuitry of the 35 GHz radar, are shown in Fig. 1. The scatterometers are capable of measuring directly the Mueller matrix of a distributed target using the coherent-on-receive (COR) technique, [4]. With the COR technique, 4 to 6 different polarizations (V, H, 45L, LHC, 135L, and RHC) are transmitted sequentially. Each radar is capable of simultaneous detection of the vertical and horizontal components of the backscattered signal, preserving the phase-difference between the two components. The Stokes vector of the scattered field is recorded for each transmitted polarization and then the Mueller matrix of the target is determined from the ensemble averages of the measured Stokes vectors, following the procedure outlined by Ulaby *et al.* [4,5].

The calibration of the scatterometers was performed in two steps. First, the receiver was calibrated using an odd-bounce reflector (a metallic sphere) and a polarizing grid placed in front of the receiving antenna. The receiver distortion matrix was determined by making the measurements with the polarizer positioned at each of three different angles. Second, the actually transmitted polarizations were determined using the calibrated receiver and the odd-bounce reflector. More details on the calibration technique are given in [6].

2.2   Surface Preparation and Characterization

The wavelengths corresponding to 35 and 94 GHz are 8.6 mm and 3.2 mm, respectively. To insure that the backscattering measurements cover a wide range of surface roughness relative to λ, special care was taken in preparing the three soil surfaces. Initially, all the surfaces were cleared from grass and vegetation debris. Then, in order to have a "smooth" surface with rms height less than 1 mm, a heavy roller was moved across surface S1. This technique resulted in a compacted soil medium with an rms height $s = 0.66$ mm. Surface S2 was a slightly rough surface with $s = 2.62$ mm, and for surface S3 the top layer was turned over by a hand shovel resulting in an undulating surface with $s = 7.77$ mm. Surface height characterization was performed by a laser profiler, as will be discussed later. Samples of surface profiles of the three surfaces and their auto-correlation functions are shown in Figure 2. A summary of the roughness parameters for the three surfaces is given in Table 1. Two sets of measurements were conducted, one for dry soil conditions and the other for wet soil conditions (see Table 2).

For each soil surface, the radar backscatter data was collected at incidence angles of 20°, 45°, and 70°, under wet and dry soil conditions. For all observations, the distance from the radars to the surfaces was kept at about 10 m. At normal incidence, the antenna spot sizes for the 35 GHz and 94 GHz radars were 0.6 m and 0.3 m, respectively. Furthermore, to achieve good statistical

3

representation of the measured backscatter, sixty independent spatial samples were collected for each surface. Additional independent samples were obtained by frequency averaging over the 1-GHz bandwidth. Overall, between 120 samples at $\theta = 20^{\circ}$ and 240 samples at $\theta = 70^{\circ}$ were collected for each target.

Although both the backscattering coefficients, σ_{vv}^{o}, σ_{hh}^{o}, and σ_{hv}^{o}, and the statistics of the phase-differences, ϕ_{hh-vv} and ϕ_{hv-vv}, can easily be derived from the Mueller matrix [7], only the backscattering coefficients are discussed in this paper. The measured phase-difference statistics are the subject of a separate report.

The height profile of each soil surface was measured by a laser profiler mounted on an x-y table. The profiler, which is driven by stepper motors, measured 30-cm long linear segments with 0.3 mm horizontal resolution and 0.3 mm vertical resolution. At least five height profiles of different areas were recorded for each surface. The rms height s and correlation length l are listed in Table 1 for each of the three surfaces.

The soil particle size distribution is shown in Fig. 3(a), indicating that the bulk of the soil material consists of fine sand (diameter ≥ 0.02 mm). To investigate the void size distribution of the soil medium, thin soil slices were collected and then photographed by a microscope camera. Two histograms of the void-size distribution were generated, one for bulk soil density $\rho_b = 1.69$ g/cm^3 (for soil surface S1) and another for $\rho_b = 1.32$ g/cm^3 (for soil surface S3), by treating the voids as spherical in shape. The mean void diameter was calculated to be 0.165 mm for the high-density soil, compared to 0.242 mm for the low-density soil. The void size distribution of the soil with $\rho_b = 1.69$ g/cm^3 is shown in Fig. 3(b).

In conjunction with the radar measurements, the soil bulk density ρ_b and the volumetric moisture content m_v were measured by collecting 1-cm thick soil samples for each of the top 3-cm soil layers. The average values of ρ_b and m_v are listed in Table 2, for all three surfaces.

In order to compare the radar observations to theoretical models, we need to obtain good estimates of the soil's dielectric constant or relate the dielectric constant to the soil's physical properties. Unfortunately, no theoretical or empirical model is available in the literature that can correctly predict the effective dielectric constant of soils at MMW frequencies. In this paper, the effective dielectric constant of the soils observed in this study were estimated by applying the semi-empirical formula found in [8,9]. The results are given in Table 2. For the measured dry surfaces with low moisture content, it is difficult to determine accurately the amount of free water. In addition, it was observed that the first few millimeters of the soil medium were very dry, and the soil wetness increased gradually with depth. The values given in Table 2 for the dielectric constants of the dry soil surfaces are for the very top surface layer. The thickness of that dry surface layer plays an important role in determining the relative contribution of volume scattering to the total backscatter, as discussed later in Section 4.3.

4

3 SURFACE SCATTERING

This section examines the experimental behavior of the backscattering coefficient σ^o as a function of (1) the radar parameters: frequency. receive-transmit polarization configuration. and the incidence angle θ, and (2) the soil surface parameters: the rms surface height s, the surface correlation length l, and moisture content m_v. Where appropriate, semi-empirical expressions are introduced to characterize the observed radar response. This is done in lieu of using theoretical models because comparison of the measured data with values calculated in accordance with the commonly available scattering models (small perturbation. physical optics. and geometric optics) reveals poor agreement between the theoretical predictions and the experimental observations, as shown in Fig.4(a) for the smoothest surface at 35 GHz, whose roughness parameters fall in the validity range of the physical ·tics model, and in Fig.4(b) for the other two surfaces at 94 GHz, for which the geometric optics model is supposed to be applicable.

In general, two scattering mechanisms contribute to the backscattering coefficient σ^o (Fig. 5), a surface scattering contribution σ^s which is a function of the surface height statistics and ϵ_r of the lower half space, and a volume scattering contribution σ^v that is due to inclusions underneath the rough interface:

$$\sigma^o_{ij} = \sigma^s_{ij} + \sigma^v_{ij} \qquad\qquad i, j = h \ or \ v. \qquad (1)$$

The volume scattering contribution is in turn governed by the height statistics of the rough interface and the size and shape distributions of the inclusions in the soil medium (air voids in this case) and the dielectric constant of the host material (soil particles). Calculations based on radiative transfer theory reveal that σ^v is much smaller than the observed scattering coefficient σ^o, and hence much smaller than σ^s, except for dry soil at 94 GHz. This can be explained by noting that at 35 GHz the air voids are very small in size (see Fig. 3(b)) relative to λ, and at 94 GHz the attenuation in wet soil reduces the penetration depth to a very thin surface layer, thereby reducing the volume scattering contribution to a negligible level. First, we will limit the analysis to the wet soil cases in order to examine the surface scattering component alone and then we will use radiative transfer theory to model the volume-scattering component (Section 4). Hence, for the cases presented in this section, $\sigma^o = \sigma^s$.

As was stated earlier, the radar observations were made at 35 GHz and 94 GHz for each of three surfaces with widely different roughnesses. Figure 6 displays the angular variation of σ^o, for each of the three principal polarization configurations, for the surface with the smallest value of ks (surface S1 with $s = 0.66$ mm, observed at 35 GHz) and the surface with the largest value of ks (surface S3 with $s = 7.77$ mm, observed at 94 GHz). We note that the curves for the co-polarized scattering coefficients, σ^o_{vv} and σ^o_{hh}, diverge as a function of θ for the smooth surface represented by Fig. 6(a), but they remain approximately equal for the very rough surface represented by Fig. 6(b). This behavior is consistant with previous observations made at centimeter wavelengths [1]. We also note that the difference in level between the σ^o_{vv} and σ^o_{hv} curves is at least 18 dB for the smooth surface (actually 21 dB at 20°, decreasing to 18 dB at 70°), whereas the difference never exceeds 13 dB for the very rough surface. These observations clearly indicate that surface roughness exercises a significant influence on both the co-polarized ratio $p = \sigma^s_{hh}/\sigma^s_{vv}$ and the cross-polarized

ratio $q = \sigma_{hv}^s / \sigma_{vv}^s$. It should be noted that the continuous curves shown in Fig. 6 are based on the semi-empirical expressions introduced later in this section.

The three surfaces examined in this study were prepared to replicate a wide range of naturally occuring surface roughness conditions. Surface S1 represents a packed-down dirt road surface, surface S3 represents a freshly plowed soil surface, and S2 represents what surface S3 would look like after cultivation by a farm implement to break down the large soil clods or after natural smoothing action by rain and wind. An examination of Table 1 shows that among the three surfaces, the surface correlation length l varies over a narrower range of $1.5 : 1$ (between a minimum of 2 cm for S3 and a maximum of 3 cm for S2). The corresponding range on the kl scale (where $k = 2\pi/\lambda$), is approximately $4 : 1$. In contrast, the rms height s varies over a range of $12 : 1$, and ks covers the range $32 : 1$. A third surface roughness parameter of interest is the ratio $m = s/l$ which is equal to or proportional to the rms slope of the surface, with the proportionality constant being determined by the form of the surface autocorrelation function. For the three surfaces, m varies from 0.025 for S1 to 0.39 for S2. A detailed analysis was conducted to determine the sensitivities of the backscattering coefficients σ_{vv}^o, σ_{hh}^o, and σ_{hv}^o to s, l, ks, kl, and m. Plots of the backscattering coefficients *versus* the five surface roughness descriptors revealed the following: (a) strong but different dependences on s at 35 GHz and 94 GHz, (b) the individual frequency plots coincide with each other when the data is plotted against ks, (c) random variations with l and kl, and (d) the variation with m is driven by the dependence on s. Considering that l exhibits a relatively narrow range among the three surfaces, it is not surprising that s was found to be the primary parameter governing the dependence of the radar backscatter on surface roughness.

3.1   Co-Polarization Ratio

The dependences of the co-polarized and cross-polarized ratios p and q on ks are illustrated in Fig. 7. At $\theta = 20°$, p exhibits no discernible dependence on ks, as expected, because θ is close to normal incidence. At the higher angles of $45°$ and $70°$, p increases with increasing ks until ks reaches a value of 4, beyond which p assumes the constant ratio of 1.0. The continuous curves shown in Fig. 7(a) are based on the following expression:

$$p = \frac{\sigma_{hh}^s}{\sigma_{vv}^s} = \left[1 - \left(\frac{2\theta}{\pi} \right)^{1/(3\Gamma_o)} \ exp[-0.4ks] \right]^2 \tag{2}$$

where θ is the incidence angle in radians and Γ_o is the reflectivity for normal incidence,

$$\Gamma_o = \left| \frac{1 - \sqrt{\epsilon_r}}{1 + \sqrt{\epsilon_r}} \right|^2 \tag{3}$$

The form of (2), which was adapted from the experience gained previously from the centimeter-wave study [1], includes a dependence on the dielectric constant ϵ_r. The plots shown in Fig. 7(a) correspond to $\epsilon_r = 5.07 + j2.56$, which is in the middle of the range of the dielectric constants corresponding to the wet-soil surfaces observed by the radar (see Table 2). Thus, part of the data scatter in Fig. 7(a) is attributed to the non-uniformity of dielectric constants among the data points.

6

3.2 Cross-Polarization Ratio

The cross-polarization ratio q. which exhibits an inverse negative exponential dependence on ks for all angles of incidence (Fig. 7(b)), is modeled by the expression:

$$q = \frac{\sigma_{hv}^s}{\sigma_{vv}^s} = 0.23 \sqrt{\Gamma_o} \left[1 - exp(-0.5 \sin\theta \, ks)\right] \tag{4}$$

To eliminate the dependence on the dielectric constant ϵ_r, the ratio q shown in Fig. 7(b) has been normalized by dividing it by $\Gamma_o^{1/2}$ for both the data points and the expression given by (4).

3.3 σ_{vv}^s Response

So far we have characterized the ratios of σ_{hh}^s and σ_{hv}^s with respect to σ_{vv}^s through (2) and (4). Now, we turn our attention to the response of σ_{vv}^s to θ, ks and ϵ_r. The proposed functional form is:

$$\sigma_{vv}^s = g \, \frac{cos^x\theta}{\sqrt{p}} \left[\Gamma_v(\theta) + \Gamma_h(\theta)\right] \tag{5}$$

where p is given by (2), $\Gamma_v(\theta)$ and $\Gamma_h(\theta)$ are the Fresnel reflectivities at incidence angle θ for v and h polarizations, respectively, and the function g is given by:

$$g = 2.2 \, (1 - exp[-0.2ks]) \tag{6}$$

The exponent of the $\cos\theta$ term in (5) accounts for the change in the angular dependency of σ_{vv}^s as a function of ks, and is given by:

$$x = 3.5 + \frac{1}{\pi} \, tan^{-1}[10 \, (1.65 - ks)] \tag{7}$$

For a very rough surface with ks very large, $p \approx 1$, $g \approx 2.2$, and $x \approx 3$, in which case (5) reduces to:

$$\sigma_{vv}^s = 2.2 \, \cos^3 \theta \left[\Gamma_v(\theta) + \Gamma_h(\theta)\right], \qquad for \quad ks >> 1 \tag{8}$$

The inclusion of the sum $[\Gamma_v(\theta) + \Gamma_h(\theta)]$ in the expression for σ_{vv}^s simply insures that for a very rough surface, $\sigma_{vv}^s = \sigma_{hh}^s$, and yet the magnitudes of these two co-polarized coefficients are somehow related to the angle-dependent reflectivity of the surface.

To compare the proposed model with the experimental data (Fig. 8) we first normalized the measured values of σ_{vv}^s by dividing each by the sum of the reflectivities corresponding to the dielectric values associated with the surface and incidence angle and then plotted the results as a function of ks. The same normalization procedure was applied to (5) prior to plotting it in Fig. 8. In fact, the values of the coefficients appearing in (6) and (7) were selected by matching the expression given by (5) to the data.

7

3.4 Comparison of Model with Observations

The expressions given by (2)-(7) represent a semi-empirical model for characterizing the surface-scattering component of millimeter-wave backscattering from a random rough surface. The continuous curves shown in Fig. 6 are based on this model as are the curves shown in Fig. 9 for surface S2 (with intermediate roughness) and in Fig. 10 where the model is compared with an independent data set (not used in constructing the surface model) reported by Yamasaki, *et al.* [3] at 60 GHz, also for wet-soil surfaces.

4 VOLUME SCATTERING

Before we embark on a detailed examination of σ^v, the volume backscattering contribution to the total backscattering coefficient σ^o, it would be instructive to examine the evidence we have in support of conducting such an examination in the first place. After all, studies conducted at centimeter wavelengths have shown that the behavior of the backscatter from random surfaces can be explained by surface scattering alone, without the need to add a volume-scattering contribution. The need to consider volume scattering at millimeter wavelengths can be illustrated through an examination of the experimental data shown in Fig. 11 which include a set of plots of σ^o_{hh} and σ^o_{hv} for a dry soil surface and another set for the same surface immediately after wetting the surface with a fine mist using a sprinkler system, thereby preserving the roughness of the surface. According to surface scattering models, both theoretical and empirical, increasing the soil moisture content causes the level of σ^o to increase at all angles of incidence for all polarization configurations. This is certainly not the behavior observed in Fig. 11. For HH polarization, σ^o_{hh} of the dry surface at $\theta = 20^o$ is slightly lower than that for the wet surface, but at 70°, σ^o_{hh} for the dry soil surface is *higher* than that for the wet surface. A similar, but even more pronounced, behavior is observed for HV polarization. The explanation for these observations stems from the following properties:

1. Surface scattering increases with increasing moisture content (dielectric constant), as stated earlier.

2. For surface scattering, σ^s varies with θ as $\cos^3 \theta$ to $\cos^4 \theta$, depending on surface roughness.

3. Volume scattering decreases with increasing moisture content, in part because the air-soil transmission coefficient decreases with increasing moisture content and in large part because the extinction in the soil medium increases rapidly with moisture content.

4. The volume scattering coefficients exhibit a very weak response as a function of the incidence angle θ.

5. The dimensions of the air voids (see Fig. 3(b)), which constitute the scattering particles in the soil medium, are such that the scattering is in the Rayleigh region, which exhibits a λ^{-4}-dependence. Consequently, volume scattering is insignificantly small at centimeter wavelengths, but becomes important at millimeter wavelengths when the soil surface is dry.

8

4.1 Radiative Transfer Theory

To compute the volume scattering contribution. we propose to use radiative transfer (RT) theory. As was noted earlier, the moisture content of the wet soils was essentially uniform with depth over the top four centimeters, but for the dry soils, the top surface layer, which was on the order of 1-3 cm thick, was very dry and the soil layer underneath it was generally fairly wet. Hence. we decided to model the soil medium as a thin layer of thickness h overlying a wet-soil half space. The thin layer. which is bounded by a random surface at the air-soil interface. contains air voids (scatterers) embedded in the soil background. From the measured surface profile, extended into both the x- and y-dimensions, a probability density function is computed for the direction $\hat{n}$ of the local surface normal. For any specified direction of incidence $\hat{k}_i$, the dot product $(\hat{k}_i . \hat{n})$ determines the local angle of incidence θ_l. Hence, for any given radar incidence angle θ_i (measured relative to the normal to the mean surface). we generate a probability distribution for θ_l. Upon solving the radiative transfer equation numerically for Mie spherical particles using the technique outlined in Kuga, *et al.* [10], the total volume scattering contributed by the layer is obtained by performing an incoherent addition of the volume scattering contributions emerging from all points on the surface, realized by weighing the contributions in accordance with the probability density function of θ_l. This approach is similar to that reported in [8] for computing surface scattering from tilted perturbed planes.

Solution of the radiative transfer equations requires knowledge of the void's shapes. sizes, volume fraction and relative dielectric constant, in addition to the relative dielectric constants of both the background solid soil material and the wet soil half space. In this paper, we have assumed that the air voids are spherical in shape with a relative dielectric constant $\epsilon_a = 1.0 + j0.0$. The void-size distribution function shown in Fig. 3(b) was used in the solution of the RT equations for surfaces S1 and S2, and that corresponding to S3 (not shown) was used for the third surface. The relative dielectric constant of the background solid soil material was taken as $\epsilon_{ss} = 4.7$, based on the empirical formula $\epsilon_{ss} = (1.01 + 0.44\,\rho_{ss})^2 - 0.062$ reported in [9], where $\rho_{ss} = 2.65$ g/cm^3 is the measured solid soil density (which agrees well with ρ_{ss} of sandy soils [8,9]). The effective dielectric for the wet soil half space was assumed to be $\epsilon_2 = 7.0 + j4.0$ at 35 GHz and $\epsilon_2 = 5.0 + j2.5$ at 94 GHz. The voids volume fractions given in Table 2 were calculated on the basis of the measured bulk densities and solid soil density, $\nu_a = 1 - \rho_b/\rho_{ss}$.

The results of this approach for computing the volume backscattering contribution σ^v are summarized in the next section. By way of examining the relative importance of volume scattering, however, we calculated σ^v at 94 GHz for an upper layer containing air voids of uniform diameter, d_v. The results are shown in Fig. 12, which shows σ^v as a function of d_v for a thickness $h = 3$ cm. and as a function of h for a void diameter $d_v = 0.1$ mm. The responses to h (Fig. 12(b)) indicate that the thin surface layer "appears" semi-infinite in depth once its actual depth h exceeds about 3 cm. The variations of σ^v with d_v displayed in Fig. 12(a), which include both the Rayleigh and Mie regions, reaches saturation levels of about -4 dB for σ_{vv}^v and -7 dB for σ_{hv}^v. The saturation level for σ_{vv}^v is certainly comparable with or greater than the values measured for the wet soil surfaces at the same incidence angle and frequency, and for σ_{hv}^v, the saturation level is higher than all the wet-soil values of σ_{hv}^v displayed in Figs. 6, 9, and 10. Thus, the volume scattering contribution may

indeed be a significant, or even the dominant. contribution depending on the void-size distribution. The volume scattering coefficients plotted in Fig. 12(a) approach the saturation stage when d_v exceeds 0.5 mm, which corresponds to $kr_v = kd_v/2 = \pi d_v \sqrt{\epsilon_r}/\lambda_o \simeq 0.86$, where λ_o is the free space wavelength ($\lambda_o = 3.2$ mm at 94 GHz) and $\epsilon_r = 3.1$ is the effective dielectric constant of the dry soil background. The soils investigated in this study had void size distributions extending between 0.02 mm and about 0.4 mm, with the bulk of the voids having diameters smaller than 0.2 mm (see Fig. 3(b)).

4.2 Results

For the dry soil surfaces, the total backscattering coefficients σ_{ij}^o ($i, j = v$ or h) were computed according to (1) by adding incoherently the volume scattering contribution σ_{ij}^v. computed using the RT technique, to the surface scattering contribution σ_{ij}^s, calculated according to the empirical model described in the preceding section (equations (2)-(7)). Good overall agreement is observed between the computed values of σ_{ij}^o and the measured radar responses for all surfaces at both frequencies, as can be seen in Figures 13 through 15. In all cases, the thickness of the top dry soil surface layer was taken as 3-cm.

It must be pointed out that at 35 GHz, σ_{ij}^o is dominated by surface scattering with minimal contribution provided by volume scattering (σ_{ij}^s is typically larger than σ_{ij}^v by 10 dB). However, at 94 GHz the volume scattering component is comparable to the surface scattering component for the co-polarized scattering coefficients, as can be seen in Fig. 16(a), and for cross-polarization, σ_{hv}^o is dominated by the volume contribution (Fig. 16(b)).

4.3 Soil Moisture Dependence

The cases considered in this paper fall into two groups: (a) wet soils, which may be defined as those with moisture contents exceeding 0.12 g/cm^3 in the top 1-cm layer, and (b) dry soils, for which $m_v < 0.04$ g/cm^3 in the top 1-cm layer (see Table 2). For the wet-soil group, our analysis shows that the volume-scattering contribution may be ignored and that the total backscatter is dominated by the surface-scattering component. The volume-scattering contribution is very small because at millimeter wavelengths the penetration depth is on the order of a few millimeters when $m_v > 0.1$ g/cm^3.

For the dry-soils group, the volume-scattering contribution was computed by assuming the top surface layer to be 3 cm in thickness and totally dry. Although the measured values of m_v were very small, they were not exactly zero over the top 3-cm layer (Table 2). Nevertheless, they were assumed to be zero to simplify the calculation. A possible approach for modeling the dependence on moisture content is to treat the soil as a perfectly dry top surface layer of thickness h, overlying a very wet half-space, just as we have done in calculating the volume-scattering contributions for the dry soils examined in this study, but to also relate h to the average dielectric constant or moisture content of the upper 3-cm layer. Thus, h would vary from 3-cm for $m_v = 0$ down to zero thickness

10

for $m_t = 0.15$ g/cm^3. These figures apply to 94 GHz and are at best a rough estimate based on radiative-transfer model calculations. Had we applied this approach to the calculations performed in connection with the dry soils, h would have been reduced from 3-cm down to about 2-cm, resulting in a change of about 1-2 dB in σ^v. Thus, verification of the applicability of such a model will have to await until further experimental investigations are performed for soils with moisture contents in the 0.04 to 0.15 g/cm^3 range.

5   CONCLUSIONS

The backscattering coefficients of three soil surfaces were measured as a function of incidence angle using two scatterometers operating at 35 GHz and 94 GHz. The soil surfaces, with roughnesses ranging between $ks = 0.48$ and $ks = 15.3$, were measured under wet and dry conditions. When compared to measurements, the physical optics and geometric optics surface-scattering models, as well as the empirical surface-scattering model given in [1], failed to consistently predict the measured backscattering coefficients.

Analysis of the measured radar data indicates that in general both surface and volume scattering contributions are present at MMW frequencies. For wet soil conditions, surface scattering is the dominant contribution and it can be modeled using a set of semi-empirical expressions. The volume contribution is important when the soil surface is dry, particularly at 94 GHz. Using radiative transfer theory, the volume scattering contribution was calculated by treating the soil medium as comprised of air voids imbedded in a soil background. This approach, which led to good agreement with the experimental observations, indicates that at 94 GHz, for example, the surface and volume scattering components are of comparable magnitude for σ^o_{vv} and σ^o_{hh}, but for the cross-polarized σ^o_{hv}, volume scattering is the dominant contribution.

References

[1] Y. Oh, K. Sarabandi, and F.T. Ulaby, "An Empirical and an Inversion Technique for Radar Scattering from Bare Soil Surfaces," *IEEE Trans Geosci. Remote Sensing*, vol. GE-30, pp. 370-381, Mar. 1992.

[2] Y. Oh, K. Sarabandi, and F.T. Ulaby, "An Empirical Model for Phase Difference Statistics of Rough Surfaces," *Proceedings of IGARSS '93 Symposium*, Tokyo, Japan, vol. III, pp. 1003-1005, August 1993.

[3] H. Yamasaki, J. Awaka, A. Takahashi, K. Okamoto, and T. Ihara, "Measurements of Soil Backscatter with A 60 GHz Scatterometer," *IEEE Trans Geosci. Remote Sensing*, vol. GE-31, pp. 761-766, July 1992.

[4] F.T. Ulaby, M. Whitt and K. Sarabandi, "AVNA-Based Polarimetric Scatterometers," IEEE AP magazine, vol. 32, 1990.

[5] F.T. Ulaby and C. Elachi, *Radar Polarimetry for Geoscience Applications*, Artech House, 1990.

[6] J.B. Mead, "Polarimetric Measurements of Foliage and Terrain at 225 GHz," Ph.D. thesis, University of Massachusetts, Amherst, MA, 1990.

[7] K. Sarabandi, "Derivation of Phase Statistics of Distributed Targets from the Averaged Mueller Matrix," *Radio sci.*, vol. 27, pp. 553-560, Sept.-Oct. 1992.

[8] F.T. Ulaby, R.K. Moore, and A.K. Fung, *Microwave Remote Sensing*, Vol.II-III, Artech, 1986.

[9] M.C. Dobson, F.T. Ulaby, M. T. Hallikainen, and M.A. El-rayes, "Microwave Dielectric Behavior of Wet Soil-Part II: Dielectric Mixing Models," *IEEE Trans Geosci. Remote Sensing*, vol. GE-23, pp. 35-46, Jan. 1985.

[10] Y. Kuga, F.T. Ulaby, T. F. Haddock, and R. D. DeRoo, " Millimeter-wave Radar Scattering From Snow 1. Radiative Transfer Model," *Radio Sci.*, vol. 26, pp. 329-341, March-April 1991.

Table 1. Surface roughness statistical parameters for the three soil surfaces.

surface	$s(mm)$	$l(mm)$	Freq(GHz)	ks	kl
S1	0.66	27	35	0.48	19.8
			94	1.3	53
S2	2.62	30	35	1.92	22
			94	5.16	59
S3	7.77	20	35	5.69	14.7
			94	15.3	39.4

s = rms height
l = correlation length
$k = 2\pi / \lambda$

Table 2. Summary of soil properties.

Surface	ρ_b	ν_a	d_p mm	d_v mm	m_v 0-1 cm	m_v 2-3 cm	ϵ_r 35 GHz	ϵ_r 94 GHz
S1-dry	1.69	0.36	0.3	0.165	0.02	0.08	(3.1, 0.05)	(3.1, 0.05)
S1-wet	1.69	0.36	0.3	0.165	0.23	0.19	(7.3,4.5)	(5.0,2.4)
S2-dry	1.37	0.45	0.3	0.165	0.04	0.07	(2.5, 0.05)	(2.5, 0.05)
S2-wet	1.37	0.45	0.3	0.165	0.12	0.12	(4.6,2.0)	(3.5,1.1)
S3-dry	1.32	0.50	0.3	0.242	0.04	0.07	(2.5, 0.05)	(2.5, 0.05)
S3-wet	1.32	0.50	0.3	0.242	0.19	0.18	(5.9,3.5)	(4.1,1.9)

ρ_b = soil bulk density (g/cm^3).
ν_a = air-voids volume fraction.
d_p = mean soil particle diameter.
d_v = mean air-void diameter.
m_v = volumetric moisture content.
ϵ_r = effective dielectric constant.
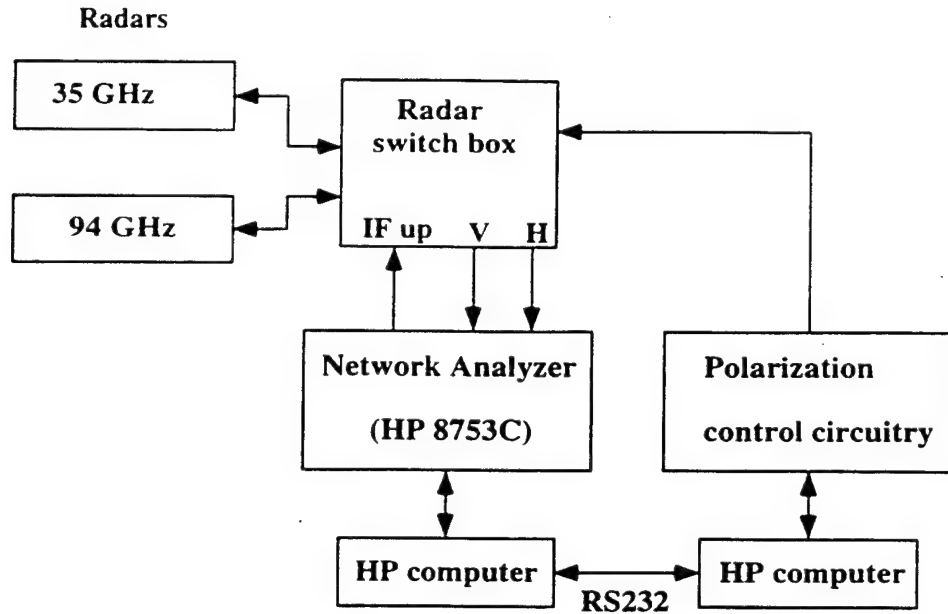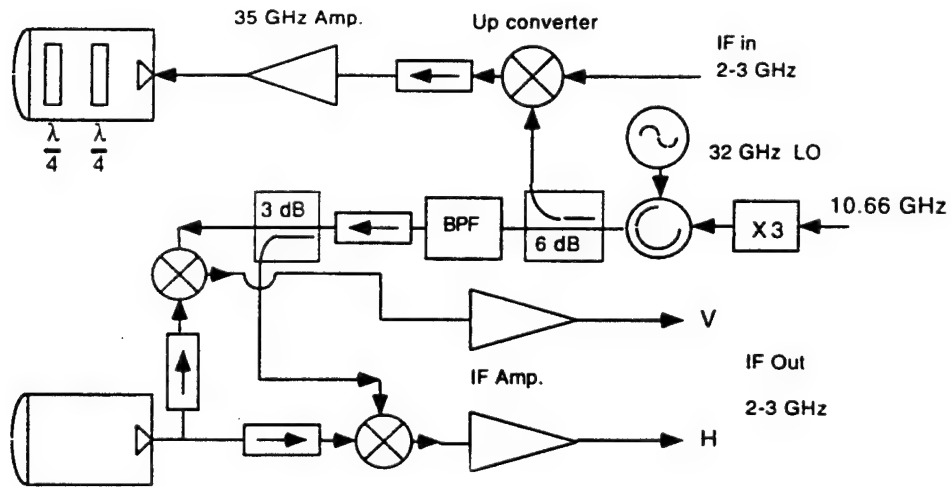
Figure 1: Overview diagram of the MMW polarimetric radar system (a) system block diagram, (b) RF front end circuitry of the 35 GHz radar.

Samples of The Surface Height Profiles
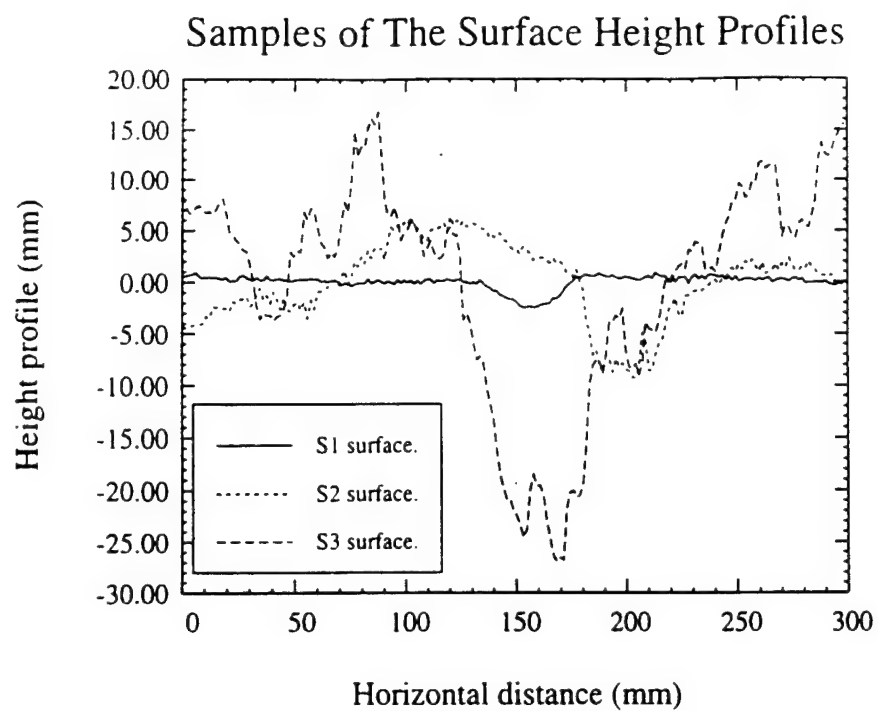
(a)
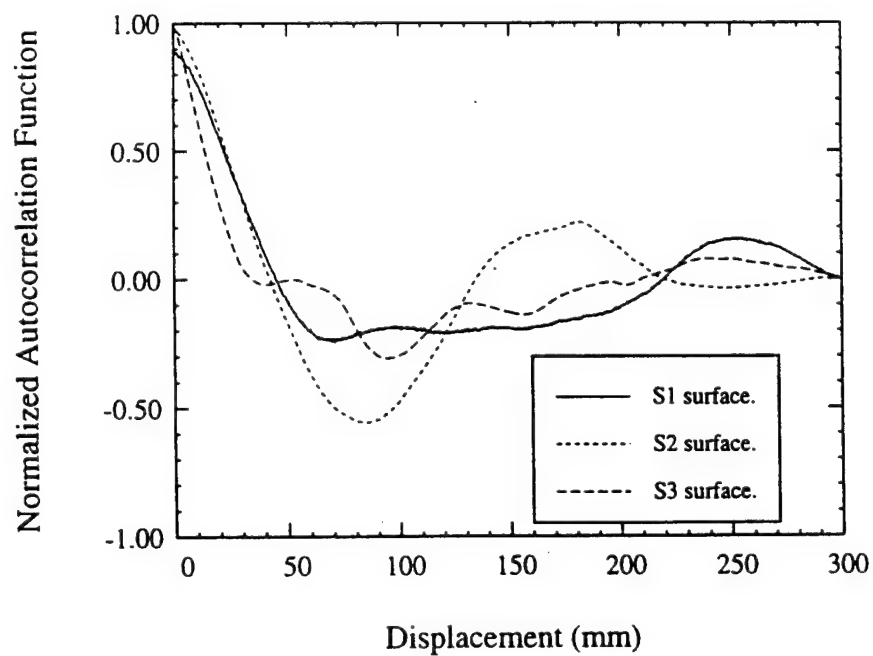
(b)

Figure 2: (a)Samples of the Surface height profiles, measured using a laser profiler. and (b) auto-correlation functions of the three surfaces.

Soil Particle Size Distribution

(a)

Histogram of Air Void Diameter
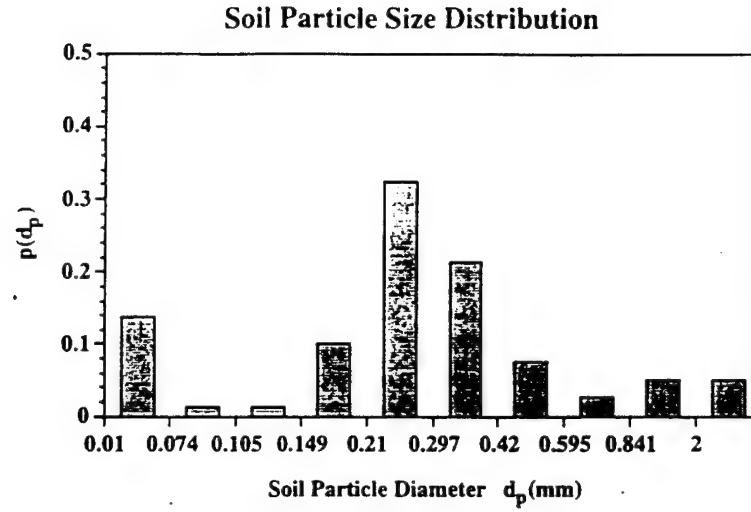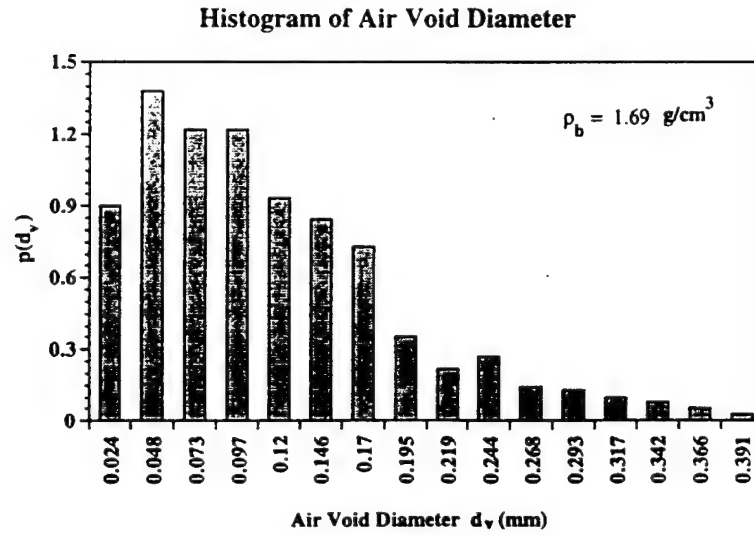
(b)

Figure 3: Histogram of (a) soil particle size distribution $p(d_p)$ and (b) void-size distribution $p(d_v)$ for the soil with $\rho_b = 1.69$ g/cm^3.

16

S1-wet at 35 GHz.
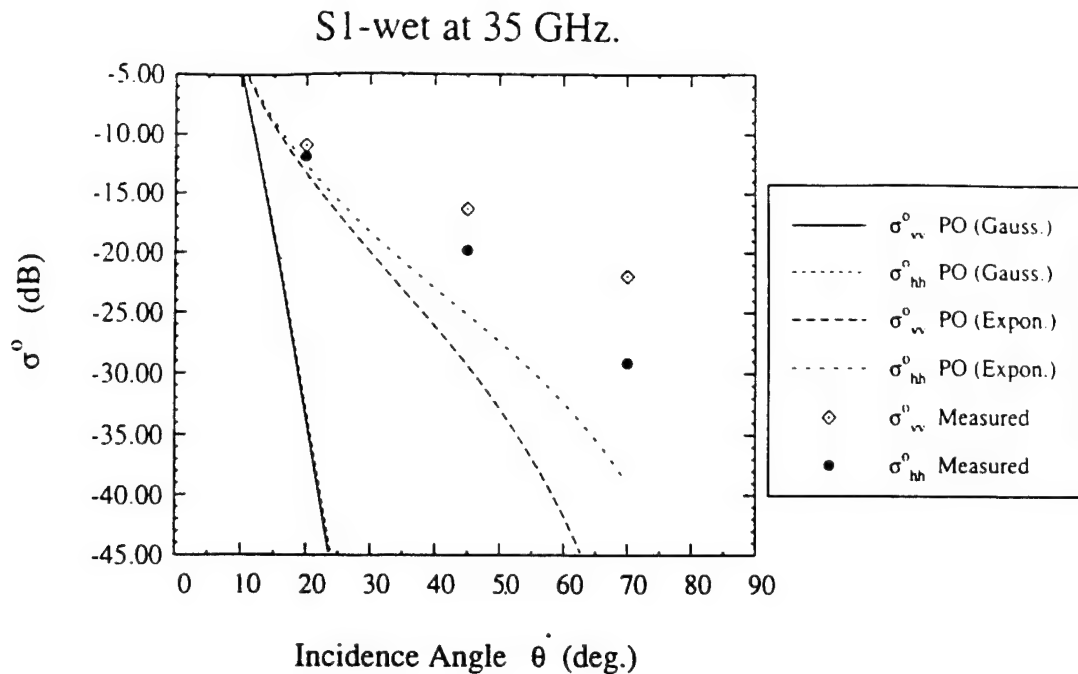
(a)
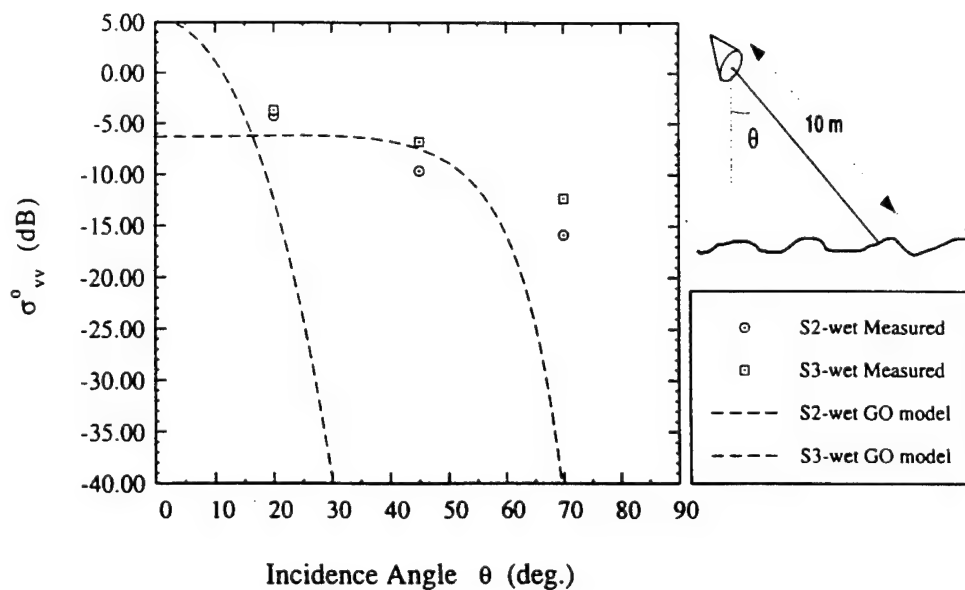
(b)

Figure 4: Comparison between (a) measured data for surface S1 and predictions based on the physical optics (PO) model at 35 GHz for both gaussian and exponential surface height autocorrelation functions, and (b) measured data for surfaces S2 and S3 and predictions based on the geometric optics (GO) model at 94 GHz.

17
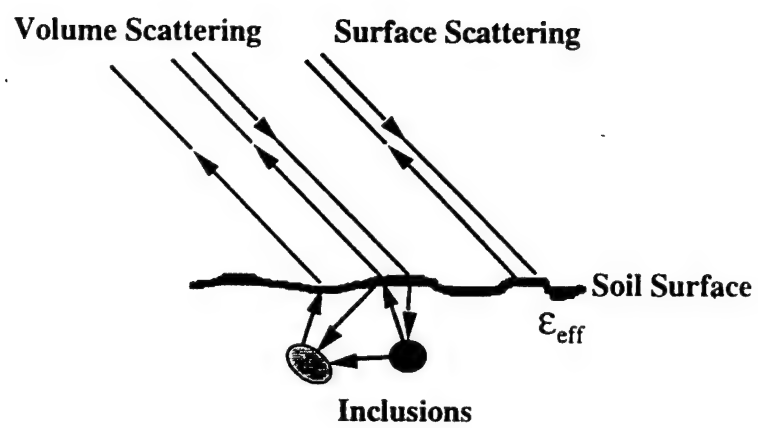
Figure 5: Surface and volume-scattering mechanisms contributing to the total backscatter.

S1-wet surface at 35 GHz.

S3-wet surface at 94 GHz.
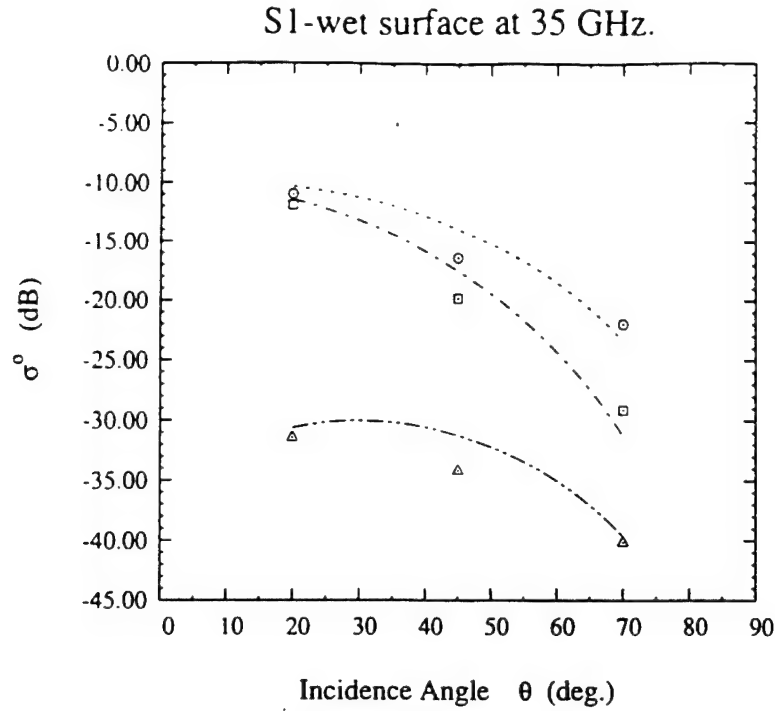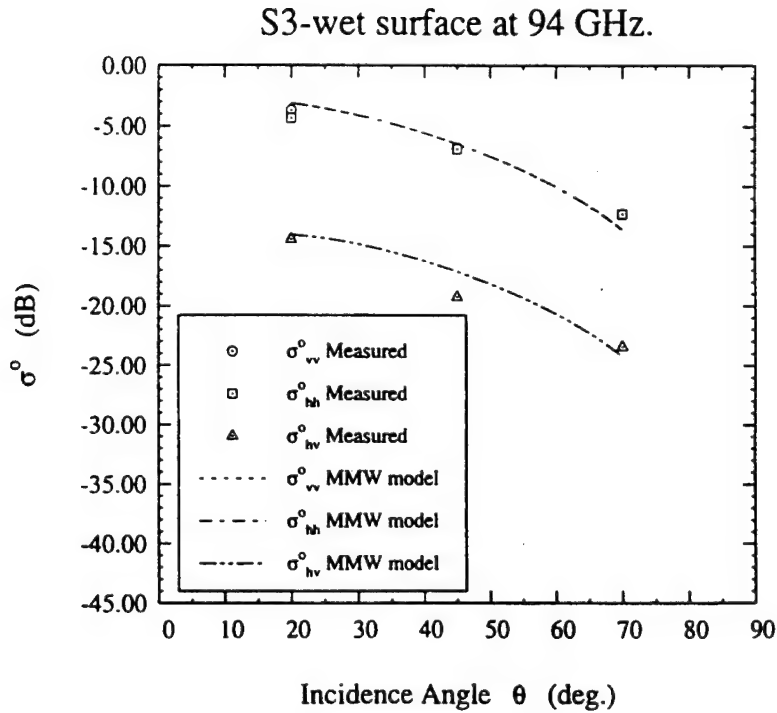
Figure 6: Comparison of the measured backscattering coefficients for wet soil surfaces with calculations based on the semi-empirical surface scattering model given in Section 3 for (a) the smoothest surface at 35 GHz ($ks = 0.48$), and (b) the roughest surface at 94 GHz ($ks = 15.3$).
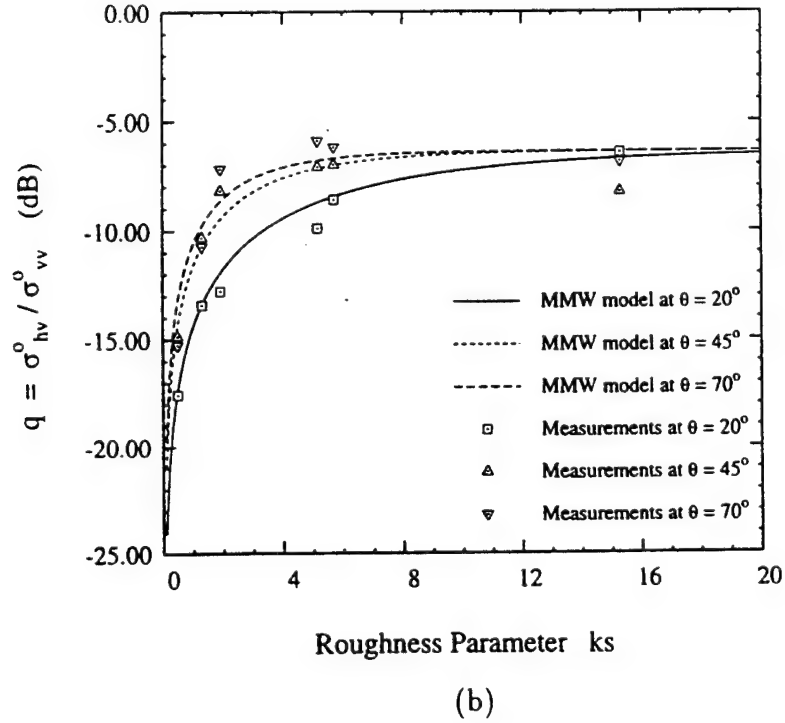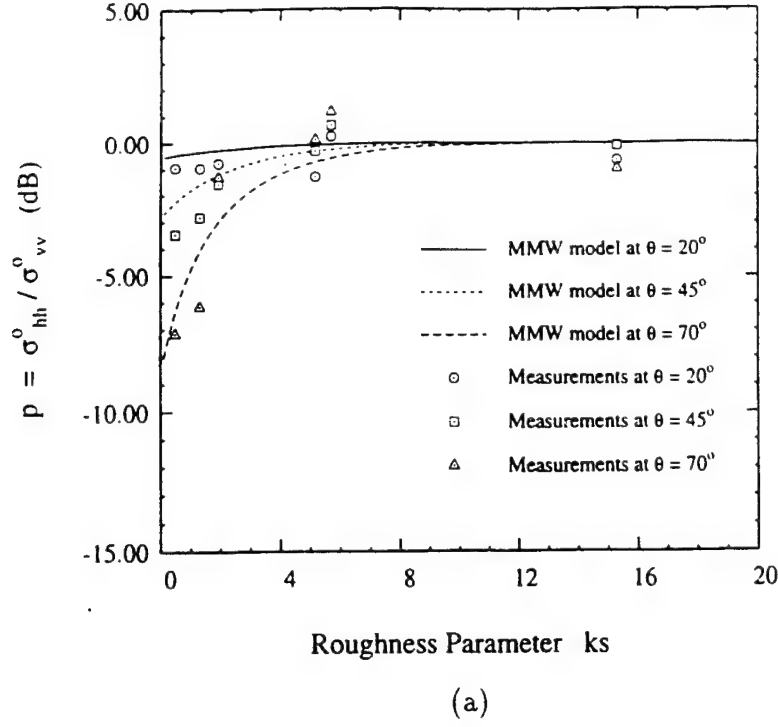
Figure 7: Measured sensitivity of (a) the co-polarized ratio p, and (b) the cross-polarized ratio q (normalized to $\sqrt{\Gamma_o}$) to surface roughness for wet soil surfaces at various incidence angles. The continuous curves are based on the expressions given in Section 3.
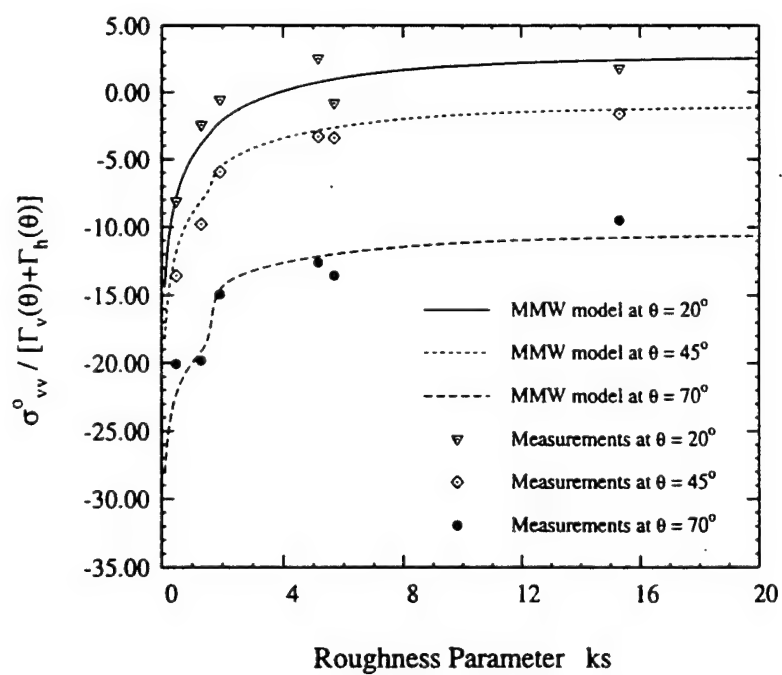
Figure 8: The sensitivity of σ_{vv}^o to surface roughness for wet soils at various incidence angles.

S2-wet surface at 35 GHz.

(a)

S2-wet surface at 94 GHz.

(b)
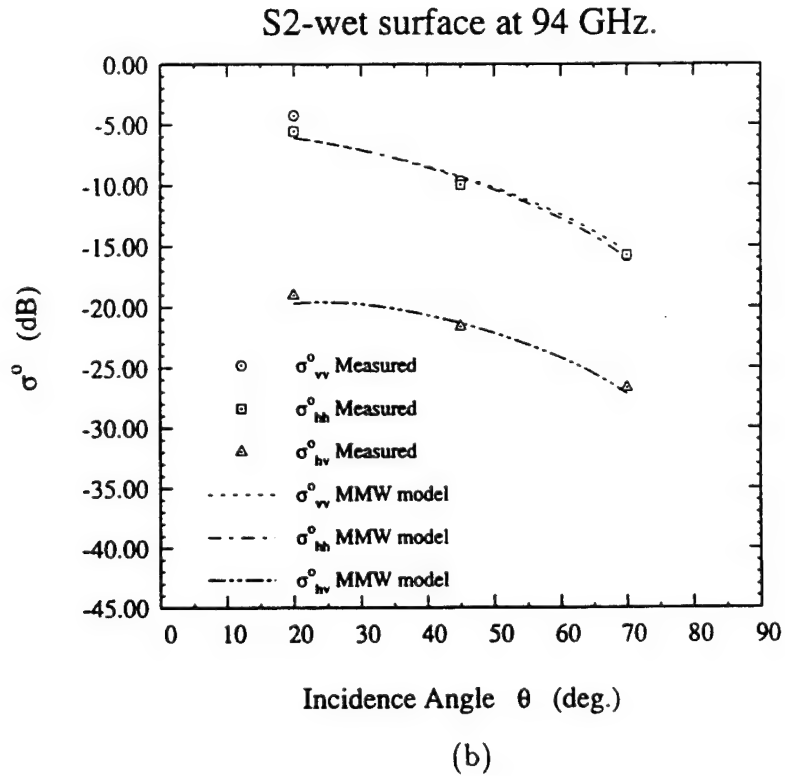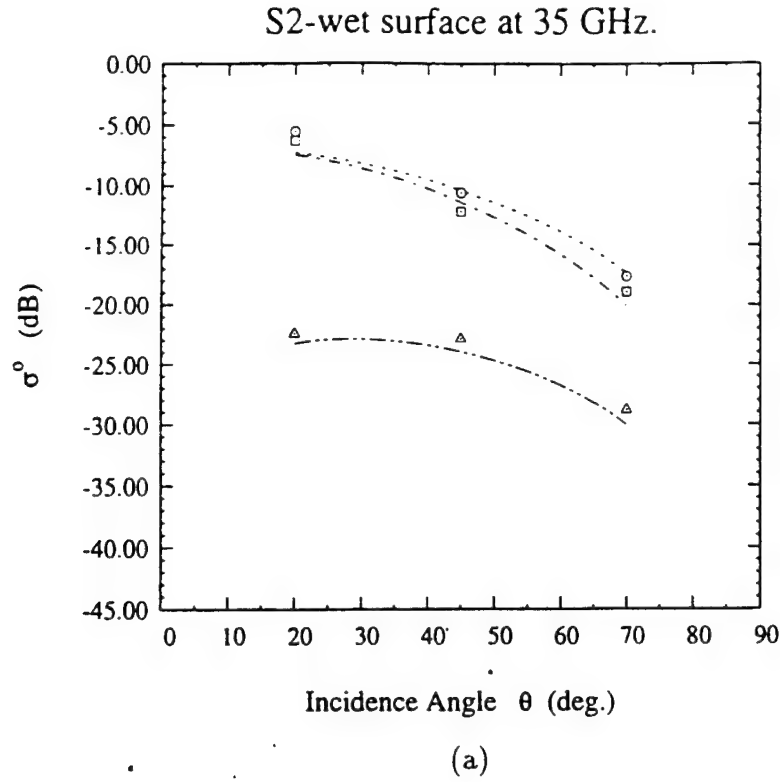
Figure 9: Comparison between measured data of S2-wet soil surface and the MMW semi-empirical surface scattering model at (a) 35 GHz, (b) 94 GHz.

22
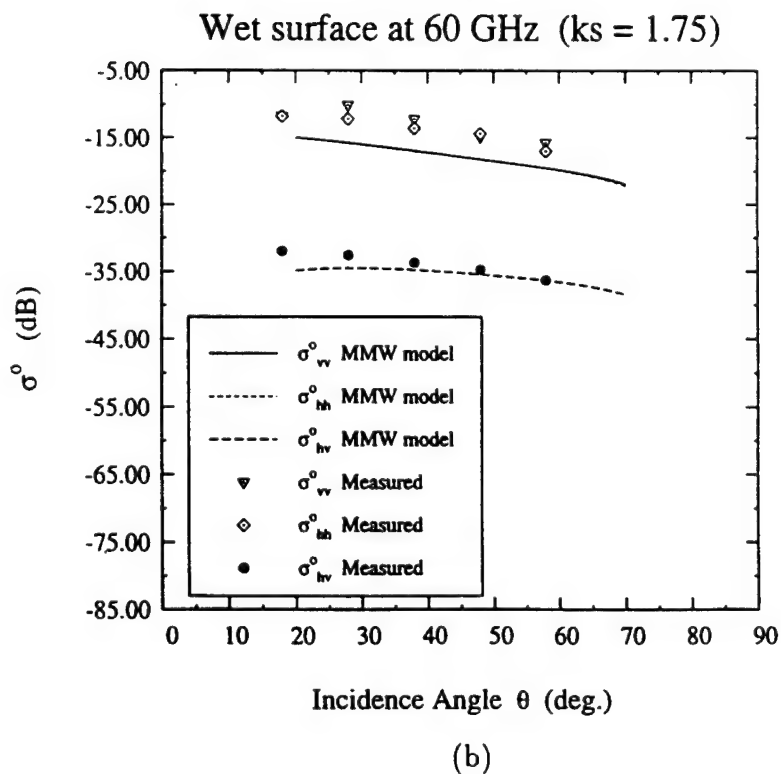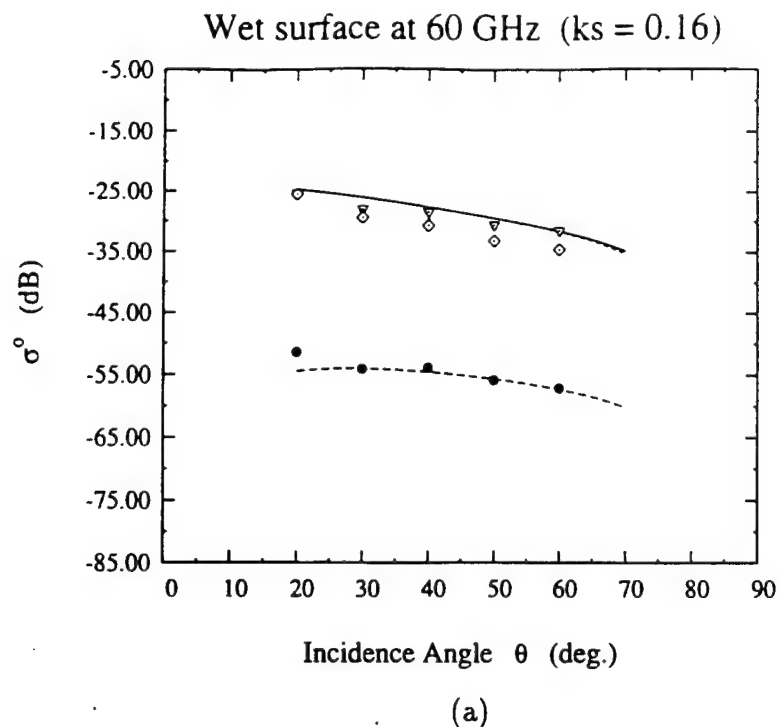
Figure 10: Comparison between measured data for wet soil surfaces ($\epsilon_r = 1.9 + j\,0.4$) at 60 GHz and the MMW semi-empirical surface scattering model for (a) $ks = 0.16$, and (b) $ks = 1.75$. (Data from Yamasaki *et al.* [3]).
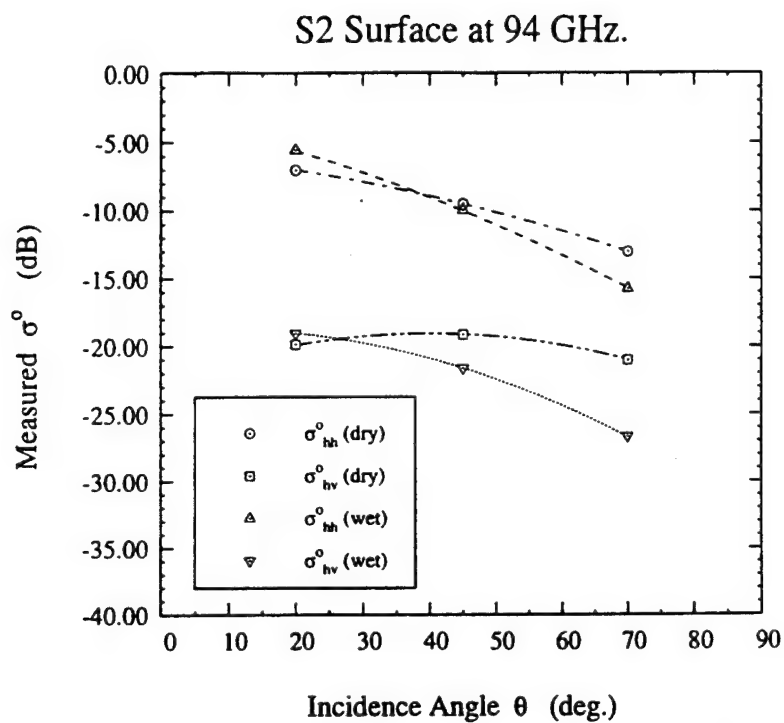
Figure 11: Measured σ_{hh}^o and σ_{hv}^o for wet and dry surface conditions at 94 GHz ($ks = 5.16$). Note that at 70°, σ^o(dry) is greater than σ^o(wet) for both polarizations, evidence of volume scattering contribution.
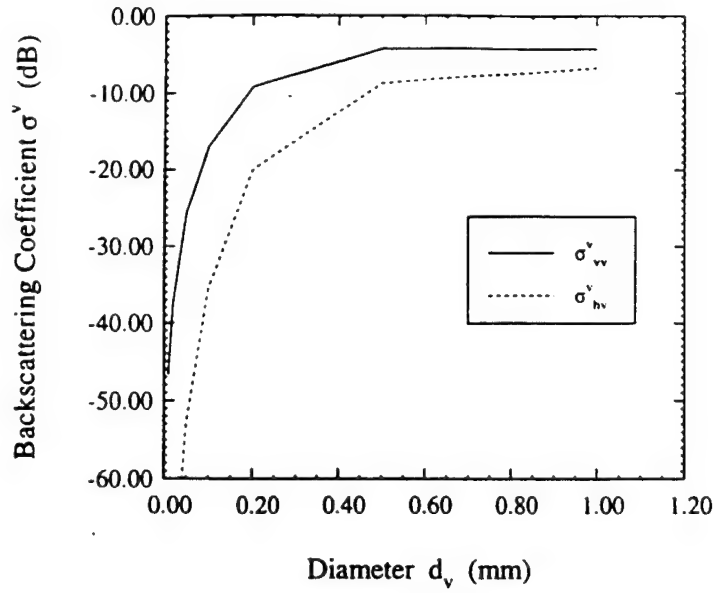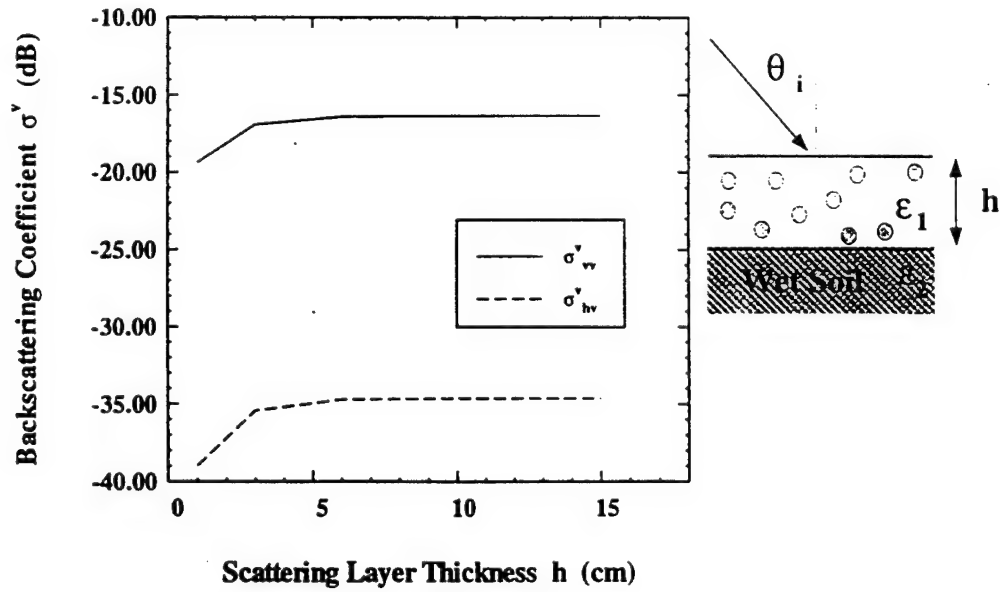
Figure 12: Computed sensitivity of σ^v to (a) particle diameter (for layer thinkness $h = 3$ cm), and (b) scattering layer thickness (for particle diameter $d_v = 0.1$ mm). The computations were conducted at 94 GHz for an incidence angle $\theta = 20°$ and void volume fraction $\nu_a = 0.36$.

25

S1-dry at 35 GHz.

(a)

S1-dry at 94 GHz.

(b)
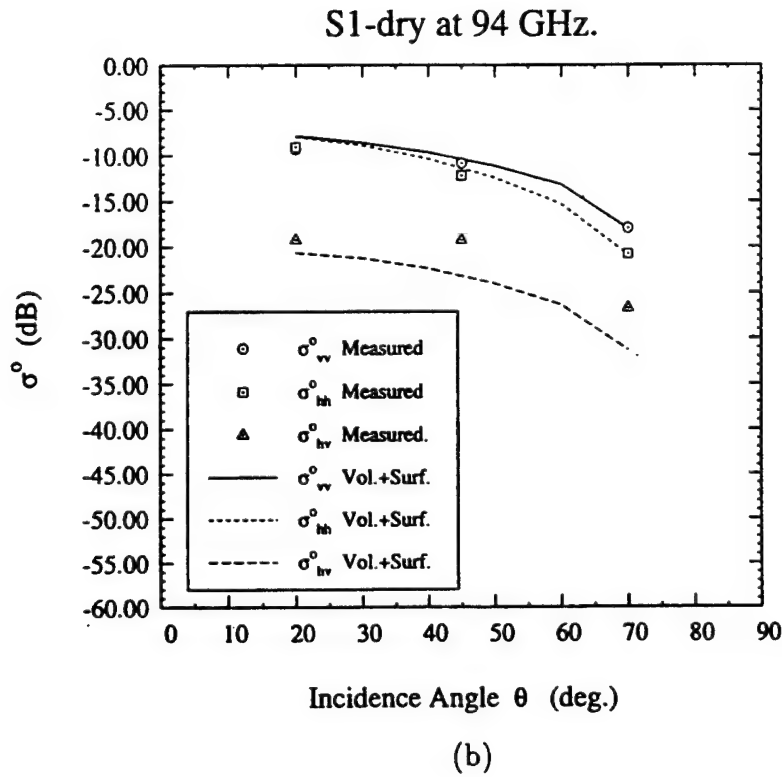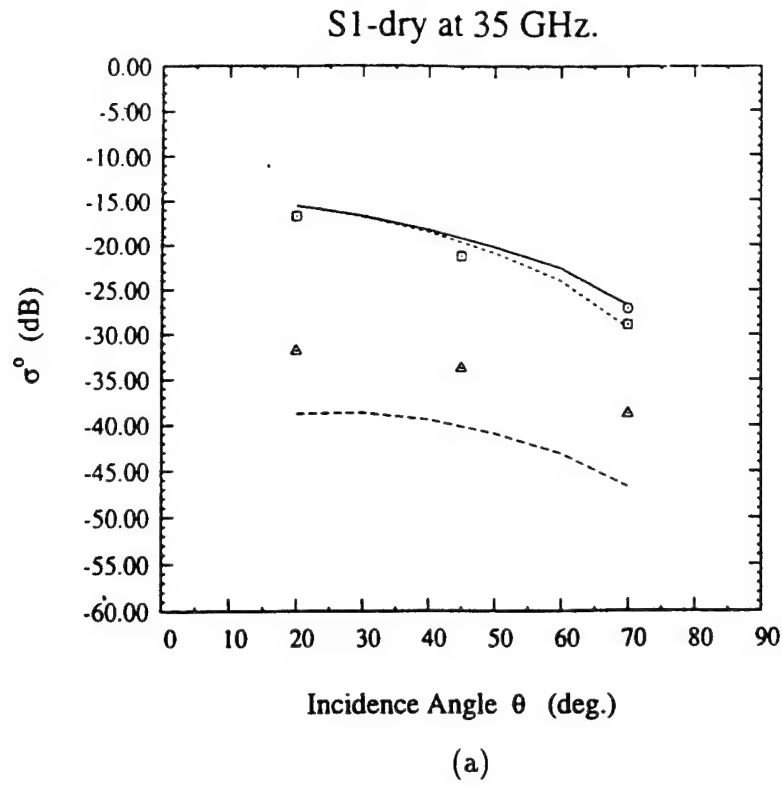
Figure 13: Comparison between the measured backscattering coefficient and the total backscattering coefficient σ^o predicted by the sum of surface and volume scattering contributions for surface S1 at (a) 35 GHz and (b) 94 GHz.
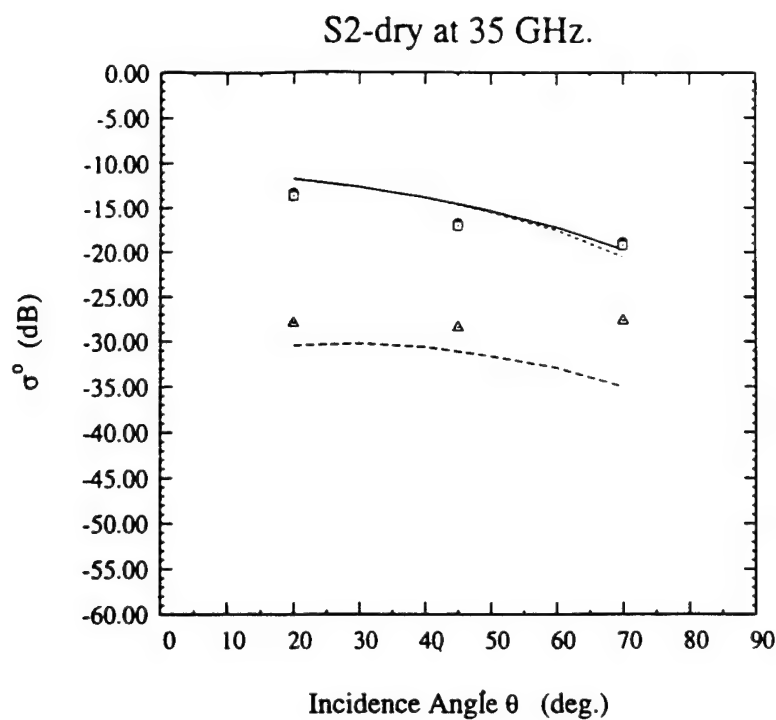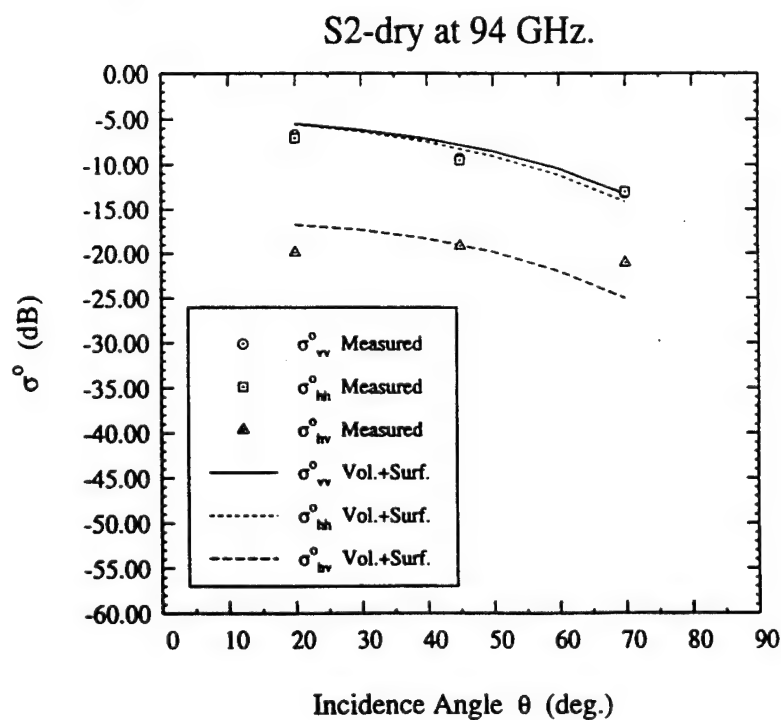
Figure 14: Comparison between the measured backscattering coefficient and the total backscattering coefficient σ^o predicted by the sum of surface and volume scattering contributions for surface S2 at (a) 35 GHz and (b) 94 GHz.
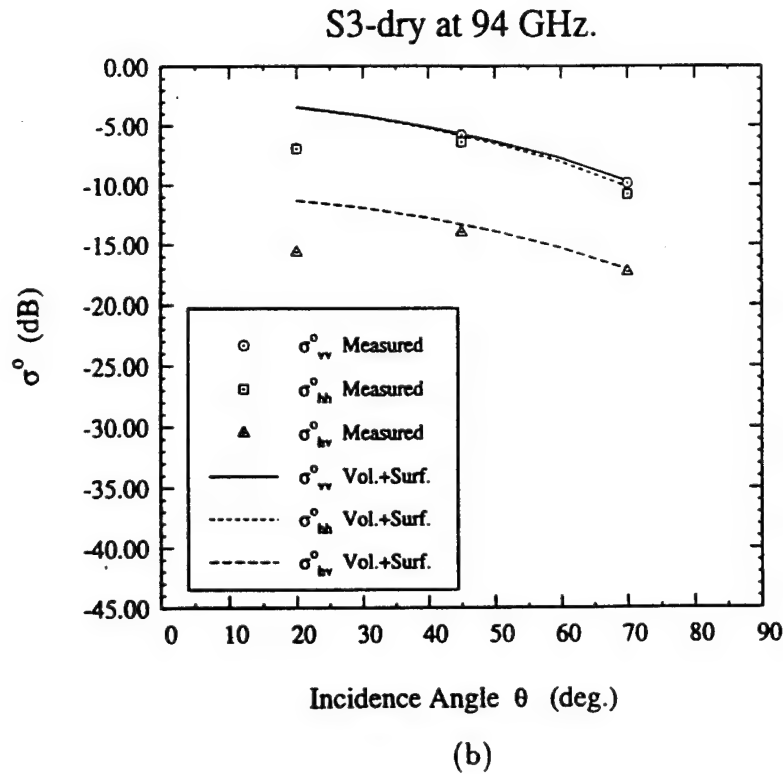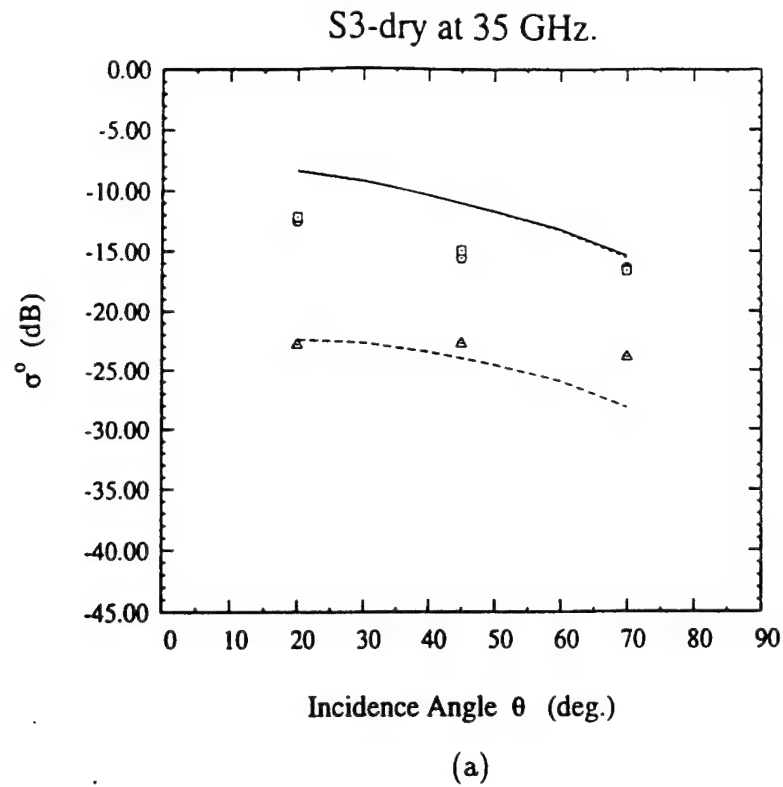
Figure 15: Comparison between the measured backscattering coefficient and the total backscattering coefficient σ° predicted by the sum of surface and volume scattering contributions for surface S3 at (a) 35 GHz and (b) 94 GHz.

S3-dry at 94 GHz.

(a)

S3-dry at 94 GHz.

(b)
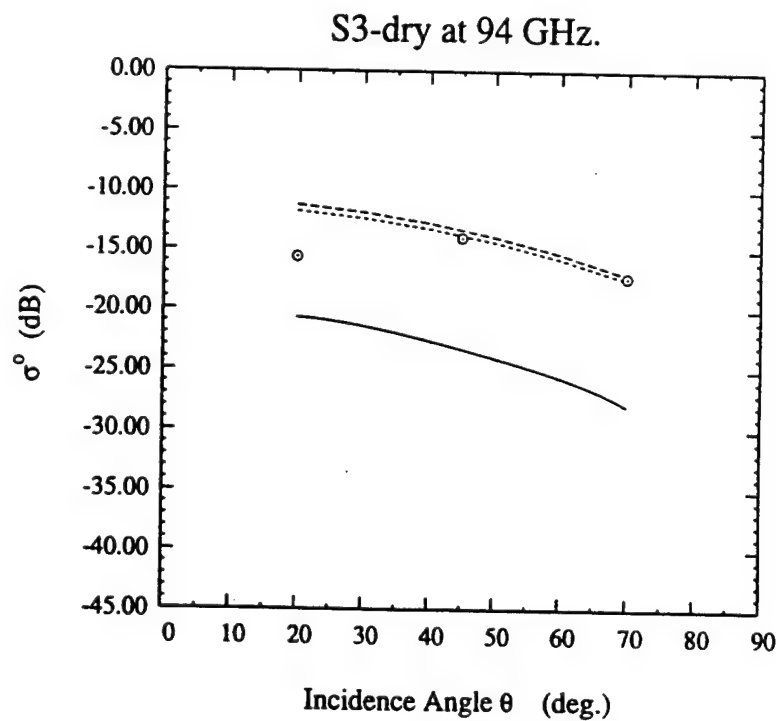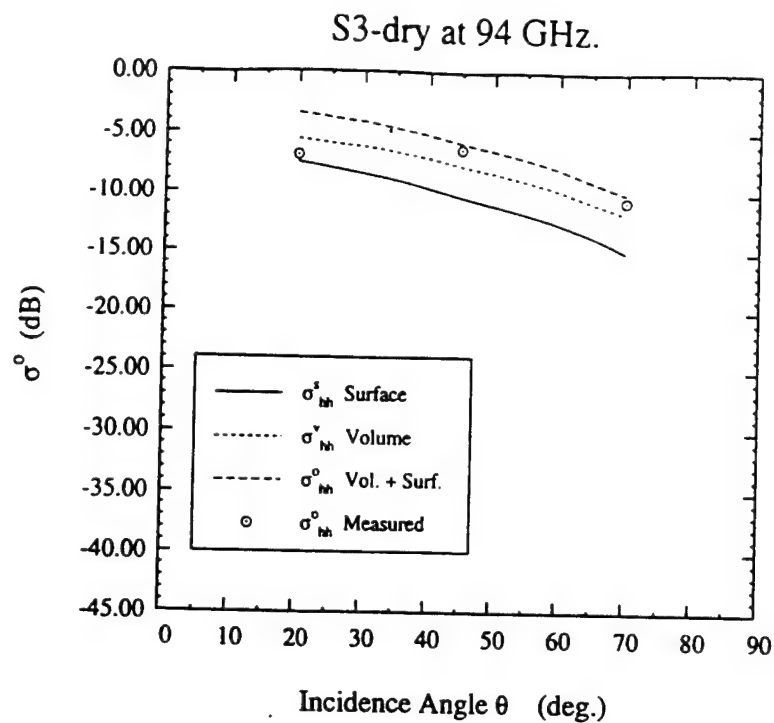
Figure 16: Contributions of the surface-scattering component alone, the volume-scattering component alone, and the sum of both components for surface S3 at 94 GHz: (a) σ_{hh}^o (b) σ_{hv}^o.

29

Measurement and Calibration of Differential Mueller Matrix of Distributed Targets

Kamal Sarabandi, *Member, IEEE*, Yisok Oh, *Student Member, IEEE*, and
Fawwaz T. Ulaby, *Fellow, IEEE*

Abstract—The recent interest in radar polarimetry has led to the development of several calibration techniques to retrieve the Mueller matrix of a distributed target from the multipolarization backscatter measurements recorded by a radar system. Because a distributed target is regarded as a statistically uniform random medium, the measurements usually are conducted for a large number of independent samples (usually spatially independent locations), from which the appropriate statistics characterizing the elements of the Mueller matrix can be derived. Existing calibration methods rely on two major assumptions. The first is that the illuminated area of the distributed target is regarded as a single equivalent point target located along the antenna's boresight direction, and that the statistics of the scattering from all of the measured equivalent point targets (representing the spatially independent samples observed by the radar) are indeed the same as the actual scattering statistics of the distributed target. The second assumption pertains to the process by which the actual measurements made by the radar for a given illuminated area are transformed into the scattering matrix of that area. The process involves measuring the radar response of a point calibration target of known scattering matrix, located along the boresight direction of the antenna, and then modifying the measured response by a constant, known as the illumination integral, when observing the distributed target. The illumination integral accounts for only magnitude variations of the illuminating fields. Thus, possible phase variations or antenna crosstalk variations (between orthogonal polarization channels) across the beam are totally ignored, which may compromise the calibration accuracy. To rectify this deficiency of existing calibration techniques, a new technique is proposed with which the radar polarization distortion matrix is characterized completely by measuring the polarimetric response of a sphere over the entire main lobe of the antenna, rather than along only the boresight direction. Additionally, the concept of a "differential Mueller matrix" is introduced, and by defining and using a correlation–calibration matrix derived from the measured radar distortion matrices, the differential Mueller matrix is accurately calibrated. Comparison of data based on the previous and the new techniques shows significant improvement in the measurement accuracy of the copolarized and cross-polarized phase difference statistics.

I. INTRODUCTION

THE literature contains a variety of different methods for measuring the backscattering cross section of point targets. In all cases, however, the calibration part of

the measurement process involves a comparison of the measured radar response due to the unknown target with the measured response due to a calibration target of known radar cross section. Under ideal conditions, both the unknown and calibration targets are placed along the antenna boresight direction, thereby ensuring that both targets are subjected to the same illumination by the radar antenna. The situation is markedly different for distributed targets; the unknown distributed target is illuminated by the full antenna beam, whereas the calibration target—being of necessity a point target—is illuminated by only a narrow segment of the beam centered around the boresight direction. Consequently, both the magnitude and phase variations across the antenna pattern become part of the measurement process.

The magnitude variation usually is taken into account through a calculation of the illumination integral [1]–[4], but the phase variation has so far been ignored. The role of this phase variation across the beam with regard to polarimetric radar measurements and the means for taking it into account in the measurement process are the subject of this paper.

Terrain surfaces, including vegetation-covered and snow-covered ground, are treated as random media with statistically uniform properties. In radar measurements, the quantities of interest are the statistical properties of the scattered field per unit area. One such quantity is the scattering coefficient σ^o, which is defined in terms of the second moment of the scattered field:

$$\sigma^o = \lim_{r \to \infty} \lim_{A \to \infty} \frac{4\pi r^2}{A} \cdot \frac{\langle |E^s|^2 \rangle}{|E^i|^2}$$

where E^i and E^s are the incident and scattered fields, A is the illuminated area, and r is the range between the target area and the observation point. The above definition of σ^o is based on the assumption that the target is illuminated by a plane wave. Although in practice such a condition cannot be absolutely satisfied, it can be approximately satisfied under certain circumstances. The correlation length l of a distributed target represents the distance over which two points are likely to be correlated, implying that the currents induced at the two points due to an incident wave will likely be correlated as well. Thus, the correlation length may serve as the effective dimension of individual scatterers comprising the distributed target. The plane-wave approximation may be considered

valid as long as the magnitude and phase variations of the incident wave are very small across a distance of several correlation lengths. In most practical situations, this "local" plane-wave approximation is almost always satisfied. When this is not the case, the measured radar response will depend on both the illumination pattern and the statistics of the distributed target [5], [6].

An implied assumption in the preceding discussion is that the phase variation across the antenna beam is the same for both the transmit and receive antennas. When making polarimetric measurements with dual-polarized transmit and receive antennas, the phase variation of the transmit and receive patterns may be different, which may lead to errors in the measurement of the scattering matrix of the target, unless the variations are known for all of the polarization combinations used in the measurement process and they are properly accounted for in the calibration process.

In this paper, we introduce a calibration procedure that accounts for magnitude and phase imbalances and antenna crosstalk across the entire main beam of the antenna. By applying this procedure, we can make accurate measurements of the differential Mueller matrix of a distributed target using the local plane-wave approximation. The differential Mueller matrix can then be used to compute the scattering coefficient for any desired combination of receive and transmit antenna polarizations, and by employing a recently developed technique [7], the statistics of the polarization phase differences can also be obtained. By way of illustrating the utility of the proposed measurement technique, we will compare the results of backscatter measurements acquired by a polarimetric scatterometer system for bare soil surfaces using the new technique with those based on calibrating the system with the traditional approach, which relies on measuring the response due to a calibration target placed along only the boresight direction of the antenna beam.

II. THEORY

Consider a planar distributed target illuminated by a polarimetric radar system as shown in Fig. 1. Suppose the distributed target is statistically homogeneous and the antenna beam is narrow enough so that the backscattering statistics of the target can be assumed constant over the illuminated area. Let us subdivide the illumination area into a finite number of pixels, each including many scatterers (or many correlation lengths), and denote the scattering matrix of the ijth pixel by $\Delta \overline{\overline{S}}(x_i, y_j)$. The scattering matrix of each pixel can be considered as a complex random vector. If the radar system and its antenna are ideal, the scattered field associated with the ijth pixel is related to the incident field by

$$\begin{bmatrix} E_v^s \\ E_h^s \end{bmatrix} = K \frac{e^{2ik_0 r(x_i, y_j)}}{r(x_i, y_j)^2} \begin{bmatrix} \Delta S_{vv}(x_i, y_j) & \Delta S_{vh}(x_i, y_j) \\ \Delta S_{hv}(x_i, y_i) & \Delta S_{hh}(x_i, y_j) \end{bmatrix} \begin{bmatrix} E_v^i \\ E_h^i \end{bmatrix}$$
(1)

where E_v and E_h are the components of the electric field along two orthogonal directions in a plane perpendicular
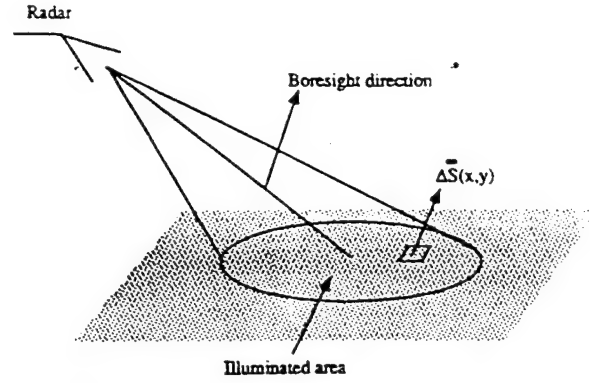

Fig. 1. Geometry of a radar system illuminating a homogeneous distributed target.

to the direction of propagation and K is a constant. In reality, radar systems are not ideal in the sense that the vertical and horizontal channels of the transmitter and receiver are not identical, and the radar antenna introduces some coupling between the vertical and horizontal signals at both transmission and reception. Consequently, the measured scattering matrix $\overline{\overline{U}}$ is related to the actual scattering matrix of a point target $\overline{\overline{S}}$ by [8]

$$\overline{\overline{U}} = \frac{e^{2ik_0 r}}{r^2} \overline{\overline{R}} \, \overline{\overline{S}} \, \overline{\overline{T}}$$
(2)

where $\overline{\overline{R}}$ and $\overline{\overline{T}}$ are known as the receive and transmit distortion matrices. For small point targets where the illumination pattern of the incident field can be approximated by a uniform plane wave, measurement of $\overline{\overline{S}}$ is rather straightforward, and in recent years, this problem has been investigated thoroughly by many investigators [9]–[11]. The distortion matrices are obtained by measuring one or more targets of known scattering matrices, and then by inverting (2), the scattering matrix of the unknown target is obtained. In the case of distributed targets, however, distributed calibration targets do not exist. Moreover, the distortion matrices and the distance to the scattering points are all functions of position. That is, for the ijth pixel, the measured differential scattering matrix $\Delta \overline{\overline{U}}$ can be expressed by

$$\Delta \overline{\overline{U}} = \frac{e^{2ik_0 r(x_i, y_j)}}{r^2(x_i, y_j)} \overline{\overline{R}}(x_i, y_j)$$
$$\cdot \begin{bmatrix} \Delta S_{vv}(x_i, y_j) & \Delta S_{vh}(x_i, y_j) \\ \Delta S_{hv}(x_i, y_j) & \Delta S_{hh}(x_i, y_j) \end{bmatrix} \overline{\overline{T}}(x_i, y_j).$$
(3)

The radar measures the sum of fields backscattered from all pixels within the illuminated area coherently, i.e.,

$$\overline{\overline{U}} = \sum_i \sum_j \frac{e^{2ik_0 r(x_i, y_j)}}{r^2(x_i, y_j)} \overline{\overline{R}}(x_i, y_j) \Delta \overline{\overline{S}}(x_i, y_j) \overline{\overline{T}}(x_i, y_j).$$
(4)

Thus, the measured scattering matrix is a linear function of the random scattering matrices of the pixels. For uniform distributed targets, we are interested in deriving information about the statistics of the differential scatter-

ing matrix from statistics of the measured scattering matrix $\overline{\overline{\mathbf{U}}}$. One step in relating the desired quantities to the measured ones is to perform a calibration procedure to remove the distortions caused by the radar and the antenna systems. The traditional approach used for calibrating polarimetric measurements of extended-area targets relies on two approximations. First, it is assumed that for each measured sample, the differential scattering matrix of the illuminated area is equal to some equivalent scattering matrix at boresight. Using this approximation, it is hoped that the equivalent scattering matrix has the same statistics as the original differential scattering matrix. This approximation is purely heuristic and cannot be justified mathematically. Second, the measured data for each sample are calibrated as if they were a point target, and the result is modified by a constant known as the illumination integral to account for the nonuniform illumination [3], [4]; thus, the crosstalk variations away from the antenna's boresight direction over the illuminated area are ignored. The illumination integral accounts for only magnitude variations of the gain patterns of the transmitter and receiver antennas, and no provision is made for accounting for any possible phase variations in the radiation patterns.

In this paper, we attempt to derive the second moments of the differential scattering matrix from the statistics of the measured matrix without making any approximation in the radar distortion matrices or using the equivalent differential scattering matrix representation. In random polarimetry, the scattering characteristics of a distributed target usually are represented by its Mueller matrix, which is the averaged Stokes matrix [4]. The Mueller matrix contains the second moments of the scattering matrix elements. By the central limit theorem, if the scatterers in the illuminated area are numerous and are of the same type, then the statistics describing the scattering are Gaussian (Rayleigh statistics). In such cases, knowledge of the Mueller matrix is sufficient to describe the scattering statistics of the target [7].

In a manner analogous with the definition of the scattering coefficient as the scattering cross section per unit area, let us define the differential Mueller matrix $\overline{\overline{\mathbf{M}}}^o$ as the ratio of the Mueller matrix $(\Delta \overline{\overline{\mathbf{M}}})$ derived from the differential scattering matrix $(\Delta \overline{\mathbf{S}})$ to the differential area, i.e.,

$$\overline{\overline{\mathbf{M}}}^o = \lim_{\Delta A \to 0} \frac{\Delta \overline{\overline{\mathbf{M}}}}{\Delta A}.$$

To compute the differential Mueller matrix, the ensemble average of the cross products of the differential matrix components is needed. Let us define

$$\overline{\overline{\mathbf{W}}}^o = \begin{bmatrix} \langle S_{vv}^{o*} S_{vv}^o \rangle & \langle S_{vh}^{o*} S_{vh}^o \rangle & \langle S_{vh}^{o*} S_{vv}^o \rangle & \langle S_{vv}^{o*} S_{vh}^o \rangle \\ \langle S_{hv}^{o*} S_{hv}^o \rangle & \langle S_{hh}^{o*} S_{hh}^o \rangle & \langle S_{hh}^{o*} S_{hv}^o \rangle & \langle S_{hv}^{o*} S_{hh}^o \rangle \\ \langle S_{hv}^{o*} S_{vv}^o \rangle & \langle S_{hh}^{o*} S_{vh}^o \rangle & \langle S_{hh}^{o*} S_{vv}^o \rangle & \langle S_{hv}^{o*} S_{vh}^o \rangle \\ \langle S_{vv}^{o*} S_{hv}^o \rangle & \langle S_{vh}^{o*} S_{hh}^o \rangle & \langle S_{vh}^{o*} S_{hv}^o \rangle & \langle S_{vv}^{o*} S_{hh}^o \rangle \end{bmatrix}$$

$$(5)$$

where

$$\langle S_{pq}^{o*} S_{st}^o \rangle = \lim_{\Delta A \to 0} \frac{\langle \Delta S_{pq}^* \Delta S_{st} \rangle}{\Delta A}.$$

In terms of the correlation matrix $\overline{\overline{\mathbf{W}}}^o$, the differential Mueller matrix can be computed from

$$\overline{\overline{\mathbf{M}}}^o = 4 \pi \nu \overline{\overline{\mathbf{W}}}^o \nu^{-1} \tag{6}$$

where [4]

$$\nu = \begin{pmatrix} 1 & 0 & 0 & 0 \\ 0 & 1 & 0 & 0 \\ 0 & 0 & 1 & 1 \\ 0 & 0 & -i & i \end{pmatrix}.$$

In order to calibrate a radar system so as to measure the differential Mueller matrix, let us represent each 2×2 matrix in (4) by a corresponding four-component vector, in which case (4) simplifies to

$$\overline{\mathscr{U}} = \sum_i \sum_j \frac{e^{2ik_0 r(x_i, y_j)}}{r^2(x_i, y_j)} \overline{\overline{\mathbf{D}}}(x_i, y_j) \overline{\Delta \mathscr{S}}(x_i, y_j) \tag{7}$$

where

$$\overline{\mathscr{U}} = \begin{bmatrix} U_{vv} \\ U_{vh} \\ U_{hv} \\ U_{hh} \end{bmatrix}, \qquad \overline{\Delta \mathscr{S}}(x_i, y_j) = \begin{bmatrix} \Delta S_{vv}(x_i, y_j) \\ \Delta S_{vh}(x_i, y_j) \\ \Delta S_{hv}(x_i, y_j) \\ \Delta S_{hh}(x_i, y_j) \end{bmatrix} \tag{8}$$

$$\overline{\mathscr{R}}(x_i, y_j) = \begin{bmatrix} R_{vv}(x_i, y_j) \\ R_{vh}(x_i, y_j) \\ R_{hv}(x_i, y_j) \\ R_{hh}(x_i, y_j) \end{bmatrix}, \qquad \overline{\mathscr{T}}(x_i, y_j) = \begin{bmatrix} T_{vv}(x_i, y_j) \\ T_{vh}(x_i, y_j) \\ T_{hv}(x_i, y_j) \\ T_{hh}(x_i, y_j) \end{bmatrix}$$

and it can be easily shown that

$$\overline{\overline{\mathbf{D}}}(x_i, y_j) = \begin{bmatrix} R_{vv}T_{vv} & R_{vv}T_{vh} & R_{vh}T_{vv} & R_{vh}T_{vh} \\ R_{vv}T_{hv} & R_{vv}T_{hh} & R_{vh}T_{hv} & R_{vh}T_{hh} \\ R_{hv}T_{vv} & R_{hv}T_{vh} & R_{hh}T_{vv} & R_{hh}T_{vh} \\ R_{hv}T_{hv} & R_{hv}T_{hh} & R_{hh}T_{hv} & R_{hh}T_{hh} \end{bmatrix}. \tag{9}$$

The mth component of the measured target vector $(\overline{\mathscr{U}}_m)$ defined by (8) can be obtained from (7), and is given by

$$\mathscr{U}_m = \sum_i \sum_j \frac{e^{2ik_0 r(x_i, y_j)}}{r^2(x_i, y_j)} \left[\sum_{l=1}^{4} D_{ml}(x_i, y_j) \Delta \mathscr{S}_l(x_i, y_j) \right].$$

Thus, the averaged cross products of these components are

$$\langle \mathscr{U}_m \mathscr{U}_n^* \rangle = \sum_i \sum_j \sum_{i'} \sum_{j'} \frac{e^{2ik_0 [r(x_i, y_j) - r(x_{i'}, y_{j'})]}}{r^2(x_i, y_j) r^2(x_{i'}, y_{j'})}$$

$$\cdot \sum_{l=1}^{4} \sum_{p=1}^{4} D_{ml}(x_i, y_j) D_{np}^*(x_{i'}, y_{j'})$$

$$\left\langle \Delta \mathscr{S}_l(x_i, y_j) \Delta \mathscr{S}_p^*(x_{i'}, y_{j'}) \right\rangle. \tag{10}$$

If the number of scatterers in each pixel is assumed to be large, or the correlation length of the surface is much smaller than the pixel dimensions, then

$$\langle \Delta \mathscr{S}_l(x_i, y_j) \Delta \mathscr{S}_p^*(x_{i'}, y_{j'}) \rangle$$

$$= \begin{cases} 0, & i \neq i' \text{ and } j \neq j' \\ \langle \mathscr{S}_l^o \mathscr{S}_p^{o*} \rangle \Delta A_{ij}, & i = i' \text{ and } j = j'. \end{cases}$$

It should be mentioned here again that the target is assumed to be statistically homogeneous, and the antenna beam is assumed to have a narrow beam. Hence, $\langle \mathscr{S}_l^o \mathscr{S}_p^{o*} \rangle$ is not a function of position within the illuminated area. In the limit as ΔA approaches zero, (10) takes the following form:

$$\langle \mathscr{U}_m \mathscr{U}_n^* \rangle = \sum_{l=1}^{4} \sum_{p=1}^{4} \left[\int \int_A \frac{1}{r^4(x, y)} D_{ml}(x, y) \right.$$

$$\left. \cdot D_{np}^*(x, y) \, dx \, dy \right] \langle \mathscr{S}_l^o \mathscr{S}_p^{o*} \rangle. \quad (11)$$

Equation (11) is valid for all combinations of m and n and, therefore, it constitutes 16 equations for the 16 correlation unknowns. Let us denote the measured correlations by a 16-component vector $\bar{\mathscr{Y}}$, and the actual correlations by another 16-component vector $\bar{\mathscr{X}}$ so that

$$\mathscr{X}_i = \langle \mathscr{S}_l^o \mathscr{S}_p^{o*} \rangle, \quad i = 4(l-1) + p$$

$$\mathscr{Y}_j = \langle \mathscr{U}_m \mathscr{U}_n^* \rangle, \quad j = 4(m-1) + n.$$

In this form, (11) reduces to the following matrix equation:

$$\bar{\mathscr{Y}} = \bar{\bar{\mathbf{B}}} \bar{\mathscr{X}} \quad (12)$$

where the ij element of $\bar{\bar{\mathbf{B}}}$ is given by

$$b_{ij} = \int \int_A \frac{1}{r^4(x, y)} D_{ml}(x, y) D_{np}^*(x, y) \, dx \, dy \quad (13)$$

and, as before,

$$i = 4(l-1) + p, \quad j = 4(m-1) + n.$$

Once the elements of the correlation calibration matrix $\bar{\bar{\mathbf{B}}}$ are found from (13), (12) can be inverted to obtain the correlation vector $\bar{\mathscr{X}}$. The elements of the correlation vector are not arbitrary complex numbers; for example, $\mathscr{X}_2$ and $\mathscr{X}_5$ are complex conjugate of each other and $\mathscr{X}_1$ is a real number; thus, these relationships can be used as a criterion for calibration accuracy. The differential Mueller matrix can be obtained from the correlation matrix $\bar{\bar{\mathbf{W}}}^o$ whose entries in terms of the vector $\bar{\mathscr{X}}$ are given by

$$\bar{\bar{\mathbf{W}}}^o = \begin{bmatrix} \mathscr{X}_1 & \mathscr{X}_6 & \mathscr{X}_2 & \mathscr{X}_5 \\ \mathscr{X}_{11} & \mathscr{X}_{16} & \mathscr{X}_{12} & \mathscr{X}_{15} \\ \mathscr{X}_3 & \mathscr{X}_8 & \mathscr{X}_4 & \mathscr{X}_7 \\ \mathscr{X}_9 & \mathscr{X}_{14} & \mathscr{X}_{10} & \mathscr{X}_{13} \end{bmatrix}.$$

Evaluation of the elements of $\bar{\bar{\mathbf{B}}}$ requires knowledge of the radar distortion matrices over the main lobe of the antenna system. The distortion matrices of the radar can be found by applying the calibration method presented in the next section.

III. CALIBRATION PROCEDURE

As was shown in the previous section, the correlation vector $\bar{\mathscr{X}}$ can be obtained if the calibration matrix $\bar{\bar{\mathbf{D}}}(x, y)$ given by (9) is known. A simplified block diagram of a radar system is shown in Fig. 2. The quantities $\bar{t}_v, \bar{t}_h, \bar{r}_v, \bar{r}_h$ represent fluctuating factors of the channel imbalances caused by the active devices in the radar system. Without loss of generality, it is assumed that the nominal value of these factors is one, and their rate of change determines how often the radar must be calibrated. The antenna system also causes some channel distortion due to variations in the antenna pattern and path length differences. The crosstalk contamination occurs in the antenna structure, which is also a function of the direction of radiation. It has been shown that the antenna system, together with two orthogonal directions in a plane perpendicular to the direction of propagation, can be represented as a four-port passive network [8]. Using the reciprocity properties of passive networks, the distortion matrices of the antenna system were shown to be [8]

$$\bar{\bar{\mathscr{R}}}_a(\psi, \xi)$$

$$= \begin{bmatrix} r_v(\psi, \xi) & 0 \\ 0 & r_h(\psi, \xi) \end{bmatrix} \begin{bmatrix} 1 & C(\psi, \xi) \\ C(\psi, \xi) & 1 \end{bmatrix} \quad (14)$$

$$\bar{\bar{\mathscr{T}}}_a(\psi, \xi) = \begin{bmatrix} 1 & C(\psi, \xi) \\ C(\psi, \xi) & 1 \end{bmatrix} \begin{bmatrix} t_v(\psi, \xi) & 0 \\ 0 & t_h(\psi, \xi) \end{bmatrix} \quad (15)$$

where ψ, ξ are some coordinate angles defined with respect to the boresight direction of propagation. The quantity $C(\psi, \xi)$ is the antenna crosstalk factor and $r_v(\psi, \xi), r_h(\psi, \xi), t_v(\psi, \xi), t_h(\psi, \xi)$ are the channel imbalances caused by the antenna system. These quantities are not subject to change due to variations in active devices, and once they are determined, they can be used repeatedly.

In order to find the radar distortion parameters at a given point (x, y) on the surface, we first need to specify a convenient coordinate system with respect to the antenna's boresight direction so that the distortions become independent of incidence angle and range to the target. The azimuth-over-elevation coordinate angles (ψ, ξ) provide a coordinate system that is appropriate for antenna pattern measurements. The angle ξ specifies the elevation angle and ψ specifies the azimuth angle in a plane with elevation ξ, as shown in Fig. 3. The mapping from (ψ, ξ) coordinates to (x, y) coordinates can be obtained by considering a radar at height h with incidence angle θ_0 and the boresight direction in the y–z plane, as shown in Fig. 4. It is easy to show that constant-ξ curves on the surface of a sphere map to constant-y lines and constant-ψ curves map to hyperbolic curves. The mapping functions are
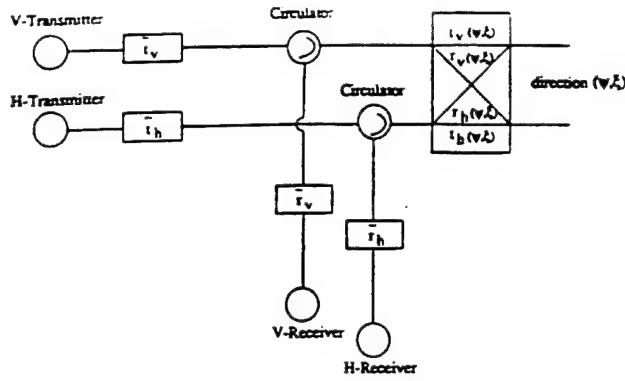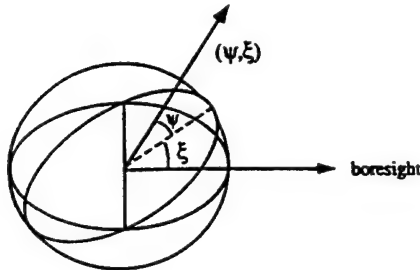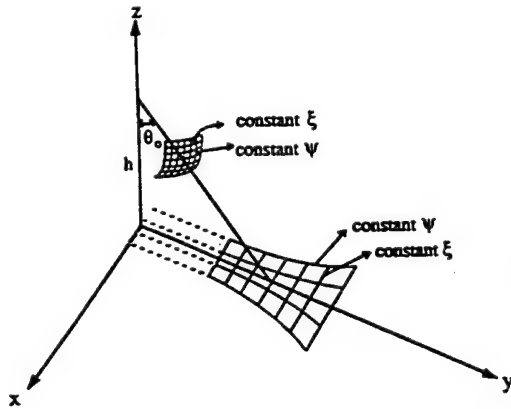
Fig. 2.   Simplified block diagram of a polarimetric radar system.

Fig. 3.   Azimuth-over-elevation coordinate system (ψ, ξ) specifying a point on the surface of a sphere.

Fig. 4.   Geometry of a radar above x–y plane and transformation of azimuth-over-elevation coordinate to Cartesian coordinate.

given by

$$x = \frac{h \tan \psi}{\cos (\theta_0 + \xi)}$$

$$y = h \tan (\theta_0 + \xi)$$

where $\psi = \xi = 0$ represents the boresight direction.

The entries of the calibration matrix $\overline{\overline{D}}(\psi, \xi)$ as defined by (9) should be obtained through a calibration procedure. Following the single-target calibration technique given in [8], a single sphere is sufficient to determine the channel imbalances as well as the antenna crosstalk factor

for a given direction. Hence. by placing a sphere with radar cross section σ^s at a distance r_0 and a direction (ψ, ξ) with respect to the radar, the receive and transmit distortion parameters can be obtained as follows:

$$R_{vv}T_{vv} = r_0^2 e^{-2ik_0 r_0} \frac{U_{vv}^s}{(1 + C^2)\sqrt{\sigma^s/4\pi}}$$

$$\beta \triangleq \frac{R_{hh}}{R_{vv}} = \frac{2C}{(1 + C^2)} \frac{U_{hh}^s}{U_{vh}^s}$$

$$\alpha \triangleq \frac{T_{hh}}{T_{vv}} = \frac{1 + C^2}{2C} \frac{U_{vh}^s}{U_{vv}^s}$$

$$C = \pm \frac{1}{\sqrt{a}}(1 - \sqrt{1 - a}) \qquad (16)$$

where

$$a \triangleq \frac{U_{vh}^s U_{hv}^s}{U_{vv}^s U_{hh}^s}$$

and $\overline{\overline{U}}^s$ is the measured (uncalibrated) response of the sphere at a specific direction (ψ, ξ). In terms of the known quantities given by (16), the calibration matrix $\overline{\overline{D}}$ can be written as

$$\overline{\overline{D}}(\psi, \xi) = R_{vv}T_{vv} \begin{bmatrix} 1 & C\alpha & C & C^2\alpha \\ C & \alpha & C^2 & C\alpha \\ C\beta & C^2\alpha\beta & \beta & C\alpha\beta \\ C^2\beta & C\alpha\beta & C\beta & \alpha\beta \end{bmatrix} \quad (17)$$

where the dependences on ψ and ξ of all parameters is understood.

In practice, it is impossible to measure the sphere for all values of ψ and ξ within the desired domain; however, by discretizing the domain of ψ and ξ (main lobe) into sufficiently small subdomains over which the antenna characteristics are almost constant, the integral given by (13) can be evaluated with good accuracy.

Polarimetric measurement of a sphere over the entire range of ψ and ξ is very time consuming, and under field conditions, performing these measurements seems impossible. However, this measurement can be performed in an anechoic chamber with the desired resolution $\Delta\psi$ and $\Delta\xi$ only once, and then under field conditions, we need to measure the sphere response only at boresight to keep track of variations in the active devices. Without loss of generality, let us assume that $\bar{r}_v = \bar{r}_h = \bar{t}_v = \bar{t}_h = 1$ for the sphere measurements when performed in the anechoic chamber, and that these quantities can assume other values for the measurements made under field conditions. If the measured distortion parameters at boresight (field condition) are denoted by prime and calculated from (16), then the channel imbalances corresponding to the field
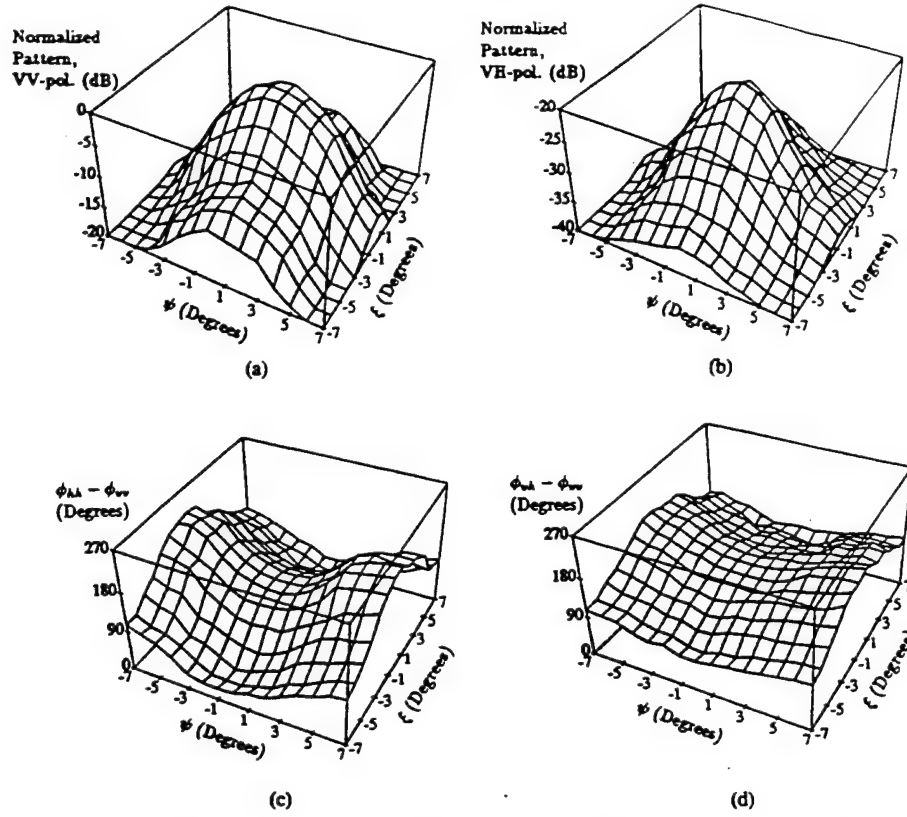
Fig. 5. Polarimetric response of a metallic sphere over the entire mainlobe of X-band scatterometer; normalized σ_{vv} (a) corresponds to G_v^2 and normalized σ_{vh} (b) corresponds to $G_v G_h$; phase difference between copolarized (c) and cross-polarized (d) components of the sphere response correspond to phase variation of the co- and cross-polarized patterns of the antenna.

measurements are

$$\bar{r}_v \bar{t}_v = \left(\frac{r_0'}{r_0} \right)^2 e^{-2ik_0(r_0'-r_0)} \frac{R_{vv}'(0,0) T_{vv}'(0,0)}{R_{vv}(0,0), T_{vv}(0,0)}$$

$$\frac{\bar{t}_h}{\bar{t}_v} = \frac{T_{hh}'(0,0)}{T_{vv}'(0,0)} \cdot \frac{T_{vv}(0,0)}{T_{hh}(0,0)}$$

$$\frac{\bar{r}_h}{\bar{r}_v} = \frac{R_{hh}'(0,0)}{R_{vv}'(0,0)} \cdot \frac{R_{vv}(0,0)}{R_{hh}(0,0)}. \tag{18}$$

Now, the calibration matrix at any direction ($\overline{\overline{D}}'(\psi, \xi)$) can be obtained from (17) by replacing $R_{vv} T_{vv}$, α, and β by $R_{vv}' T_{vv}'$, α', and β' where

$$R_{vv}' T_{vv}' = \bar{r}_v \bar{t}_v R_{vv} T_{vv}$$

$$\alpha' = \frac{\bar{t}_h}{\bar{t}_v} \alpha$$

$$\beta' = \frac{\bar{r}_h}{\bar{r}_v} \beta. \tag{19}$$

Having found the calibration matrices for all subdomains, the element ij of the correlation–calibration matrix ($\overline{\overline{B}}$), as given by (13), in the azimuth-over-elevation coordinate system takes the following form:

$$b_{ij} = \int \int_\Omega D_{ml}(\psi, \xi) D_{np}^*(\psi, \xi)$$

$$\cdot \frac{\cos^2 \psi \cos(\theta_0 + \xi)}{h^2} d\psi \, d\xi \tag{20}$$

where Ω is the solid angle subtended by the illuminated area (main lobe of the antenna).

IV. EXPERIMENTAL PROCEDURE AND COMPARISON

To demonstrate the performance of the new calibration technique, the polarimetric response of a random rough surface was measured by a truck-mounted L-, C-, and X-band polarimetric scatterometer with center frequencies at 1.25, 5.3, and 9.5 GHz. Prior to these measurements, each scatterometer was calibrated in an anechoic chamber. The scatterometer was mounted on an azimuth-over-elevation positioner at one end of the chamber, and a 36 cm metallic sphere was positioned at the antenna boresight at a distance of 12 m. Then the polarimetric response of the sphere was measured over the mainlobe of the antenna. The sphere measurements at L-band, which has the widest beam of the three systems, was performed over $(\psi, \xi) \in [-21°, +21°]$ in steps of 3°, and the ranges of (ψ, ξ) for C- and X-band were $\pm 10.5°$ and $\pm 7°$ with steps of 1.5° and 1°, respectively. To improve the signal-to-noise ratio by removing the background contribution, the chamber in the absence of the sphere was also measured for all values of ψ and ξ.

Fig. 5(a) and (b) shows the co- and cross-polarized responses of the sphere at X-band, and Fig. 5(c) and (d) shows the co- and cross-polarized phase differences ($\phi_{hh} - \phi_{vv}, \phi_{hv} - \phi_{vv}$). Similar patterns were obtained for the L- and C-band. Using the sphere responses, the
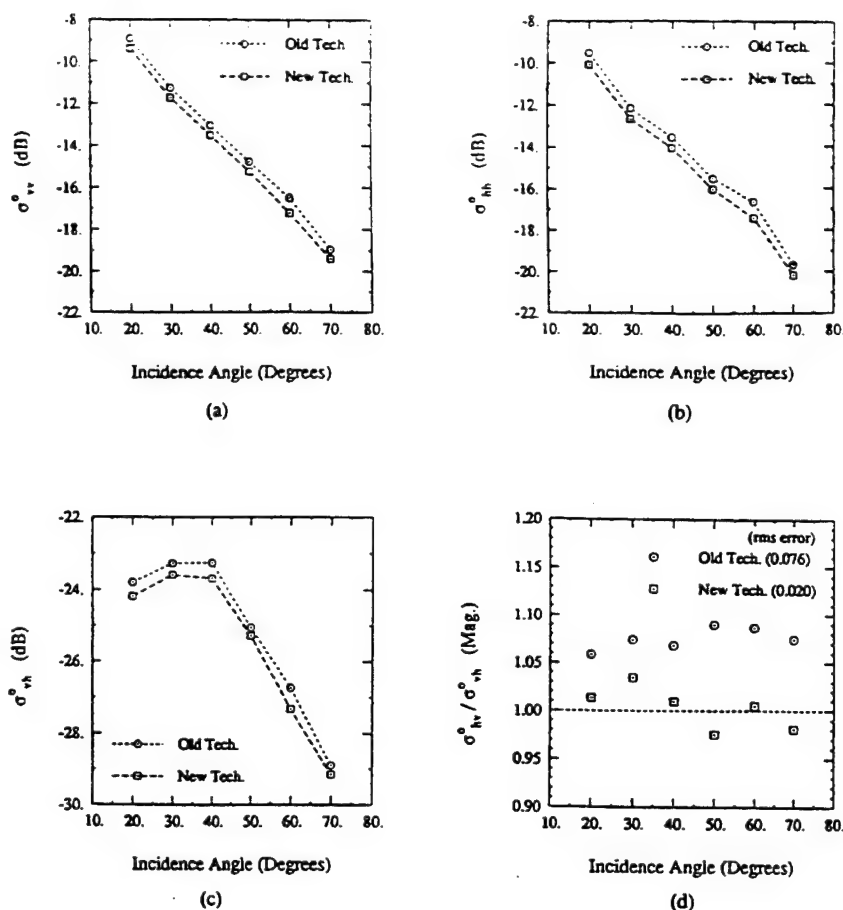
Fig. 6. Comparison between the new and old calibration techniques applied to the X-band measured backscatter from a bare soil surface. (a), (b), and (c) show the difference in the co- and cross-polarized backscattering coefficients, and (d) demonstrates the enhancement in the ratio of the cross-polarized backscattering coefficients obtained by the new method.

correlation–calibration matrices were determined as outlined in the previous section.

To evaluate the improvement provided by the new calibration technique, we shall compare results of polarimetric observations of a bare soil surface processed using the new technique with those obtained previously on the basis of the boresight-only calibration technique. The data were acquired from a truck-mounted 17-m-high platform for a rough surface with a measured rms height of 0.56 cm and a correlation length of 8 cm. The polarimetric backscatter response was measured as a function of incidence angle over the range 20°–70°. To reduce the effect of speckle on the measured data, 100 spatially independent samples were measured at each frequency and incidence angle. Also, the response of the sphere at the boresight was measured to account for any possible changes in the active devices. The collected backscatter data were calibrated by the new and old methods. The first test of accuracy of the new calibration algorithm was to make sure that the components of the correlation vector $\mathscr{Z}$ satisfy their mutual relationships, as explained in Section II. For all cases, these relationships were found to be valid within ±0.05%.

The second step in the evaluation process is the relative comparison of the backscattering coefficients and phase statistics derived from the two techniques. Fig. 6(a)–(c) shows the co- and cross-polarized backscattering coefficients as a function of incidence angle, calibrated by the old and the new methods. The differences in backscattering coefficients, as shown in these figures, are less than 0.75 dB. It was found that the difference in backscattering coefficients is less than 1 dB for all frequencies and incidence angles. Although 1 dB error in $\sigma°$ may seem negligible, in some cases, such as the variation with soil moisture content for which the total dynamic range of $\sigma°$ is about 5 dB, the 1 dB error becomes significant. Fig. 6(d) shows the ratio of two cross-polarized scattering coefficients after calibration by each of the two methods. Theoretically, this ratio must be one and independent of incidence angle. In this figure, it is shown that the new calibration method more closely agrees with theoretical expectations than the old method.

The third step involves a comparison of the phase difference statistics of the distributed target. It has been shown that when the dimensions of the antenna footprint are much larger than the correlation length, the probability density function (pdf) of the phase differences can be expressed in terms of two parameters: the degree of correlation (α) and the polarized phase difference (ζ) [7]. The degree of correlation is a measure of the width of the

pdf, and the polarized phase difference represents the phase difference at which the pdf is maximum. These parameters can be computed directly from the components of the Mueller matrix and are given by [7]

$$\alpha = \frac{1}{2}\sqrt{\frac{(\mathcal{M}_{33}+\mathcal{M}_{44})^2+(\mathcal{M}_{34}-\mathcal{M}_{43})^2}{\mathcal{M}_{11}\mathcal{M}_{22}}}$$

$$\zeta = \tan^{-1}\left(\frac{\mathcal{M}_{34}-\mathcal{M}_{43}}{\mathcal{M}_{33}+\mathcal{M}_{44}}\right).$$

Parameter α varies from zero to one, where zero corresponds to a uniform distribution and one corresponds to a delta-function distribution (fully polarized wave). Parameter ζ varies between $-180°$ and $180°$.

Fig. 7(a)–(c) shows the degree of correlation calculated by the new and old methods for the copolarized phase difference ($\phi_{hh} - \phi_{vv}$) at the L-, C-, and X-band, respectively. There is a significant difference between the two methods in all cases. The partially polarized backscattered Stokes vector obtained by the old calibration method appears more unpolarized than the Stokes vector obtained by the new method. The virtue of this result can be checked in the limiting case if an analytical solution is available. A first-order solution of the small perturbation method for slightly rough surfaces shows that the backscatter signal is fully polarized, and therefore, the pdf of the copolarized phase difference is a delta function, corresponding to $\alpha = 1$. The roughness parameters of the surface under investigation falls within the validity region of the small perturbation method at L-band. The value of α at L-band derived from the new calibration method is in much closer agreement with theoretical expectations than the value obtained by the old method. Fig. 8(a)–(c) shows plots of the copolarized phase difference at the L-, C-, and X-band, respectively. At the L- and X-bands, the value of ζ obtained by the two methods are positive and not very different from each other. Also, it noted that ζ has a positive slope with incidence angle. However, this is not the case for the C-band; the value of ζ obtained by the old method is negative, has a negative slope, while the behavior of ζ obtained by the new method is very similar to that at the other two frequencies. This deviation is due to the large variation of phase difference between the V- and H-channels of the C-band radar over the illumination area, and since the old method does not account for phase variations, it is incapable of correcting the resulting errors. Similar results were observed for the statistics of the cross-polarized phase difference ($\phi_{hv} - \phi_{vv}$).

V. CONCLUSIONS

A rigorous method is presented for calibrating polarimetric backscatter measurements of distributed targets. By characterizing the radar distortions over the entire mainlobe of the antenna, the differential Mueller matrix
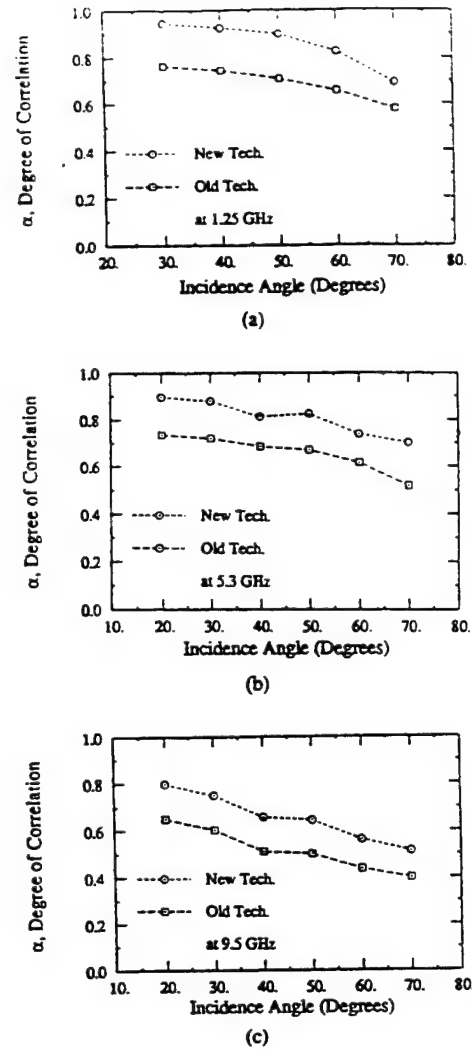

Fig. 7. Degree of correlation for copolarized components of the scattering matrix for the L-band (a), C-band (b), and X-band (c).

is derived from the measured scattering matrices with a high degree of accuracy. It is shown that the radar distortions can be determined by measuring the polarimetric response of a metallic sphere over the main lobe of the antenna. The radar distortions are categorized into two groups, namely, distortions caused by the active devices, and distortions caused by the antenna structure (passive). Since passive distortions are immune to changes once they are determined, they can be used repeatedly. The active distortions can be obtained by measuring the sphere response only at boresight, thereby reducing the time required for calibration under field conditions. The calibration algorithm was applied to backscatter data collected from a rough surface by L-, C-, and X-band scatterometers. Comparison of results obtained with the new algorithm with the results derived from the old calibration method show that the discrepancy between the two methods is less 1 dB for the backscattering coefficients. The discrepancy, however, is more drastic for the phase-difference statistics, indicating that removal of the radar distortions from the cross products of the scattering matrix elements (differential Mueller matrix elements)
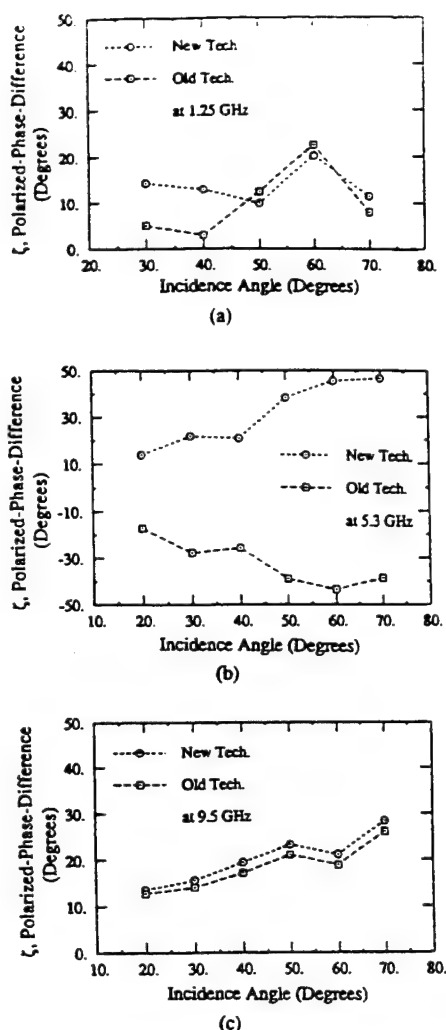
(a)

(b)

(c)

Fig. 8.   Polarized phase difference for copolarized components of the scattering matrix for the L-band (a), C-band (b), and X-band (c).

cannot be accomplished with the traditional calibration methods.

REFERENCES

[1] F. T. Ulaby, R. K. Moore, and A. K. Fung, *Microwave Remote Sensing: Active and Passive, Vol. II—Radar Remote Sensing and Scattering Emission Theory.* Dedham, MA: Artech House, 1986.

[2] K. Sarabandi, Y. Oh, and F. T. Ulaby, "Polarimetric radar measurements of bare soil surfaces at microwave frequencies," in *Proc. IEEE Geosci. Remote Sensing Symp.*, Espoo, Finland, June 1991.

[3] M. A. Tassoudji, K. Sarabandi, and F. T. Ulaby, "Design consideration and implementation of the LCX polarimetric scatterometer (POLARSCAT)," Radiation Lab. Rep. 022486-T-2, Univ. Michigan, Ann Arbor, June 1989.

[4] F. T. Ulaby and C. Elachi, *Radar Polarimetry for Geoscience Applications.* Dedham, MA: Artech House, 1990.

[5] H. J. Eom and W. M. Boerner, "Rough surface incoherent backscattering of spherical wave," *IEICE Trans.*, vol. E 74, Jan. 1991.

[6] A. K. Fung and H. J. Eom, "Coherent scattering of spherical wave from an irregular surface," *IEEE Trans. Antennas Propagat.*, vol. AP-31, Jan. 1983.

[7] K. Sarabandi, "Derivation of phase statistics from the Mueller matrix," *Radio Sci.*, vol. 27, Sept.–Oct. 1992.

[8] K. Sarabandi and F. T. Ulaby, "A convenient technique for polarimetric calibration of radar systems," *IEEE Trans Geosci Remote Sensing*, vol. 28, Nov. 1990.

[9] R. M. Barnes, "Polarimetric calibration using in-scene reflectors," Rep. TT.65, M.I.T. Lincoln Lab., Lexington, MA, Sept. 1986.

[10] M. W. Whitt, F. T. Ulaby, P. Polatin, and V .V. Liepa, "A general polarimetric radar calibration technique," *IEEE Trans. Antennas Propagat.*, vol. 39, Jan. 1991.

[11] K. Sarabandi, F. T. Ulaby, and M. A. Tassoudji, "Calibration of polarimetric radar systems with good polarization isolation," *IEEE Trans. Geosci. Remote Sensing*, vol. 28, Jan. 1990.

Kamal Sarabandi (S'87–M'90) was born in Tehran, Iran, on November 4, 1956. He received the B.S. degree in electrical engineering from Sharif University of Technology, Tehran, Iran, in 1980. He entered the graduate program at the University of Michigan in 1984, and received the M.S.E. degree in electrical engineering in 1986, and the M.S. degree in mathematics and the Ph.D. degree in electrical engineering in 1989.

From 1980 to 1984 he worked as a Microwave Engineer in the Telecommunication Research Center in Iran. He is presently an Assistant Professor in the Department of Electrical Engineering and Computer Science, University of Michigan. His research interests include electromagnetic scattering, microwave remote sensing, and calibration of polarimetric SAR systems.

Dr. Sarabandi is a member of the Electromagnetics Academy and USNC/URSI Commission F.
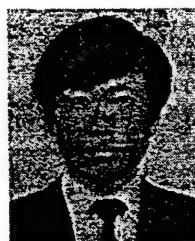
Yisok Oh (S'88) received the B.S. degree in electrical engineering from Yonsei University, Seoul, Korea, in 1982, and the M.S. degree in electrical engineering from the University of Missouri, Rolla, in 1988.

He is currently working towards the Ph.D. degree in electrical engineering at the University of Michigan, Ann Arbor, where he is a Research Assistant with the Radiation Laboratory. His research interests include microwave remote sensing, with an emphasis on the interface between experimental measurements and theoretical models for electromagnetic wave scattering from earth terrain.

Fawwaz T. Ulaby (M'68–SM'74–F'80) received the B.S. degree in physics from the American University of Beirut, Lebanon, in 1964 and the M.S.E.E. and Ph.D. degrees in electrical engineering from the University of Texas, Austin, in 1966 and 1968, respectively.

He is currently a Professor of Electrical Engineering and Computer Science at the University of Michigan, Ann Arbor, and Director of the NASA Center for Space Terahertz Technology. His current interests include microwave and millimeter-wave remote sensing, radar systems, and radio wave propagation. He has authored several books and published over 400 papers and reports on these subjects.

Dr. Ulaby is the recipient of numerous awards, including the IEEE Geoscience and Remote Sensing Distinguished Achievement award in 1983, the IEEE Centennial Medal in 1984, the Kuwait Prize in Applied Science in 1986, and the NASA Achievement Award in 1990.

Bistatic Specular Scattering from Rough Dielectric Surfaces

Roger D. De Roo, *Student Member, IEEE*, and Fawwaz T. Ulaby, *Fellow, IEEE*

Abstract— An experimental investigation was conducted to determine the nature of bistatic scattering from rough dielectric surfaces at 10 GHz. This paper focusses specifically on the dependence of coherent and incoherent scattered fields on surface roughness for the specular direction. The measurements, which were conducted for a smooth surface with $ks < 0.2$ (where $k = 2\pi/\lambda$ and s is the rms surface height) and for three rough surfaces with $ks = 0.5$, 1.39, and 1.94, included observations over the range of incidence angles from 20° to 65° for both horizontal and vertical polarizations. For the coherent component, the reflectivity was found to behave in accordance with the prediction of the Physical Optics model, although it was observed that the Brewster angle exhibited a small negative shift with increasing roughness. The first-order solution of Physical Optics also provided good agreement with observations for hh-polarized incoherent scattering coefficient, but it failed to predict the behavior of the vv-polarized scattering coefficient in the angular range around the Brewster angle. A second-order solution is proposed which appears to partially address the deficiency of the Physical Optics model.

Fig. 1. Calculated coherent reflectivity for v polarization using the Physical Optics model for a Gaussian surface with ks vaired from 0 to 2.5, and $\epsilon = 3$.

I. INTRODUCTION

SCATTERING of electromagnetic fields by random rough surfaces in the backscatter direction has many uses and has been investigated extensively over the past few decades. By comparison, very few experimental investigations have been attempted to evaluate forward scattering in the specular direction. This is in part because the applications for specular scattering are not as straightforward as for backscattering. The many theoretical developments for scattering from random rough surfaces, while developed for the general bistatic case, have only been extensively used and tested for backscattering. Therefore, the usefulness and validity of these theories for specular scattering is largely unknown.

Recent developments in the modeling of terrain for radar backscattering indicate that specular scattering from a rough ground surface combined with scattering by an overstructure (such as trees or crops) can contribute significantly to the backscattering from the terrain as a whole [1]–[5]. Therefore an understanding of the nature of specular radar scattering and knowledge of the behavior of specular scattering theories are needed. Several experimental investigations were conducted at centimeter wavelengths in the 1946–1960 period to evaluate the variation of the coherent and incoherent components of the specularly reflected energy as a function of surface
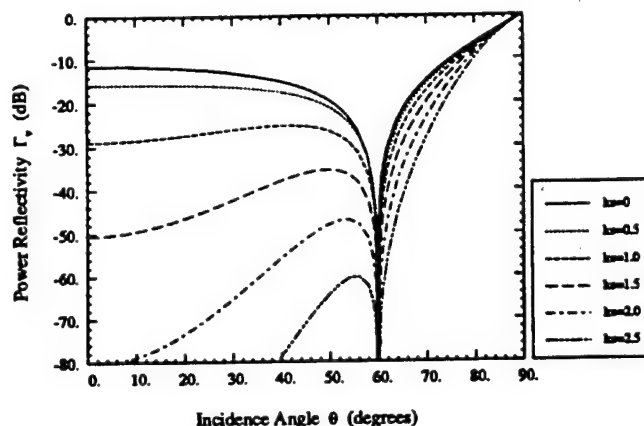
roughness. The results for the coherent component, which is represented by the reflection coefficient, are summarized in Beckmann and Spizzichino [6]. According to these results, the overall variation of the reflection coefficient with ks, where $k = 2\pi/\lambda$, and s is the rms height, may be explained by the coherent scattering term of the Physical Optics surface scattering model [6], [7]. The data, however, are rather lacking in several respects: (1) marginal accuracy with regard to both the measured reflected signal and the surface rms height, (2) limited dynamic range (10 dB relative to the level of the signal reflected from a perfectly smooth surface), and (3) no examination of the behavior in the angular region around the Brewster angle. Additional bistatic measurements were reported by Cosgriff *et al* [8] in 1960, but the data were not calibrated, nor were the surfaces characterized.

More recently, Ulaby *et al.* [9] measured bistatic scattering from sand and gravel surfaces at 35 GHz, and while the data were calibrated and the surfaces were characterized, no comparison to a theoretical prediction was given. In the optical regime, Saillard and Maystre [10] have measured the bistatic scattering of light from dielectric surfaces, and have observed a change in the Brewster angle as the roughness of the surface increased. Greffet [11] explained their observations using the Small Perturbation Method [12]. However, the Small Perturbation Method does not explain the observations reported in our present study: the first-order Small Perturbation Method predicts that the Brewster angle will move toward grazing as the roughness increases, while our observations indicate the opposite.
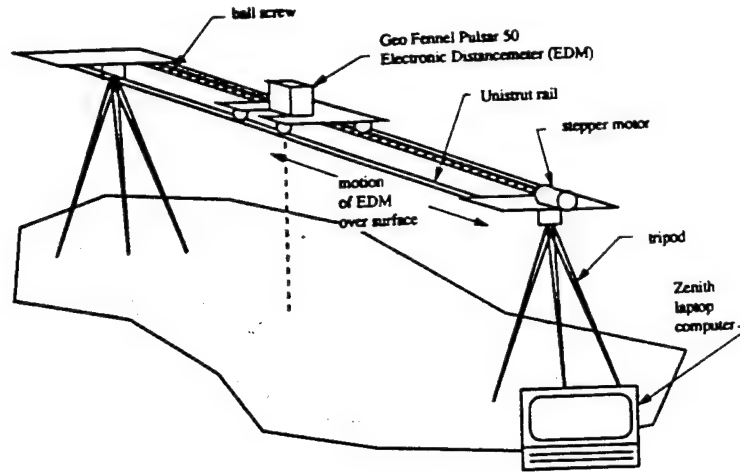
Fig. 2. Diagram of Laser Profiler.

There are three major rough surface scattering approaches which have long held the acceptance of the scientific community as valid for some ranges of surface roughness. The Geometric Optics (GO) model, the Physical Optics (PO) model, and the Small Perturbation Method (SPM) are the three theoretical approaches most commonly used at microwave frequencies for characterizing scattering from random rough surfaces [7]. While both GO and PO models rely on the Kirchhoff approach of using the tangent-plane approximation, they yield very different predictions for the scattering of waves from a rough surface. In particular, the GO model does not predict any coherent reflectivity from rough surfaces. This may appear to be an inadequacy of the GO approach; however, the GO approach is valid only for surfaces so rough that any coherent scattering would be very small anyway. The PO model, on the other hand, has a simple expression for the coherent scattering component, but the complete expression for incoherent scattering, even for single scattering, has not yet been formulated. SPM is a different approach, but its range of validity is restricted to surfaces with small rms heights and slopes. Because the ranges of validity for the GO and SPM theories are outside the range of rms heights described in this paper, comparisons to GO and SPM will not be discussed.

In this paper we will examine experimental measurements of the coherent and incoherent scattering components in the specular directions at 10 GHz for several dry sand surfaces covering a wide range of rms heights (0.5 mm to 1.4 cm). The measurements were conducted over an incidence angle range extending from 20° to 65° for both horizontal and vertical polarizations. The sand, with a relative dielectric constant of 3.0 and negligible loss factor, exhibits a null for vertical polarization at the Brewster angle of 60°. The experimental data are compared with predictions based on a revision of the Physical Optics solution that is slightly different from and more accurate than the standard form available in the literature [7].

II. PHYSICAL OPTICS MODEL—A VECTOR SOLUTION

The Physical Optics approach involves integration of the Kirchhoff scattered field over the rough surface. The coherent field reflection coefficient from a surface with a Gaussian height distribution is given by [7]:

$$R_q(\theta) = R_{q0}e^{-2k^2s^2\cos^2\theta}\delta_{pq} \qquad (1)$$

where the polarization subscripts p, q are either h or v, and $\cos\theta = -\hat{z}\cdot\hat{k}_i$. The angle θ is both the angle of incidence and reflection; coherent scattering occurs only in the specular direction from the mean surface. The reflection coefficient R_{q0} for a plane surface is given by (15) and (16) below. Fig. 1 shows $\Gamma_v(\theta) = |R_v(\theta)|^2$ for several values of ks. The Brewster angle does not change with surface roughness, but the coherent scattered power decreases very rapidly with increasing roughness.

The power in the incoherent reflected field may be given by a Taylor series in surface slope distributions. In Ulaby et al. [7] the Physical Optics solution is called the Scalar Approximation because slopes are ignored in the surface local coordinate system, leading to a decoupling of polarizations in the vector scattering equations. As a result, co-polarized scattering in the plane of incidence is fairly accurate, but cross-polarized scattering is zero. With the inclusion of surface slopes transverse to the plane of incidence in the vectorial solution to the Physical Optics approximation, depolarization in the plane of incidence is predicted when the Taylor series is expanded to the second order in surface slopes. The derivation is given in Appendix A. In the specular scattering direction, the first order terms are zero. The Physical Optics expression for incoherent scattering in the specular direction, which includes the zeroth and the important part of the second order terms, is given by (see last paragraph of Appendix A):

$$\sigma_{pq}^0 = 2k^2\cos^2\theta|a'_{0pq}|^2I'_0 + 4k^4s^4\cos^4\theta(|a'_{lpq}|^2 + |a'_{tpq}|^2)I'_{20} \qquad (2)$$

where

$$I'_0 = e^{-4k^2s^2\cos^2\theta}\int_0^\infty \left(e^{4k^2s^2\cos^2\theta\rho(\xi)} - 1\right)\xi d\xi \qquad (3)$$

$$I'_{20} = \int_0^\infty \left(\frac{\partial\rho(\xi)}{\partial\xi}\right)^2 e^{-4k^2s^2\cos^2\theta(1-\rho(\xi))}\xi d\xi \qquad (4)$$

and

$$a'_{0hh} = R_{h0} \tag{5}$$

$$a'_{lhh} = R_{h1} \tag{6}$$

$$a'_{0vv} = R_{v0} \tag{7}$$

$$a'_{lvv} = R_{v1} \tag{8}$$

$$a'_{thh} = a'_{tvv} = 0 \tag{9}$$

$$a'_{0vh} = a'_{lvh} = a'_{0hv} = a'_{lhv} = 0 \tag{10}$$

$$a'_{tvh} = (R_{h0} \cos^2 \theta + R_{v0})/\sin \theta \tag{11}$$

$$a'_{thv} = -(R_{v0} \cos^2 \theta + R_{h0})/\sin \theta \tag{12}$$

The a'_{0pq} terms are the zeroth-order terms (scalar approximation); the a'_{lpq} and a'_{tpq} terms are the second-order terms due to slopes longitudinal and transverse to the plane of incidence. The function $\rho(\xi)$ is the normalized correlation function of the surface, and the parameters $R_{v0}, R_{h0}, R_{v1}, R_{h1}$ are the coefficients of the (field) reflectivity local to the surface when expanded in terms of surface slopes:

$$R_h(x,y) = R_{h0} + R_{h1} Z_l(x,y) + \cdots \tag{13}$$

$$R_v(x,y) = R_{v0} + R_{v1} Z_l(x,y) + \cdots \tag{14}$$

where $Z_l(x,y)$ is the surface slope longitudinal to the direction of the incident wave at the (x,y) lateral coordinates of the surface. The zeroth-order terms are identical to the reflection coefficients for a smooth surface. In particular,

$$R_{h0} = \frac{\eta_2 \cos \theta - \eta_1 \cos \theta_t}{\eta_2 \cos \theta + \eta_1 \cos \theta_t} \tag{15}$$

$$R_{v0} = \frac{\eta_1 \cos \theta - \eta_2 \cos \theta_t}{\eta_1 \cos \theta + \eta_2 \cos \theta_t} \tag{16}$$

$$R_{h1} = \frac{\eta_2 \sin \theta(1 - R_{h0}) - \eta_1 \frac{k_1 \cos \theta}{k_2 \cos \theta_t} \sin \theta_t(1 + R_{h0})}{\eta_2 \cos \theta + \eta_1 \cos \theta_t} \tag{17}$$

$$R_{v1} = \frac{\eta_1 \sin \theta(1 - R_{v0}) - \eta_2 \frac{k_1 \cos \theta}{k_2 \cos \theta_t} \sin \theta_t(1 + R_{v0})}{\eta_1 \cos \theta + \eta_2 \cos \theta_t} \tag{18}$$

where θ_t is related to θ by Snell's Law: $k_1 \sin \theta = k_2 \sin \theta_t$, and $\eta = \sqrt{\mu/\epsilon}$. These first-order coefficients are different from those found in Ulaby et al [7] and Ulaby and Elachi [13] due to the incorporation of a more precise method for expanding the local angle of transmission.

The zeroth-order terms dominate co-polarized scattering except near the Brewster angle, where the zeroth-order terms tend toward zero. For cross-polarization, the zeroth-order terms predict no scattering for all specular angles, and therefore cross-polarized scattering is determined by the second-order terms. Unfortunately, this is still a single-scattering theory, and depolarization is very small compared to other possible sources, such as multiple scattering or volume scattering. Thus it provides a simple estimate of the minimum expected cross-polarized scattering in the specular scattering direction. The
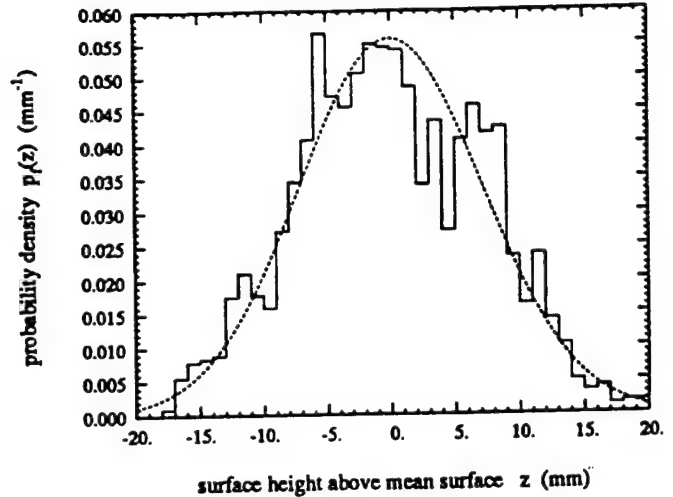
(a)
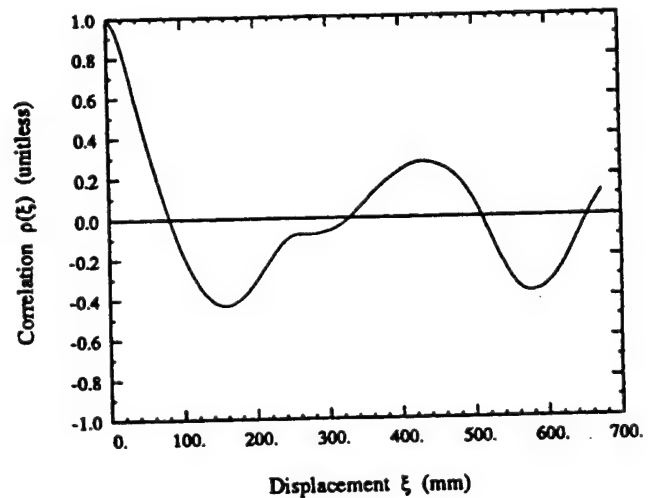
(b)

Fig. 3. Typical results of surface characterization of one of the surfaces measured in this study: (a) Histogram of measured heights for a slightly rough surface and the Gaussian probability distribution used to model it; a total of 4353 height measurements were made, from which the rms height was calculated to be $s = 6.9$ mm. (b) Measured autocorrelation function of the same surface.

co-polarized second-order terms are all negligible except in the vicinity of the Brewster angle, where the zeroth-order terms vanish for vv polarization. The second-order terms all tend toward zero at grazing, and the cross polarized terms tend toward zero at nadir.

The fact that the Kirchhoff approximation is capable of predicting any cross-polarized single scattering in the plane of incidence is somewhat surprising. However, this is possible because the Physical Optics approximation is used in the derivation; use of the Geometric Optics approximation neglects diffraction and is incapable of predicting cross-polarized scattering. While expressions similar to, but not identical with, those described here for the higher order terms of the Physical Optics model have been presented in the past [14], and have been unsuccessful in matching experimental measurements of
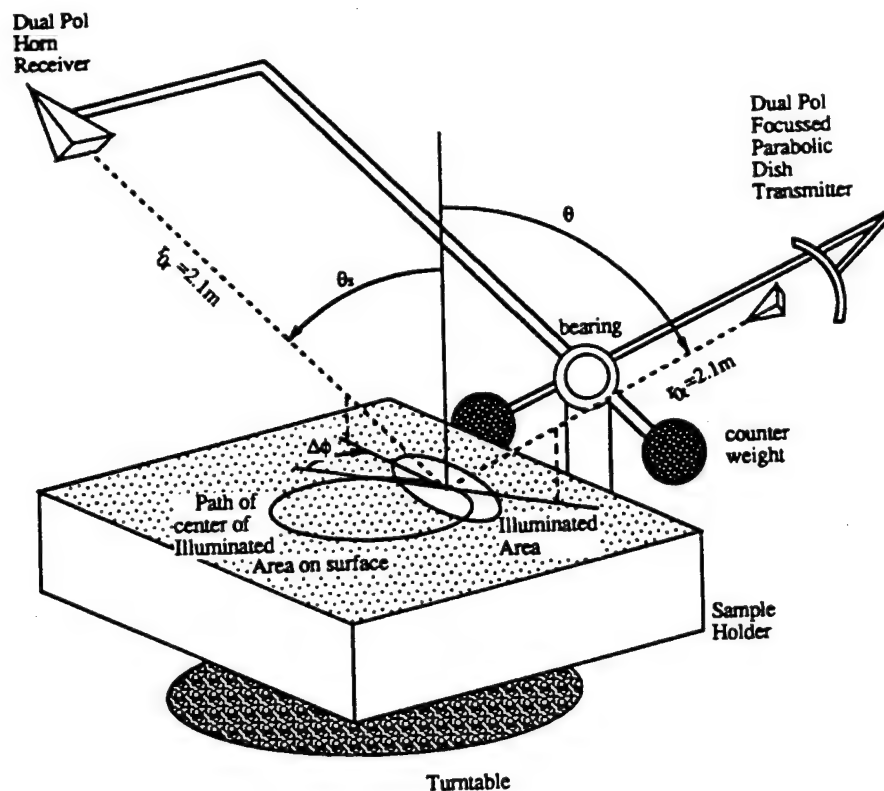
Fig. 4. Diagram of the Bistatic Facility.

the cross-polarized scattering coefficient [15], the authors are not aware of any attempt to use the higher order terms to explain scattering in the vicinity of the Brewster angle.

III. MEASUREMENT DESCRIPTION

A. Laser Profiler

The measurements shown in this paper are for random surfaces with varying roughness. The surfaces were characterized by a Laser Profiler, a device engineered at the University of Michigan to measure 2 meter linear or 1 meter by 1 meter square sections of surface profiles. The Profiler is shown in 2 meter linear mode in Fig. 2. Using a Pulsar 50 Electronic Distancemeter manufactured by GEO Fennel, it can measure profiles of surfaces without direct contact. The profiler has a horizontal resolution of 1 mm and a vertical resolution of 2 mm. Fig. 3(a) is an example of the height histogram generated from the profile measured for one of the surfaces, and Fig. 3(b) shows the corresponding correlation function.

B. Bistatic Facility

The configuration shown in Fig. 4 depicts the indoor bistatic radar system used for making the measurements reported in this paper. It is a stepped-frequency (8.5–10 GHz) measurement system capable of measuring the scattering matrix **S** of the target contained in the area or volume formed by the intersection of the transmit and receive antenna beams. Using an HP8720 vector network analyzer with an amplifier on the transmitting antenna, the system measures a complex voltage

for any pair of v or h receive and transmit polarization states. With proper calibration, it is capable of measuring all four complex elements of the scattering matrix of the target surface. The hardware allows the transmitter and receiver to be located independently at any point on a hemispherical shell 2.1 m from the center of the target. In practice, however, measurements are accurate only when both antennas are within 70° of nadir.

The receive antenna is a dual-polarized horn antenna with a beamwidth of 12°, and the transmit antenna is a dual-polarized parabolic dish whose feed was designed such that the main beam of the parabolic dish is focused at a range equal to the distance to the target surface, which is held constant for all measurements. Because of the larger aperture (30 cm diameter), the transmit antenna has a narrow beam of 5°, which dictates the extent of the surface area responsible for the scattered energy. By using a focused beam antenna, we achieve a narrow-beam configuration without having to satisfy the usual far-field criterion. A baffle made of radar absorbing material was placed in the direct path between the transmitter and reciever to insure proper isolation of the two antennas.

To separate the measured signal into its coherent and incoherent components, it is necessary to measure many statistically independent samples of the random surface characterizing the target surface. This is achieved by rotating the sample holder in increments of 10°, thereby realizing 36 spatial samples per full rotation. The spatial correlation of the measured incoherent power indicates that measurements decorrelated every 15°, resulting in 24 independent samples per surface. Measurements of smooth surfaces indicate that phase coherence is maintained between independent samples.
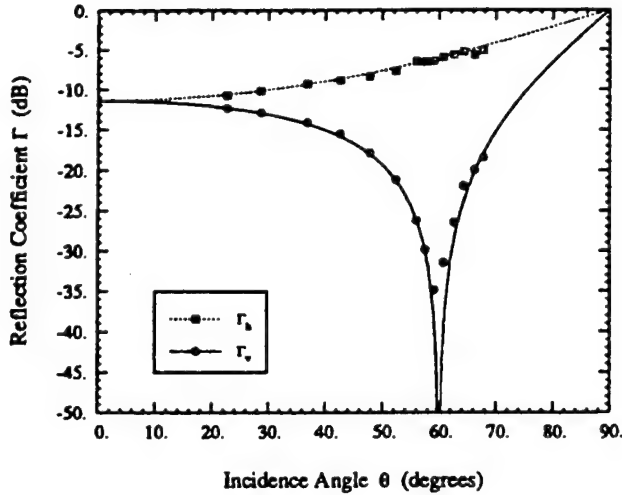
Fig. 5. Measured coherent reflectivity of a smooth surface with $\epsilon = 3.0$ and $ks < 0.2$: squares denote horizontal polarization and circles denote vertical polarization. Continuous curves are predictions based on Physical Optics. The angle of minimum reflectivity for vertical polarization is $60°$.

The total path length, from transmitter to target to receiver, has a standard deviation less than 4 mm ($7°$ at 9.25 GHz) for the set of independent samples.

C. Separation of Coherent and Incoherent Power

The Bistatic Facility measures a complex voltage V_m which is proportional to the scattered electric field for each polarization state at each spatially independent sample of the surface. Because the scattered electric field is composed of a coherent component from the mean surface and an incoherent component from the rough surface and/or volume, the measured voltage will also have a coherent and incoherent component: $V_m = V_{coh} + V_{incoh}$. These two components can be separated because the incoherent component has a zero mean: $\langle V_{incoh} \rangle = 0$. Provided a large number of independent samples are measured, the coherent power P^{coh} is proportional to the square of the complex average of the measured voltages:

$$P^{coh} = |V_{coh}|^2 = |\overline{V_m}|^2 \qquad (19)$$

The incoherent power P^{incoh} is then proportional to the variance of the fluctuating component of the measured voltage:

$$P^{incoh} = \langle |V_{incoh}|^2 \rangle = \overline{|V_m - \overline{V_m}|^2} \qquad (20)$$

D. Calibration

The bistatic measurement system is calibrated using a bistatic adaptation of the polarimetric backscattering calibration technique developed by Sarabandi and Ulaby [16]. For measurements corresponding to the bistatic specular configuration, a large, flat conducting plate is used as a calibration target. Further verification is obtained by measuring a conducting hemisphere placed on the calibration target. The radar cross section of the hemispherical target was calculated via Physical Optics. Calibration to date has been accurate to within 0.5 dB in magnitude and $10°$ in co-polarized phase difference at

boresight. The system is extremely stable; while the calibration procedure is performed for each day of measurements, calibrations have been good for up to 5 days.

The bistatic facility measures E_{pq}, the p polarized field due to a q polarized transmitted field. The power in this measured field P_{pq}, is composed of a coherent and an incoherent component:

$$P_{pq} = P_{pq}^{coh} + P_{pq}^{incoh} \qquad (21)$$

$$P_{pq}^{coh} = P_q^t \frac{|K_{pq}|^2}{(4\pi)^2 (r_{0r} + r_{0t})^2} \Gamma_{pq} \qquad (22)$$

$$P_{pq}^{incoh} = P_q^t \frac{|K_{pq}|^2}{(4\pi)^3} \sigma_{pq}^0 \lambda^2 \int_{A_{ill}} \frac{g_p^r(x,y) g_q^t(x,y)}{r_r^2(x,y) r_t^2(x,y)} dx dy \qquad (23)$$

$$= P_q^t \frac{|K_{pq}|^2}{(4\pi)^3} \sigma_{pq}^0 I_{A_{ill}\,pq} \qquad (24)$$

where the coherent power reflection coefficient, and therefore the coherent power, exists only for co-polarized scattering: $P_{pq}^{coh} = \Gamma_{pq} = 0$ if $p \neq q$.

The co-polarized coherent power reflection coefficient is calculated by comparing the coherent power from a target to that from a large flat conducting plate, for which $\Gamma_{pp}^{cal} = 1$ and $\sigma_{pq}^0 = 0$. Thus,

$$\Gamma_{pp} = \frac{P_{pp}^{coh}}{P_{pp}^{cal}} \qquad (25)$$

The co-polarized differential scattering coefficient is calculated by comparing the incoherent power from a target to that of the calibration power. $I_{A_{ill}pq}$ was calculated from extensive measurements of the normalized antenna patterns for both antennas, for each of the principal polarization states, over the entire main lobe of the antennas, at the boresight ranges r_{0r} and r_{0t}. Thus,

$$\sigma_{pp}^0 = \frac{4\pi}{(r_{0t} + r_{0r})^2 I_{A_{ill}\,pp}} \frac{P_{pp}^{incoh}}{P_{pp}^{cal}} \qquad (26)$$

IV. RESULTS

A. Surface Characterizations

The shape of a random rough surface is described by the surface height distribution function and the surface height correlation function. For a surface whose height is given by $z = f(x, y)$, the surface-height probability density function is given by $p_f(z)$, and is assumed to be Gaussian:

$$p_f(z) = \frac{1}{\sqrt{2\pi}s} e^{-\frac{1}{2} \frac{z^2}{s^2}} \qquad (27)$$

Measurements by this and other experimenters [17], [18] indicate that this assumption is appropriate. Fig. 3(a) shows the fit between a histogram of measured surface heights and equation (27). The surface height characteristics can be specified by a single parameter, s, which is the root-mean-squared surface deviation from the mean planar surface located at $z = 0$.

The other statistical descriptor of random rough surfaces is the normalized correlation function, denoted by ρ. It describes
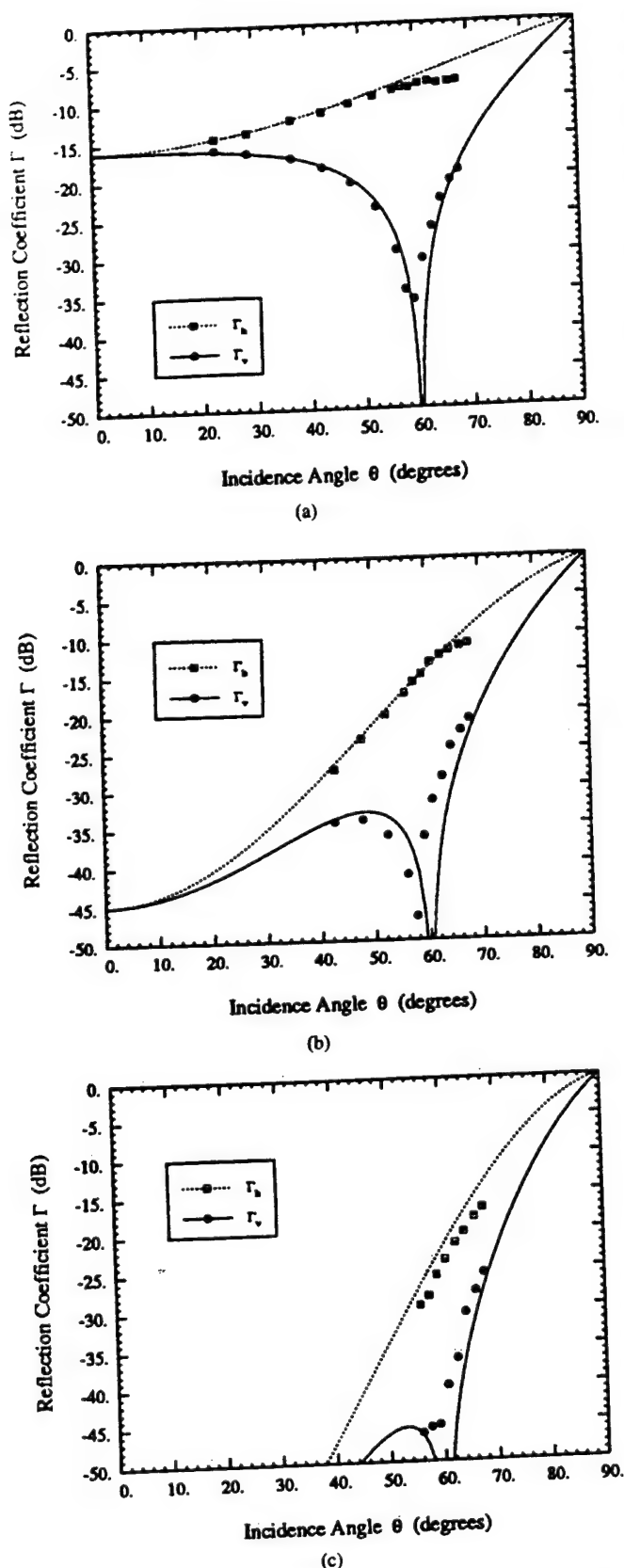
(a)

(b)

(c)

Fig. 6. Measured coherent reflectivity of three rough surfaces. Continuous curves are predictions based on Physical Optics. In all cases, the surfaces have a relative dielectric constant $\epsilon = 3.0$. (a) $ks = 0.515, kl = 5.4$, (b) $ks = 1.39, kl = 10.6$, (c) $ks = 1.94, kl = 11.8$.

the degree to which the height at one location given by $z = f(x,y)$, is correlated to the height at another location,

given by $z' = f(x',y')$. For surfaces described by a stationary random process, ρ can be expressed in terms of the lateral separations $u = x - x'$ and $v = y - y'$ between the two locations on the surface. Moreover, if the surface statistics are symmetric under azimuthal rotations, the correlation function can be described by a single variable $\xi = \sqrt{u^2 + v^2}$, which specifies the absolute value of the lateral separation. Unlike the surface height distribution function, the correlation function may take on several forms for naturally occurring randomly rough surfaces. The vast majority of the literature on rough surface scattering assumes that the surface statistics are azimuthally symmetric and Gaussian, while many measurements of commonly occurring surfaces in microwave remote sensing situations indicate that an exponential correlation function may be more appropriate [19].

A correlation function for a surface with a correlation length of 52.5 mm is shown in Fig. 3(b). It was generated by averaging the individual autocorrelations of 3 linear profiles of the surface. Experimentation has shown that only 3 profile measurements averaged together are neccessary to accurately determine the correlation length and shape of this and other surfaces, but many more are needed to demonstrate that the correlation function tends toward zero beyond a few correlation lengths. For the purposes of this paper, the correlation length of a surface is that length at which the normalized correlation function is e^{-1}. As a result of the negative values of the correlation function, several of the integrals used to predict scattering characteristics ((3) and (4)) may yield values which are obviously incorrect. However, only a few surface profiles are needed to determine the shape of the correlation function within one correlation length, and if the rest of the correlation function tends towards zero, this portion of the correlation function dominates the integrals. The effect of the shape of the correlation function within one correlation length can be explored by considering several analytical forms for the correlation function.

B. Coherent Scattering

At the Brewster angle, the reflectivity for the vertical polarization is identically zero for a smooth interface between two lossless dielectric media. Whether or not it remains identically zero for a slightly rough surface is not clear. The Physical Optics approach clearly predicts that this is so; moreover, it predicts that the minimum reflectivity remains at the same incidence angle as for a smooth surface. This can be seen in Fig. 1. However, the Small Perturbation method predicts that the angle of minimum reflection for vertical polarization increases slightly with increasing roughness of the surface [11]. The fact that Physical Optics does not predict a change in angle while the Small Perturbation does is a consequence of the fact that the correction to the Fresnel coefficient is multiplicative for Physical Optics while it is additive for Small Perturbation. Additional terms in the Small Perturbation expansion may move this minimum angle back toward the smooth-surface Brewster angle.

a Fig. 5 shows measurements of the reflection coefficient for a smooth dry surface with $ks < 0.2$ (the rms height s was
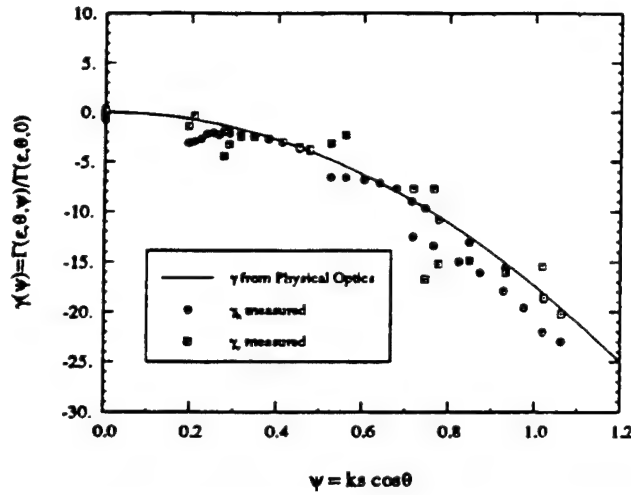
Fig. 7. The reduction of coherent scattering from a surface due to roughness. Shown is the measured coherent reflectivity of several surfaces (all with with $\epsilon' = 3$) but differing roughness parameters ψ, normalized to the reflection coefficient of a smooth surface. The angles of incidence range from 20° to 70° and the roughness ks ranges from 0 to 2. The continuous curve is the Physical Optics prediction for surfaces with Gaussian-height probability densities.

smaller than 1 mm, the measurement precision of the laser profileometer). The curves in Fig. 5 were calculated using the Fresnel reflection coefficient formulas given by (15) and (16) for a surface with a relative dielectric constant $\epsilon = 3.0 + j0$. The dielectric constant for the sand medium was measured by a dielectric probe, which gave a value of $\epsilon' = 3.0$ for the real part and a value of $\epsilon'' < 0.03$ for the imaginary part. Because $\epsilon''/\epsilon' \ll 1$ and the inclusion of ϵ'' as high as 0.05 does not significantly change the results of any of the calculations in this paper, it was ignored. The excellent agreement between the measured data and the calculated curves presented in Fig. 5 provides testimony to the measurement accuracy of the system.

Fig. 6 compares measured values of the power reflection coefficient Γ with curves calculated using Physical Optics (equation (1)) for surfaces with $ks = 0.515, 1.39$, and 1.94. Although good overall agreement is observed between theory and experimental observations, it should be noted that the location of the Brewster angle exhibits a slight shift towards decreasing angle of incidence; the Brewster angle shifts from 60° for the smooth surface shown in Fig. 5 to 58° for the surface with $ks = 1.39$ (Fig. 6(b)) and to about 56° for the surface with $ks = 1.94$ (Fig. 6(c)). The shift is toward decreasing angle of incidence, which is opposite to the direction predicted by the Small Perturbation Method.

By way of summary, Fig. 7 shows the dependence of the q-polarized normalized power reflection coefficient γ_q on the roughness parameter ψ, where
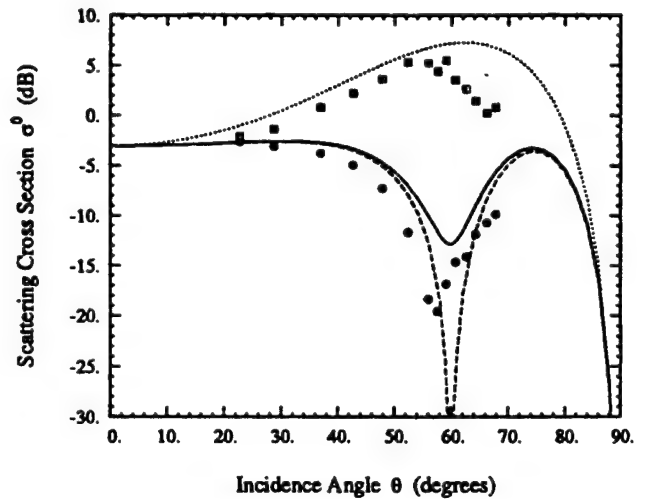
$$\gamma_q(\psi) = \frac{\Gamma_q(\epsilon, \theta, \psi)}{\Gamma_{q0}(\epsilon, \theta, 0)} = \frac{|R_q|^2}{|R_{q0}|^2} \qquad (28)$$
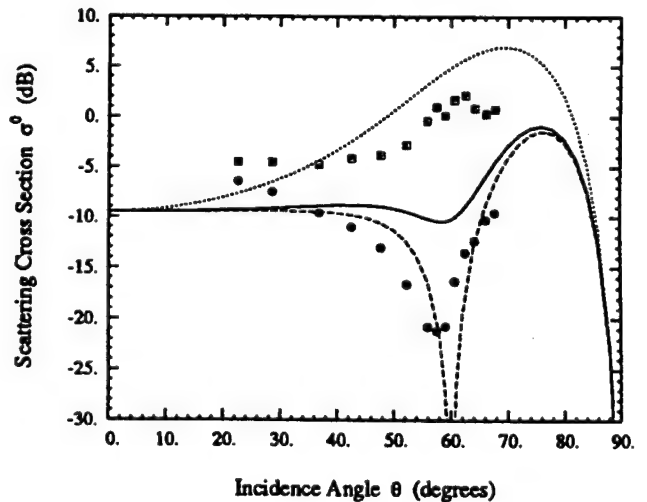
$$= e^{4\psi^2} \qquad (29)$$

and $\psi = ks \cos \theta$.
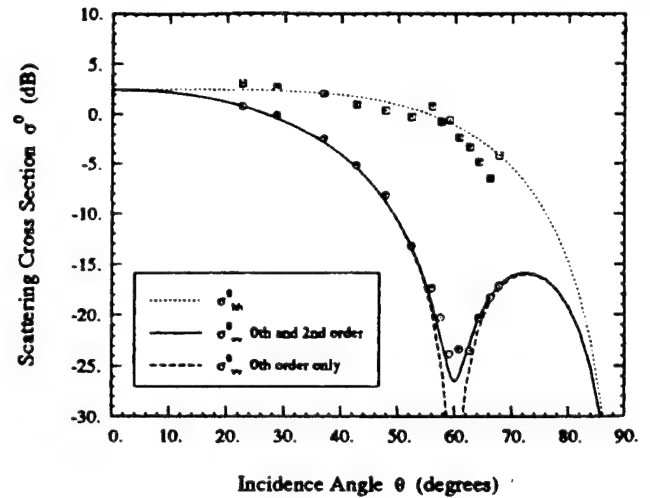
(a)

(b)

(c)

Fig. 8. Measured co-polarized specular scattering coefficient for three rough surfaces. Continuous curves are based on Physical Optics: the dashed curve corresponds to the zeroth-order term for σ_{vv}^0, the solid curve to σ_{vv}^0 with both the zeroth-order and second-order terms included; the dotted curve corresponds to σ_{hh}^0. The second-order term is negligible for hh polarization. In all cases, the surfaces have a relative dielectric constant $\epsilon = 3.0$ and an exponential correlation function was used. (a) $ks = 0.515, kl = 5.4$, (b) $ks = 1.39, kl = 10.6$, (c) $ks = 1.94, kl = 11.8$.

C. Incoherent Scattering

As was discussed previously in Section II, the expression given by (2) for the bistatic specular scattering coefficient consists of two terms, a zeroth-order term and a second-order term, with the latter being the result of a new derivation of the Physical Optics model given in Appendix A. Fig. 8(a) shows the measured values of σ_{vv}^0 and σ_{hh}^0 for a slightly rough surface with $ks = 0.515$, plotted as a function of incidence angle, as well as plots for the same quantities calculated in accordance with (2). The calculated curves include a pair for the zeroth-order term alone, and a pair for the sum of the zeroth-order and second-order terms. For hh polarization, the second-order term is much smaller than the zeroth-order term, and therefore its contribution is insignificant. The same observation applies to vv polarization for angles more than $5°$ away from the Brewster angle, but in the vicinity of the Brewster angle, the second order term becomes the dominant contribution and it correctly predicts the level of the experimental observations.

Unfortunately, for the rougher surfaces shown in Figs. 8(b) and (c) with $ks = 1.39$ and 1.94, the model overestimates the level of σ^0, particularly for vv polarization in the vicinity of the Brewster angle. The measured data fall in between the curves calculated on the basis of the zeroth-order term alone and the curves based on both terms. Thus, despite the improvement that the proposed model provides for the slightly-rough case shown in Fig. 8(a), it is inadequate for very rough surfaces.

V. CONCLUSION

Several measurements of specular scattering from rough surfaces at 10 GHz are presented. They indicate that the Physical Optics predictions for coherent scattering are very good for surface roughness as large as $ks = 2.0$, with the exception that the theory does not predict a shifting of the Brewster angle by a few degrees towards nadir. A theoretical explanation of this phenomenon is unresolved. For co-polarized incoherent scattering, Physical Optics has been shown to be an adequate descriptor for a surface with $ks = 0.515$, but rapidly loses its quantitative predictive value for $ks > 1$.

APPENDIX A. A VECTOR PHYSICAL OPTICS DEVELOPMENT

In Ulaby *et al.* [7], the Physical Optics solution for scattering from a dielectric rough surface is presented under the scalar approximation. This approximation leaves out many terms, some of which change the results of the calculations significantly. In particular, cross-polarized scattering is neglected in the plane of incidence under the scalar approximation. What follows is a full vector solution to the Physical Optics problem, including vector terms which are neglected via the scalar approximation and some higher order terms in the expansion of the solution with respect to surface slope, with the rest of the assumptions remaining the same as in Ulaby *et al.* [7].

The solution starts with the exact Stratton-Chu integral equation for the p-polarized scattered far field due to a q-polarized wave ($\hat{q}E_0e^{-jk\hat{n}_i\cdot\vec{r}}$) incident upon a rough surface:

$$E_{pq}^s = \frac{-jk_se^{-jk_sR_0}}{4\pi R_0}\hat{n}_s \times \int [(\hat{n} \times \vec{E}) - \eta_s\hat{n}_s \times (\hat{n} \times \vec{H})]$$
$$\times e^{jk_s\hat{n}_s\cdot\vec{r}}dS \tag{A.1}$$

$$= \frac{-jk_se^{-jk_sR_0}}{4\pi R_0}E_0 \int U_{pq}e^{jk_s(\hat{n}_s-\hat{n}_i)\cdot\vec{r}}dS \tag{A.2}$$

where the singly scattered fields on the surface are calculated via the tangent plane approximation and are given by:

$$\hat{n}_1 \times \vec{E} = [R_h(\hat{q} \cdot \hat{t})(\hat{n}_1 \times \hat{t})$$
$$+ R_v(\hat{n}_1 \cdot \hat{n}_i)(\hat{q} \cdot \hat{d})\hat{t}]E_0 \tag{A.3}$$

$$\eta_1\hat{n}_1 \times \vec{H} = [R_h(\hat{n}_1 \cdot \hat{n}_i)(\hat{q} \cdot \hat{t})\hat{t}$$
$$- R_v(\hat{q} \cdot \hat{d})(\hat{n}_1 \times \hat{t})]E_0 \tag{A.4}$$

where $\hat{n}_i$ is the incident wave direction, $\hat{q}$ is the incident wave polarization direction, $\hat{n}_1$ is the unit normal to the surface, $\hat{t} = \hat{n}_i \times \hat{n}_1/|\hat{n}_i \times \hat{n}_1|$, and $\hat{d} = \hat{n}_i \times \hat{t}$. Also, R_v and R_h are the v- and h- polarized Fresnel Reflection coefficients local to a point on the surface. These quantities, and the appropriate vector products, are defined in Ulaby *et al.* [7]; however, the exact expressions for U_{pq} under the single scattering tangent plane approximation do not appear there and hence are given here for reference:

$$U_{hh} = \frac{1}{D_1^2D_2}[R_vZ_t((\sin\theta\sin\Delta\phi + Z_t^s\cos\theta + Z_tZ_l^s\sin\theta)$$
$$+ (\cos\theta + Z_l\sin\theta)(\sin\theta\cos\theta_s\sin\Delta\phi$$
$$+ Z_t^s\cos\theta\cos\theta_s - Z_t\sin\theta\sin\theta_s))$$
$$- R_h(\sin\theta - Z_l\cos\theta)((\cos\theta + Z_l\sin\theta)$$
$$\times (\sin\theta\cos\Delta\phi - Z_l^s\cos\theta)$$
$$+ (\sin\theta\cos\theta_s\cos\Delta\phi - Z_l^s\cos\theta\cos\theta_s$$
$$+ Z_tZ_t^s\sin\theta\cos\theta_s - Z_l\sin\theta\sin\theta_s$$
$$+ (Z_l^2 + Z_t^2)\cos\theta\sin\theta_s))] \tag{A.5}$$

$$U_{vh} = \frac{1}{D_1^2D_2}[-R_h(\sin\theta - Z_l\cos\theta)((\sin\theta\sin\Delta\phi$$
$$+ Z_t^s\cos\theta + Z_tZ_l^s\sin\theta) + (\cos\theta + Z_l\sin\theta)$$
$$\times (\sin\theta\cos\theta_s\sin\Delta\phi + Z_t^s\cos\theta\cos\theta_s$$
$$- Z_t\sin\theta\sin\theta_s))$$
$$- R_vZ_t((\sin\theta\cos\theta_s\cos\Delta\phi - Z_l^s\cos\theta\cos\theta_s$$
$$+ Z_tZ_t^s\sin\theta\cos\theta_s - Z_l\sin\theta\sin\theta_s$$
$$+ (Z_l^2 + Z_t^2)\cos\theta\sin\theta_s)$$
$$+ (\cos\theta + Z_l\sin\theta)$$
$$\times (\sin\theta\cos\Delta\phi - Z_l^s\cos\theta))] \tag{A.6}$$

$$U_{hv} = \frac{1}{D_1^2D_2}[R_hZ_t((\cos\theta + Z_l\sin\theta)$$
$$\times (\sin\theta\cos\Delta\phi - Z_l^s\cos\theta)$$
$$+ (\sin\theta\cos\theta_s\cos\Delta\phi - Z_l^s\cos\theta\cos\theta_s$$
$$+ Z_tZ_t^s\sin\theta\cos\theta_s - Z_l\sin\theta\sin\theta_s$$
$$+ (Z_l^2 + Z_t^2)\cos\theta\sin\theta_s))$$
$$+ R_v(\sin\theta - Z_l\cos\theta)$$
$$\times ((\sin\theta\sin\Delta\phi + Z_t^s\cos\theta + Z_tZ_l^s\sin\theta)$$
$$+ (\cos\theta + Z_l\sin\theta)(\sin\theta\cos\theta_s\sin\Delta\phi$$
$$+ Z_t^s\cos\theta\cos\theta_s - Z_t\sin\theta\sin\theta_s))] \tag{A.7}$$

$$U_{vv} = \frac{1}{D_1^2 D_2}[R_h Z_t((\cos\theta + Z_l \sin\theta)$$

$$(\sin\theta\cos\theta_s \sin\Delta\phi + Z_t^s \cos\theta\cos\theta_s$$

$$- Z_t \sin\theta\sin\theta_s)$$

$$+ (\sin\theta\sin\Delta\phi + Z_t^s \cos\theta + Z_t Z_t^s \sin\theta))$$

$$- R_v(\sin\theta - Z_l \cos\theta)((\sin\theta\cos\theta_s \cos\Delta\phi$$

$$- Z_t^s \cos\theta\cos\theta_s + Z_t Z_t^s \sin\theta\cos\theta_s$$

$$- Z_l \sin\theta\sin\theta_s + (Z_l^2 + Z_t^2)\cos\theta\sin\theta_s)$$

$$+ (\cos\theta + Z_l \sin\theta)(\sin\theta\cos\Delta\phi - Z_l^s \cos\theta))] \tag{A.8}$$

where θ and θ_s describe the incident and scattered elevation angles measured from nadir, respectively, $\Delta\phi$ describes the angular change in azimuthal direction between the incident and scattered waves, Z_l and Z_t represent the surface slopes within (longitudinal to) and transverse to the plane of incidence, respectively, Z_l^s and Z_t^s represent the surface slopes within (longitudinal to) and transverse to the plane of the scattered wave, respectively, $D_1 = |\hat{n}_i \times \hat{n}_1| = \sqrt{(\sin\theta - Z_l \cos\theta)^2 + Z_t^2}$, and $D_2 = \sqrt{1 + Z_l^2 + Z_t^2}$.

Unfortunately, the exact expressions for U are not mathematically tractable in the Stratton-Chu integral, as the surface slopes are random functions of the location on the surface. An approximate solution can be obtained by expanding U in a Taylor series in slopes and retaining only the first two terms:

$$U_{pq} = U_{pq}^{(0)} + U_{pq}^{(1)} + \cdots \tag{A.9}$$

$$= \frac{1}{D_2}(a_{0pq} + (a_{lipq}Z_l + a_{tipq}Z_t + a_{lspq}Z_l^s$$

$$+ a_{tspq}Z_t^s)/\sin\theta + \cdots) \tag{A.10}$$

Note that D_2 need not be expanded as it will be cancelled upon integration over $dS = D_2 dx dy$, but D_1 is Taylor expanded as follows:

$$\frac{1}{D_1^2} = \frac{1}{(\sin\theta - Z_l \cos\theta)^2 + Z_t^2} \tag{A.11}$$

$$= \frac{1}{\sin^2\theta}\left(1 - \frac{Z_t^2}{\sin^2\theta} + 2\frac{Z_l}{\tan\theta}\right.$$

$$\left. + 3\frac{Z_l^2}{\tan^2\theta} + \cdots\right) \tag{A.12}$$

Similarly, the reflection coefficients local to the surface are also expanded in terms of slopes:

$$R_v = R_{v0} + R_{v1}Z_l + \cdots \tag{A.13}$$

$$R_h = R_{h0} + R_{h1}Z_l + \cdots \tag{A.14}$$

The reflection coefficients are not dependent on Z_l^s or Z_t^s, and depend on even powers only of Z_t. The a coefficients in the expansion of U are, for all principal linear polarization combinations, given by:

$$a_{0hh} = -R_{h0}(\cos\theta + \cos\theta_s)\cos\Delta\phi \tag{A.15}$$

$$a_{0vh} = -R_{h0}(1 + \cos\theta\cos\theta_s)\sin\Delta\phi \tag{A.16}$$

$$a_{0hv} = R_{v0}(1 + \cos\theta\cos\theta_s)\sin\Delta\phi \tag{A.17}$$

$$a_{0vv} = -R_{v0}(\cos\theta + \cos\theta_s)\cos\Delta\phi \tag{A.18}$$

$$a_{lihh} = R_{h0}(\sin\theta\sin\theta_s - (1 + \cos\theta\cos\theta_s)\cos\Delta\phi)$$

$$- R_{h1}\sin\theta\cos\Delta\phi(\cos\theta + \cos\theta_s) \tag{A.19}$$

$$a_{lshh} = R_{h0}\cos\theta(\cos\theta + \cos\theta_s) \tag{A.20}$$

$$a_{tihh} = R_{v0}\sin\Delta\phi(1 + \cos\theta\cos\theta_s) \tag{A.21}$$

$$a_{tshh} = 0 \tag{A.22}$$

$$a_{livh} = -R_{h0}\sin\Delta\phi(\cos\theta + \cos\theta_s)$$

$$- R_{h1}\sin\theta\sin\Delta\phi(1 + \cos\theta\cos\theta_s) \tag{A.23}$$

$$a_{lsvh} = 0 \tag{A.24}$$

$$a_{tivh} = R_{h0}\sin\theta\cos\theta\sin\theta_s$$

$$- R_{v0}\cos\Delta\phi(\cos\theta + \cos\theta_s) \tag{A.25}$$

$$a_{tsvh} = -R_{h0}\cos\theta(1 + \cos\theta\cos\theta_s) \tag{A.26}$$

$$a_{lihv} = R_{v0}\sin\Delta\phi(\cos\theta + \cos\theta_s)$$

$$+ R_{v1}\sin\theta\sin\Delta\phi(1 + \cos\theta\cos\theta_s) \tag{A.27}$$

$$a_{lshv} = 0 \tag{A.28}$$

$$a_{tihv} = -R_{v0}\sin\theta\cos\theta\sin\theta_s$$

$$+ R_{h0}\cos\Delta\phi(\cos\theta + \cos\theta_s) \tag{A.29}$$

$$a_{tshv} = R_{v0}\cos\theta(1 + \cos\theta\cos\theta_s) \tag{A.30}$$

$$a_{livv} = R_{v0}(\sin\theta\sin\theta_s - (1 + \cos\theta\cos\theta_s)\cos\Delta\phi)$$

$$- R_{v1}\sin\theta(\cos\theta + \cos\theta_s)\cos\Delta\phi \tag{A.31}$$

$$a_{lsvv} = R_{v0}\cos\theta(\cos\theta + \cos\theta_s) \tag{A.32}$$

$$a_{tivv} = R_{h0}\sin\Delta\phi(1 + \cos\theta\cos\theta_s) \tag{A.33}$$

$$a_{tsvv} = 0 \tag{A.34}$$

A. Differential Radar Cross Section

The elements of the covariance matrix [13] are given by:

$$\langle S_{mn} S_{pq}^* \rangle = \int\int \langle U_{mn}^* U_{pq}^* e^{jk(\hat{n}_s - \hat{n}_i)\cdot(\vec{r} - \vec{r}')} \rangle dS dS' \tag{A.35}$$

from which the differential radar cross section can be derived:

$$\sigma_{pq}^0 = \frac{k^2}{4\pi A_0}\langle S_{pq} S_{pq}^* \rangle \tag{A.36}$$

Using (A.9):

$$U_{mn} U_{pq}^* \approx U_{mn}^{(0)} U_{pq}^{(0)*} + (U_{mn}^{(0)} U_{pq}^{(1)*} + U_{mn}^{(1)} U_{pq}^{(0)*}) + U_{mn}^{(1)} U_{pq}^{(1)*} \tag{A.37}$$

and evaluating these separately, we can express σ^0 as:

$$\sigma_{pq}^0 \approx \frac{k^2}{4\pi A_0}\left(\langle S_{pq} S_{pq}^* \rangle_{s^0} + \langle S_{pq} S_{pq}^* \rangle_{s^1}\right.$$

$$\left. + \langle S_{pq} S_{pq}^* \rangle_{s^2}\right) \tag{A.38}$$

$$\langle S_{mn} S_{pq}^* \rangle_{s^0} = \int\int \langle U_{mn}^{(0)} U_{pq}^{(0)*} e^{jk(\hat{n}_s - \hat{n}_i)\cdot(\vec{r} - \vec{r}')} \rangle dS dS' \tag{A.39}$$

$$\langle S_{mn} S_{pq}^* \rangle_{s^1} = \int\int \langle (U_{mn}^{(0)} U_{pq}^{(1)*} + U_{mn}^{(1)} U_{pq}^{(0)*})$$

$$e^{jk(\hat{n}_s - \hat{n}_i)\cdot(\vec{r} - \vec{r}')} \rangle dS dS' \tag{A.40}$$

$$\langle S_{mn} S_{pq}^* \rangle_{s^2} = \int\int \langle U_{mn}^{(1)} U_{pq}^{(1)*} e^{jk(\hat{n}_s - \hat{n}_i)\cdot(\vec{r} - \vec{r}')} \rangle dS dS' \tag{A.41}$$

To obtain explicit expressions for σ_{pq}^0, the following relations will be used [7]:

$$\langle e^{jq_z(z-z')}\rangle = e^{-q_z^2 s^2(1-\rho(\xi))} \tag{A.42}$$

$$\langle Z_x e^{jq_z(z-z')}\rangle = \langle Z_x' e^{jq_z(z-z')}\rangle = -jq_z s^2 \cos\alpha \frac{\partial\rho(\xi)}{\partial\xi}$$
$$e^{-q_z^2 s^2(1-\rho(\xi))} \tag{A.43}$$

$$\langle Z_y e^{jq_z(z-z')}\rangle = \langle Z_y' e^{jq_z(z-z')}\rangle = -jq_z s^2 \sin\alpha \frac{\partial\rho(\xi)}{\partial\xi}$$
$$e^{-q_z^2 s^2(1-\rho(\xi))} \tag{A.44}$$

$$\langle Z_x Z_x' e^{jq_z(z-z')}\rangle = -\cos^2\alpha \left(q_z s^2 \frac{\partial\rho(\xi)}{\partial\xi}\right)^2$$
$$e^{-q_z^2 s^2(1-\rho(\xi))} \tag{A.45}$$

$$\langle Z_y Z_y' e^{jq_z(z-z')}\rangle = -\sin^2\alpha \left(q_z s^2 \frac{\partial\rho(\xi)}{\partial\xi}\right)^2$$
$$e^{-q_z^2 s^2(1-\rho(\xi))} \tag{A.46}$$

$$\langle Z_x Z_y' e^{jq_z(z-z')}\rangle = \langle Z_y Z_x' e^{jq_z(z-z')}\rangle = -\sin\alpha\cos\alpha$$
$$\times \left(q_z s^2 \frac{\partial\rho(\xi)}{\partial\xi}\right)^2 e^{-q_z^2 s^2(1-\rho(\xi))} \tag{A.47}$$

as well as the following Bessel function integral identity:

$$\int_{2\pi} \cos(n\alpha+\beta)e^{jx\cos\alpha}d\alpha = 2\pi j^n \cos\beta J_n(x) \tag{A.48}$$

where $q_z = k(\cos\theta + \cos\theta_s)$, s is the rms height, (ξ,α) are the polar coordinates of the difference between the unprimed and primed surface locations, and $\rho(\xi)$ is the normalized surface height correlation function.

B. Zeroth Order Term

The analysis of the zeroth order term is straightforward and yields the traditional coefficients for Physical Optics:

$$\frac{k^2}{4\pi A_0}\langle S_{mn}S_{pq}^*\rangle_{s^0} = \frac{1}{4\pi}k^2 a_{0mn}a_{0pq}^* I_0 \frac{1}{4\pi}k^2 a_{0mn}a_{0pq}^* I_0 \tag{A.49}$$

where

$$I_0 = 2\pi e^{-q_z^2 s^2} \int_0^\infty [e^{q_z^2 s^2 \rho(\xi)} - 1]J_0(q_t\xi)\xi d\xi \tag{A.50}$$

$$q_t = k\sqrt{\sin^2\theta + \sin^2\theta_s - 2\sin\theta\sin\theta_s\cos\Delta\phi} \tag{A.51}$$

This term represents the expected power in a particular direction due to the correlation of the height of the surface at one point to the height at another point. This term is the largest contribution to σ^0.

C. First Order Term

The first order term in Ulaby et al. [7] is that of the scalar approximation. Below is the full vector solution under the tangent plane approximation:

$$\frac{k^2}{4\pi A_0}\langle S_{mn}S_{pq}^*\rangle_{s^1} = \frac{-k^2}{4\pi q_z \sin\theta}[(a_{0mn}a_{lipq}^* + a_{limn}a_{0pq}^*)q_{li}$$
$$+ (a_{0mn}a_{lspq}^* + a_{lsmn}a_{0pq}^*)q_{ls}$$
$$+ (a_{0mn}a_{tipq}^* + a_{timn}a_{0pq}^*)q_{ti}$$
$$+ (a_{0mn}a_{tspq}^* + a_{tsmn}a_{0pq}^*)q_{ts}]I_0 \tag{A.52}$$

where

$$q_{li} = k(\sin\theta_s \cos\Delta\phi - \sin\theta) \tag{A.53}$$
$$q_{ti} = k\sin\theta_s \sin\Delta\phi \tag{A.54}$$
$$q_{ls} = k(\sin\theta_s - \sin\theta\cos\Delta\phi) \tag{A.55}$$
$$q_{ts} = k\sin\theta \sin\Delta\phi \tag{A.56}$$

This term represents the expected power in a particular direction due to the correlation of height of the surface at one point to the slope at another point. This term is negligible for scattering in the plane of incidence.

D. Second Order Term

The cross-slope term does not appear in Ulaby et al [7], but is nonetheless an analytic term. It is given by:

$$\frac{k^2}{4\pi A_0}\langle S_{mn}S_{pq}^*\rangle_{s^2}$$
$$= \frac{k^2 q_z^2 s^4}{4\sin^2\theta}\{[a_{limn}a_{lipq}^* + a_{lsmn}a_{lspq}^*$$
$$+ a_{timn}a_{tipq}^* + a_{tsmn}a_{tspq}^*$$
$$+ ((a_{lsmn}a_{tipq}^* + a_{timn}a_{lspq}^*)$$
$$- (a_{limn}a_{tspq}^* + a_{tsmn}a_{lipq}^*))\sin\Delta\phi$$
$$+ ((a_{limn}a_{lspq}^* + a_{lsmn}a_{lipq}^*)$$
$$+ (a_{timn}a_{tspq}^* + a_{tsmn}a_{tipq}^*))\cos\Delta\phi]I_{20}$$
$$- [(a_{limn}a_{lipq}^* - a_{timn}a_{tipq}^*)(q_{li}^2 - q_{ti}^2)$$
$$+ (a_{lsmn}a_{lspq}^* - a_{tsmn}a_{tspq}^*)(q_{ls}^2 - q_{ts}^2)$$
$$- (a_{limn}a_{tipq}^* + a_{timn}a_{lipq}^*)q_{ti}q_{li}$$
$$- (a_{lsmn}a_{tspq}^* + a_{tsmn}a_{lspq}^*)q_{ts}q_{ls}$$
$$+ ((a_{limn}a_{tspq}^* + a_{tsmn}a_{lipq}^*)$$
$$+ (a_{lsmn}a_{tipq}^* + a_{timn}a_{lspq}^*))(q_{ti}q_{ls} + q_{li}q_{ts})$$
$$+ ((a_{limn}a_{lspq}^* + a_{lsmn}a_{lipq}^*)$$
$$- (a_{timn}a_{tspq}^* + a_{tsmn}a_{tipq}^*))$$
$$\times (q_{li}q_{ls} + q_{ti}q_{ts})]I_{22}\} \tag{A.57}$$

where

$$I_{20} = \int_0^\infty \left(\frac{\partial\rho(\xi)}{\partial\xi}\right)^2 J_0(q_t\xi)e^{-q_z^2 s^2(1-\rho(\xi))}\xi d\xi \tag{A.58}$$

$$I_{22} = \int_0^\infty \left(\frac{\partial\rho(\xi)}{\partial\xi}\right)^2 \frac{J_2(q_t\xi)}{q_t^2}e^{-q_z^2 s^2(1-\rho(\xi))}\xi d\xi \tag{A.59}$$

This term represents the expected power in a particular direction due to the correlation of slope of the surface at one point to the slope at another point. This term is significant for cross polarization in the plane of incidence, and when the angle of incidence is near the Brewster angle for the mean surface.

E. Evaluation of the I Integrals for Common Correlation Functions

The remaining integrals can be further simplified if we assume a form for the correlation function $\rho(\xi)$. In particular, if it is Gaussian, i.e., $\rho(\xi) = e^{-\xi^2/l^2}$, then

$$I_0 = \pi l^2 e^{-q_z^2 s^2} \sum_{i=1}^{\infty} \frac{(q_z s)^{2i}}{i! i} e^{-\frac{q_t^2 l^2}{4i}} \quad (A.60)$$

$$I_{20} = 2e^{-q_z^2 s^2} \sum_{i=1}^{\infty} \frac{i(q_z s)^{2(i-1)}}{(i+1)!(i+1)} e^{-\frac{q_t^2 l^2}{4(i+1)}} \left(1 - \frac{q_t^2 l^2}{4(i+1)}\right) \quad (A.61)$$

$$I_{22} = \frac{1}{2} l^2 e^{-q_z^2 s^2} \sum_{i=1}^{\infty} \frac{i(q_z s)^{2(i-1)}}{(i+1)!(i+1)^2} e^{-\frac{q_t^2 l^2}{4(i+1)}} \quad (A.62)$$

or, if the correlation function is exponential, i.e., $\rho(\xi) = e^{-\xi/l}$, then

$$I_0 = 2\pi l^2 e^{-q_z^2 s^2} \sum_{i=1}^{\infty} \frac{(q_z s)^{2i}}{(i-1)!(i^2 + q_t^2 l^2)^{\frac{3}{2}}} \quad (A.63)$$

$$I_{20} = e^{-q_z^2 s^2} \sum_{i=1}^{\infty} \frac{(i+1)(q_z s)^{2(i-1)}}{(i-1)!(i^2 + q_t^2 l^2)^{\frac{3}{2}}} \quad (A.64)$$

$$I_{22} = 2l^2 e^{-q_z^2 s^2} \sum_{i=1}^{\infty} \frac{(q_z s)^{2(i-1)}(\sqrt{(i+1)^2 + q_t^2 l^2} - (i+1))}{(i-1)!((i+1)^2 + q_t^2 l^2)^{\frac{3}{2}} q_t^2 l^2}$$
$$\times \left(1 - (i+1)\frac{\sqrt{(i+1)^2 + q_t^2 l^2} - (i+1)}{2q_t^2 l^2}\right) \quad (A.65)$$

F. Special Case: Forward Scattering in the Specular Direction

For forward scattering in the specular direction, $\theta_s \to \theta, \Delta\phi \to 0$, and $q_t \to 0$, and the general expressions above simplify considerably:

$$\frac{k^2}{4\pi A_0} \langle S_{mn} S_{pq}^* \rangle_{s^0} = \frac{1}{4\pi} k^2 a_{0mn} a_{0pq}^* I_0 \quad (A.66)$$

$$\frac{k^2}{4\pi A_0} \langle S_{mn} S_{pq}^* \rangle_{s^1} = 0 \quad (A.67)$$

$$\frac{k^2}{4\pi A_0} \langle S_{mn} S_{pq}^* \rangle_{s^2} = \frac{k^4 s^4}{\tan^2 \theta} [(a_{limn} + a_{lsmn})(a_{lipq}^* + a_{lspq}^*) + (a_{timn} + a_{tsmn})(a_{tipq}^* + a_{tspq}^*)] I_{20} \quad (A.68)$$

where

$$a_{0hh} = -2R_{h0} \cos\theta \quad (A.69)$$
$$a_{0vh} = a_{0hv} = 0 \quad (A.70)$$
$$a_{0vv} = -2R_{v0} \cos\theta \quad (A.71)$$
$$a_{livv} + a_{lsvv} = -2R_{v1} \sin\theta \cos\theta \quad (A.72)$$
$$a_{livh} + a_{lsvh} = a_{lihv} + a_{lshv} = 0 \quad (A.73)$$
$$a_{lihh} + a_{lshh} = -2R_{h1} \sin\theta \cos\theta \quad (A.74)$$
$$a_{tivh} + a_{tsvh} = -2(R_{h0} \cos^2\theta + R_{v0}) \cos\theta \quad (A.75)$$
$$a_{tihv} + a_{tshv} = 2(R_{v0} \cos^2\theta + R_{h0}) \cos\theta \quad (A.76)$$
$$a_{tivv} + a_{tsvv} = a_{tihh} + a_{tshh} = 0 \quad (A.77)$$

$$I_0 = 2\pi e^{-q_z^2 s^2} \int_0^{\infty} [e^{q_z^2 s^2 \rho(\xi)} - 1]\xi d\xi \quad (A.78)$$

$$I_{20} = \int_0^{\infty} \left(\frac{\partial \rho(\xi)}{\partial \xi}\right)^2 e^{-q_z^2 s^2(1-\rho(\xi))} \xi d\xi \quad (A.79)$$

For the principal linear polarizations $pq = hh, hv, vh, vv$, the incoherent specular scattering coefficient can be obtained by setting $mn = pq$ in (A.66) and (A.68) and the resultant expressions in (A.38) This process leads to the expression given in 920.

REFERENCES

[1] K. C. McDonald, M. C. Dobson and F. T. Ulaby, "Using MIMICS to model L-band multi-angle and multi-temporal backscatter from a walnut orchard," *IEEE Transactions on Geoscience and Remote Sensing*, vol. 28, no. 3, pp. 477–491, May 1990.
[2] K. C. McDonald, M. C. Dobson and F. T. Ulaby, "Modeling multi-frequency diurnal backscatter from a walnut orchard," *IEEE Transactions on Geoscience and Remote Sensing*, vol. 29, no. 6, pp. 852–863, 1991.
[3] K. C. McDonald, *Modeling Microwave Backscatter from Tree Canopies*, PhD dissertation, University of Michigan, Ann Arbor, 1991.
[4] F. T. Ulaby, K. Sarabandi, K. C. McDonald, M. Whitt and M. C. Dobson, "Michigan Microwave Conopy Scattering Model," *International Journal of Remote Sensing*, vol. 11, no. 7, pp. 1223–1253, 1990.
[5] M. Whitt, *Microwave Scattering from Periodic Row-Structured Vegetation*, PhD dissertation, University of Michigan, Ann Arbor, 1991.
[6] P. Beckmann and A. Spizzichino, *The Scattering of Electromagnetic Waves from Rough Surfaces*, Pergamon Press, Oxford, 1963.
[7] F. T. Ulaby, R. K. Moore and A. K. Fung, *Microwave Remote Sensing: Active and Passive*, volume 2, Addison-Wesley, Reading, Massachusetts, 1982.
[8] R. L. Cosgriff, W. H. Peake and R. C. Taylor, "Terrain scattering properties for sensor system design," *Technical Report* 181, Ohio State University, 1960.
[9] F. T. Ulaby, T. F. Haddock and M. E. Coluzzi, "Millimeter-wave bistatic radar measurements of sand and gravel," in *Digest, IEEE International Geoscience and Remote Sensing Symposium* (IGARSS'87), pp. 281–286, Ann Arbor, MI, May 1987.
[10] M. Saillard and D. Maystre, "Scattering from metallic and dielectric rough surfaces," *Journal of the Optical Society of America A*, vol. 7, no. 6, pp. 982–990, June 1990.
[11] J.-J. Greffet, "Theoretical model of the shift of the Brewster angle on a rough surface," *Optics Letters*, vol. 17, no. 4, pp. 238–240, February 1992.
[12] S. O. Rice, "Reflection of electromagnetic waves from slightly rough surfaces," *Communications in Pure and Applied Mathematics*, vol. 4, pp. 351–378, 1951.
[13] F. T. Ulaby and E. C. Elachi, *Radar Polarimetry for Geoscience Applications*, Artech House, Norwood, Massachusetts, 1990.
[14] J. C. Leader, "Bidirectional scattering of electromagnetic waves from rough surfaces," *Journal of Applied Physics*, vol. 42, no. 12, pp. 4808–4816, November 1971.
[15] J. C. Leader and W. A. J. Dalton, "Bidirectional scattering of electromagnetic waves from the volume of dielectric materials," *Journal of Applied Physics*, vol. 43, no. 7, pp. 3080–3090, July 1972.
[16] K. Sarabandi and F. T. Ulaby, "A convenient technique for polarimetric calibration of single-antenna radar systems," *IEEE Transactions on Geoscience and Remote Sensing*, vol. 28, no. 6, pp. 1022–1033, November 1990.
[17] K. A. O'Donnell and E. R. Mendez, "Experimental study of scattering from characterized random surfaces," *Journal of the Optical Society of America*, vol. 4, no. 7, pp. 1194–1205, July 1987.
[18] E. R. Mendez and K. A. O'Donnell, "Observation of depolarization and backscattering enhancement in light scattering from Gaussian random surfaces," *Optics Communications*, vol. 61, no. 2, pp. 91–95, January 1987.
[19] Y. Oh, K. Sarabandi and F. T. Ulaby, "An empirical model and an inversion technique for radar scattering from bare soil surfaces," *IEEE Transactions on Geoscience and Remote Sensing*, vol. 30, no. 2, pp. 370–381, March 1992.

Roger D. De Roo (S'88) was born in Ridgewood, NJ, on February 29, 1964. He received the B.S. degree in letters and engineering from Calvin College, Grand Rapids, MI, in 1986, and the B.S.E. and M.S.E. degrees from the University of Michigan, Ann Arbor, both in electrical engineering, in 1986 and 1989, respectively.

He is currently a candidate for the Ph.D. degree at the University of Michigan. His research interests include modeling and measurement of bistatic scattering of electromagnetic waves from rough surfaces and modeling electromagnetic scattering from vegetation.

Fawwaz T. Ulaby (M'68–SM'74–F'80) received the B.S. degree in physics from the American University of Beirut, Lebanon, in 1964 and the M.S.E.E. and Ph.D. degrees in electrical engineering from the University of Texas, Austin, TX, in 1966 and 1968, respectively.

Dr. Ulaby is the Williams Professor of Electrical Engineering and Computer Science and the Director of the NASA Center for Space Terahertz Technology at the University of Michigan, Ann Arbor. His current interests include microwave and millimeter-wave remote sensing, radar systems, and radio wave propagation. He is the recipient of numerous awards, including the Eta Kappa Nu Association C. Holmes MacDonald Award as "An Outstanding Electrical Engineering Professor in the United States of America for 1975," the IEEE Geoscience and Remote Sensing Distinguished Achievement Award (1983), the IEEE Centennial Medal (1984), the American Society of Photogrammetry's Presidential Citation for Meritorious Service (1984), the Kuwait Prize in applied science (1986), the NASA Group Achievement Award (1990), and the University of Michigan Distinguished Faculty Achievement Award (1991).

Professor Ulaby served as president of the IEEE Geoscience and Remote Sensing Society (1980–1982), as Executive Editor of its *Transactions* (1983–1985), and as General Chairman of several international symposia. he is a member of URSI Commission F and served on several scientific boards and professional committees.

Snow Probe for *In Situ* Determination of Wetness and Density

John R. Kendra, *Student Member, IEEE*, Fawwaz T. Ulaby, *Fellow, IEEE*, and Kamal Sarabandi, *Senior Member, IEEE*

Abstract—The amount of water present in liquid form in a snowpack exercises a strong influence on the radar and radiometric responses of snow. Conventional techniques for measuring the liquid water content m_v suffer from various shortcomings, which include poor accuracy, long analysis time, poor spatial resolution, and/or cumbersome and inconvenient procedures. This paper describes the development of a hand-held electromagnetic sensor for quick and easy determination of snow liquid water content and density. A novel design of this probe affords several important advantages over existing similar sensors. Among these are improved spatial resolution and accuracy, and reduced sensitivity to interference by objects or media outside the sample volume of the sensor. The sensor actually measures the complex dielectric constant of the snow medium, and the water content and density must be obtained through the use of empirical or semi-empirical relations. To test the suitability of existing models and allow the development of new models, the snow probe was tested against the freezing calorimeter and gravimetric density determinations. From these comparisons, valid models were selected or developed. Based on the use of these models, the following specifications were established for the snow probe: 1) liquid water content measurement accuracy = $\pm 0.66\%$ in the wetness range from 0 to 10% by volume and 2) wet snow density measurement accuracy = ± 0.05 g/cm^3 in the density range from 0.1 to 0.6 g/cm^3.

I. INTRODUCTION

IN the study of microwave remote sensing of snow, it is necessary to consider the presence of liquid water in the snowpack. The dielectric constant of water is large (e.g., $\epsilon_w = 88 - j9.8$ at 1 GHz [1]) relative to that of ice ($\epsilon_i \approx 3.15 - j0.001$ [2]), and therefore even a very small amount of water will cause a substantial change in the overall dielectric properties of the snow medium, particularly with respect to the imaginary part. These changes will, in turn, influence the radar backscatter and microwave emission responses of the snowpack.

Among instruments available for measuring the volumetric liquid-water content of snow, m_v, under field conditions, the freezing calorimeter [3]–[5] offers the best accuracy ($\approx 1\%$) and has been one of the most widely used in support of quantitative snow-research investigations. In practice, however, the freezing calorimeter technique suffers from a number of drawbacks. First, the time required to perform an individual measurement of m_v is about thirty minutes. Improving the temporal resolution to a shorter interval would require the use of multiple instruments, thereby increasing the cost and

necessary manpower. Second, the technique is rather involved, requiring the use of a freezing agent and the careful execution of several steps. Third, the freezing calorimeter actually measures the mass fraction of liquid water in the snow sample, W, not the volumetric water content m_v. To convert W to m_v, a separate measurement of snow density is required. Fourth, because a relatively large snow sample (about 250 cm^3) is needed to achieve acceptable measurement accuracy, it is difficult to obtain the sample from a thin horizontal layer, thereby rendering the technique impractical for profiling the variation of m_v with depth. Yet, the depth profile of m_v, which can exhibit rapid spatial and temporal variations [6], [7], is one of the most important parameters of a snowpack, both in terms of the snowpack hydrology and the effect that m_v has on the microwave emission and scattering behavior of the snow layer.

In experimental investigations of the radar response of snow-covered ground, it is essential to measure the depth profile of m_v with good spatial resolution (2–3 cm) and adequate temporal resolution (a few minutes), particularly during the rapid melting and freezing intervals of the diurnal cycle. There have in recent years appeared a host of instruments [8] which retrieve snow parameters quickly and nondestructively, by measuring the dielectric constant of snow and relating it to the physical parameters. Of these techniques, the most attractive candidate has been the "Snow Fork," a microwave instrument developed in Finland [1]. The strengths of this technique are the simplicity of the equipment and speed of the measurement, high spatial resolution, and the ability to measure both the real and imaginary parts of the dielectric constant of snow, allowing for more powerful algorithms allowing determination of snow wetness and density with a single measurement. In the process of examining the Snow Fork approach, we decided to modify the basic design to improve the sensitivity of the instrument to m_v and reduce the effective sampled volume of the snow medium, thereby improving the spatial resolution of the sensor. Our modified design, which we shall refer to as the "Snow Probe" is described in Section II. The snow probe measures the real and imaginary parts of the relative dielectric constant of the snow medium, from which the liquid water content m_v and the snow density ρ_s are calculated through the use of empirical or semi-empirical relations. The degree to which such relations are valid is established through a comparison with direct techniques. Therefore, in the process of developing a snow probe algorithm, it was necessary to perform independent measurements of ρ_s and m_v. Density measurements were performed with a standard tube of known volume, whose weight is measured both empty
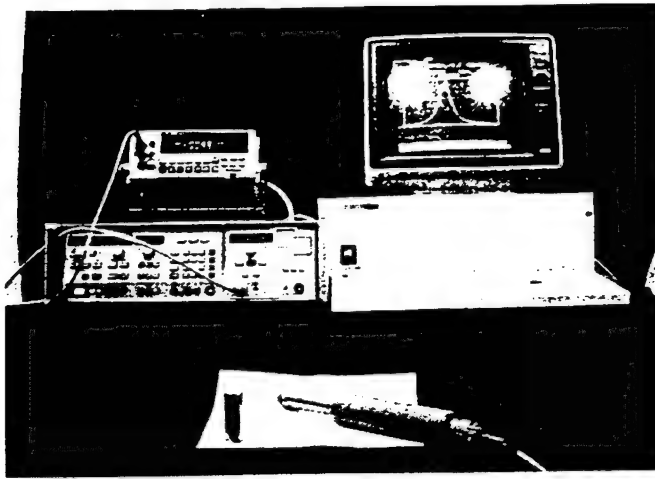
Fig. 1.   Photograph of snow probe system.

and full of snow. For a direct technique for measuring m_v we evaluated two candidates: 1) the freezing calorimeter; and 2) the dilatometer [9], which measures the change in volume that occurs as a sample melts completely. The dilatometer approach was rejected because of poor measurement accuracy and long measurement time (about one hour). The form of the relations which were ultimately established as a result of these comparison studies is described in Section III.

II. SNOW DIELECTRIC PROBE

A. Snow Probe Measurement System

Figs. 1 and 2 show a photograph of the snow probe measurement system, and a schematic diagram, respectively. The sweep oscillator, under computer control, sweeps (in discrete 10 MHz steps) over a relatively large frequency range. This serves to determine, within ±5 MHz, the frequency at which the detected voltage is a maximum, corresponding to the resonant frequency of the probe. The RF power transmitted through the snow probe is converted to video by the crystal detector, measured by the voltmeter, which in turn sends the voltage values to the computer. The frequency spectrum is generated in real-time on the monitor of the computer. In the second pass, a much narrower frequency range is centered around the peak location and swept with a finer step size (≈ 1 MHz). The center frequency and the 3-dB bandwidth around it are found, and from these, first the dielectric constant and then the snow parameters m_v and ρ_s are determined according to procedures described in detail in Section III of this paper.

As it is depicted in these figures, the snow probe is connected to a coaxial cable approximately 15 meters long. This arrangement is suitable, for example, for cases in which measurements are required in an area fairly local to truck mounted radars. For more remote field applications, the functions of the hardware shown would need to be combined into a portable unit. The technology for building a compact unit is well established.

B. Sensor Design

The snow probe is essentially a transmission-type electromagnetic resonator. The resonant structure used in the original
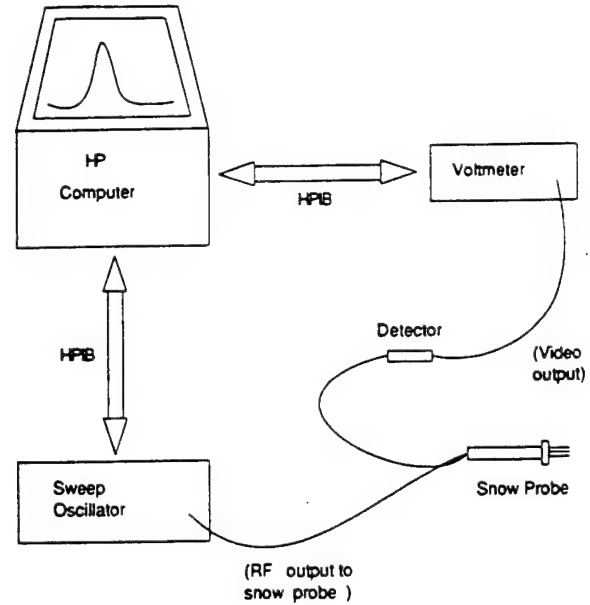
Fig. 2.   Schematic diagram of snow probe system.

design [1] was a twin-pronged fork. This structure behaves as a two wire transmission line shorted on one end and open on the other. It is resonant at the frequency for which the length of the resonant structure is equivalent to $\lambda/4$ in the surrounding medium. The RF power is fed in and out of the structure using coupling loops.

For our design, we used a coaxial type resonator, as illustrated in Fig. 3. The skeleton of the outer conductor is achieved using four prongs. The principle is basically the same: a quarter wavelength cavity, open on one end, shorted on the other, with power delivered in and out through coupling loops. The coaxial design was chosen for purposes of spatial resolution. Being a shielded design, the electric field is confined to the volume contained within the resonant cavity, as opposed to the original design, which used only two prongs. The coaxial design also had a much higher quality factor, (≈ 110 versus 40–70 for the original design) which, as discussed below, allows for more accurate determination of the complex dielectric constant. A photograph of the snow probe is shown in Fig. 4. The stainless-steel band encircling the resonant structure near the bottom is necessary to defeat competing two-wire resonances which are otherwise excited between any given pair of the outer prongs.

The real part of the dielectric constant is determined by the resonant frequency of the transmission spectrum, or equivalently, the frequency at which maximum transmission occurs. As mentioned above, this corresponds to the frequency for which the wavelength in the medium is equal to four times the length of the resonator. If the measured resonant frequency is f_a in air and f_s in snow, then the real part of the dielectric constant is given by

$$\epsilon_s' = \left(\frac{f_a}{f_s} \right)^2. \tag{1}$$

The imaginary part of ϵ_s is determined from the change in Q_m, the measured quality factor of the resonator. The quality factor may be determined by measuring Δf, the half-power
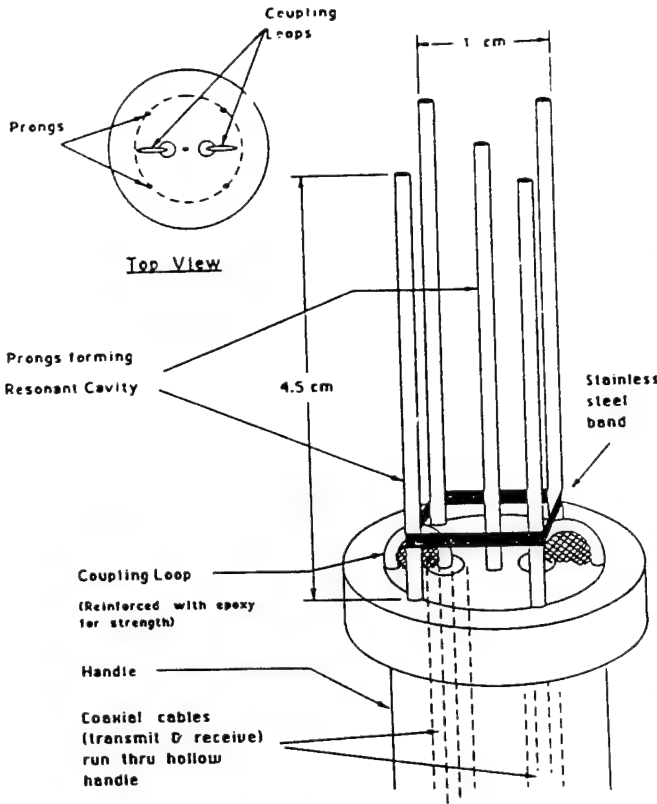
Fig. 3. Illustration of snow probe. Coaxial transmission lines extend through handle. At the face of the snow probe, the center conductors of the coaxial lines extend beyond and curl over to form coupling loops.
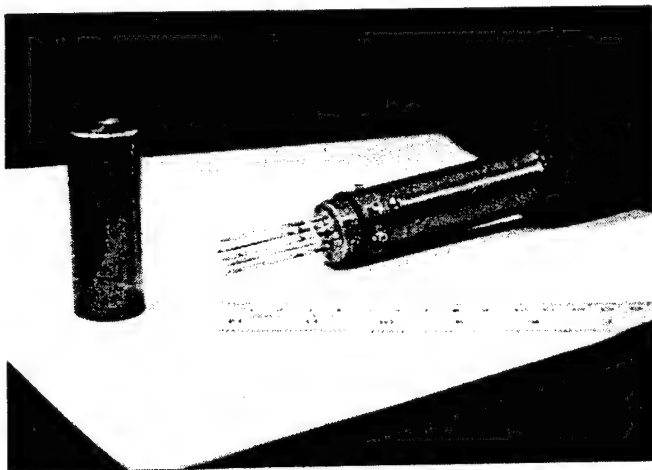

Fig. 4. Photograph of snow probe with cap.

bandwidth [10]:

$$Q_m = \frac{f_r}{\Delta f} \tag{2}$$

where f_r is the resonant frequency (f_a or f_s, depending on whether the medium is air or snow). For the snow probe, power losses exist because of radiation, finite conductivity of the conductors, coupling mechanisms (i.e., coupling loops), and dissipation in a lossy dielectric. Thus the measured Q is

TABLE I
SUMMARY OF TEST MATERIAL PROPERTIES AND MEASUREMENTS

Material	$\bar{\epsilon}$	(GHz) f_R	Q_m
Air	$1.0 - j0.0$	1.716	125.2
Sand	$2.78 - j3.70e^{-2}$	1.036	51.7
Sugar	$1.98 - j7.8e^{-3}$	1.229	89.3
Coffee	$1.50 - j3.32e^{-2}$	1.431	30.4
Wax	$2.26 - j0.3e^{-3}$	1.150	137.0

given by [10]

$$\frac{1}{Q_m} = \frac{1}{Q_R} + \frac{\epsilon''}{\epsilon'} \tag{3}$$

where Q_m is the measured Q when the probe is inserted in the snow medium, and Q_R is the quality factor describing collectively radiation losses, losses due to the finite conductivity of the conductors, and the power losses due to the external coupling mechanisms for the dielectric-filled snow probe. To calculate ϵ'', from (3), one must not only measure Q_m and know ϵ', but the value of Q_R should be known also. As long as $\tan\delta = \epsilon''/\epsilon'$ is very small, which is the case for snow, it is reasonable to assume that Q_R is a function of ϵ' only. This assumption was verified experimentally by measuring Q_R for each of five materials with known dielectric properties (Table I). For each material, Q_m was calculated by (2) on the basis of measurements of Δf and f_r and then it was used in (3) to compute Q_R. The values of ϵ' and ϵ'' of the test materials given in Table I were measured with an L-band cavity resonator. This process not only validated the assumption that Q_R is dependent on ϵ' only, but it also produced an expression for computing it:

$$\frac{1}{Q_R} = \frac{(pf_r + b) \times 10^{-3}}{f_r} \tag{4}$$

where p and b are constants and f_r is the resonant frequency associated with the material under test (which is related to ϵ' by $\epsilon' = (f_a/f_r)^2$). For the probe used in this study, $p = 8.381$ and $b = 0.7426$ when f_r is in GHz. Combining (2), (3), and (4) and specializing the notation to snow (by adding a subscript s to ϵ'' and replacing the subscript r by s in f_r) we obtain the expression

$$\epsilon'' = \left(\frac{f_a}{f_s}\right)^2 \left[\frac{\Delta f_s}{f_s} - \left(p + \frac{b}{f_s}\right)\right]. \tag{5}$$

Equations (1) and (5) constitute the basic relations used for determining ϵ_s' and ϵ_s'' from measurements of f_a, the resonant frequency when the probe is in air, and f_s and Δf_s, the resonant frequency and associated 3-dB bandwidth measured when the probe is inserted in the snow sample.

C. Spatial Resolution/Outside Interference

As mentioned earlier, the partially shielded design of this sensor reduces its sensitivity to permittivity variations outside the sample volume. By sample volume, we refer to the volume inside the cylinder described by the four outside prongs (Fig.

3). The coaxial design will tend to produce greater field confinement relative to a twin-prong structure.

The effective sample volume was tested in the following way: a cardboard box (30 cm × 30 cm) was filled with sugar to a depth of ≈16 cm. The snow probe was inserted into the sugar at a position in the center of the top surface, and then the dielectric constant was measured. Next, a thin metal plate (square, ≈25 cm on a side) was inserted into the sugar, parallel to and resting against one side of the box. The dielectric constant was remeasured. The metal plate was incrementally moved closer to the sensor position, with dielectric measurements recorded at each sensor-to-plate distance. The results of the experiment are shown in Fig. 5, in which ϵ'' is plotted as a function of the sensor-to-plate separation.

The plate appears to have a weak influence on the measurement, even at a distance of only 0.6 cm. To put this variation into perspective, had the material been snow, and using the relations given in Section III-A, the fluctuation in the estimate of liquid water would have ranged from $m_v = 0.6\%$ to $m_v = 0.8 \%$. The real part of the dielectric constant (not shown in Fig. 5) stayed within the range 2.00–2.01 during the experiment. The results of this experiment, which essentially confirm the expectation that the electric field is confined to the volume enclosed by the four prongs, translate into a vertical resolution of about 2 cm when the snow probe is inserted into the snowpack horizontally (the snow probe cross section is 1 cm × 1 cm).

There is necessarily a compromise between the ability to make high spatial resolution measurements and maximum ruggedness of design. The overall small size of the probe requires the use of small diameter prongs as well to insure that the snow volume which is being sampled is not compressed to the point of compromising the measurement. Though we used stainless steel for the prongs to afford maximum strength, it is still possible—for snow samples which are especially dense, coarse, or icy—to have some bending of the prongs occur. For some extreme cases the probe might not be a practical option for a measuring device. In these cases, it may also be the case that the simple relationships (which will be described in Section III) between dielectric constant and snow parameters no longer hold.

III. RETRIEVAL OF SNOW DENSITY AND LIQUID WATER CONTENT

The preceding section described the design and operation of the snow probe and the procedure used for measuring ϵ'_s and ϵ''_s of the snow medium. The next step is to use these measurements to determine the density ρ_s and liquid-water content m_v. This is accomplished by using a set of empirical or semi-empirical relationships relating the dielectric constant of wet snow to its density and liquid-water content. These relationships express the dielectric constant of wet snow ϵ_{ws} in terms of ϵ_{ds}, the dielectric constant of the snow in the absence of liquid water, plus additional terms that account for the increase in ϵ' and ϵ'' due to the presence of liquid water:

$$\epsilon'_{ws} = \epsilon'_{ds} + \Delta' \tag{6}$$

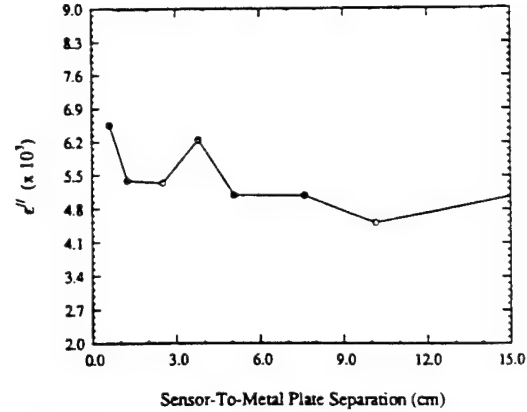$$\epsilon''_{ws} = \epsilon''_{ds} + \Delta'' \tag{7}$$

Fig. 5. Variation in measurement of ϵ'' of suger as a function of sensor proximity to metal plate. (Real part ϵ' stayed in the range 2.00–2.01.)

where Δ' and Δ'' represent the incremental increases due to m_v. The particular expressions for these quantities which we adopt for evaluation are based on the dispersion behavior of liquid water [2]:

$$\Delta' = 0.02m_v^{1.015} + \frac{0.073m_v^{1.31}}{1 + (f_s/f_w)^2} \tag{8}$$

$$\Delta'' = \frac{0.073(f_s/f_w)m_v^{1.31}}{1 + (f/f_w)^2} \tag{9}$$

where f_s is the resonant frequency at which ϵ'_{ws} and ϵ''_{ws} are measured by the probe, $f_w = 9.07$ GHz is the relaxation frequency of water at 0°C, and m_v is expressed in percent. Thus, the quantities measured by the snow probe are ϵ'_{ws}, ϵ''_{ws}, and f_s, and the quantities we wish to retrieve are m_v and ρ_{ws}, the latter being the density of the wet snow medium.

A. Liquid-Water Content

In the frequency range around 1 GHz, which is the operational frequency range of the probe, the dielectric loss factor of dry snow ϵ''_{ds} is less than 4×10^{-4} (for a snow density ρ_{ds} less than 0.5 g/cm³). For $m_v = 1\%$, the increment Δ'' given by (9) is equal to 7.5×10^{-3}, which is approximately 20 times larger than the first term. Hence, ϵ''_{ds} may be ignored in (7) and the equation can be solved to express m_v in terms of ϵ''_{ws}:

$$m_v = \left\{ \frac{\epsilon''_{ws}[1 + (f_s/f_w)^2]}{0.073(f_s/f_w)} \right\}^{\frac{1}{1.31}}. \tag{10}$$

The applicability of this retrieval procedure was evaluated by comparing the results obtained using (10) on the basis of the snow-probe measurements with those measured with a freezing calorimeter. The freezing calorimeter measures the liquid water mass fraction W, from which m_v was calculated by using the relationship

$$m_v = 100\rho_{ws}W \tag{11}$$

where ρ_{ws} is the density of the wet snow sample, which was measured gravimetrically.

The results for the liquid water content comparison are shown in Fig. 6. The error bars associated with the freezing calorimeter data points show the range of results obtained
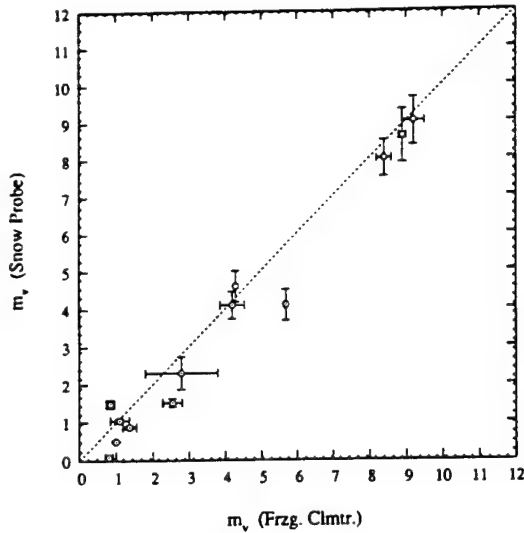
Fig. 6. Comparison of snow wetness results obtained via snow probe and freezing calorimetry, respectively. Snow probe data points are based on an average of twelve separate measurements.
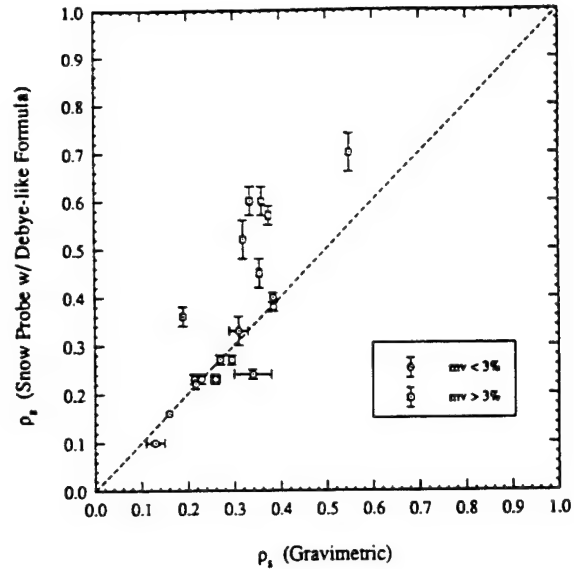

Fig. 7. Comparison of snow density results obtained via snow probe (in conjuction with Debye-like relation) and gravimetric measurements. Data points represented with squares were from snowpacks having volumetric wetness levels of >3%; with circles, <3%.

from typically two separate (and usually simultaneous) determinations. (Data points with no error bars indicate only a single measurement or that only the mean value of a set was available.) The freezing calorimeter has generally excellent precision.

The values for m_v obtained from the snow-probe dielectric measurements are computed by (10). The data points and error bars shown for the snow probe are based on an average of twelve separate measurements made for each snow sample and the uncertainty of the estimate of the mean value as represented by the error bars was computed as $\pm \sigma / \sqrt{N}$ where σ is the standard deviation of the set of measurements and N is the number of measurements in that set. From the figure, the agreement between the two techniques is generally very good, and, with the exception of an outlier at the 6% level, the use of the snow probe and (9) gives results which are within $\pm 0.5\%$ of the freezing calorimeter results. This result strongly supports the validity of (9).

B. Snow Density

With m_v known, through the retrieval procedure described in the preceding section, we now turn our attention to using (6) and (8) in order to retrieve the wet snow density ρ_{ws} from ϵ'_{ws}, the dielectric constant of the wet snow medium measured by the snow probe. To do so, we first express ρ_{ws} in terms of ρ_{ds}, the density of the snow had the liquid water been removed,

$$\rho_{ws} = \rho_{ds} + m_v/100. \tag{12}$$

Next, we use the expression [11],

$$\epsilon'_{ds} = 1 + 1.7\rho_{ds} + 0.7\rho_{ds}^2, \tag{13}$$

and combine it with (6) to obtain the result:

$$\epsilon'_{ws} = 1 + 1.7\rho_{ds} + 0.7\rho_{ds}^2 + \Delta', \tag{14}$$

where Δ' is given in (8). Upon combining (12) and (14) and solving for ρ_{ws}, we obtain the expression

$$\rho_{ws} = (m_v/100) - 1.214 \\ + \sqrt{1.474 - 1.428(1 - \epsilon'_{ws} + \Delta')}, \tag{15}$$

in which only the positive root is considered. To compute ρ_{ws} from (15), we use the value of m_v determined in the previous section through (10), the value of ϵ'_{ws} measured by the snow probe, and the value of Δ' calculated from (8). The values of ρ_s (for both wet and dry snow) determined through this procedure are compared with gravimetric measurements of ρ_s in Fig. 7. The data points for which good agreement is found correspond to snow samples having low wetness levels, <3%, for which the contribution Δ' is small anyway. For the samples in which the m_v is more appreciable, there is a significant disagreement between the measurements and the model given by (8).

The errors in density estimates are caused by the model underestimating the incremental increase $\Delta\epsilon'_{ws}$ for the higher wetness cases. Shown in Fig. 8 is a plot of $\Delta\epsilon'_{ws}$ as a function of m_v computed on the basis of (8), and the measurement points were calculated from $\Delta\epsilon'_{ws} = \epsilon'_{ws} - \epsilon'_{ds}$, with ϵ'_{ws} being the value measured by the probe and ϵ'_{ds} determined from (12) and (13). The curve drawn through the data points is generated using a simple polynomial fit, given by

$$\Delta\epsilon'_{ws} = 0.187m_v + 0.0045m_v^2. \tag{16}$$

The agreement between the gravimetric density technique and the snow probe using (16) is shown in Fig. 10. A very good fit can also be obtained via (8) by modifying the term $0.02m_v^{1.015}$ to $0.08m_v^{1.015}$; however, an arbitrary adjustment defeats the purpose of using a model which is based on physical arguments. The Debye-like model of (8) has essentially the same frequency dependance as the real part
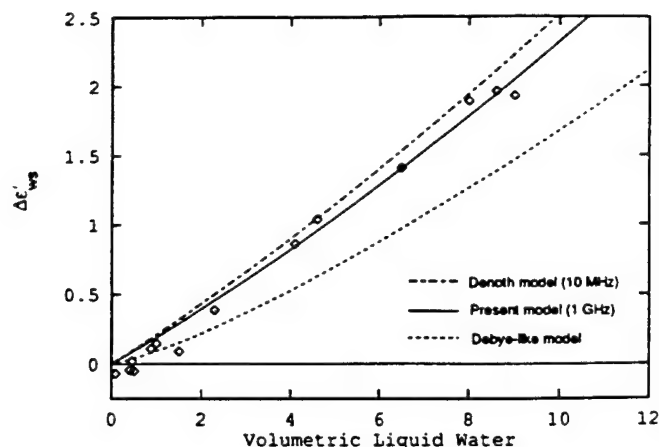
Fig. 8. $\Delta\epsilon'_{ws}$ versus m_v. Shown is data and best fit curve, plus a model obtained from a comparable study at 10 MHz, and Debye-like model.

Fig. 9. Real part of permittivity of water at 0°C.

of the dielectric constant of water, and its empirically-derived coefficients—which effectively reduce the value of this quantity from the theoretical value of the pure material—account for the water being distributed in particle form within a host having a dielectric constant somewhere between those of air and ice. With this understanding, there does not appear to be any reason why a model which works well between 3 and (at least) 15 GHz should need to be significantly modified to work at 1 GHz; physically speaking, the only difference between 3 GHz and 1 GHz is that the dielectric constant of water increases from ≈ 80 to ≈ 87.

The literature contains certain pertinent experimental results that should be considered. Tiuri *et al*. [11] report measurements also at 1 GHz. In these measurements, a dilatometer technique was primarily employed for wetness measurements, but a capacitor technique was used for some of the samples corresponding to the lowest m_v levels. The dielectric measurements were made with the Snow Fork developed at the Helsinki University of Technology. The relationship they report is,

$$\Delta\epsilon'_{ws} = 0.089m_v + 0.72m_v^2. \tag{17}$$

This function, when plotted, closely resembles the Debye-like model (8) evaluated at 1 GHz. Most recently Denoth [12] reported measurements made at 10 MHz, in which dielectric measurements were made using a simple plate capacitor and liquid water measurements were made using a freezing calorimeter. The relation he reports is,

$$\Delta\epsilon'_{ws} = 0.206m_v + 0.0046m_v^2. \tag{18}$$

Denoth observes that this relation should continue to be valid up to approximately 2 GHz, since ϵ' of the constituents of wet snow—ice, air, and water—are all exactly or nearly frequency-independent in this range. In particular, for water, as seen in Fig. 9, the real part of the dielectric constant of water, ϵ'_w, at 1 GHz differs from that of 10 MHz by only 1.1%. Also noted on the figure is the region through which the Debye-like model of [2] was reported to be valid (although above 15 GHz, the empirical coefficients shown in (8) are slightly modified as a function of frequency). The best fit function for the 10 MHz data, given by (18), is also shown in Fig.
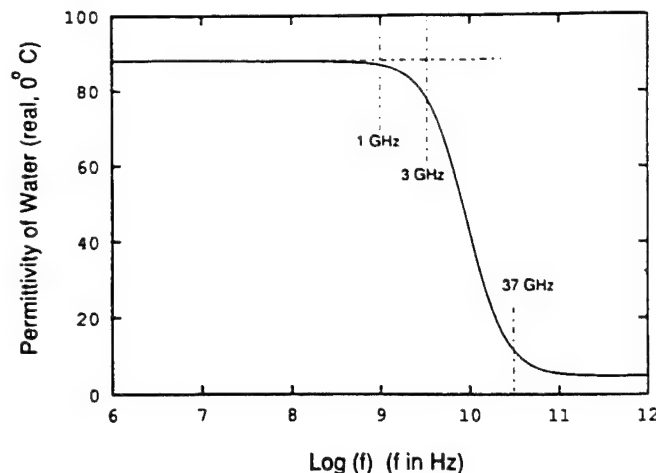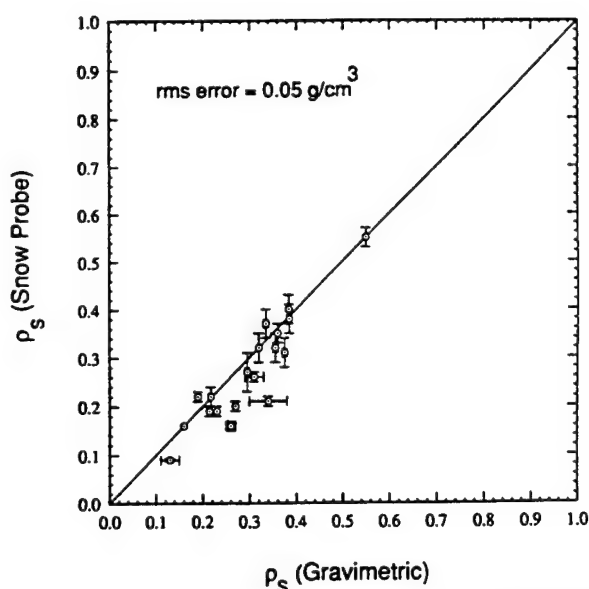
Fig. 10. Comparison of snow density results obtained via snow probe (with associated empirical algorithm) and gravimetric measurements.

8. The close agreement between the results at 10 MHz and 1 GHz tends to bear out Denoth's prediction and suggest that at these frequencies, where scattering is an unimportant factor in calculating the dielectric constant, ϵ'_{ws} is directly relatable to ϵ'_w. In effect, a model like (8) *should* be expected to work, but, in its present form, does not appear to. Regarding the discrepancy between our results and those of [11], a possible explanation is that they used a dilatometer to measure wetness (we found the dilatometer to give very unsatisfactory performance), whereas our standard (which was also used in [12]) was the freezing calorimeter technique whose accuracy and precision has been demonstrated.

IV. APPLICATION

Fig. 11 is a nomogram, based on these equations which have been found to be valid in the specified ranges. It consists of contours of constant m_v and ρ_{ds}, respectively, in a two-dimensional representation bounded by the two parameters
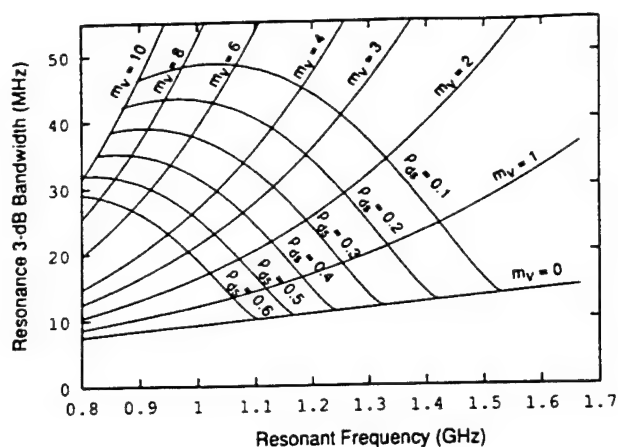
Fig. 11. Nomogram giving snow liquid water content (m_v) and equivalent dry snow density (ρ_{ds}) in terms of two parameters directly measured by the snow probe: resonant frequency (f) and resonance (3-dB) bandwidth (Δf).
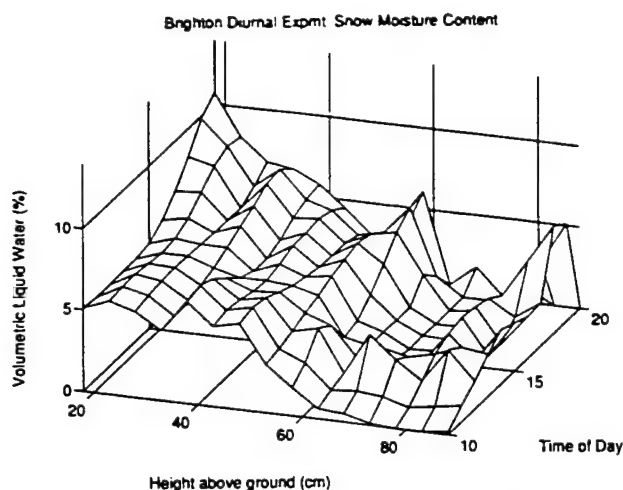

Fig. 12. Snow moisture measured via the snow probe in a 0.88-m snowpack over a diurnal cycle, shown as a function of time and height above the ground.

which are directly obtained by the snow probe: resonant frequency and bandwidth (3-dB) of the resonance spectrum. With the measurement of these two quantities, m_v and ρ_{ds} may be uniquely specified. Dry-snow density, ρ_{ds}, is related through (12) to wet-snow density ρ_{ws}.

As an example of the utility of the snow probe for elucidating snowpack character and behavior, we present in Fig. 12 snow wetness data measured for an 0.88-m deep snowpack over a diurnal cycle. During the period shown, from 10 a.m. to 8 p.m., the temperature rose from freezing to 6°C and down to −3°C again at 8 p.m.. The lowest 16-cm of the pack was solid ice; therefore measurements start at 18-cm above ground, and were made at roughly 5-cm intervals. Among the interesting features in the figure, even at 10 a.m., after subfreezing night temperatures, and while the surface is still completely dry, there is appreciable moisture deeper down in the snowpack. At the top surface, between the hours of 6 and 8 p.m., there was significant wetness which then quickly froze at about 8 p.m.

V. SUMMARY

This paper has described the development and validation of an electromagnetic sensor and associated algorithm for the purpose of rapid (≈ 20 s) and nondestructive determination of snow liquid water content and density. The sensor is similar in principle to an existing device known as a "Snow Fork," but offers additional advantages in spatial resolution and accuracy owing to a novel coaxial-cavity design. Also, the algorithm employed with that device [1] for relating complex dielectric constant to snow parameters does not agree with the results of the present study. We have consequently developed new relations for that purpose.

Direct methods of snow wetness determination were evaluated for their suitability as standards against which the snow probe could be tested. The dilatometer, though simple in principle, was found to give very unfavorable performance. The freezing calorimeter, which has, as a system, been brought to a high degree of sophistication in our lab, was found

capable of delivering accuracy better than ±1%, and excellent precision.

The snow probe determines the dielectric constant directly. Empirical and semi-empirical models are used with this information to compute liquid water volume fraction and density. To test the suitability of existing models and/or allow the development of new models, the snow probe was tested against the freezing calorimeter and gravimetric density determinations. Originally, The relations set forth by Hallikainen et al. [2] were employed to translate measured dielectric constant to snow parameters. The equation relating ϵ''_{ws} to m_v and frequency was found to be entirely valid. However, the equation predicting $\Delta\epsilon'$ in terms of m_v and frequency was found to underestimate this quantity, leading to substantial errors in the estimates of ρ_{ds}. A purely empirical relation, given in (16) was obtained instead, and will be used in our parameter retrieval algorithm for the snow probe. Through the use of these functions, in association with the complex dielectric measurements of the snow probe, the following specifications are established: liquid water content measurement accuracy ±0.66% in the wetness range from 0 to 10% by volume; wet snow density measurement accuracy ±0.05 g/cm^3 in the density range from 0.1 to 0.6 g/cm^3.

Two examples of pertinent experimental results were compared against ours: Denoth's measurements [12] at 10 MHz are very similar to ours; those reported by Tiuri et al. [11] at 1 GHz differ considerably from ours but agree well with the model given by (8), our own starting point. Denoth [12], noting the diversity of empirical relations for the dielectric constant of wet snow suggests that because of the influence of the shape of the water component, and the stage of metamorphism of the snow sample, "a valid simple relation between $\Delta\epsilon'$ or ϵ'' and liquid water content W may not exist." This may be the case, but the results of the present study are very consistent with results presented in [12] for the case of $\Delta\epsilon'$, and in [2] for the case of ϵ''. Accurate snow measurements of dielectric constant and liquid water content are notoriously difficult to make. This has doubtlessly been a factor in the diversity of results, and is motivation for the development of instruments such as has been the focus of this present investigation.

REFERENCES

[1] A. Sihvola and M. Tiuri, "Snow fork for field determination of the density and wetness profiles of a snow pack," *IEEE Trans. Geosci. Remote Sensing*, vol. Ge-24, pp. 717–721, 1986.

[2] M. Hallikainen, F. T. Ulaby, and M. Abdelrazik, "Dielectric properties of snow in the 3 to 37 GHz range," *IEEE Trans. Antennas Propagat.*, vol. AP-34, pp. 1329–1339, 1986.

[3] R. T. Austin, "Determination of the liquid water content of snow by freezing calorimetry," Univ. of Michigan Radiation Lab Report 022872-2, Jan. 1990.

[4] E. B. Jones, A. Rango, and S. M. Howell, "Snowpack liquid water determinations using freezing calorimetry," *Nordic Hydrol.*, vol. 14, pp. 113–126, 1983.

[5] W. H. Stiles and F. T. Ulaby, "Microwave remote sensing of snow-packs," NASA Contractor Report 3263, June 1980.

[6] S. C. Colbeck, "The layered character of snow covers," *Revs. of Geophys.*, vol. 29, pp. 81–96, 1991.

[7] D. A. Ellerbruch and H. S. Boyne, "Snow stratigraphy and water equivalence measured with an active microwave system," *J. Glaciol.*, vol. 26, pp. 225–233, 1980.

[8] A. Denoth *et al.*, "A comparative study of instruments for measuring the liquid water content of snow," *J. Appl. Phys.*, vol. 56, no. 7, 1984.

[9] M. A. H. Leino, P. Pihkala, and E. Spring, "A device for practical determination of the free water content of snow," *Acta Polytechnica Scandinavica*, Applied Physics Series No. 135, 1982.

[10] R. E. Collin, *Foundations for Microwave Engineering*. New York: McGraw-Hill, 1966.

[11] M. E. Tiuri, A. H. Sihvola, E. G. Nyfors, and M. T. Hallikainen, "The complex dielectric constant of snow at microwave frequencies," *IEEE J. Oceanic Eng.*, vol. OE-9, pp. 377–382, 1984.

[12] A. Denoth, "Snow dielectric measurements," *Adv. Space Res.*, vol. 9, no. 1, pp. 233–243, 1989.

John R. Kendra (S'92) received the B.S.E.E. degree from the University of Houston in 1989, and the M.S.E.E. degree in 1990 from the University of Michigan.

Since September 1989 he has been a Graduate Research Assistant in the Radiation Laboratory at the University of Michigan, working in the areas of microwave and millimeter-wave remote sensing. He is currently pursuing the Ph.D. degree. His research interests include microwave remote sensing of snow, and volume scattering phenomena in random media.

Fawwaz T. Ulaby (M'68–SM'74–F'80), for a photograph and biography, see p. 985 of the September 1994 issue of this TRANSACTIONS.

Kamal Sarabandi (S'87–M'90–SM'92), for a photograph and biography, see p. 984 of the September 1994 issue of this TRANSACTIONS.

AGARD

ADVISORY GROUP FOR AEROSPACE RESEARCH & DEVELOPMENT

7 RUE ANCELLE 92200 NEUILLY SUR SEINE FRANCE

**Paper Reprinted from
AGARD Conference Proceedings 542**

Atmospheric Propagation Effects through Natural and Man-Made Obscurants for Visible to MM-Wave Radiation

(Les Effets des Conditions Défavorables de
Propagation sur les Systèmes Optiques,
IR et à Ondes Millimétriques)

*Presented at the Electromagnetic Wave Propagation Panel Symposium,
held in Palma de Mallorca, Spain, 17th—20th May 1993.*
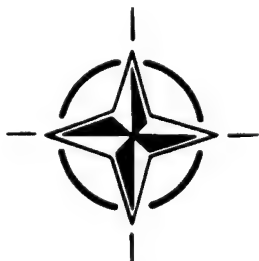
NORTH ATLANTIC TREATY ORGANIZATION

A HYBRID ELECTROMAGNETIC - STATISTICAL APPROACH FOR CHARACTERIZING MMW SCATTERING BY TERRAIN

Fawwaz T. Ulaby, Paul Siqueira, and Kamal Sarabandi
The Radiation Laboratory
Department of Electrical Engineering and Computer Science
The University of Michigan
Ann Arbor, MI 48109-2122
USA

SUMMARY

The performance of millimeter-wave (MMW) radar systems in target detection navigation and other applications depends in part on the scattering characteristics of the terrain background. Two different approaches have been pursued in the literature for characterizing MMW scattering by terrain. The first approach relies on the development of electromagnetic scattering models that relate the backscattering coefficient σ° of a given terrain type (such as bare ground surfaces, snow cover, and vegetation) to the physical properties of the terrain target, and then verifying model predictions though experimental observations conducted under semi-controlled field conditions. The second approach is entirely empirical in nature; it relies on the acquisition of extensive radar data from which statistical distributions are generated. The University of Michigan has been involved in a research program, supported by the U.S. Army Research Office, whose goal is to pursue both approaches as well as to develop a hybrid approach that combines the strengths of both approaches. This paper provides an overview of how the hybrid approach can be used to simulate the statistical properties of terrain backscatter at millimeter wavelengths for several types of terrain, including bare soil surfaces, vegetation, and snow cover. The hybrid approach incorporates scintillation effects associated with coherent sensors together with information about the mix of terrain categories present in the scene. Two types of input data (or a merged set of both) can be used as input to the clutter simulation package: (a) measured data that is available in a University of Michigan data base, or (b) data generated by electromagnetic models. The data base is available in a University of Michigan Handbook that contains MMW scattering observations reported in the literature for certain terrain types and conditions. Alternatively, a set of electromagnetic models can be used for calculating the backscattering coefficient σ° of the specified terrain type. These models, which are semi-empirical in form, are based on highly complicated theoretical models that had been tested against experimental observations. With this approach, it is possible to generate a probability density function for the backscatter from a certain type of terrain without the need for a measured clutter data base. This is particularly attractive at millimeter wavelengths because only a limited amount of terrain clutter data is currently available.

1 INTRODUCTION

By way of introducing the subject of terrain clutter at millimeter wavelengths, let us start by considering the case of a radar system designed to detect hard targets against the terrain background. Figure 1(a) depicts a radar beam with resolution area A illuminating a target with backscattering radar cross section (RCS) σ_t. The terrain background is a statistically homogeneous background with mean clutter RCS $\sigma_{c0} = \sigma^\circ A$, where σ° is the (average) backscattering coefficient of the terrain. In this case, the signal to noise ratio is given by:

$$\frac{S}{N} = \frac{\sigma_t}{\sigma_{c0}} = \frac{\sigma_t}{\sigma^\circ A} \ . \tag{1}$$

Because terrain scattering is noise-like in character, its variability behaves according to Rayleigh fading statistics [1], which leads to the following expression for the probability density function (pdf) of the envelope voltage V_e at the output of the receiver's envelope detector:

$$p(V_e) = \frac{2V_e}{\sigma_{c0}} \exp\left[-\frac{(V_e^2 + \sigma_t)}{\sigma_{c0}}\right] I_0\left(\frac{2V_e\sqrt{\sigma_t}}{\sigma_{c0}}\right) \tag{2}$$

where $I_0(\ )$ is the zeroth-order Bessel function.
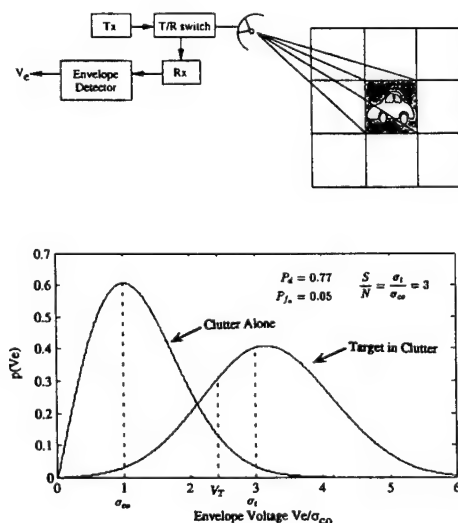

Figure 1. Probability density functions for clutter alone and clutter with a target with RCS = 5 dB above the average clutter cross section, σ_{c0}.

If no target is present ($\sigma_t = 0$), Eq. (2) reduces to:

$$p(V_{e0}) = \frac{2V_{e0}}{\sigma_{c0}} \exp\left(-\frac{V_{e0}^2}{\sigma_{c0}}\right) , \qquad (3)$$

where V_{e0} denotes V_e with no target present. For a specified theshold voltage V_T, the false alarm probability P_{fa} is given by:

$$\begin{aligned} P_{fa} &= \int_{V_T}^{\infty} p(V_{e0})\,dV_{e0} \\ &= \exp\left(-\frac{V_T^2}{\sigma_{c0}}\right) , \end{aligned} \qquad (4).$$

and the corresponding detection probability P_d is obtained by integrating $p(V_e)$ over the limits V_T to ∞:

$$P_d = \int_{V_T}^{\infty} \frac{2V_e}{\sigma_{c0}} \exp\left[-\frac{(V_e^2 + \sigma_t)}{\sigma_{c0}}\right] I_0\left(\frac{2V_e\sqrt{\sigma_t}}{\sigma_{c0}}\right) dV_e \quad (5)$$

Figure 1(b) shows plots of $p(V_{e0})$ for $\sigma_{c0} = 1m^2$ and $p(V_e)$ for $S/N = \sigma_t/\sigma_{c0} = 3$ (5 dB). The indicated threshold voltage V_T was chosen to yield a probability of false alarm $P_{fa} = 0.05$; the corresponding value of P_d is 77%.

The preceding treatment, which describes the radar detection problem on the basis of a single pulse for statistically homogeneous clutter, is standard textbook material. Extensions include the integration of multiple pulses to increase P_d [2] and the use of frequency averaging [3] to decrease the variability of the clutter RCS (narrower $p(V_{e0})$), which also leads to improved P_d. Another extension relates to the nonuniform terrain situation for which the backscattering coefficient σ° is characterized by its own pdf $p(\sigma^\circ)$, rather than having a constant value as was assumed in the preceding expressions. Examples of such situations may include a background comprised of a single terrain type (such as vegetation cover) but with varying physical characteristics (height, moisture content, and geometry of vegetation elements) or a background comprised of a mixture of different types of terrain (vegetation, roads, water bodies, etc.). The methodology for characterizing the combined effects of fading variations and a non-constant σ° is described in [1].

For any radar-detection situation, regardless of whether or not multiple-pulse integration or frequency averaging is used, the two fundamental quantities governing the detection performance of the radar system are the target RCS (or $p(\sigma_t)$ if it is a fluctuating target), and the mean clutter RCS σ_{c0} (or $p(\sigma_{c0}) = \frac{1}{A}p(\sigma^\circ)$ for nonuniform terrain). Characterizing σ_t is outside the scope of this presentation, and therefore it will not be addressed. The remaining part of this paper will focus on two approaches for characterizing $\sigma^\circ = \sigma_{c0}/A$ and $p(\sigma^\circ)$, namely (a) the data-base approach, which relies on measured distributions of σ° for specific types of terrain, and (b) the electromagnetic model approach, which uses electromagnetic scattering models to compute $p(\sigma^\circ)$ for a given set of terrain conditions, specified in terms of the ranges of variability of pertinent physical parameters. Whereas either approach may be used at centimeter wavelengths, it is not possible to rely on the data-base approach alone at millimeter wavelengths because only a limited amount of terrain-specific clutter measurements is available at the present time. The next section describes a hybrid approach that utilizes both of the aforementioned approaches for characterizing terrain clutter. The sections that follow present electromagnetic models for snow cover and soil surfaces at 35 and 94 GHz. Models for other types of terrain are under development and will be presented in future publications.

2 HYBRID APPROACH FOR CHARACTERIZING CLUTTER

Figure 2 shows a simplified representation of the simulation package that uses the hybrid approach for evaluating the detection performance of a radar system. The radar system specifications include: (a) the operating frequency f, (b) the incidence angle θ (relative to nadir), (c) the receive / transmit antenna polarization configuration, (d) the number of pulses N_p available for integration, and (e) the spatial resolution area A. The terrain is specified as belonging to one of the categories / sub-categories given in Figure 3. The classification system depicted in Figure 3 forms the basis for the data base contained in the Handbook of Radar Scattering Statistics for Terrain [1], which exists in both hard-cover form and as a software package. The Handbook data base contains calibrated experimental measurements of σ° reported in the open literature, but it is not inclusive of all such data. Only data that had been judged as satisfying certain data-quality criteria were included in the data base. For each terrain category, the data are grouped into distinct frequency bands covering the range from 1 GHz to 100 GHz, but for most terrain categories, the number of data points at frequencies above 30 GHz is either very small or identically zero. This is precisely the motivation for proposing the use of electromagnetic (EM) models for generating a supplementary data base.
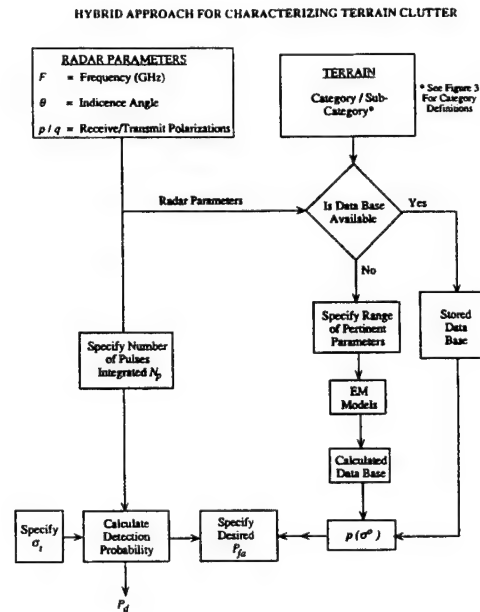
HYBRID APPROACH FOR CHARACTERIZING TERRAIN CLUTTER

Figure 2. Flow-chart representation of the radar-detection performance simulation package.

In the flow chart given in Figure 2, this option follows from the response to the question: "Is a measured data base available (in the Handbook)?" The question refers to the category specified in the preceding step, subject to the radar parameters specified in the "Radar Parameters" block. If the answer to the question is negative, EM models of the form given in later sections are used to generate the supplementary data base. To do this, the user has to specify the range of pertinent parameters. For snow-covered terrain, for example, the user will be asked to specify the expected ranges of snow depth and air temperature. Similar specifications apply to other terrain categories. As a result of this process, a pdf for

σ°, $p(\sigma^\circ)$, is generated by merging the supplementary data base calculated from the EM models with whatever data base of measured data that happens to be available in the Handbook. The term "Handbook" refers to data in [1] as well as more recent MMW data given in [4].
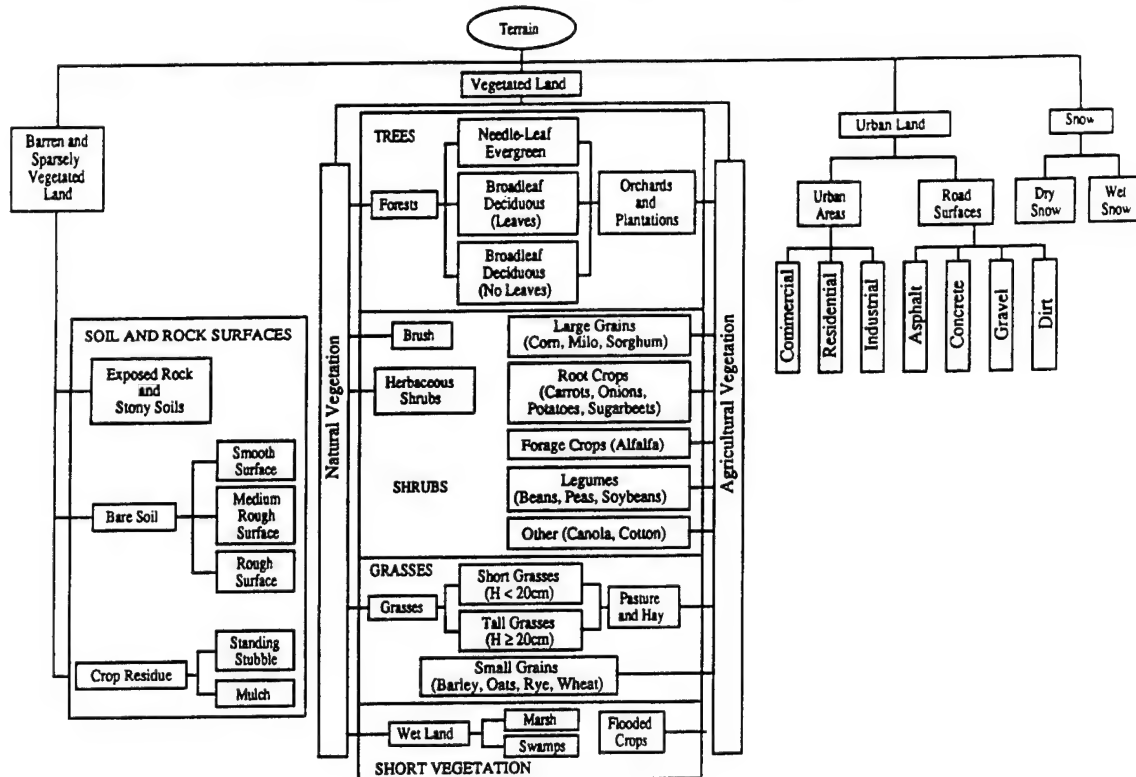
RADAR TERRAIN CLASSIFICATION SYSTEM

Figure 3. Radar terrain classification system.

With $p(\sigma^\circ)$ available, the pdf of the clutter cross section $p(\sigma_c)$ can be readily calculated by incorporating the variations due to signal fading fluctuations, as described in Section 3-5 of [1]. Upon additionally specifying the desired false alarm probability P_{fa} and the number of pulses used for incoherent integration, the program then calculates the expected detection probability P_d for a given hard-target cross section σ_t. This procedure can serve as an effective tool for evaluating the detection performance of MMW radar sensors.

3   EXAMPLES OF AVAILABLE MMW CLUTTER DATA

Most experimental measurements of radar backscatter reported in the literature, which are in the form of plots of σ° as a function of the incidence angle θ, pertain to a specific terrain type and condition. Data of this form are available in [4] for HH, HV, and VV polarizations at 35, 94, 140, and 215 GHz for various types of terrain including trees, grasses, road surfaces, dry snow, wet snow, and ice-covered ground. From this collection of data, histograms have been generated for specific combinations of frequency band, incidence angle, polarization configuration, and terrain type and condition. The histogram is an unnormalized pdf of σ°. An example is shown in Figure 4 for dry snow at 35 GHz for

$\theta = 50^\circ$. Because of the limited number of available data points, the histogram is not a smooth continuous function of σ°. Consequently, when such data is used in the radar detection- performance analysis, it is replaced with a Gaussian distribution having the same mean value and standard deviation as those calculated from the histogram. Analysis of the dependence of the mean value $\bar{\sigma}^\circ$ and the standard deviation S(of σ°) on the incidence angle θ led to the following functional form:

$$\bar{\sigma}^\circ_{\mathrm{dB}} = P_1 + P_2 \exp(-P_3\theta) + P_4 \cos(P_5\theta + P_6) \qquad (6)$$
$$S_{\mathrm{dB}} = M_1 + M_2 \exp(-M_3\theta) \qquad (7)$$

where θ is the incidence angle in radians and the coefficients P_1 to P_6 and M_1 to M_3 assume fixed values for a specific terrain category and polarization configuration. The values of these coefficients are given in Table 1 for six terrain categories for which sufficient data exists to justify the curve fitting procedure. All the cases given in Table 1 are based on 35 GHz observations; insufficient data exists at the present time for higher MMW frequencies.
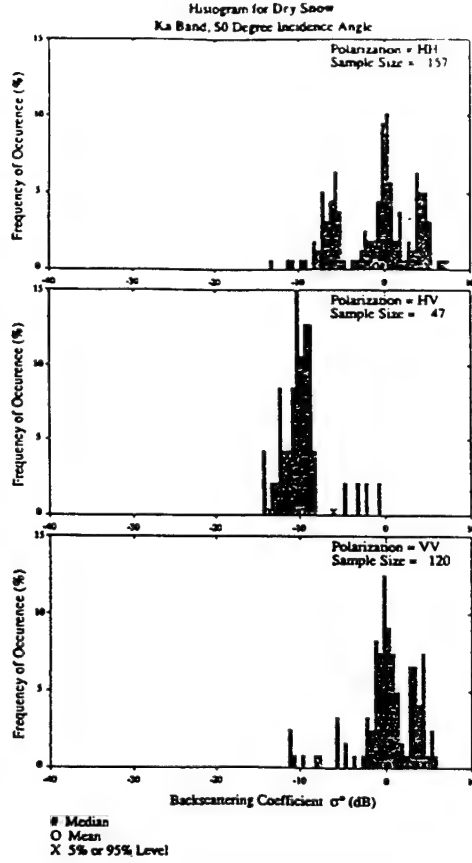
Histogram for Dry Snow
Ka Band, 50 Degree Incidence Angle

Polarization = HH
Sample Size = 157

Polarization = HV
Sample Size = 47

Polarization = VV
Sample Size = 120

Backscattering Coefficient σ° (dB)

\# Median
O Mean
X 5% or 95% Level

Figure 4. Histograms of σ° for dry snow at 35 GHz.

TABLE 1. Values of coefficients P_1 to P_6 and M_1 to M_3 associated with Equations (6) and (7), which characterize the angular dependence of the mean value $\bar\sigma^\circ$ (dB) and standard deviation S(dB) for various types of terrain at 35 GHz.

Terrain	Pol.	Angular Range	$\bar\sigma^\circ$(dB) Coefficients						S(dB) Coefficients		
			P_1	P_2	P_3	P_4	P_5	P_6	M_1	M_2	M_3
Grasses	HH	10-70	-99	92.4	0.04	1.17	5.0	-1.9	3.5	-1.1	1.6
	VV	10-70	-99	91.8	0.04	1.10	5.0	-2.1	3.0	-2.6	5.1
Shrubs	HH	20-70	-41	27.8	0.08	-8.7	0.9	3.1	2.2	4.4	4.6
	VV	20-70	-44	41.6	0.22	-0.8	5.0	-1.4	2.1	2.9	4.4
Short Vegetation	HH	10-80	-99	79.1	0.26	-30	0.7	2.1	2.8	3.1	15
	VV	10-80	-99	80.3	0.28	-30	0.8	2.0	2.7	0	0
Road Surfaces	HH	10-70	-95	99	0.69	30	1.3	-1.7	7.2	-5.2	0.8
	VV	10-70	-85	99	0.80	-30	1.6	1.1	3.2	0	0
Dry Snow	HH	0-75	-84	99	0.30	8.9	2.7	-3.1	-9	13.5	0.06
	VV	0-70	-88	99	0.22	7.4	2.8	-3.1	-9	13.8	0.08
Wet Snow	HH	0-70	44	-13	-0.86	29	1.1	2.8	-8.2	15	-0.08
	VV	0-70	-34	7.9	15	30	0.78	-0.4	5.5	1.4	0.55

Following the standard assumption that σ° (dB) is a Gaussian-distributed variable, it follows that σ°, expressed in natural units of m^2/m^2, is log-normally distributed. That is, with

$$\sigma^\circ_{dB} = 10 \log \sigma^\circ, \qquad (8)$$

The pdf of σ° is given by:

$$p(\sigma^\circ) = \frac{4.34}{\sqrt{2\pi}\sigma^\circ S_{dB}} \exp\left[-[10\log\sigma^\circ - \bar\sigma^\circ_{dB}]^2 / 2S^2_{dB}\right] \quad (9)$$

where $\bar\sigma^\circ_{dB}$ and S_{dB} are the mean and standard derivations of σ° in dB, as determined from the histogram of the experimental data. By way of illustration, Figure 5 shows plots of $p(\sigma^\circ)$ for short vegetation, road surfaces, and dry snow cover, all for HH polarization at an incidence angle of 50°. These are the type of the probability density functions generated by the simulation package flow-charted in Figure 2.

35 GHz
HH polarization
$\theta=50^\circ$

Surface type	$\bar\sigma^\circ$ dB	S (dB)
Road Surfaces	-15.5	4.8
Short Vegetation	-9.2	2.5
Dry Snow	-1.1	4.5

σ° (m^2/m^2)
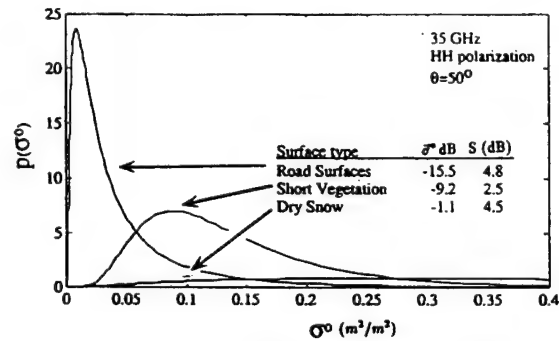
Figure 5. Probability density functions for short vegetation, road surfaces and dry snow cover at 35 GHz; $\bar\sigma^\circ$ (dB) and S (dB) are the mean value and associated standard deviation, both in dB, of the measured σ° (dB) distribution.

4 ELECTROMAGNETIC MODELS FOR TERRAIN CLUTTER

As was stated in earlier section, radar clutter data currently available at millimeter wavelengths is deficient in the following ways: (1) most of the available data is at 35 GHz, with negligible amount of data available at the higher atmospheric window frequenies of 94, 140, and 215 GHz, (2) for some types of terrain, insufficient data exists even at 35 GHz, and (3) for those terrain types for which data is available at 35 GHz, the terrain conditions represented by the data may be too broad in comparison to terrain situations of interest, thereby resulting in σ° distributions that cover a wider range of values than necessary, which in turn leads to poorer estimates of the false alarm and detection probabilities P_{fa} and P_d.

In principal, a possible solution to this problem is to develop a set of electromagnetic scattering models that can relate σ° to the physical properties of the terrain. Using calibrated scatterometer systems, numerous experiments were conducted over the past several years to determine the dependence of σ° on pertinent terrain parameters, and to serve as the basis for evaluating the applicability of theoretical models. Typical examples illustrating the agreement between experimental observations and theoretical predictions are shown in Figures 6 and 7 for snow. Figure 6 shows the angular dependence of σ° at 95 GHz for snow cover with 5% liquid water content, and Figure 7 shows the diurnal variation of σ° at 35, 95, and 140 GHz, which is in response
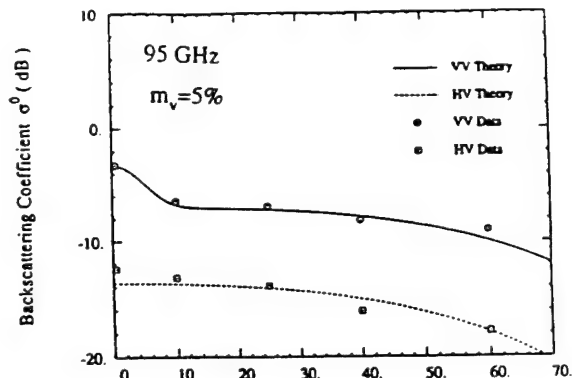
Figure 6. Measured and calculated angular variation of σ° for wet snow with 5% wetness at 95 GHz.

to variations in liquid water content. The theoretical model that was used in this case was a numerical radiative transfer model that accounts for multiple scattering in the snow volume [5,6]. Although the model provides good predictions of σ°, it is fairly complicated mathematically and its code is computationally intensive.
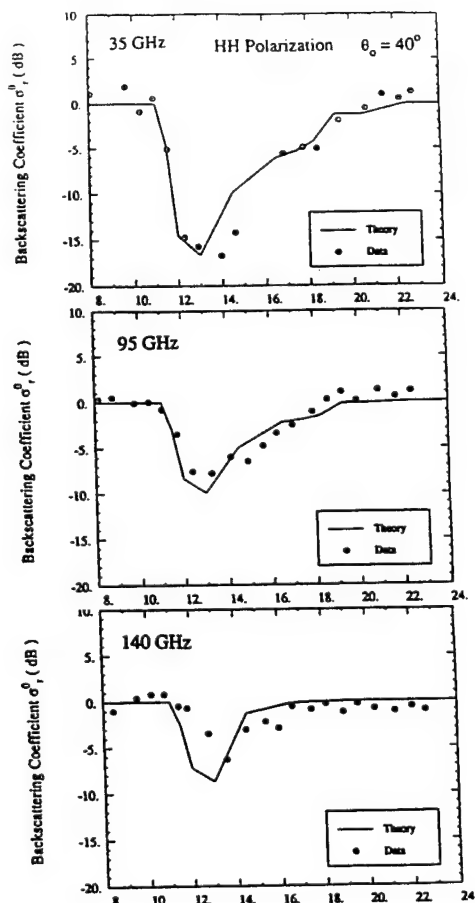

Figure 7. Comparison of measured and calculated diurnal response of σ° for snow at 35, 95, and 140 GHz. The incidence angle is 40°, snow density is 0.32 g/cm^3, and the snow depth is 12 cm.

Similar models, with similarly good prediction capabilities but complicated mathematical formulations, have been developed for vegetation [7] and bare-ground surfaces. Unfortunately, because of their mathematically complicated form, these models are not being used by the radar community at large. To overcome this problem, we have developed relatively simple semi-empirical expressions that yield results within typically 1 dB of the values provided by the elaborate theoretical models. The next two sub-sections present these expressions, together with curves illustrating the behavior of σ°, for snow cover and bare-ground surfaces. Similar expressions are under development for other terrain types and will be presented in future publications.

4.1 Snow Cover

At millimeter wavelengths, the HH and VV polarized backscattering coefficients of snow-covered terrain are essentially identical in magnitude over the angular region between 10° and 70° from nadir. Hence, a single expression is used for both co-polarized backscattering coefficients. The parameters governing the magnitude of σ° are the incidence angle θ, the snow depth h (cm), and the volumetric liquid water content m_v (%). Secondary in importance are the snow density ρ and the ice crystal size distribution. The expressions given below were computed for a typical value of $\rho = 0.3$ g/cm^3 and for a Gaussian distribution of ice particle diameters with a mean value of 1 mm and a standard deviation of 0.2 mm. Deviations from these conditions can lead to errors on the order of 1-3 dB.

For snow depth $h \geq 10$ cm, the following expression was found to provide excellent fits to experimental data as well as to values computed with the theoretical radiative transfer model:

$$\sigma^\circ(\theta, h, m_v) = \{A[1 - \exp(-B\,h\,\sec\theta')]\exp(-C\,m_v)\}$$
$$+ D\exp(-E\,m_v)\}\cos\theta + F \qquad (10)$$

with θ', the refraction angle in the snow medium, being related to the incidence angle θ by:

$$\theta' = \sin^{-1}\left[\frac{\sin\theta}{\sqrt{1.61 + 0.035m_v}}\right] . \qquad (11)$$

The constant coefficients A through F have the following values:

Coefficient	35 GHz	94 GHz
A	1.4	1.4
B	1.8×10^{-2}	5.6×10^{-2}
C	1.4	0.52
D	0.33	0.03
E	0.01	- 0.27
F	- 0.17	0.05

The variation of σ° with $\theta, h,$ and m_v is illustrated by the sets of curves shown in Figure 8 for 35 GHz and in Figure 9 for 94 GHz. The points denoted by stars in the figures represent the values of σ° calculated using the theoretical radiative transfer model [5,6], which are included in the figures for only a few cases in order to illustrate the magnitude of the error between the exact theoretical calculations and those calculated on the basis of the expression given by (10).
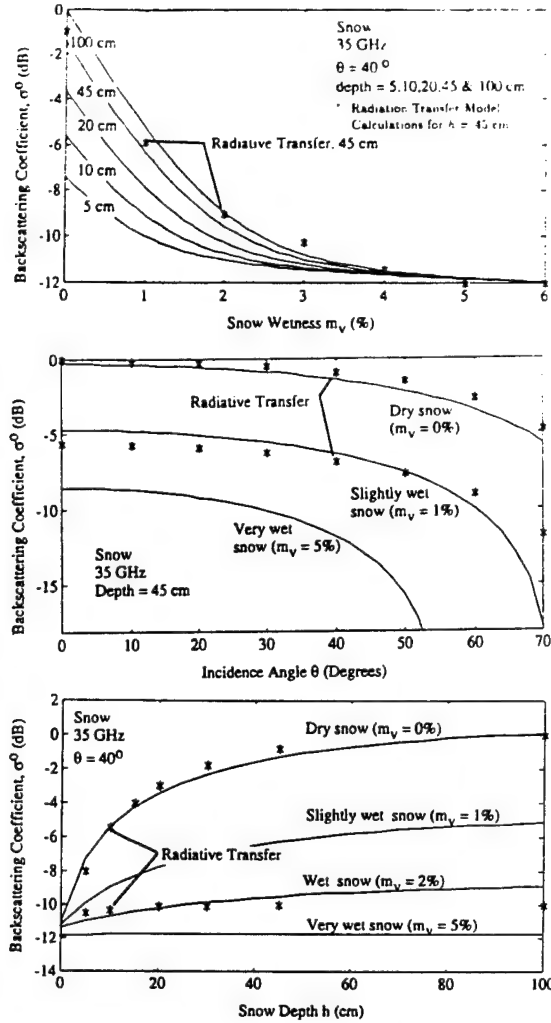
Figure 8. Variation of σ^o with incidence angle θ, snow depth h and liquid water content m_v at 35 GHz.
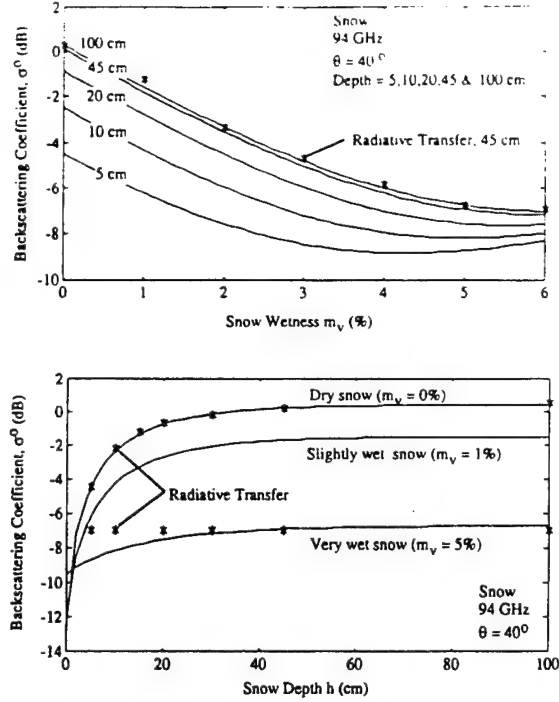

Figure 9. Variations of co-polarized σ^o with snow depth h and snow liquid water content m_v at 94 GHz.

Surface Scattering Component

The surface scattering component σ^s is a function of the incidence angle θ, the volumetic moisture content of the surface layer m_v, and the electromagnetic roughness of the surface ks, where $k = 2\pi/\lambda$ and s is the rms height of the surface. Based on experimental observaions made at 35 and 94 GHz for surfaces with various roughnesses and moisture contents, the following expressions were generated for the vv, hh, and hv polarization components of σ^s:

$$\sigma^s_{vv} = g\frac{\cos^x \theta}{\sqrt{P}}\left[\Gamma_v(\theta) + \Gamma_h(\theta)\right] \tag{13}$$

$$\sigma^s_{hh} = P\sigma^s_v v \tag{14}$$

$$\sigma^s_{hv} = q\sigma^s_v v \tag{15}$$

where

$$q = \frac{\sigma^s_{hv}}{\sigma^s_{vv}} = 0.23\sqrt{\Gamma_0}\left[1 - \exp(-0.2ks)\right] \tag{16}$$

$$P = \frac{\sigma^s_{hh}}{\sigma^s_{vv}} = \left[1 - \left(\frac{2\theta}{\pi}\right)^{1/(3\Gamma_0)} \cdot \exp(-0.4ks)\right]^2 \tag{17}$$

$$g = 0.7\tau\left[1 - \exp\left(-0.65(ks)^{1.8}\right)\right]$$
$$\qquad + 2.2(1-\tau)\left[1 - \exp(-0.2ks)\right] \tag{18}$$

$$x = 3.5 + \frac{1}{\pi}\tan^{-1}\left[10(1.65 - ks)\right] \tag{19}$$

$$\tau = \frac{1}{2} + \frac{1}{\pi}\tan^{-1}\left[100(0.08 - m_v)\right] \tag{20}$$

and $\Gamma_v(\theta)$ and $\Gamma_h(\theta)$ are the Fresnel reflectivities of the surface and θ is measured in radians.

4.2 Bare-Soil Surfaces

In general, scattering by a soil surface may contain two scattering components, one due to scattering by the surface itself and another due to particle scattering in the soil medium. Thus, the backscattering coefficient may be expressed as:

$$\sigma^o = \sigma^s + \sigma^v , \tag{12}$$

where the superscripts s and v denote surface and volume scattering, respectively. The models given below for σ^s and σ^v are based on a combination of semi- empirical models and theoretical models that were generated through comparison with experimental data measured at 35 and 94 GHz.

Volume Scattering Component

The volume scattering component σ^v is a function of θ, the moisture content m_v and the mean particle diameter d_0. Comparison of the magnitude of σ^v to σ^s reveals that $\sigma^v \gg \sigma^s$ at 35 GHz, but at 94 GHz σ^v may be smaller than σ^s for wet soil or larger than σ^s for very dry soil. Hence, expressions for σ^v are given for 94 GHz only. With d_0 expressed in mm, the following expressions were established on the basis of matcyhing a radiative transfer model to experimental data:

$$\sigma_{vv}^v = [(11.75 - 0.8\cos\theta)d_0]^{2.73} \; e^{-0.6m_*} \qquad (21)$$

$$\sigma_{hh}^v = [(6.15 + 4.77\cos\theta)d_0]^{2.73} \; e^{-0.6m_*} \qquad (22)$$

The dependence of the total soil backscattering coefficient at 35 GHz on surface roughness ks and moisture content m_v is shown in Figure 10. The relative importance of the volume and surface components at 94 GHz is depicted in Figure 11 and the total backscattering coefficient is plotted in Figure 12 as a function of m_v for three different values of d_0. It is clear that if m_v exceeds 0.1, surface scattering becomes the dominant contribution.

Figure 11. Variation of volume scattering component σ^v at 94 GHz with mean particle diameter d_0. The level of the surface scattering component is indicated for comparison for three roughnesses.
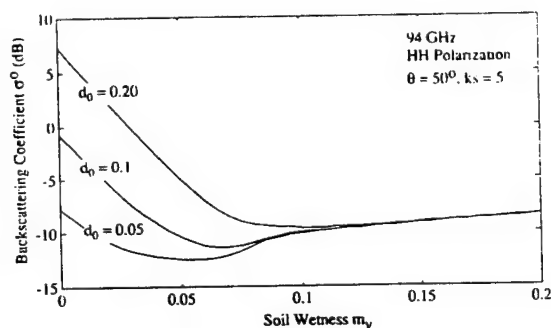
Figure 12. Variation of σ° at 94 GHz with m_v for moderately rough surface with $ks = 5$.

Figure 10. Dependence of σ° at 35 GHz on soil wetness and electromagnetic surfaced roughness ks for vv and hh polarizations.

5 CONCLUSIONS

A hybrid model has been presented for evaluating the detection performance of a millimeter-wave radar against terrain clutter. In the case of terrain types and conditions for which sufficient experimental data exists to characterize the probability density function of the backscattering coefficient σ^0–which is limited to 35 GHz for a few types of terrain, the simulation model uses standard procedures for computing the false alarm and detection probabilities, P_{fa} and P_d.

For radars operating at 94 GHz, as well as for 35-GHz radars operating in terrain backgrounds for which sufficient experimental observatiosn are not available, the hybrid model generates the requisite clutter pdf on the basis of electromagnetic models that were developed through careful experimental investigations. In this paper, electromagnetic models are provided for snow cover and for bare soil surfaces. Similar models for vegetation cover and road surfaces are under development and will be presented in future publications.

References

[1] Ulaby, F.T., and M.C. Dobson, *Handbook of Radar Scattering Statistics for Terrain*, Artech House, Norwood, Massachusetts, 1989.

[2] Skolnik, M.I., *Introduction to Radar Systems*, McGraw Hill, New York, 1980, Chapter 2.

[3] Ulaby, F.T., T.F. Haddock, and R.T. Austin, "Fluctu-ation Statistics of Millimeter-Wave Scattering for Dis-tributed Targets," *IEEE Trans. Geosci. Remote Sens-ing*, Vol. 26, No. 3, May 1988, pp. 268-281.

[4] Ulaby, F.T., and T.F. Haddock, "Millimeter-Wave Radar Scattering From Terrain: Data Handbook, Version 2, University of Michigan Radation Laboratory Technical Report 026247-4-T, September 1990.

[5] Kuga, Y., F.T. Ulaby, T.F. Haddock, and R. DeRoo, "Millimeter-Wave Radar Scattering From Snow: Part I-Radiative Transfer Model with Quasi-Crystalline Ap-proximation," *Radio Science*, Vol. 26, March 1991, pp. 329-341.

[6] Ulaby, F.T., T. Haddock, R. Austin and Y. Kuga, "Millimeter-Wave Radar Scattering From Snow: Part II-Comparison of Theory with Experimental Observa-tions," *Radio Science*, Vol. 26, March 1991, pp. 343-351.

[7] Ulaby, F.T., T.H. Haddock, and Y. Kuga, Measurement and Modeling of Millimeter-Wave Scat-tering From Tree Foliage" *Radio Science*, Vol. 25, 1990, pp. 193-203.

Discussion

Discussor's name :   E. Schweicher, BE

Comment/Question :

Is it true that the receiving antenna is a corrugated horn?

Author/Presenter's reply :

Yes it is for all four radar systems

Discussor's name :   H. B. Wallace, US

Comment/Question :

How do you relate the PdF of the clutter data to the instrumentation spatial resolution and the postulated system resolution in your models?

Author/Presenter's reply :

For resolution cells containing several correlation lengths, Rayleigh statistics is applicable, but for sub-correlation length size cells, we need to develop different statistical models. We are working on that now.

A Waveguide Polarization Controller

Kamal Sarabandi

Abstract—In this paper a novel waveguide polarizer is introduced that does not require rotary joints and the frequency of operation can easily be adjusted by a few set screws. In this method the degenerate eigenvalues of a circular waveguide are separated by deforming the waveguide cross section slightly. In order to generate a desired polarization, the orientation angle of the deformation point with respect to the polarization of the incident wave can be adjusted using a rotary roller mechanism concentric with the circular waveguide. Analysis of the problem based on the finite element method and an approximate analytical method is given. A prototype model at 34.5 GHz is built and tested. Experimental results shows excellent agreement with the theoretical prediction.

I. INTRODUCTION

Polarization agility in a military or remote sensing radar enhances the ability of the radar system in detection and measurement of a feature of interest in a radar scene [1]. Traditionally, the desired polarization in a transmitter is generated by employing one or two dielectric septum polarizers or corrugated dielectric wave-plates [2]. In the dielectric septum polarizer, a thin dielectric sheet of quarter-wavelength long is placed longitudinally in a circular waveguide which introduces a $\pi/2$ phase difference between two modes in space quadrature. Since the output polarization of a septum polarizer depends on the relative orientation of the dielectric septum with respect to the polarization of the incident wave, waveguide rotary joints are required to generate a set of desired polarizations. Although a choke is usually used with a waveguide rotary joint to reduce reflection at the interface of the flanges, the VSWR as a function of twist angle can be as high as 1.4 at X-band [3]. The somewhat random phase and amplitude variations as a function of twist angle caused by the rotary joint, degrade the performance of the polarizer.

An alternative way of controlling the polarization at millimeter and submillimeter wavelengths is to place an anisotropic (or corrugated) dielectric plate in front of the transmitter [4]. Since the dielectric wave-plate is illuminated by a spherical phase front, the axial ratio degrades away from the bore sight. Problems such as interaction of the corrugated dielectric wave-plate with the antenna and different attenuation for the components of the wave parallel and perpendicular to the optical axis degrades the polarization purity of the device.

It is shown that a squeezed rectangular waveguide can be used as a phase shifter [2], [5]. Based on this idea, design and analysis of a squeezed circular waveguide polarizer is presented. This polarizer does not require rotary joints and its center frequency can easily be adjusted by set screws.

II. THEORETICAL ANALYSIS

In this section theoretical analysis of squeezed waveguide polarizers is considered. The analysis involves two steps: 1) the mechanical

Fig. 1. Mechanical design of the squeezed waveguide polarizer (a prototype at Ka-band).

and 2) electrical design consideration of a pinched cylindrical waveguide. In the mechanical analysis the objective is determination of the cross section geometry of the pinched cylinder and in the electrical analysis determination of the first two eigenvalues (cutoff frequencies) of the deformed waveguide is of interest.

A. Mechanical Analysis

Fig. 1 shows the mechanical design of the rotatable waveguide squeezer. Two thick circular metallic disks are positioned concentric with the waveguide axis at each end of the waveguide section. Each concentric disk is supported over the waveguide surface by a bearing which facilitates rotation of the disk around the circular waveguide. The concentric disks are connected to each other by two shafts parallel to the axis and placed on opposite sides of the waveguide. The shafts are free to slide up and down in radial slots machined in the concentric disks. These shafts are the axes of two long roller bearings that are pinching the circular waveguide along two opposite lines parallel to the waveguide axis as shown in Fig. 1. The radial distance of the two osculating lines from the waveguide axis can be adjusted by the set screws, thereby the circular waveguide can be deformed to achieve the desired mode separation. In tuning the mode separation using the set screws, one must be careful not to exceed displacements outside the elastic region of the waveguide tubing.

The property of material, wall thickness, length of the osculating line (pinched section), and the inner radius of the waveguide are the influential parameters for proper mechanical design of the squeezed waveguide polarizer. The inner dimension of the circular waveguide is determined by the frequency of operation, thus is not a free parameter in mechanical design. The phase difference between the two orthogonal modes is proportional to the displacement of the waveguide wall from its normal configuration. Therefore in order to

get a larger phase difference for a given length of osculating line. the waveguide material must be chosen such that the ratio of the yield stress (S_y) to the Young's modulus of elasticity (E) is maximum amongst all possible alloys. Referring to a table of properties of metals [6]. it can be seen that alloys of beryllium copper have the largest yield stress (as high as 175 Ksi) while their modulus of elasticity is reasonably low (around 18 Mpsi). Aside from its elastic property. beryllium copper has other properties suitable for this design such as strength, corrosion resistance, and high electrical conductivity.

Structural analysis of the pinched cylinder is required to obtain the stress distribution and the cross section deformation. The stress distribution in the waveguide wall is required to assure that the stress does not exceed the yield stress of the material. For this problem a finite element code (I-DEAS) was used to calculate the stress distribution and cross section deformation. It was found that the maximum stress is at the edge of the osculating lines and is almost linearly proportional to the thickness as long as $\tau/r \ll 1$. It was also found that for thin shells the cross section of the deformed waveguide is almost elliptical when the relative displacement $(\Delta r/r)$ is under 7%. It is better to keep the displacement under 5% and achieve the desired phase shift by adjusting the length of the osculating line because the maximum stress increases rapidly with increasing displacement.

B. Numerical Solution

The finite element method offers an efficient numerical procedure in the calculation of the eigenvalues of a waveguide with arbitrary cross section [7]. This technique is well-known and here only a brief discussion of the method is outlined. For homogeneously-filled waveguides the longitudinal component of the electric (TM case) or magnetic (TE case) field, denoted by ψ, satisfies the homogeneous Helmholtz's equation $(\nabla^2 + K_c^2)\psi = 0$, where K_c is the cutoff wave number. It is shown that the solution to the Helmholtz's equation minimizes the following functional [8]

$$F(\psi) = \frac{\int\int_S \nabla\psi \cdot \nabla\psi \, ds}{\int\int_S \psi^2 ds} \tag{1}$$

and the minimum is equal to the smallest eigenvalue $\lambda = K_c^2$. To find the minima of the functional the eigenfunction ψ is approximated by a piecewise linear function. In this approximation the cross section of the waveguide is discretized into small triangular elements with unknown values of ψ at each node of the elements. Substituting the piecewise linear function into the functional (1) and searching for the minima by setting $\frac{\delta}{\delta\psi_j} = 0$, the following matrix equation is obtained

$$\mathbf{A}\Psi = K_c^2 \mathbf{B}\Psi. \tag{2}$$

Equation (2) is recognized as the generalized eigenvalue problem which can be solved for K_c numerically using a standard method [9].

C. Asymptotic Solution

As was discussed in the mechanical design section a slightly pinched circular cylinder deforms into an almost elliptical cylinders. The degenerate eigenvalues of the circular waveguides get separated into the so called even and odd modes of elliptical waveguides. The analytical solution for the cutoff frequencies and the associated phase constants of elliptical waveguides is known and therefore the phase difference between the dominant even and odd modes can be calculated [10]. In this section a simple closed form expression for the cutoff frequencies of the first two dominant modes of the almost circular waveguide is obtained.

Consider the elliptic coordinate system (μ, η, z) with parameter ρ. In this coordinate system. surfaces of constant μ specify confocal elliptical cylinders with ρ being half the distance between the foci. For the squeezed cylinder of radius r. represent the displacement of the surface at the pinched point by Δr. In this case the major and minor axes of the ellipse are $2(r + \Delta r)$ and $2(r - \Delta r)$ respectively. It is assumed that the relative displacement $\delta = \Delta r/r \ll 1$. The interfocal distance 2ρ in terms of relative displacement δ and radius of the original cylinder r is given by

$$\rho = 2r\sqrt{\delta} \tag{3}$$

and $\mu_0 = \tanh^{-1}[(1-\delta)/(1+\delta)]$ specifies the surface of the ellipse. The fields inside the elliptical cylinder may be expanded in terms of elliptical harmonic functions also known as angular $(S_m^c(\eta), S_m^o(\eta))$ and radial $(R_m^c(\mu), R_m^o(\mu))$ Mathieu functions [12]. Since the dominant mode of a circular waveguide is TE_{11}, the first two modes in the almost circular elliptical waveguide are TE_{11}^c and TE_{11}^o. To obtain an approximate solution for the cutoff frequencies of these modes, expansions of the radial Mathieu functions of the first kind in terms of Bessel functions are needed. For odd orders of the radial Mathieu functions, these expansions are given by [11]

$$R_{2m+1}^c(\mu, q) = \frac{S_{2m+1}^{c'}(\pi/2, q)}{\sqrt{q} A_1^{(2m+1)}}$$
$$\times \sum_{k=0}^{\infty}(-1)^{k+1} A_{2k+1}^{(2m+1)} J_{2k+1}(2\sqrt{q}\cosh\mu) \tag{4}$$

$$R_{2m+1}^o(\mu, q) = \frac{S_{2m+1}^{o'}(0, q)}{\sqrt{q} B_1^{(2m+1)}}$$
$$\times \sum_{k=0}^{\infty} B_{2k+1}^{(2m+1)} J_{2k+1}(2\sqrt{q}\sinh\mu) \tag{5}$$

where $q = \frac{1}{4}K_c^2\rho^2 = K_c^2 r^2 \delta$ and K_c is the cutoff wave number $(K_c = 2\pi/\lambda)$. The coefficients $A_{2k+1}^{(2m+1)}$ and $B_{2k+1}^{(2m+1)}$ in (4) and (5) are functions of q. The first even and odd modes correspond to $m = 0$ in the above equations. Since $q \ll 1$, a power series expansion of the angular Mathieu functions can be used in (4) and (5). Keeping the terms up to the first order in q, after some tedious algebraic manipulation it can be shown that

$$R_1^c(\mu, q) \approx \frac{1}{\sqrt{q}}\left[1 + \frac{3q}{8}J_1(2\sqrt{q}\cosh\mu) + \frac{q}{8}J_3(2\sqrt{q}\cosh\mu)\right] \tag{6}$$

$$R_1^o(\mu, q) \approx \frac{1}{\sqrt{q}}\left[1 - \frac{3q}{8}J_1(2\sqrt{q}\sinh\mu) - \frac{q}{8}J_3(2\sqrt{q}\sinh\mu)\right]. \tag{7}$$

For TE waves the boundary condition requires that

$$\frac{d}{d\mu}R_1^{c,o}(\mu, q) = 0 \qquad \text{at} \quad \mu = \mu_0. \tag{8}$$

The solution of these equations for q give the cutoff frequencies for the even and odd TE_{1n} modes. The dominant cutoff frequencies of the slightly deformed circular waveguide are slightly different from that of the circular waveguide, thus to the first order in δ

$$K_c^{c,o} \approx k_c^0(1 + \kappa^{c,o}\delta)$$

where $k_c^0 = 1.841/r$ is the cutoff wave number for the circular waveguide. Substituting (6) and (7) into (8), noting that $\cosh\mu_0 = (1 + \delta)/(2\sqrt{\delta})$ and $\sinh\mu_0 = (1 - \delta)/(2\sqrt{\delta})$, and then expanding the Bessel functions in terms their Taylor series to the first order in δ, it can be shown that

$$K_c^c \approx k_c^0(1 - 0.9183\delta) \tag{9}$$

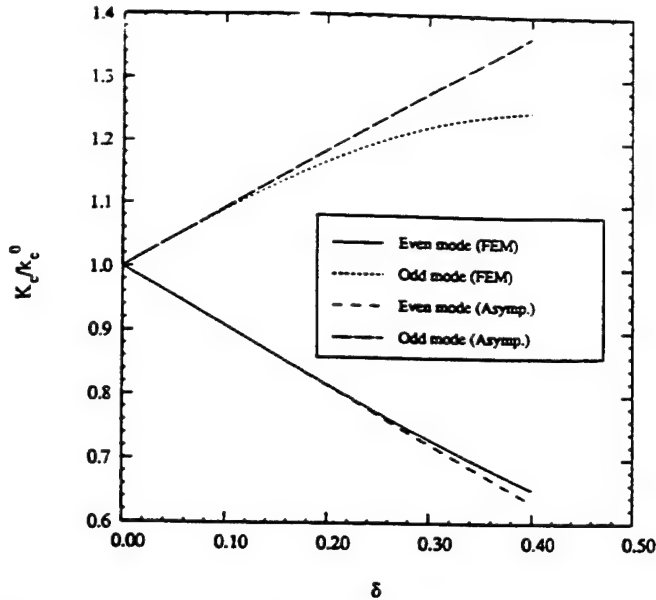$$K_c^o \approx k_c^0(1 + 0.9183\delta). \tag{10}$$

Fig. 2. First two cutoff wave number for an elliptical waveguide with axial ratio $\frac{1+\delta}{1-\delta}$ normalized to the dominant cutoff wave number of the circular waveguide ($\delta = 0$).

The cutoff wavenumbers given by (9) and (10) are comparered with those computed from the finite element code in Fig. 2. It can be seen that the asymptotic expression provides accurate results for values of δ as high as 10% for the odd mode and 20% for the even mode.

III. EXPERIMENTAL RESULTS

A squeezed waveguide polarizer with a rotary mechanism was designed and tested at Ka-band frequencies. A cylindrical brass tube of inner diameter of 6.35 mm, outer diameter of 7.14 mm, and length 8 cm was chosen as the circular waveguide.

Knowing the cross section geometry and the displacement, the length of the osculating line can be determined from the required phase difference between the orthogonal modes. In practice, after setting the displacement to the nominal design value, fine adjustment may be required to get the precise desired phase shift between the orthogonal modes. To characterize the performance of the squeezed waveguide polarizer and fine-tune the phase shift, a new test setup is designed as shown in Fig. 3. An HP 8753C network analyzer is used as the sweeper and dual vector receiver. Since the operating frequency of the network analyzer is limited to 3 GHz, one up-converter and two down-converter (harmonic mixers) are used to extend the operating frequency to Ka-band. To increase the isolation between the up-converter and down-converters, bandpass filters were inserted in each branch of the power splitter.

The RF port of the up-converter is a rectangular waveguide oriented vertically and connected to the polarizer *via* a rectangular-to-circular waveguide adapter. The output of the polarizer is connected to an orthogonal mode transducer (OMT) with 40 dB isolation between the two orthogonal ports. The OMT at the output of the polarizer is oriented so that the orthogonal ports are at $45°$ with respect to the vertical direction. When the waveguide squeezer is unloaded, the polarizer does not modify the incident wave and the signals received in the A and B ports of the network analyzer should be identical. However, due to path length differences and variations in amplifier gains and mixer conversion losses, the received signal in the A and B ports are not identical. The measured A and B for the unsqueezed polarizer are used to find the differences between the two channels.
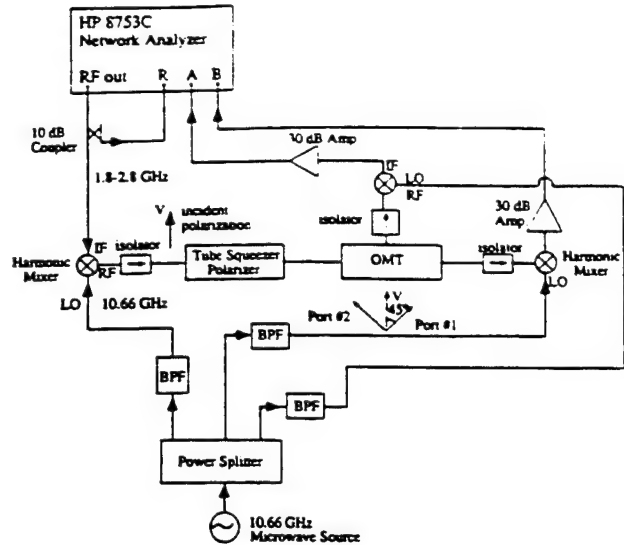
Fig. 3. Experimental setup for tuning and characterizing the prototype Ka-band squeezed waveguide polarizer.

Suppose $\hat{o}$ and $\hat{e}$ are two orthogonal unit vectors along the minor and major axes of the deformed waveguide and α is the angle between $\hat{o}$ and $\hat{v}$ (the polarization of the incident wave). Depending on the orientation angle α, the incident wave can excite both modes of propagations one with the electric field along the major axis, and the other one with the electric field along the minor axis of the ellipse. The component of the incident wave along the minor axis propagates more slowly than the component along the major axis which produces a phase difference ϕ between the two components. By decomposing the field at the output of the polarizer into two components along the ports of the OMT, it can be shown that the calibrated signal at the A and B ports of the network analyzer must satisfy

$$\frac{A}{B} = \frac{1 - e^{-j\phi}\tan(\alpha - 45)\cot(\alpha)}{\tan(\alpha - 45) + e^{-j\phi}\cot(\alpha)}. \quad (11)$$

In order to fine tune the polarizer for the desired ϕ, we notice that at the rotation angle $\alpha = 45°$, the phase difference between A and B signals is ϕ. In this experiment the rotary disk of the polarizer was engaged with a stepper motor to facilitate accurate positioning of the vectors $\hat{o}$ and $\hat{e}$ with respect to $\hat{v}$ within a fraction of a degree. For the prototype polarizer with $L = 1.9$ cm, $r = 0.317$ cm, and $f = 34.5$ GHz, the phase difference can be calculated from

$$\phi = L(k_z^e - k_z^o) \quad (12)$$

where k_z^e and k_z^o can be obtained from (9) and (10) respectively. To achieve a $90°$ phase shift a displacement of 5.5% is required which was verified experimentally. Fig. 4 compare the phase of the measured A/B to the expression (12) as a function of rotation angle. It can be seen that the agreement is excellent. In a separate measurement setup it was found that the return loss (S_{11}) of the polarizer was better than 40 dB.

IV. CONCLUSION

A new design for waveguide polarizers was presented. In this technique the degenerate eigenvalues of a circular waveguide are separated by deforming the cross section. The circular cylinder is pinched from the opposite sides so that the first two modes are in space quadrature. By choosing the length of the deformed section and the relative displacement a phase difference of $\pi/2$ between the two modes is introduced. The output polarization is controlled
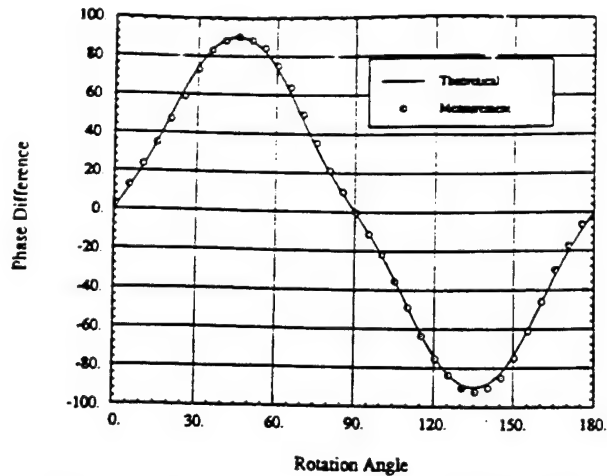
Fig. 4.   The measured and calculated phase difference of the signals at the OMT output (A and B).

by a rotatable waveguide squeezer which facilitates rotation of the major axis of the deformed cross section with respect to the input polarization. The new polarizer does not require rotary joints and its center frequency can easily be adjusted using a few set screws. Analytical and numerical design procedures are presented and a prototype model at Ka-band is built and test.

REFERENCES

[1]   D. Giuli. "Polarization diversity in radars." *Proc. IEEE*. vol. 74. pp. 245–269. Feb. 1986.

[2]   A. F. Harvey. *Microwave Engineering*.   New York: Academic Press. 1963.

[3]   F. E. Ehlers. "Waveguide rotary joints," in G. L. Ragan. Ed.. *Microwave Transmission Circuits*.   Cambridge, MA: M.I.T. Radiation Laboratory Series, 1964.

[4]   H. S. Krischbaum and L. Chen. "A method of producing broadband circular polarization employing an anisotropic dielectric." *IRE Trans. Microwave Theory Tech.*, vol. MMT-5, no. 3, pp. 199–203, July 1957.

[5]   H. Schrank and G. Seck. "The spread-squeeze waveguide polarizer," *IEEE Antennas Propagat. Newsletter*, Oct. 1984.

[6]   E. Oberg. F. D. Jones, and H. L. Horton, *Machinery's Handbook*.   New York: Industrial Press, 1988.

[7]   P. Silvester, "A general high-order finite-element waveguide analysis program," *IEEE Trans. Microwave Theory Tech.*, vol. MTT-17, Apr. 1969.

[8]   J. W. Dettman, *Mathematical Methods in Physics and Engineering*. New York: Dover, 1988. pp. 149–169.

[9]   J. H. Wilkinson, *The Algebraic Eigenvalue Problem*.   New York: Oxford University Press, 1965.

[10]   L. J. Chu, "Electromagnetic waves in elliptic hollow pipes of metal," *J. Appl. Phys.*, vol. 9, pp. 583–591, Sept. 1938.

[11]   M. Abramowitz and I. A. Stegun, *Handbook of Mathematical Functions*. New York: Dover, 1972, pp. 722–746.

Statistical properties of the Mueller matrix of distributed targets

F.T. Ulaby

K. Sarabandi

A. Nashashibi

Abstract: As a consequence of the reciprocity relation, the scattering matrix measured in the backscattering direction by a polarimetric radar system consists of five quantities: $|S_{vv}|$, $|S_{hh}|$, and $|S_{hv}|$, which are the magnitudes of the linearly polarised scattering amplitudes, and ϕ_c and ϕ_x, which are the co-polarised and crosspolarised phase angles. For statistically homogeneous, distributed terrain targets, the magnitudes are Rayleigh distributed and their means are related to the target's geometrical and dielectrical properties, but their normalised probability density functions are target independent. For most natural targets, the crosspolarised phase angle ϕ_x is uniformly distributed over $[0, 2\pi]$, and therefore contains no target-specific information. The co-polarised phase angle ϕ_c, on the other hand, is shown to exhibit a probability density function (PDF) that is characterised completely by two parameters α and ζ, both of which are related to the elements of the Mueller matrix of the target. The parameter α governs the width of the PDF and ζ governs the mean value of ϕ_c. It is further shown that the three magnitudes $|S_{vv}|$, $|S_{hh}|$, and $|S_{hv}|$ and the two parameters α and ζ completely specify the Mueller matrix, and therefore contain all the statistical information available from the polarimetric backscatter response of the target. These results are verified with experimental observations that show that α and ζ are related to the physical and dielectric properties of soil and vegetation targets.

1 Introduction

Unlike conventional SAR, which generates a high-resolution display of the radar backscattering coefficient of the imaged scene for the specific transmit-receive polarisation configuration used by the radar antenna, a coherent, polarimetric SAR measures the scattering matrix S (on a pixel by pixel basis) from which the scattering cross section σ (or scattering coefficient $\sigma^\circ = \sigma/A$, where A is the pixel area) can be computed for any desired transmit and receive polarisation combination

through the application of the polarisation synthesis technique [1, 2]. Several models have recently been developed to characterise the polarimetric response of terrain, such as soil and vegetation-covered surfaces [3–5], with the expectation of using the models to extract more detailed information about the terrain from its polarimetric response than is available from conventional SAR data [6]. Because radar is a narrow-bandwidth coherent sensor, the radar image of a statistically homogeneous scene will exhibit 'speckle' due to signal fading scintillations [7], which usually necessitates spatial averaging of several pixels prior to interpreting the data. To apply the polarisation synthesis technique, one could follow either of two basic procedures. In the first procedure, the scattering cross section σ is synthesised for each pixel using the scattering matrix measured for that pixel, and then σ is averaged over however many pixels are deemed necessary for interpreting the data. In the second procedure, each of the measured (2×2) complex scattering matrices are first converted to their corresponding 4×4 real Mueller matrices (or Stokes scattering operators or Stokes covariance matrices), the averaging is performed over the 4×4 real matrices, and then the polarisation synthesis technique is applied to the averaged 4×4 matrix [1]. For a distributed target represented by many pixels in a radar image (such as an ocean surface, or a forest canopy), a coherent polarimetric radar offers two basic types of information: (a) the synthesised polarisation response, which represents the average scattering coefficient as a function of all possible combinations of transmit and receive antenna polarisations, and (b) the probability density functions of the magnitudes and polarisation phase differences (which are defined in the next Section). For statistically distributed targets, the magnitude of the backscattered signal is Rayleigh distributed regardless of the geometrical and dielectric properties of the target. Hence, only the mean value of the magnitude contains information about the target. The polarisation phase differences are ϕ_c and ϕ_x, where $\phi_c = \phi_{hh} - \phi_{vv}$ is the co-polarised phase angle, $\phi_x = \phi_{hv} - \phi_{vv} = \phi_{vh} - \phi_{vv}$ is the crosspolarised phase angle, and ϕ_{ij} is the phase of the received electric field for receive polarisation i and transmit polarisation j. The subscripts h and v refer to horizontal and vertical polarisation respectively. Experimental data acquired by coherent polarimetric SAR systems and by polarimetric scatterometer systems have shown that the crosspolarised phase angle ϕ_x is uniformly distributed over $[0, 2\pi]$ for any distributed target. Hence, ϕ_x does not contain information about the target. In contrast, the probability density function of ϕ_c is strongly dependent upon both

the sensor parameters (incidence angle and wavelength) and the target parameters (roughness, dielectric constant, geometry, etc.)

To measure the scattering matrix S, the measuring radar system should maintain good phase stability over the duration of the measurement. Usually the four elements of S are measured by transmitting a linear polarisation, such as v, and recording both the h- and v-polarised backscattered signals, and then repeating the process after changing the transmit signal to h polarisation. This can be accomplished by alternating the polarisation of the transmitted pulses. The movement of a SAR between adjacent pulses results in some decorrelation between the received signals because they will not view exactly the same area on the ground. This problem can be corrected, however, by proper sampling and interpolation, albeit at the cost of increased complexity of the SAR signal processor.

The data available from a calibrated polarimetric SAR image of a statistically homogeneous distributed target can be used in either one of two forms. The first consists of the means of the three principal polarisation magnitudes, $\langle S_{vv} S_{vv}^* \rangle$, $\langle S_{hh} S_{hh}^* \rangle$ and $\langle S_{hv} S_{hv}^* \rangle$, and the PDF of ϕ_c, $f(\phi_c)$. The goal is to relate these quantities to the physical and dielectric properties of the target, with the ultimate objective being to invert the process so as to infer the properties of the target from the radar observations. The second form is the Mueller matrix M, whose elements are given by ensemble averages of various products of the elements of the scattering matrix S. The Mueller-matrix form is used for polarisation synthesis (which can also be realised from the measured S matrices directly), but more importantly it is the only means available for comparing measured data with theoretical models. Scattering models of the polarimetric response of terrain are inherently ensemble-average processes and their output products are expressions of the Mueller matrix, M. Three of the elements of M are identical to the magnitudes mentioned earlier, but until recently, it was not possible to obtain $f(\phi_c)$ from M. Hence, it was not possible to compare the measured $f(\phi_c)$ with theoretical predictions nor to evaluate the potential information about the target contained in $f(\phi_c)$. Based on a recent study by Sarabandi [8], $f(\phi_c)$ can be completely specified in terms of two parameters, α and ζ, both of which are given explicitly in terms of the elements of M, thereby providing the missing link between the statistics of the polarimetric response available from the SAR measurements and the expressions for the Mueller matrix available from theoretical models. This is examined in the present paper and verified with experimental data for soil surfaces and small trees.

Another important application of the link between $f(\phi_c)$ and M pertains to nonfully coherent polarimetric radar techniques that measure M directly. At centimetre wavelengths SAR technology is capable of maintaining phase coherence at the level necessary for measuring the scattering matrix S with good magnitude and phase accuracy, but phase stability requirements are more difficult to achieve at the shorter millimetre wavelengths, particularly at the 140 and 215 GHz atmospheric window frequencies. These limitations have led researchers to develop an alternative measurement technique which requires the system to be able to measure the phase difference between the two simultaneously received orthogonal polarisation channels, but does not require phase stability from one pulse to the next [9–11]. This coherent-on-receive polarimetric radar technique does

not measure the scattering matrix S, but measures the Mueller matrix directly, instead.

2 Polarimetric response

The object located at the centre of the co-ordinate system shown in Fig. 1 is illuminated by a plane wave radiated by a transmitting antenna in the direction $\hat{k}_t$. The angles (θ_i, ϕ_i) specify the direction of the unit vector $\hat{k}_t$. In
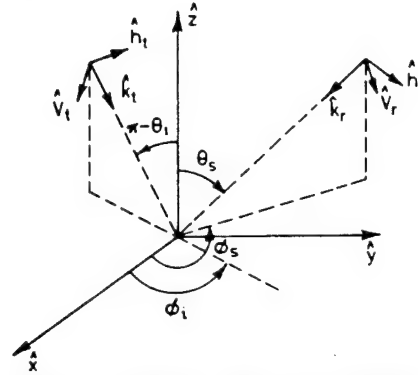

Fig. 1 Co-ordinate systems and scattering geometry for the backscatter alignment (BSA) convention

general the incident wave may be composed of a vertical polarisation component $\hat{v}_t$ and a horizontal component $\hat{h}_t$, defined such that the co-ordinate system $(\hat{k}_t, \hat{v}_t, \hat{h}_t)$ coincides with the $(\hat{r}, \hat{\theta}, \hat{\phi})$ of a standard spherical co-ordinate system. Although our interest is in the backscatter situation, wherein the transmit and receive antennas are co-located, the configuration shown in Fig. 1 corresponds to the general bistatic case, chosen for ease of illustration. The receive antenna observes the target in the direction $\hat{k}_r$ and its polarisation unit vectors $\hat{v}_r$ and $\hat{h}_r$ are defined as if it were a transmitting antenna, in accordance with the backscatter alignment convention. Using this convention, in the backscatter case the angles shown are related by $\theta_s = \pi - \theta_i$ and $\phi_s = \pi + \phi_i$, and the transmit and receive unit vectors become coincident: $(\hat{k}_t, \hat{v}_t, \hat{h}_t) = (\hat{k}_r, \hat{v}_r, \hat{h}_r)$.

2.1 Scattering matrix
In general, the electric field of the plane wave radiated by the transmitting antenna is elliptically polarised with complex polarisation components E_v^t and E_h^t. Thus

$$E^t = E_v^t \hat{v}_t + E_h^t \hat{h}_t \tag{1}$$

with the phase reference of E^t chosen to be at the centre of the illuminated target (i.e., at the centre of the co-ordinate system). The field of the spherical wave scattered by the target in the direction of the receive antenna, defined in terms of the polarisation vectors of the receive antenna, is given by

$$E^r = E_v^r \hat{v}_r + E_h^r \hat{h}_r \tag{2}$$

and it is related to E^t by [12, 13]:

$$E^r = \frac{e^{ikr}}{r} S E^t \tag{3}$$

where r is the distance between the target and the receive antenna and S is the scattering matrix of the scattering target,

$$S = \begin{bmatrix} S_{vv} & S_{vh} \\ S_{hv} & S_{hh} \end{bmatrix} \tag{4}$$

The elements S_{ij} of S are called the scattering amplitudes, and the subscripts ij denote the polarisation configuration of the receive and transmit fields, in that order. To

measure the scattering amplitudes of a given target, one needs to use a coherent radar system with dual polarisation capability for both transmission and reception. Upon transmitting a vertically polarised wave $E^t = E^t_v \hat{v}_t$, and recording both components of the received wave (E^r_v and E^r_h) using a dual polarised antenna, the scattering amplitudes S_{vv} and S_{hv} can be determined from

$$S_{vv} = \left[\frac{e^{ikr}}{r}\right]^{-1} \frac{E^r_v}{E^t_v} \tag{5}$$

$$S_{hv} = \left[\frac{e^{ikr}}{r}\right]^{-1} \frac{E^r_h}{E^t_v} \tag{6}$$

The factor $[e^{ikr}/r]^{-1}$ can be determined by measuring the field backscattered from a target with known scattering matrix, such as a metallic sphere. A similar procedure involving the transmission of a horizontally polarised wave leads to the determination of S_{hh} and S_{vh}.

Each scattering amplitude S_{ij} is a complex quantity comprised of a magnitude $|S_{ij}|$ and a phase angle ϕ_{ij},

$$S_{ij} = |S_{ij}|e^{i\phi_{ij}}, \quad i, j = v \text{ or } h \tag{7}$$

and for backscattering, the reciprocity relation for polarised scattering mandates that the crosspolarised scattering amplitudes be equal,

$$S_{hv} = S_{vh} \tag{8}$$

Using eqns. 7 and 8, the scattering matrix can be written in the form

$$S = e^{i\phi_{vv}}\begin{bmatrix} |S_{vv}| & |S_{vh}|\,e^{i\phi_x} \\ |S_{vh}|\,e^{i\phi_x} & |S_{hh}|\,e^{i\phi_c} \end{bmatrix} \tag{9}$$

where

$$\phi_x = \phi_{hv} - \phi_{vv} = \phi_{vh} - \phi_{vv} \tag{10}$$

$$\phi_c = \phi_{hh} - \phi_{vv} \tag{11}$$

thus referencing all phase angles to the phase angle of the vv-polarised element. We shall henceforth refer to ϕ_x and ϕ_c as the cross- and co-polarised phase angles, respectively.

2.2 Polarisation synthesis for a point target

With S known, the radar cross section (RCS) for any of the principal linear polarisation combinations can be obtained from

$$\sigma_{ij} = 4\pi|S_{ij}|^2; \quad i, j = v \text{ or } h \tag{12}$$

To compute the radar cross section for any other polarisation combination, we first need to define the polarisation vectors $\hat{p}^t$ and $\hat{p}^r$ of the transmit and receive antennas. If the field E that would be radiated by an antenna is

$$E = E_v \hat{v} + E_h \hat{h}$$
$$= a_v e^{-i\delta_v}\hat{v} + a_h e^{-i\delta_h}\hat{h} \tag{13}$$

where a_v and a_h are the magnitudes of the v- and h-polarised components and ϕ_v and ϕ_h are the corresponding phase angles, then the antenna polarisation vector, written in matrix form, is given by

$$p = \frac{E}{|E|} = \begin{bmatrix} \cos\alpha \\ \sin\alpha\, e^{-i\delta} \end{bmatrix} \tag{14}$$

where $\tan\alpha = a_h/a_v$ and $\delta = \delta_h - \delta_v$. A factor of $e^{-i\delta_v}$ multiplying the matrix in eqn. 14 has been suppressed for convenience because it is not needed in the application of the polarisation synthesis technique. Often, wave polar-

isation is described in terms of the polarisation ellipse (Fig. 2), characterised by the rotation angle ψ and ellipticity angle χ, which are related to α and δ by

$$\tan 2\psi = (\tan 2\alpha)\cos\delta \tag{15}$$

$$\sin 2\chi = (\sin 2\alpha)\sin\delta \tag{16}$$
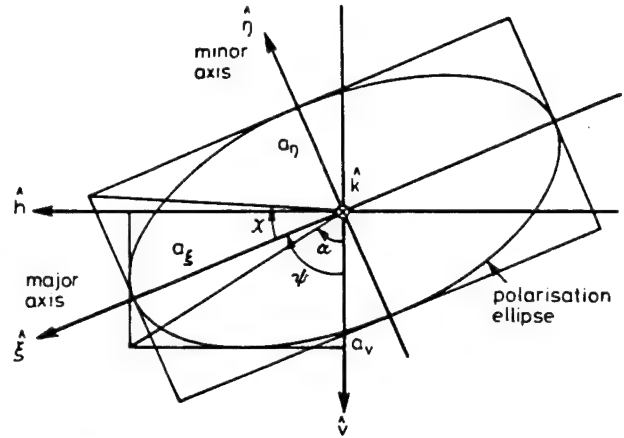
Fig. 2 Polarisation ellipse in the v–h plane for a wave travelling in the $\hat{k}$ direction

and conversely,

$$\cos 2\alpha = (\cos 2\chi)(\cos 2\psi) \tag{17}$$

$$\tan\delta = \frac{\tan 2\chi}{\sin 2\psi} \tag{18}$$

For a target with scattering matrix S, its radar cross section can be computed for any receive and transmit polarisation, defined by the polarisation angles (ψ_r, χ_r) and (ψ_t, χ_t) — or equivalently, by the parameters (α_r, δ_r) and (α_t, δ_t) — by applying the polarisation synthesis equation [11]:

$$\sigma(\psi_r, \chi_r; \psi_t, \chi_t) = 4\pi|p^r \cdot Sp^t|^2 \tag{19}$$

2.3 Synthesis for a distributed target

Unlike point targets, soil surfaces and vegetation canopies are distributed targets, composed of randomly-distributed scatterers. The backscatter behaviour of a distributed target is characterised by the backscattering coefficient, σ^0, which is the ensemble average of the radar cross section, σ, per unit area,

$$\sigma^0 = \frac{\langle\sigma\rangle}{A} \tag{20}$$

where A is the illuminated area. For the principal linear polarisations, the synthesis process is straightforward: simply measure S for each of many independent samples of the distributed target (or pixels of resolution area A, in the case of an imaging radar), and then compute

$$\sigma^0_{ij} = \frac{4\pi}{AN}\sum_{l=1}^{N}|S_{ij}|^2_l, \quad ij = v \text{ or } h \tag{21}$$

where N is the number of independent samples measured. For other polarisation combinations of transmit and receive polarisations, two approaches are available, both of which provide identical results.

Scattering matrix approach: The first approach is basically identical to the synthesis technique used in conjunction with point targets. Thus,

$$\sigma^\circ(\psi_r, \chi_r; \psi_t, \chi_t) = \frac{4\pi}{AN} \sum_{l=1}^{N} |p' \cdot S_l p^t|^2 \tag{22}$$

where S_l is the measured scattering matrix of the lth sample.

Stokes scattering operator approach: Instead of synthesising the backscatter N times and then averaging the sum to obtain σ^0, as outlined in the preceding approach, it is possible to use a computationally more efficient approach, based on the Stokes scattering operator [1, p. 32]. To show the procedure, we start with the modified Stokes vector representation of a polarised wave,

$$F(\psi, \chi) = \begin{bmatrix} I_v \\ I_h \\ U \\ V \end{bmatrix} = \begin{bmatrix} \langle |E_v|^2 \rangle \\ \langle |E_h|^2 \rangle \\ \langle 2 \operatorname{Re}(E_v E_h^*) \rangle \\ \langle 2 \operatorname{Im}(E_v E_h^*) \rangle \end{bmatrix} \tag{23}$$

where $\langle \ \rangle$ denotes ensemble average. Upon applying eqn. 3, it can be shown [1] that the transmitted and scattered modified Stokes vectors are related by the modified Mueller matrix M,

$$F^r = \frac{1}{r^2} M F^t \tag{24}$$

with the elements of M being real quantities, given in terms of the elements of the scattering matrix S,

$$M = \left\langle \begin{bmatrix} |S_{vv}|^2 & |S_{vh}|^2 \\ |S_{hv}|^2 & |S_{hh}|^2 \\ 2 \operatorname{Re}(S_{vv} S_{hv}^*) & 2 \operatorname{Re}(S_{vh} S_{hh}^*) \\ 2 \operatorname{Im}(S_{vv} S_{hv}^*) & 2 \operatorname{Im}(S_{vh} S_{hh}^*) \end{bmatrix} \right.$$

$$\left. \cdots \begin{bmatrix} \operatorname{Re}(S_{vh}^* S_{vv}) & -\operatorname{Im}(S_{vh}^* S_{vv}) \\ \operatorname{Re}(S_{hh}^* S_{hv}) & -\operatorname{Im}(S_{hv} S_{hh}^*) \\ \operatorname{Re}(S_{vv} S_{hh}^* + S_{vh} S_{hv}^*) & -\operatorname{Im}(S_{vv} S_{hh}^* - S_{vh} S_{hv}^*) \\ \operatorname{Im}(S_{vv} S_{hh}^* + S_{vh} S_{hv}^*) & \operatorname{Re}(S_{vv} S_{hh}^* - S_{vh} S_{hv}^*) \end{bmatrix} \right\rangle \tag{25}$$

For a distributed target, the following polarisation synthesis equation is applicable [11]:

$$\sigma^\circ(\psi_r, \chi_r; \psi_t, \chi_t) = \frac{4\pi}{A} A^r \cdot QMA^t \tag{26}$$

where A^r and A^t are the normalised modified Stokes vectors for the receive and transmit antennas $[A = F/(I_v + I_h)]$, A is the illuminated area, and Q is a diagonal transformation matrix given by

$$Q = \begin{bmatrix} 1 & 0 & 0 & 0 \\ 0 & 1 & 0 & 0 \\ 0 & 0 & \frac{1}{2} & 0 \\ 0 & 0 & 0 & -\frac{1}{2} \end{bmatrix} \tag{27}$$

3 Statistical properties of the Mueller matrix

The polarisation synthesis capability provided by a polarimetric radar offers a number of obvious advantages, including the optimisation of the radar response to enhance discrimination between different types of terrain and the detection of point targets against the background

clutter [1, Chapt. 7]. These applications, however, are not the subject of this paper.

The intent of this paper is to examine the statistical properties of the Mueller matrix M. We start by defining each of the scattering amplitudes in terms of its real and imaginary components,

$$S_{vv} = |S_{vv}| e^{i\phi_{vv}} = \rho_1 e^{i\phi_{vv}} = x_1 + ix_2 \tag{28}$$

$$S_{hh} = |S_{hh}| e^{i\phi_{hh}} = \rho_2 e^{i\phi_{hh}} = x_3 + ix_4 \tag{29}$$

$$S_{hv} = |S_{hv}| e^{i\phi_{hv}} = \rho_3 e^{i\phi_{hv}} = x_5 + ix_6 \tag{30}$$

where $\rho_1 = |S_{vv}|$, $\rho_2 = |S_{hh}|$, $\rho_3 = |S_{hv}|$, and because of the reciprocity relation, $S_{hv} = S_{vh}$ for backscatter.

3.1 Statistics of the individual magnitudes and phases

When a radar illuminates a volume of a random medium or an area of a random surface, many point scatterers contribute to the total scattered electric field received by the radar. Hence, each of the scattering amplitudes is represented by a sum of the form

$$S_{pq} = |S_{pq}| e^{i\phi_{pq}} = \sum_{n=1}^{N} |S_{pq}^n| e^{i\phi_{pq}^n}, \quad p, q = v, h \tag{31}$$

where N is the total number of scatterers and $|S_{pq}^n|$ and ϕ_{pq}^n are the magnitude and phase angle of the field due to the nth scatterer. The phase angle ϕ_{pq}^n includes a phase delay related to the scatterer's location with respect to a reference position (such as the centre of the distributed target). Because the scatterers are randomly located within the illuminated volume (or area), the magnitude $|S_{pq}^n|$ and phase ϕ_{pq}^n are statistically independent variables. For N large, this independence leads to the result that the real and imaginary parts of S_{pq} are independent, zero-mean, Gaussian random variables with equal variances [7, p. 38–43]. For S_{vv}, for example, these properties can be shown to lead to the following probability density functions for the magnitude ρ_1 and phase angle ϕ_{vv} of S_{vv}

$$f_{\rho_1}(\rho_1) = \frac{\rho_1}{\lambda_{11}} \exp\left(-\frac{\rho_1}{2\lambda_{11}}\right) \tag{32}$$

$$f_{\phi_{vv}}(\phi_{vv}) = \frac{1}{2\pi} \tag{33}$$

where $\lambda_{11} = \langle x_1^2 \rangle = \langle x_2^2 \rangle = \lambda_{22}$ is the variance of both x_1 and x_2. The PDF given by eqn. 32 is the Rayleigh distribution with mean $\langle \rho_1 \rangle = \langle |S_{vv}| \rangle = \sqrt{(\pi \lambda_{11}/2)}$.

Experimental verification of the assumption that x_1 and x_2 are Gaussian-distributed random variables with equal variances is given in Fig. 3, which displays the PDFs of x_1, x_2, x_3, and x_4, based on approximately 1000 measurements of a random soil surface observed by a truck-mounted polarimetric scatterometer at 4.75 GHz. Similar results were also observed for the crosspolarised components x_5 and x_6.

The power, $\rho_1^2 = \langle S_{vv} S_{vv}^* \rangle$, is characterised by an exponential distribution,

$$f_{\rho_1^2}(\rho_1^2) = \frac{1}{2\lambda_{11}} \exp\left(-\frac{\rho_1^2}{2\lambda_{11}}\right) \tag{34}$$

with mean value

$$\langle \rho_1^2 \rangle = \langle S_{vv} S_{vv}^* \rangle = 2\lambda_{11} = M_{11} \tag{35}$$

where M_{11} is the 11th element of the Mueller matrix given by eqn. 25. Because the PDF given by eqn. 34 is a

single-parameter distribution, the mean value M_{11} is sufficient for characterising the statistical behaviour of $|S_{vv}|^2$. Similar distributions and statements apply to the powers $|S_{hh}|^2$ and $|S_{hv}|^2$.
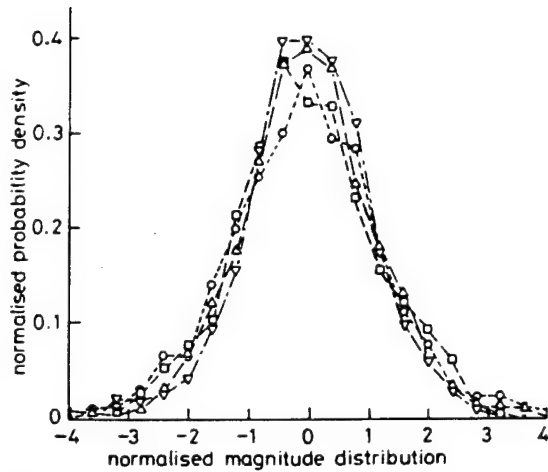

Fig. 3 *Histogram of the real and imaginary parts of S_{vv} and S_{hh} for a rough surface with rms height 0.32 cm and correlation length 9.9 cm at C-band and 30° incidence angle*

-- O -- Real (S_{vv})
— □ — Imag (S_{vv})
— △ — Real (S_{hh})
— ▽ — Imag (S_{hh})

3.2 Statistics of the phase differences

Although individually the phase angles ϕ_{vv}, ϕ_{hh}, and ϕ_{hv} are uniformly distributed over $[-\pi, \pi]$, and therefore contain no information about the target's geometrical and dielectric properties, their differences $\phi_c = \phi_{hh} - \phi_{vv}$ and $\phi_x = \phi_{hv} - \phi_{vv}$ may not be uniformly distributed and may in fact be related to the target's properties. As will be discussed later, the crosspolarised phase angle ϕ_x is approximately uniformly distributed over $[-\pi, \pi]$ for most natural targets (such as soil surfaces and vegetation), but the copolarised phase angle ϕ_c is approximately Gaussian in shape with its mean and variance being directly related to the elements of the Mueller matrix M.

Using the statistical properties of the scattering amplitudes given in the preceding section, closed form solutions are available in Appendix 8 for the probability density functions of ϕ_c and ϕ_x. The PDF of ϕ_c is given by (81)

$$f(\phi_c) = \frac{\lambda_{11}\lambda_{33} - \lambda_{13}^2 - \lambda_{14}^2}{2\pi(\lambda_{11}\lambda_{33} - D^2)}\left\{1 + \frac{D}{\sqrt{(\lambda_{11}\lambda_{33} - D^2)}}\right.$$
$$\left. \times \left[\frac{\pi}{2} + \tan^{-1}\frac{D}{\sqrt{(\lambda_{11}\lambda_{33} - D^2)}}\right]\right\} \quad (36)$$

where

$$D = \lambda_{13}\cos\phi_c + \lambda_{14}\sin\phi_c \quad (37)$$

and the quantities λ_{13}, λ_{14}, λ_{11}, and λ_{33} are all expressed in terms of the elements of the Mueller matrix. The validity of eqn. 36 has been verified against experimental data for a variety of distributed targets using both truck-mounted radar measurements and airborne SAR observations. By way of illustration, we show in Fig. 4a a histogram of $f(\phi_c)$ based on direct measurements of ϕ_c for a slightly rough surface and a plot of $f(\phi_c)$ computed according to eqn. 36 and the measured Mueller matrix of the surface. Excellent agreement is observed between the measured histogram and the theoretical expression in

terms of the shape of the PDF and the mean value and stadard deviation of ϕ_c. Similar remarks apply to Fig. 4b for the crosspolarised phase difference ϕ_x, for which the theoretical PDF was calculated using (84). The experimental data used in Fig. 4 were measured by a truck-
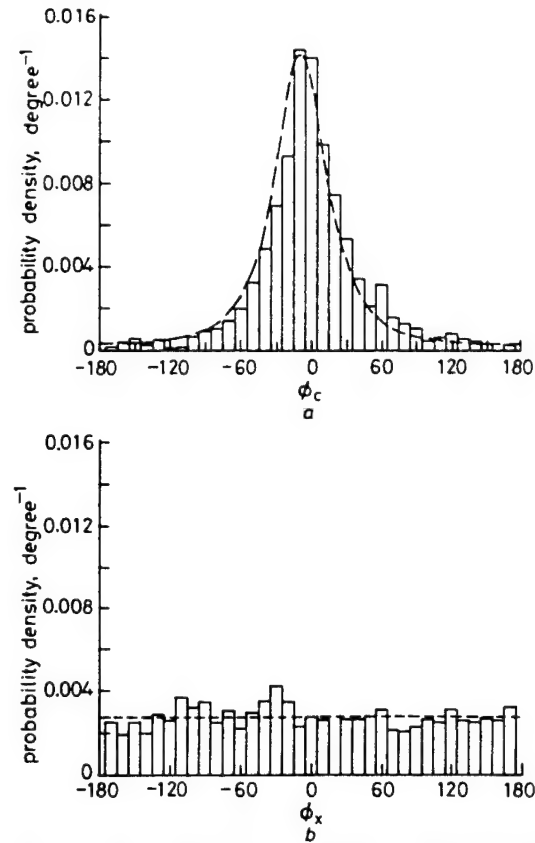
Fig. 4 *Measured and calculated probability density functions*

a the co-polarised phase angle $\phi_c = \phi_{hh} - \phi_{vv}$
——— Measured (Mean = −5.0°, Std. Dev. = 47.7°)
- - - - Calculated (Mean = −7.8°, Std. Dev. = 47.2°)
b the cross-polarised phase angle $\phi_x = \phi_{hv} - \phi_{vv}$. The target is a slightly rough soil surface with rms height of 0.32 cm, observed at a frequency of 4.75 GHz and incidence angle of 30°
——— Measured (Mean = −1.0°, Std. Dev. = 102.5°)
- - - - Calculated (Mean = 0.8°, Std. Dev. = 103.7°)

mounted polarimetric scatterometer. An example depicting similar results based on airborne SAR observations of grass-covered terrain is shown in Fig. 5.
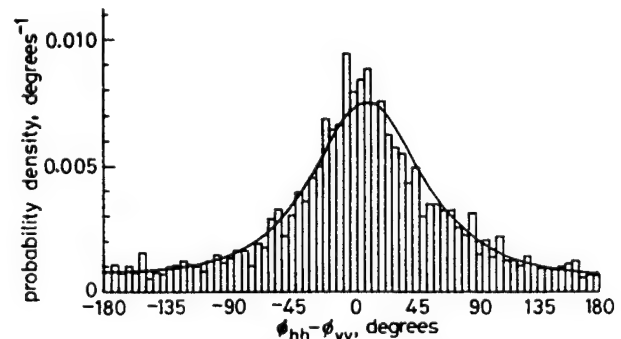
Fig. 5 *Measured and calculated $f(\phi_c)$ for a grassy area in Northern Michigan observed by a 1.2 GHz SAR in April 1990*

The PDF of ϕ_x shown in Fig 4b, which is essentially a uniform distribution over $[-\pi, \pi]$, is typical for most natural terrain surfaces and volumes. If the crosspolarised scattering amplitude S_{hv} is statistically independent of S_{vv}, and since ϕ_{hv} and ϕ_{vv} are each uniformly distributed over $[-\pi, \pi]$, it can be easily shown that $\phi_x = \phi_{hv} - \phi_{vv}$ is uniformly distributed over $[-\pi, \pi]$.

However, the converse is not necessarily true; that is, if ϕ_x is uniformly distributed over $[-\pi, \pi]$, it does not necessarily follow that S_{hc} and S_{vv} are statistically independent.

Let us now return to further examination of the copolarised phase difference ϕ_c. If S_{vc} and S_{hh} are totally uncorrelated, then

$$\lambda_{13} = \langle x_1 x_3 \rangle = 0 \tag{38}$$

$$\lambda_{14} = \langle x_1 x_4 \rangle = 0 \tag{39}$$

as a result of which we have $f(\phi_c) = 1/(2\pi)$, as expected. On the other hand, if the scattered wave always has the same polarisation independent of which segment area of the target is under observation, which implies that S_{vv} and S_{hh} are totally correlated, then the determinant of the covariance matrix given in Appendix 8 becomes zero and $f(\phi_c)$ becomes a delta function. For the general case, we can rewrite eqn. 36 in the form

$$f(\phi_c) = \frac{1 - \alpha^2}{2\pi[1 - \alpha^2 \cos^2(\phi - \zeta)]}$$

$$\times \left\{ 1 + \frac{a \cos(\phi - \zeta)}{\sqrt{[1 - \alpha^2 \cos^2(\phi - \zeta)]}} \right.$$

$$\left. \times \left[\frac{\pi}{2} + \tan^{-1} \frac{\alpha \cos(\phi - \zeta)}{\sqrt{[1 - \alpha^2 \cos^2(\phi - \zeta)]}} \right] \right\} \tag{40}$$

where

$$\alpha = \sqrt{\left(\frac{\lambda_{13}^2 + \lambda_{14}^2}{\lambda_{11} \lambda_{33}} \right)} \tag{41}$$

$$\zeta = \tan^{-1} \frac{\lambda_{14}}{\lambda_{13}} \tag{42}$$

The parameter α, referred to as the degree of correlation [8], is a measure of the width of the PDF, and the parameter ζ is the value of ϕ_c at which $f(\phi_c)$ is a maximum. Fig. 6a shows plots of $f(\phi_c)$ for different values of ζ, with α held constant, and Fig. 6b shows plots of $f(\phi_c)$ for various values of α with ζ held constant. These two parameters completely specify $f(\phi_c)$.

3.3 The Mueller matrix

The Mueller matrix of a distributed target for which S_{hv} is uncorrelated with S_{vv} and S_{hh} contains only eight nonzero elements

$$M = \begin{bmatrix} M_{11} & M_{12} & 0 & 0 \\ M_{21} & M_{22} & 0 & 0 \\ 0 & 0 & M_{33} & M_{34} \\ 0 & 0 & M_{43} & M_{M44} \end{bmatrix} \tag{43}$$

with four of them given by:

$$M_{11} = \langle |S_{vv}|^2 \rangle \tag{44}$$

$$M_{22} = \langle |S_{hh}| \rangle^2 \tag{45}$$

$$M_{12} = M_{21} = \langle |S_{hv}|^2 \rangle \tag{46}$$

Using eqns. 41 and 42 and the relations given in Appendix 8, the other four elements of M, which are defined in eqn. 25, can be expressed in terms of the three principal magnitudes given by eqns. 44–46 and the parameters α

and ζ

$$M_{33} = \alpha \cos \zeta \sqrt{(M_{11} M_{22})} + M_{12} \tag{47}$$

$$M_{44} = \alpha \cos \zeta \sqrt{(M_{11} M_{22})} - M_{12} \tag{48}$$

$$M_{34} = \alpha \sin \zeta \sqrt{(M_{11} M_{22})} \tag{49}$$

$$M_{43} = -\alpha \sin \zeta \sqrt{(M_{11} M_{22})} \tag{50}$$
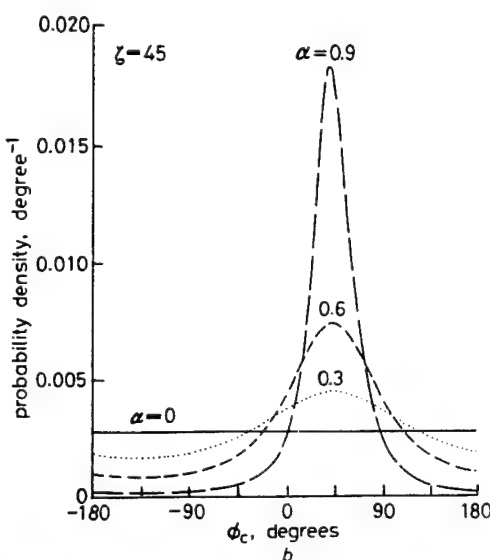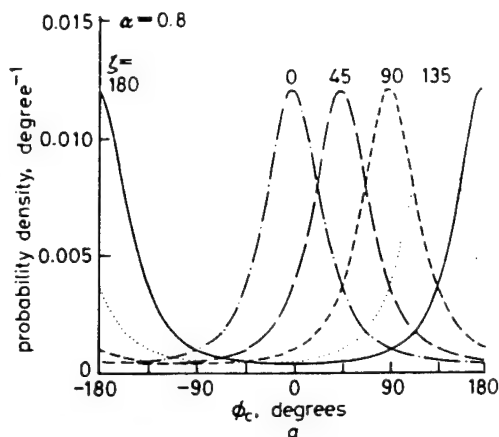
Fig. 6 Plots of $f(\phi_c)$
a various values of ζ at $\alpha = 0.8$
b various values of α at $\zeta = 45°$

3.4 Degree of polarisation

For a statistically homogeneous distributed target characterised by a Mueller matrix M, illuminated by a modified Stokes vector $F^i = [I_{vi} I_{hi} U_i V_i]^T$ and resulting in a backscattered modified Stokes vector $F^s = [I_{vs} I_{hs} U_s V_s]^T$, in accordance with eqn. 24, the degree of polarisation of the backscattered wave is given by

$$m = \left[\frac{(I_{vs} - I_{hs})^2 + U_s^2 + V_s^2}{(I_{vs} + I_{hs})^2} \right]^{1/2} \tag{51}$$

As was noted earlier in Section 3.2, most natural targets exhibit the property that the crosspolarised scattering amplitude S_{hv} is uncorrelated with the co-polarised scattering amplitudes S_{vv} and S_{hh}, which leads to the result that eight of the elements of M are zero, as shown by eqn. 43. For this class of targets, m is given by

$$m = \left[\frac{\begin{array}{c} a_1 I_{vi}^2 + a_2 I_{hi}^2 + a_3 U_i^2 + a_4 V_i^2 \\ + a_5 I_{hi} I_{vi} + a_6 U_i V_i \end{array}}{b_1 I_{vi}^2 + b_2 I_{hi}^2 + b_3 I_{vi} I_{hi}} \right]^{1/2} \tag{52}$$

where

$$a_1 = (M_{11} - M_{12})^2$$

$$a_2 = (M_{22} - M_{12})^2$$

$$a_3 = M_{33}^2 + M_{43}^2$$

$$a_4 = M_{34}^2 + M_{44}^2$$

$$a_5 = 2(M_{11} - M_{12})(M_{12} - M_{22})$$

$$a_6 = 2(M_{33} M_{34} + M_{43} M_{44})$$

$$b_1 = (M_{11} + M_{12})^2$$

$$b_2 = (M_{12} + M_{22})^2$$

$$b_3 = 2(M_{11} + M_{12})(M_{12} + M_{22})$$

Expressions for the non-zero elements of the Mueller matrix are given in Section 3.3 in terms of the magnitudes and phase parameters. Using the definition $\sigma_{ij}^\circ = (4\pi/A)\langle|S_{ij}|^2\rangle$ for the backscattering coefficient, we will now consider eqn. 52 for specific incident polarisations.

3.4.1 Vertical polarisation:
$$F_v^i = [1 \quad 0 \quad 0 \quad 0]^T$$

$$m_v = \sqrt{\left(\frac{a_1}{b_1}\right)} = \frac{M_{11} - M_{12}}{M_{11} + M_{12}} = \frac{\sigma_{vv}^\circ - \sigma_{vh}^\circ}{\sigma_{vv}^\circ + \sigma_{vh}^\circ} \quad (53)$$

3.4.2 Horizontal polarisation:
$$F_h^i = [0 \quad 1 \quad 0 \quad 0]^T$$

$$m_h = \sqrt{\left(\frac{a_2}{b_2}\right)} = \frac{M_{22} - M_{12}}{M_{22} + M_{12}} = \frac{\sigma_{hh}^\circ - \sigma_{vh}^\circ}{\sigma_{hh}^\circ + \sigma_{vh}^\circ} \quad (54)$$

3.4.3 Other polarisations:
The following expressions apply to four different configurations of the polarisation state of the incident wave, in accordance with the following definitions of the coefficients a–c:

	a	b	c
45° linear	1	0	1
135° linear	−1	0	1
Right-hand circular	0	−1	−1
Left-hand circular	0	1	−1

$$F^i = \begin{bmatrix} \frac{1}{2} & \frac{1}{2} & a & b \end{bmatrix}$$

$$m = \left[\frac{(M_{11} - M_{22})^2 + 4[M_{12}^2 + M_{11} M_{22} \alpha^2 + 2cM_{12}\alpha \cos\zeta\sqrt{(M_{11}M_{22})}]}{(M_{11} + M_{22} + 2M_{12})^2} \right]^{1/2}$$

$$= \left[\frac{(\sigma_{vv}^\circ - \sigma_{hh}^\circ)^2 + 4[\sigma_{hv}^{\circ 2} + \sigma_{vv}^\circ \sigma_{hh}^\circ \alpha^2 + 2c\sigma_{hv}^\circ\alpha \cos\zeta\sqrt{(\sigma_{vv}^\circ \sigma_{hh}^\circ)}]}{(\sigma_{vv}^\circ + \sigma_{hh}^\circ + 2\sigma_{hv}^\circ)^2} \right]^{1/2} \quad (55)$$

According to the above expression, $m(45°) = m(135°)$ and $m(\text{RHC}) = m(\text{LHC})$.

4 Experimental observations of phase-difference statistics

The preceding section established that for random media for which the like- and crosspolarised scattering amplitudes are statistically uncorrelated, the Mueller matrix of the medium is completely specified by the three principal magnitudes, represented by the backscattering coefficients σ_{vv}°, σ_{hh}°, and σ_{vh}°, and two parameters, α and ζ, that characterise the probability density function of the co-polarised phase difference ϕ_c. The literature contains many examples, based on both theory and experimental

observations, illustrating the relationships between the backscattering coefficients and the physical and dielectric properties of the target, but very few examples have been published on the behaviour of ϕ_c. In this section, we shall present examples of experimental measurements for a bare soil surface, a corn canopy, and small trees.

4.1 Bare-soil surface

Using a truck-mounted polarimetric scatterometer, backscatter measurements were conducted for four bare-soil fields with different surface roughnesses covering a 10 : 1 range in RMS height (0.32 cm to 3.2 cm). Each field was observed at 1.5, 4.75, and 9.5 GHz at multiple incidence angles extending from 20° to 70°, in 10° steps. A histogram of $f(\phi_c)$ for one of the fields was presented earlier in Fig. 4a. Whereas both the mean and standard deviation of ϕ_c, $\bar{\phi}_c$ and σ_{ϕ_c}, respectively, exhibit variations with surface roughness, incidence angle, and wavelength, the variations of $\bar{\phi}_c$ were relatively small in comparison with the variations observed for σ_{ϕ_c}. By way of example, we show in Fig. 7a plots of σ_{ϕ_c} as a function of incidence
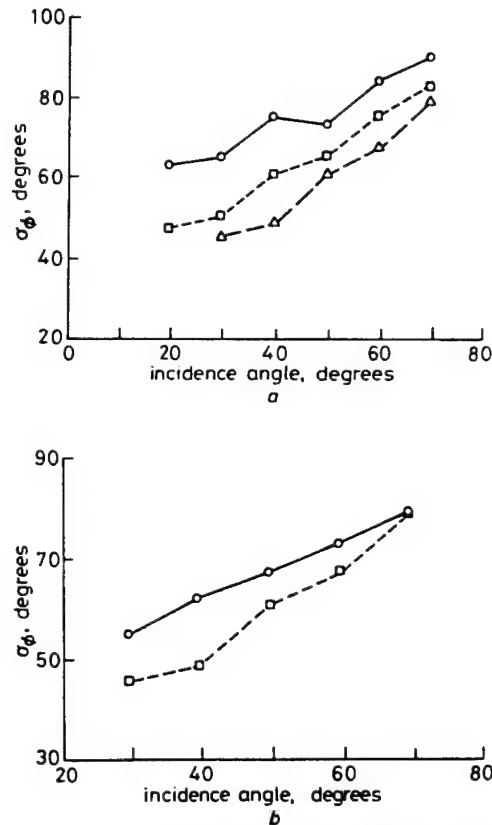
Fig. 7 *Standard deviation of the co-polarised phase angle as a function of incidence angle*

a a slightly rough field at three microwave frequencies
   rms height = 0.32 cm
   —○— 9.50 GHz
   --□-- 4.75 GHz
   —△— 1.50 GHz
b for two fields with very different surface roughnesses at 1.5 GHz
   f = 1.5 GHz
   —○— rms height = 0.32 cm
   --□-- rms height = 3.02 cm

angle for a smooth surface at three frequencies, and plots for two different surface roughnesses at 1.5 GHz in Fig. 7b. The standard deviation σ_{ϕ_c}, or equivalently the parameter α defined by eqn. 42, is a measure of the degree of correlation between the co-polarised components of the scattering matrix. For the case of total correlation

between S_{vv} and S_{hh}, $\sigma_{\phi_c} = 0$ and $\alpha = 1$, and for the opposite extreme of total uncorrelation, $\sigma_{\phi_c} = 104°$ and $\alpha = 0$. The results in Fig. 7 suggest that the degree of correlation decreases with increasing incidence angle and with increasing electromagnetic roughness $ks = 2\pi s/\lambda$, where s is the RMS height.

4.2 Corn canopy

Whereas $f(\phi_c)$ corresponding to a surface usually has a mean $\bar{\phi}_c$ that rarely exceeds 40°, $\bar{\phi}_c$ may be much larger for certain types of vegetation. A specific example is vegetation canopies comprised of plants with vertical stalks or trees with vertical trunks. Fig. 8 shows plots of $f(\phi_c)$
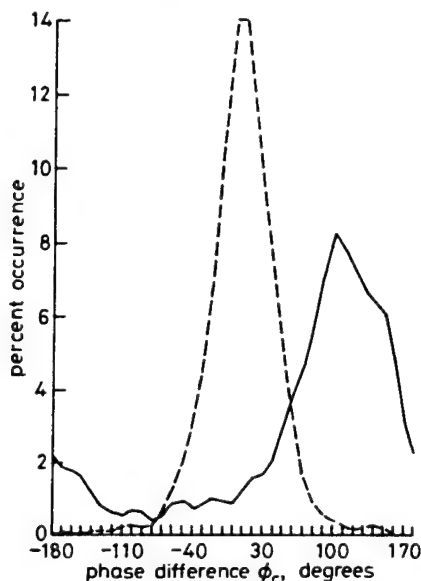
Fig. 8 *Measured co-polarised phase angle distributions for two corn fields observed by a 1.2 GHz polarimetric SAR at incidence angles of 19° and 50°*

——— Field 50 (corn)	- - - - Field 19 (corn)
theta = 50 degrees	theta = 19 degrees
N = 705	N = 523
Median = 110.5	Median = 8.4
Mean = 109.5	Mean = 9.0
Sigma = 63.4	Sigma = 35.5

for two fields of corn observed by a 1.2-GHz polarimetric SAR system that was flown over an agricultural area near McComb, Illinois. The swath width of the airborne SAR system covered an incidence-angle range extending from 15° to 55°. One of the fields represented in Fig. 8 was observed at an incidence angle of 19°, and the other at 50°. The mean values of ϕ_c are $\bar{\phi}_c = 9°$ for the first one and $\bar{\phi}_c = 109.5°$ for the second one. Similar distributions were extracted from the image for about 75 fields of corn. Fig. 9 shows the measured values of $\bar{\phi}_c$ for the corn fields, plotted against the incidence angle at which they were observed by the SAR. The solid curve, which provides a reasonable fit to the data, is based on direct calculations using the Michigan microwave canopy scattering model (MIMICS), which is a vector radiative transfer model for scattering from a vegetation canopy containing a trunk layer [3, 6]. The phase difference $\bar{\phi}_c$ includes the effects of propagation through a canopy containing vertical cylinders, reflection by the vertical cylinders, and reflection by the underlying ground surface. Each of these mechanisms introduces a polarisation-dependent phase shift. Through MIMICS, we can relate the mean co-polarised phase angle $\bar{\phi}_c$ to the biophysical parameters of the vegetation canopy. This is illustrated in Fig. 10 which shows a three-dimensional plot of $\bar{\phi}_c$ as a function of soil moisture content and stalk moisture content for a corn canopy

observed at 1.2 GHz. We note that $\bar{\phi}_c$ appears to be essentially insensitive to soil moisture, but very sensitive to stalk moisture content. The vv-polarised backscattering coefficient, on the other hand, exhibits a strong
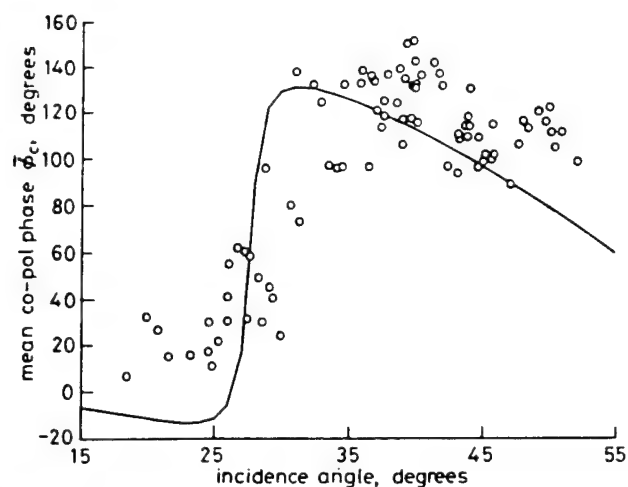
Fig. 9 *Measured and calculated mean co-polarised phase angle for corn fields observed by a 1.2 GHz SAR system*

O   Measured from SAR image
——— Calculated (MIMICS)
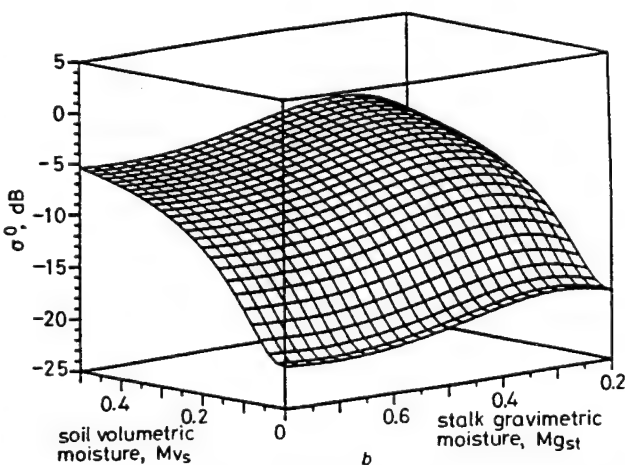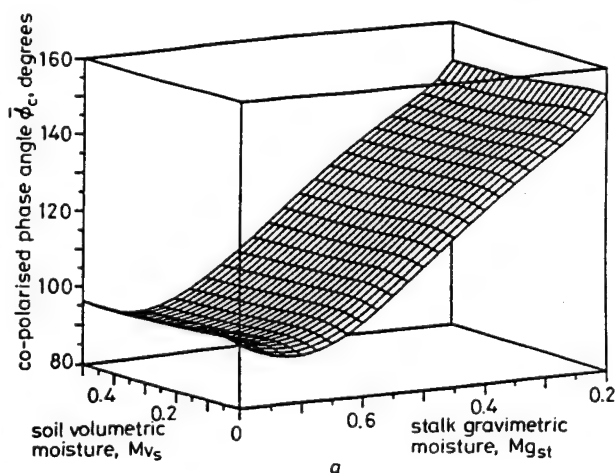
Fig. 10 *Variations*

a mean co-polarised phase angle
b vv-polarised backscattering coefficient with soil moisture content and stalk gravimetric moisture for a canopy of corn plants observed at 1.2 GHz at an incidence angle of 30°

dependence on soil moisture and only a weak dependence on trunk moisture. The combination of σ_{vv}^0 and $\bar{\phi}_c$ can provide good estimates of both of these two physical properties of the corn canopy.

4.3 Small trees
A 35-GHz polarimetric scatterometer was used in an indoor facility to measure the backscatter from small trees. Fig. 11 compares the measured PDF of ϕ_c for a
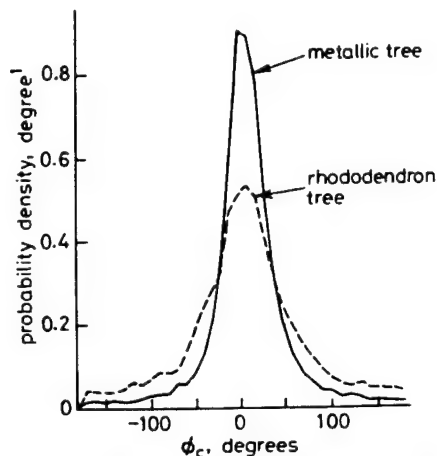

Fig. 11 *Measured $f(\phi_c)$ for a rhododendron tree and an artificial metallic tree at 35 GHz*

rhododendron tree, approximately 1 m in height, when observed along the broadside direction, with similar measurements for an artificial tree with metallic branches. This was part of a study to examine the variation of $f(\phi_c)$ with the dielectric properties of trees. The PDF of the metallic tree is much narrower than that of the rhododendron tree, with $\alpha = 0.89$ for the metallic tree, compared to $\alpha = 0.66$ for the real tree. Another example from the same study is presented in Fig. 12 in
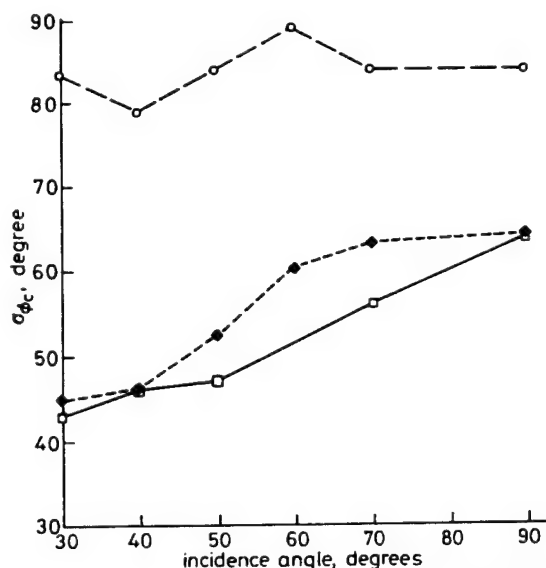
Fig. 12 *Measured standard deviation of co-polarised phase difference at 35 GHz for three types of tress*

—□— Rhododendron
-- ◆ -- Spirea
—○— Spruce

which plots are shown for the standard deviation σ_{ϕ_c} as a function of incidence angle (with $\theta = 90°$ representing the broadside direction) for three types of small trees. We note that the spirea tree exhibits a distinctly different

response from the rhododendron and spruce trees, which is attributed to the fact that the spirea tree is much denser than the other two.

At present, we are still in the early stage of developing an understanding of scattering by inhomogeneous media, particularly with regard to the statistics of the co-pol phase angle ϕ_c. The examples given in this section were merely intended to suggest that the mean value and standard deviation of ϕ_c, or alternatively the parameters α and ζ, may prove useful in providing information about the target over and beyond that provided by the backscattering coefficients alone. Hence, it is important to start examining the relationships between the statistical parameters of ϕ_c and the physical and dielectric properties of terrain through both theory and experimental observations.

5 Concluding remarks

The co-polarised phase angle ϕ_c is shown to be both sensor- and target-dependent. Its statistical properties vary with wavelength and incidence angle, surface roughness, type of vegetation cover, and vegetation geometry and biophysical properties. Further examination of the relationship between ϕ_c and the geometrical and dielectric properties of distributed targets, through both theoretical analyses and experimental observations, may lead to the development of novel tools for remotely sensing the Earth's surface with polarimetric radar systems.

6 Acknowledgment

7 References

1 ULABY, F.T., and ELACHI, C.: 'Radar polarimetry for geoscience applications' (Artech House, 1990)
2 VAN ZYL, J.J., ZEBKER, H.A., and ELACHI, C.: 'Imaging radar polarization signatures' theory and observation', *Radio Sci.*, 1987, **22**, pp. 529–543
3 ULABY, F.T., SARABANDI, K., McDONALD, K., WHITT, M., and DOBSON, C.: 'Michigan microwave canopy scattering model', *Int. J. Remote Sens.*, 1990, **11**, pp. 1223–1263
4 BORGEAUD, M., NGHIEM, S.V., SHIN, R.T., and KONG, J.A. 'Theoretical models for polarimetric microwave remote sensing of Earth terrain', *J. Electromagn. Waves and Appl.*, 1989, **3**, pp. 61–81
5 TSANG, L., and DING, K.H.: 'Polarimetric signatures of a layer of random nonspherical discrete scatters overlying a homogeneous half-space based on first- and second-order vector radiative transfer theory', *IEEE Trans.*, 1991, **GE-29**, pp. 242–253
6 McDONALD, K.C., DOBSON, M.C., and ULABY, F.T.: Using MIMICS to model L-band multiangle and multitemporal backscatter from a walnut orchard', *IEEE Trans.*, 1990, **GE-28**, pp. 477–491
7 ULABY, F.T., and DOBSON, M.C.: 'Handbook of radar scattering statistics for terrain' (Artech House, 1989)
8 SARABANDI, K.: 'Derivation of phase statistics of distributed targets from the averaged Mueller matrix'. Technical report 026511-T, 1991, Radiation laboratory, University of Michigan. Also accepted for publication in *Radio Science*
9 MEAD, J.B.: 'Polarimetric measurements of foliage and terrain at 225 GHz'. Ph.D. Thesis, Univ. of Mass., 1989
10 KUGA, Y., SARABANDI, K., NASHASHIBI, A., ULABY, F.T., and AUSTIN, R.T.: 'Millimeter wave polarimetric scatterometer systems: measurement and calibration techniques'. AGARD '91, 1991
11 ULABY, F.T., WHITT, M.W., and SARABANDI, K.: 'AVNA-based polarimetric scatterometers', *IEEE Antennas Propag. Mag.*, 1990, **32**, (5), pp. 6–17
12 SINCLAIR, G.: 'The transmission and reception of elliptically polarized waves', *Proc. IRE*, 1950, **38**, pp. 148–151
13 KENNAUGH, E.M.: 'Effects of the type of polarization on echo characteristcs'. Report 389–9, Antenna Laboratory, 1951, Ohio State University

8 Appendices

8.1 Probability density functions for co-pol and crosspol phase differences

8.1.1 Co-pol phase angle $\phi_c = \phi_{hh} - \phi_{vv}$:

Let us define the complex scattering amplitudes S_{vv} and S_{hh} in terms of the real quantities $x_1, \ldots, x_4$

$$S_{vv} = |S_{vv}|e^{i\phi_{vv}} = x_1 + ix_2 \tag{56}$$

$$S_{hh} = |S_{hh}|e^{i\phi_{hh}} = x_3 + ix_4 \tag{57}$$

where

$$x_1 = |S_{vv}|\cos\phi_{vv} = \rho_1\cos\phi_{vv} \tag{58}$$

$$x_2 = |S_{vv}|\sin\phi_{vv} = \rho_1\sin\phi_{vv} \tag{59}$$

$$x_3 = |S_{hh}|\cos\phi_{hh} = \rho_2\cos\phi_{hh} \tag{60}$$

$$x_4 = |S_{hh}|\sin\phi_{hh} = \rho_2\sin\phi_{hh} \tag{61}$$

with $\rho_1 \triangleq |S_{vv}|$ and $\rho_2 \triangleq |S_{hh}|$. Since $x_1, \ldots, x_4$ are each zero-mean Gaussian random variables, their joint PDF is given by

$$f_{\boldsymbol{X}}(x_1, \ldots, x_4) = \frac{1}{4\pi^2|\Lambda|^{1/2}}\exp\left[-\tfrac{1}{2}\tilde{X}\Lambda^{-1}X\right] \tag{62}$$

where X is the column vector

$$X = \begin{bmatrix} x_1 \\ x_2 \\ x_3 \\ x_4 \end{bmatrix} \tag{63}$$

with transpose $\tilde{X}$, and Λ is a 4×4 covariance matrix with elements

$$\lambda_{ij} = \lambda_{ji} = \langle x_i x_j \rangle, \quad i, j \in \{1, \ldots, 4\} \tag{64}$$

As was noted in Section 3.1, the real and imaginary parts of S_{vv}, x_1 and x_2, are mutually independent and identically distributed zero-mean random variables, and a similar statement applies to x_3 and x_4. Hence,

$$\lambda_{11} = \lambda_{22} = \langle x_1^2 \rangle = \langle x_2^2 \rangle = \tfrac{1}{2}\langle |S_{vv}|^2 \rangle = \frac{M_{11}}{2} \tag{65}$$

$$\lambda_{12} = \lambda_{21} = \langle x_1 x_2 \rangle = 0 \tag{66}$$

$$\lambda_{33} = \lambda_{44} = \langle x_3^2 \rangle = \langle x_4^2 \rangle = \tfrac{1}{2}\langle |S_{hh}|^2 \rangle = \frac{M_{22}}{2} \tag{67}$$

$$\lambda_{34} = \lambda_{43} = \langle x_3 x_4 \rangle = 0 \tag{68}$$

where M_{ij} is the ijth element of the Mueller matrix, as defined by eqn. 25. To characterise the remaining elements of the covariance matrix, we note that the absolute phase ϕ_{pp} is uniformly distributed over $[-\pi, \pi]$ and is independent of the magnitude $|S_{pp}|$. Hence, the random variable $(\phi_{vv} + \phi_{hh})$ is also uniformly distributed over $[-\pi, \pi]$ and is independent of $|S_{vv}\,\|\,S_{hh}|$, from which we conclude that

$$\langle |S_{vv}\,\|\,S_{hh}|\cos(\phi_{vv} + \phi_{hh})\rangle = 0 \tag{69}$$

$$\langle |S_{vv}\,\|\,S_{hh}|\sin(\phi_{vv} + \phi_{hh})\rangle = 0 \tag{70}$$

From the definitions given by eqns. 58–61, and in view of eqns. 69 and 70, we obtain the results

$$\langle x_1 x_3 - x_2 x_4 \rangle = \langle |S_{vv}\,\|\,S_{hh}|\cos(\phi_{vv} + \phi_{hh})\rangle = 0 \tag{71}$$

$$\langle x_1 x_4 + x_2 x_3 \rangle = \langle |S_{vv}\,\|\,S_{hh}|\sin(\phi_{vv} + \phi_{hh})\rangle = 0 \tag{72}$$

which, in turn, lead to the relations

$$\lambda_{13} = \lambda_{24} \tag{73}$$

$$\lambda_{14} = -\lambda_{23} \tag{74}$$

From the definitions for the elements M_{33} and M_{44} of the Mueller matrix given by eqn. 25, their sum is given by

$$\begin{aligned}
M_{33} + M_{44} &= 2\langle \mathrm{Re}\,(S_{vv}S_{hh}^*)\rangle \\
&= 2\langle |S_{vv}\,\|\,S_{hh}|\cos(\phi_{vv} - \phi_{hh})\rangle \\
&= 2\langle |S_{vv}\,\|\,S_{hh}|\cos\phi_{vv}\cos\phi_{hh}\rangle \\
&\quad + 2\langle |S_{vv}\,\|\,S_{hh}|\sin\phi_{vv}\sin\phi_{hh}\rangle \\
&= 2\lambda_{13} + 2\lambda_{24} \\
&= 4\lambda_{13}
\end{aligned} \tag{75}$$

where use was made of eqn. 73. Hence,

$$\lambda_{13} = \lambda_{31} = \frac{M_{33} + M_{44}}{4} \tag{76}$$

We can similarly show that

$$\lambda_{14} = \lambda_{41} = -\lambda_{23} = -\lambda_{32} = \frac{M_{34} - M_{43}}{4} \tag{77}$$

Upon combining these relations between the elements of the covariance matrix and the elements of the Mueller matrix, we have

$$\Lambda = \frac{1}{4}\begin{bmatrix} 2M_{11} & 0 & (M_{33}+M_{44}) & (M_{34}-M_{43}) \\ 0 & 2M_{11} & (M_{43}-M_{34}) & (M_{33}+M_{44}) \\ (M_{33}+M_{44}) & (M_{43}-M_{34}) & 2M_{22} & 0 \\ (M_{34}-M_{43}) & (M_{33}+M_{44}) & 0 & 2M_{22} \end{bmatrix} \tag{78}$$

With Λ known, let us now return to the joint density function of X given by eqn. (62) and use the rectangular to polar transformations given by eqns. 58–61 to obtain a joint density function for the magnitudes ρ_1 and ρ_2 and the phase angles ϕ_{vv} and ϕ_{hh}

$$f_{\rho_1, \rho_2, \Phi_{vv}, \Phi_{hh}}(\rho_1, \rho_2, \phi_{vv}, \phi_{hh})$$

$$= \frac{1}{4\pi^2\sqrt{(\Delta)}}\rho_1\rho_2\exp\left\{-\tfrac{1}{2}[a_1\rho_1^2 + a_2\rho_2^2 - 2a_3\rho_1\rho_2]\right\} \tag{79}$$

where

$$\Delta = |\Lambda| = (\lambda_{11}\lambda_{33} - \lambda_{13}^2 - \lambda_{14}^2)^2$$

$$a_1 = \lambda_{33}/\sqrt{\Delta}$$

$$a_2 = \lambda_{11}/\sqrt{\Delta}$$

$$a_3 = [\lambda_{13}\cos(\phi_{hh} - \phi_{vv}) + \lambda_{14}\sin(\phi_{hh} - \phi_{vv})]/\sqrt{\Delta}$$

To obtain the PDF of the co-polarised phase difference $\phi_c = \phi_{hh} - \phi_{vv}$, we first need to obtain the joint PDF of ϕ_{vv} and ϕ_{hh} from

$$f_{\Phi_{vv}, \Phi_{hh}}(\phi_{vv}, \phi_{hh})$$

$$= \int_0^\infty \int_0^\infty f_{\rho_1, \rho_2, \Phi_{vv}, \Phi_{hh}}(\rho_1, \rho_2, \phi_{vv}, \phi_{hh})\,d\rho_1\,d\rho_2 \tag{80}$$

and after carrying out the integrations with respect to ρ_1 and ρ_2, we use a transformation to obtain $f(\phi_c)$. This

process, which is detailed in Reference 8, leads to

$$f(\phi_c) = \frac{\lambda_{11}\lambda_{33} - \lambda_{13}^2 - \lambda_{14}^2}{2\pi(\lambda_{11}\lambda_{33} - D^2)} \left\{ 1 + \frac{D}{\sqrt{(\lambda_{11}\lambda_{33} - D^2)}} \right.$$
$$\left. \times \left[\frac{\pi}{2} + \tan^{-1}\frac{D}{\sqrt{(\lambda_{11}\lambda_{33} - D^2)}} \right] \right\} \qquad (81)$$

where

$$D = \lambda_{13}\cos\phi_c + \lambda_{14}\sin\phi_c \qquad (82)$$

The PDF given by eqn. 81 is completely specified by the elements of the covariance matrix Λ given by eqn. 72, all of which have been related to the elements of the Mueller matrix M.

8.1.2 Cross-Pol phase angle $\phi_x = \phi_{hv} - \phi_{vv}$: The PDF for the cross-polarised phase angle ϕ_x can be obtained by following the same steps outlined in the preceding section for the co-polarised phase angle ϕ_c. If we define

$$S_{hv} = x_5 + ix_6 \qquad (83)$$

and then repeat the steps of eqns. 58–81 with x_3 and x_4 replaced with x_5 and x_6, respectively, we obtain the PDF

$$f(\phi_x) = \frac{\lambda_{11}\lambda_{55} - \lambda_{15}^2 - \lambda_{16}^2}{2\pi(\lambda_{11}\lambda_{55} - D_1^2)} \left\{ 1 + \frac{D_1}{\sqrt{(\lambda_{11}\lambda_{55} - D_1^2)}} \right.$$
$$\left. \times \left[\frac{\pi}{2} + \tan^{-1}\frac{D_1}{\sqrt{(\lambda_{11}\lambda_{55} - D_1^2)}} \right] \right\} \qquad (84)$$

with

$$D_1 = \lambda_{15}\cos\phi_x + \lambda_{16}\sin\phi_x \qquad (85)$$

and the elements λ_{11}, λ_{55}, λ_{15}, λ_{16} being related to the elements of the Mueller matrix by

$$\lambda_{11} = \frac{M_{11}}{2}, \quad \lambda_{55} = \frac{M_{12}}{2} \qquad (86)$$

$$\lambda_{15} = \frac{M_{13}}{2}, \quad \lambda_{16} = \frac{M_{14}}{2} \qquad (87)$$

Numerical Evaluation of the Two-Dimensional Quasi-Crystalline Approximation

Paul R. Siqueira and Kamal Sarabandi
Radiation Laboratory
Electrical Engineering and Computer Science Department
University of Michigan, Ann Arbor, MI 48109-2122

Abstract

The purpose of this paper is to characterize the accuracy of the quasi-crystalline approximation and other associated methods of determining effective permittivity for two-dimensional random media. A numerical method based on the method of moments is used as a gauge for comparison with the theoretical methods. After deriving the two-dimensional quasi-crystalline approximation and presenting the numerical method, the behavior of the effective permittivity is analyzed for a range of particle sizes, volume fractions and dielectric losses. From this analysis, regions of validity for the theoretical methods are determined. An investigation is also given which explores the effect of particle arrangement methods on the pair distribution function which in turn is shown to have a significant effect on the imaginary component of the effective permittivity.

1 Introduction

In remote sensing, the propagation of electromagnetic fields through random media is often of concern. We may wish to characterize the effects of clouds or water droplets along the line of sight between an airplane and a radar installation or we may be interested in using radars to probe the random medium itself, such as in determining snow depth and particle size. In all of these problems it is necessary to predict the propagation constant in the "random" medium. When the observing wavelength is much larger than a typical dimension of the inhomogeneities making up the medium, no significant scattering occurs and we can generally approximate the medium as being electrically homogeneous. Methods which utilize this approximation are termed mixing formulae, formulae that determine the constant of propagation by combining the effect of small scale inhomogeneities through a simple algebraic equation. The most common of these formulae is the Polder-Van Santen mixing formula (PVS) [1956]. When the

1

observing wavelength and the inhomogeneities are similar in size, we must take into account scattering from individual inhomogeneities. This is typically done using a field approach based on Maxwell's equations, the most common of which are the effective field approximation (EFA, also known as Foldy's approximation) for low density media and the quasi-crystalline approximation (QCA) or the quasi-crystalline approximation with coherent potential (QCA-CP) for higher density media.

All of the aforementioned theoretical methods for determining the effective propagation constant make approximations in their formulation to make the theory tractable. As the theory becomes more complex, it becomes more difficult to test the region of validity of these approximations and to test the effects of the approximation employed in the method. The validity of these models may be checked in one of three ways: (1) theoretically, (2) experimentally or (3) numerically.

The field approaches may be checked via theoretical methods by taking the limiting case of the approach and comparing it to more standard, well accepted theoretical results. Common limiting cases use either zero or unity volume fraction or examine the problem in the low or high frequency limits. While these limiting cases perform the important task of giving a shortcut to provide a sanity check for a more complicated theory, they may often zero-out important terms in the field approach theory. Thus instead of testing the new theory, we find ourselves simply checking that the coefficients for zero or first order terms have been derived correctly.

The second method of checking the theories is to back them up with experiments. This can be the true test of any theory because it is the measurement in the end for which the theory is to be applied. Experiments, however, must be designed carefully so as to minimize experimental errors and to accurately characterize physical parameters about the random medium. For the application of the QCA and QCA-CP it is necessary to determine the pair distribution function of particle positions, a function that is very difficult to measure experimentally.

Alternatively, the pair distribution function can be specified beforehand and particle positions in a controlled experiment can be determined by a computer as was done by Mandt et al. [1992]. Finally, an experiment may be difficult and time consuming to perform over a controlled range of variables (such as volume fraction and particle size). For this reason, while an experiment may be used to test validity of a theory for a particular application, it is much more difficult to make generalizations based on this experiment.

The third method of analyzing theoretical field approaches of determining the constant of propagation is to do so numerically. This method removes the need for theoretical simplification or the problem of experimental uncertainty by solving for the electromagnetic fields directly. Numerical methods may be difficult to implement due to computational limitations or our inability to model the problem accurately. Because of the complexities of solving three-dimensional problems numerically, we have developed a method for determining the effective permittivity of a random medium in two dimensions which may be used as a tool to explore two-dimensional versions of the field theories and to provide guidance for the three-dimensional problem.

This paper addresses the two-dimensional quasi-crystalline approximation and its dependence on the pair distribution function. Section two of this paper presents a derivation of 2D-QCA based on the three-dimensional version found in Tsang et al. [1986] and gives the related results of two-dimensional EFA. Section three discusses different methods of obtaining particle arrangements and their associated pair distribution function. In the fourth section, we review a method for numerically determining the effective permittivity of a two-dimensional random medium [Sarabandi and Siqueira, 1995] and present two-dimensional theoretical results for the Polder-Van Santen mixing formula. In the fifth section of this paper, we compare the results of our numerical analysis with that of QCA.

2 Two-Dimensional Quasi-Crystalline Approximation

The two-dimensional derivation of QCA follows closely the work of Tsang et al. [1986]. where we begin with the multiple scattering equation for plane wave incidence using the T-matrix approach. Consider N cylinders. whose centers are denoted by $\bar{r}_l$ ($l = 1, \ldots, N$). randomly distributed over an area A. Expanding the fields in terms of cylindrical basis functions, it can be shown that [Tsang, 1986; pg. 454]

$$\overline{w}^{(l)} = \sum_{\substack{j=1 \\ j \neq l}}^{N} \overline{\overline{\sigma}}(k_0\overline{r_l r_j})\overline{\overline{T}}^{(j)}\overline{w}^{(j)} + e^{i\overline{k}_i \cdot \overline{r}_l}\overline{a}_{\text{inc}} \tag{1}$$

where $\overline{w}^{(l)}$ is the vector of exciting field coefficients for the lth particle, $\overline{a}_{\text{inc}}$ is the vector of coefficients for the incident field, $\overline{\overline{\sigma}}(k_0\overline{r_l r_j})$ is the translation matrix from a coordinate system centered on the jth particle to one centered on the lth particle, and $\overline{\overline{T}}^{(j)}$ is the transition matrix which translates the exciting field of the jth particle into the scattered field from the jth particle. The basis functions for the field expansions are the cylindrical functions [Chew, Wang, and Gurel, 1992]

$$\psi_n = \mathrm{H}_n^{(1)}(k_0\overline{r}_>)e^{in\phi} \tag{2}$$

$$\mathrm{Rg}\psi_n = \mathrm{J}_n(k_0\overline{r}_<)e^{in\phi} \tag{3}$$

where

$$\overline{r}_> = \text{larger}(\overline{r}, \overline{r}') \tag{4}$$

$$\overline{r}_< = \text{lesser}(\overline{r}, \overline{r}') \tag{5}$$

when $\overline{r}$ is the point of observation and $\overline{r}'$ is the source point. The incident field

$$\Phi_{\text{inc}}(\overline{r}) = \sum_{n=0}^{\infty} \overline{a}_{\text{inc}}\mathrm{Rg}\psi_n(k\overline{r}) \tag{6}$$

4

may represent either E_z (TM-polarization) or H_z (TE-polarization). By determining the expected value of (1) with respect to the lth particle, we arrive at

$$E_l\left[\overline{w}^{(l)}\right] = \sum_{\substack{j=1 \\ j \neq l}}^{N} E_l\left[\overline{\overline{\sigma}}(k_0\overline{r_l r_j})\overline{\overline{T}}^{(j)} E_{jl}\left[\overline{w}^{(j)}\right]\right] + e^{i\overline{k}_i \cdot \overline{r}_l}\overline{a}_{\text{inc}}. \qquad (7)$$

Under the conditions that the number of particles are large and particle density is not very high, we make the approximation fundamental to QCA that

$$E_{jl}\left[\overline{w}^{(j)}\right] \approx E_j\left[\overline{w}^{(j)}\right] = \overline{w}(\overline{r}_j) \qquad (8)$$

whereby, (7) becomes

$$\overline{w}(\overline{r}_l) = (N-1)\int_A \overline{\overline{\sigma}}(k_0\overline{r_l r_j})\overline{\overline{T}}^{(j)}\overline{w}(\overline{r}_j)p(\overline{r}_j|\overline{r}_l)\,d\overline{r}_j + e^{i\overline{k}_i \cdot \overline{r}_l}\overline{a}_{\text{inc}}. \qquad (9)$$

If we normalize the conditional probability $p(\overline{r}_j|\overline{r}_l)$ to the area, A, we have the pair distribution function, $g(\overline{r})$ such that

$$p(\overline{r}_j|\overline{r}_l) = \frac{1}{A}g(\overline{r}_j|\overline{r}_l) \qquad (10)$$

which has the asymptotic property of approaching unity when $\overline{r}_j - \overline{r}_l$ is large. For a large system of particles, the fraction $\frac{N-1}{A}$ is approximately the particle density, n_0. Letting A be the positive half-space $x_j > 0$ [Tsang, 1986; pg. 491]

$$\overline{w}(\overline{r}_l) = n_0 \int_{x_j>0} g(\overline{r}_j|\overline{r}_l)\overline{\overline{\sigma}}(k_0\overline{r_l r_j})\overline{\overline{T}}^{(j)}\overline{w}(\overline{r}_j)\,d\overline{r}_j + e^{i\overline{k}_i \cdot \overline{r}_l}\overline{a}_{\text{inc}} \qquad (11)$$

To evaluate the integral in (11) we use a trial solution for $\overline{w}(\overline{r}_l)$ such that it expresses a field traveling in a medium with effective constant of propagation, κ

$$\overline{w}(\overline{r}_l) = \overline{a}_E e^{i\kappa x_l}. \qquad (12)$$

After substituting (12) in (11) and making a simple coordinate transform ($\overline{r_j r_l} = \overline{r}_j - \overline{r}_l = \overline{r}$), the integral in (11) becomes

$$\begin{aligned}
\overline{\overline{s}} &= n_0 e^{i\kappa x_l}\int_S g(\overline{r})\overline{\overline{\sigma}}(k\overline{r})e^{i\kappa x}\,d\overline{r}\,\overline{\overline{T}}\overline{a}_E \\
&= n_0 e^{i\kappa x_l}\left(\int_S \overline{\overline{\sigma}}(k\overline{r})e^{i\kappa x}\,d\overline{r} + \int_S [g(\overline{r})-1]\overline{\overline{\sigma}}(k\overline{r})e^{i\kappa x}\,d\overline{r}\right)\overline{\overline{T}}\overline{a}_E \\
&= e^{i\kappa x_l}\left(\overline{\overline{I}}_1 + \overline{\overline{I}}_2\right)\overline{\overline{T}}\overline{a}_E.
\end{aligned} \qquad (13)$$

where S is the positive half-space excluding the area occupied by the lth particle. To evaluate $\overline{\overline{I}}_1$ and $\overline{\overline{I}}_2$. we use the Hankel function addition theorem [Chew et al.. 1992]

$$[\overline{\overline{\sigma}}(k_0\overline{r_jr_l})]_{nm} = H_{m-n}^{(1)}(k_0|\overline{r_jr_l}|)\epsilon^{i(m-n)o_{jl}}. \tag{14}$$

where $\overline{r_jr_l}$ is the translation vector between coordinate systems. o_{jl} is the angle that the vector makes with the x-axis. and m and n denote the harmonics in the jth and the lth coordinate systems respectively.

To solve the integral $\overline{\overline{I}}_1$, we note that

$$y_p = H_p^{(1)}(k\rho)e^{-ip\phi} \tag{15}$$

is a solution to the wave equation, as is $e^{i\mathcal{K}x}$:

$$\nabla^2 y_p + k^2 y_p = 0 \tag{16}$$

$$\nabla^2 e^{i\mathcal{K}x} + \mathcal{K}^2 e^{i\mathcal{K}x} = 0 \tag{17}$$

By multiplying (16) by $e^{i\mathcal{K}x}$ and. (17) by y_p, subtracting (17) from (16) and applying Green's second identity in two dimensions, $\overline{\overline{I}}_1$ becomes a contour integral

$$\left[\overline{\overline{I}}_1\right]_{nm} = \frac{n_0}{\mathcal{K}^2 - k^2}\int_C \left[e^{i\mathcal{K}x}\nabla y_p - y_p\nabla e^{i\mathcal{K}x}\right] \cdot d\overline{C} \tag{18}$$

(where $p = n - m$) as shown in Fig. 1. $\overline{\overline{I}}_1$ may be written in terms of the three components of the surface

$$\overline{\overline{I}}_1 = \frac{-n_0}{\mathcal{K}^2 - k^2}\left(\overline{\overline{I}}_e + \overline{\overline{I}}_d + \overline{\overline{I}}_\infty\right) \tag{19}$$

where inward pointing normals were used for convenience. By employing the far-field condition, $\overline{\overline{I}}_\infty = 0$, we are left with an integration over the exclusion disc, $\overline{\overline{I}}_e$ and the half space surface, $\overline{\overline{I}}_d$. Explicitly, the integral $\overline{\overline{I}}_e$ may be written as

$$\begin{aligned}
\left[\overline{\overline{I}}_e\right]_{nm} &= \int_{-\pi}^{\pi} e^{i\mathcal{K}\rho\cos\phi}e^{-ip\phi}H_p'^{(1)}(k\rho)k\rho\, d\phi \\
&\quad - \int_{-\pi}^{\pi} H_p^{(1)}(k\rho)e^{-ip\phi}\left(\frac{\partial}{\partial\rho}e^{i\mathcal{K}\rho\cos\phi}\right)\rho\, d\phi \\
&= k\rho H_p'^{(1)}(k\rho)Y_p - \rho H_p^{(1)}(k\rho)\frac{\partial}{\partial\rho}Y_p \tag{20}
\end{aligned}$$

6

where

$$Y_p = -\int_{-\pi}^{\pi} e^{-ip\phi} e^{i\kappa\rho\cos\phi} d\phi$$
$$= 2\pi i^p J_p(\kappa\rho). \tag{21}$$

Substituting (21) into (20) and evaluating at $\rho = b$ we have

$$\left[\overline{\overline{I}}_e\right]_{nm} = 2\pi i^p \left[kb H_p'^{(1)}(kb) J_p(\kappa b) - \kappa b H_p^{(1)}(kb) J_p'(\kappa b) \right]. \tag{22}$$

The surface integral $\overline{\overline{I}}_d$ over the planer surface $x = -x_l$ is

$$\left[\overline{\overline{I}}_d\right]_{nm} = \int_{-\infty}^{\infty} e^{i\kappa x} \frac{\partial}{\partial x} y_p - y_p \frac{\partial}{\partial x} e^{i\kappa x} dy$$
$$= e^{i\kappa x} \frac{\partial}{\partial x} X_p - i\kappa e^{i\kappa x} X_p \tag{23}$$

where

$$X_p = \int_{-\infty}^{\infty} H_p^{(1)}(k\rho) e^{-ip\phi} dy = \frac{-2}{k} e^{ik|x|}. \tag{24}$$

Substituting (24) into (23) and evaluating at $x = -x_l$ gives

$$\left[\overline{\overline{I}}_d\right]_{nm} = 2i e^{i(k-\kappa)x_l} \left[1 + \frac{\kappa}{k} \right]. \tag{25}$$

For the second integral in (13), we have

$$\left[\overline{\overline{I}}_2\right]_{nm} = n_0 \int_{\substack{\rho > b \\ x > -x_l}} [g(\overline{r}) - 1] H_p^{(1)}(k\rho) e^{-ip\phi} e^{i\kappa x} d\overline{r} \tag{26}$$

where we note that $\overline{\overline{I}}_2$ is dependent on the propagation constant κ, the pair distribution function $g(\overline{r})$, the particle diameter, and the particle location x_l. If we notice however that $[g(\overline{r}) - 1]$ is nearly zero for $|\overline{r}|$ greater than a few particle diameters, we can treat the integration as if it were over an unbounded space, thus ignoring the boundary at $x = -x_l$ (and particles near that boundary)

$$\left[\overline{\overline{I}}_2\right]_{nm} = n_o \int_{-\pi}^{\pi} \int_b^{\infty} [g(\overline{r}) - 1] H_p^{(1)}(k\rho) e^{-ip\phi} e^{i\kappa\rho\cos\phi} \rho \, d\rho \, d\phi. \tag{27}$$

Furthermore, if we assume that the pair distribution function is axially symmetric, (27) may be written as a single integral which can be calculated numerically

$$\left[\overline{\overline{I}}_2\right]_{nm} = 2\pi n_0 i^p \int_b^{\infty} [g(\rho) - 1] H_p^{(1)}(k\rho) J_p(\kappa\rho) \rho \, d\rho \tag{28}$$

7

Depending on the particular problem, the appropriate form of $\overline{\overline{I}}_2$ given by (26), (27), or (28) may be used.

Referring back to (13), we can multiply $\overline{\overline{I}}_1$ and $\overline{\overline{I}}_2$ by $e^{iK x_l}$ to get a new expression

$$\overline{\overline{s}} = \left[\overline{\overline{s}}_1 e^{iK x_l} + \overline{\overline{s}}_2 e^{ik x_l} \right] \overline{\overline{T}} \overline{a}_E \tag{29}$$

where the explicit dependence of (13) on the constant of propagation (k or κ) has been made clear. In (29) we have

$$\overline{\overline{s}}_1 = \frac{-n_0}{\kappa^2 - k^2} \overline{\overline{I}}_e + \overline{\overline{I}}_2 \tag{30}$$

and

$$\overline{\overline{s}}_2 = \frac{2i n_0 k}{\kappa - k}. \tag{31}$$

Using (29) in (11), the multiple scattering equation may be written

$$\overline{a}_E e^{iK x_l} = \left[\overline{\overline{s}}_1 e^{iK x_l} + \overline{\overline{s}}_2 e^{ik x_l} \right] \overline{\overline{T}} \overline{a}_E + e^{ik x_l} \overline{a}_{\text{inc}}. \tag{32}$$

If we balance the exponential terms of $e^{ik x_l}$ and $e^{iK x_l}$, we then have two independent equations

$$0 = \overline{\overline{s}}_2 \overline{\overline{T}} \overline{a}_E + \overline{a}_{\text{inc}} \tag{33}$$

$$\overline{a}_E = \overline{\overline{s}}_1 \overline{\overline{T}} \overline{a}_E \tag{34}$$

which comprise the Ewald-Oseen extinction theorem (33) and the Lorentz-Lorenz law (34). To find the constant of propagation, we solve (34) by noticing that the determinant of the matrix

$$\overline{\overline{Q}} = \left[\overline{\overline{s}}_1 \overline{\overline{T}} - \overline{\overline{I}} \right] \tag{35}$$

must be equal to zero for the non-trivial solution. Thus the solution for QCA rests in minimizing the determinant of a matrix whose elements are related to $\overline{\overline{s}}_1$ and the single particle transition matrix, $\overline{\overline{T}}$. Only the transition matrix in (35) is dependent on the field polarization. For a circularly symmetric cylinder, the T-matrix is diagonal and is given by [Ruck et al., 1970]

$$T_{mm}^{\text{TM}} = \frac{-k_s J_m(k_0 a) J_m'(k_s a) + k_0 J_m'(k_0 a) J_m(k_s a)}{k_s H_m^{(1)}(k_0 a) J_m'(k_s a) - k_0 H_m'^{(1)}(k_0 a) J_m(k_s a)} \delta_m \tag{36}$$

8

for the TM polarization and

$$T_{mm}^{\mathrm{TE}} = \frac{-k_s/\epsilon_s \mathrm{J}_m(k_0 a)\mathrm{J}'_m(k_s a) + k_0/\epsilon_0 \mathrm{J}'_m(k_0 a)\mathrm{J}_m(k_s a)}{k_s/\epsilon_s \mathrm{H}_m^{(1)}(k_0 a)\mathrm{J}'_m(k_s a) - k_0/\epsilon_0 \mathrm{H}_m^{\prime(1)}(k_0 a)\mathrm{J}_m(k_s a)} \delta_m \qquad (37)$$

for TE polarization. In (36) and (37), k_s and ϵ_s indicate the propagation constant and permittivity of the individual scatterers. The factor δ_m is equal to unity for $m = 0$ and two for $m \geq 1$.

Thus, to implement QCA, the matrix $\overline{\overline{Q}}$ is constructed from either of (36) or (37) from above and (30), $\overline{\overline{s}}_1$ which employs (22), $\overline{\overline{I}}_e$, and (28), $\overline{\overline{I}}_2$. The effective constant of propagation of the random medium is

$$\kappa_{\mathrm{eff}} = \min_{\kappa} \left[\det\overline{\overline{Q}}\right]. \qquad (38)$$

The user defined variables in (38) are: 1.) the pair distribution function, $g(\bar{r})$ 2.) the particle density, n_0, 3.) the particle diameter, b, and 4.) the maximum order of the cylindrical wave expansion, p_{max} such that $p \in [0, p_{\mathrm{max}}]$. From a practical point of view, the pair distribution function is the most difficult of these variables to determine.

As a basis of comparison, we may use the single scattering field approach of the effective field approximation (EFA) also known as Foldy's approximation. In two dimensions, the effective permittivity for circular inclusions determined by EFA is

$$\epsilon_{\mathrm{eff}} = 1 - n_0 \frac{4i}{k_0^2} \sum_m T_{mm}^{\mathrm{TM\ or\ TE}}. \qquad (39)$$

3 Pair Distribution Function

In the previous section we developed the theory for the two-dimensional quasi-crystalline approximation. After developing the theory it was noted that the pair distribution function was the unknown which was most difficult to characterize. In reality the pair distribution function may be estimated in one of three ways: 1.) experimentally, 2.) theoretically or 3.) numerically. Experimental estimation of

the pair distribution function is extremely difficult due to the fact that it entails a detailed study of the particle structure for each random medium being considered. A theoretical approach may be used to model the physical distribution of particles in a medium but we may be limited to only a certain class of media which may be described by the mathematical model. Alternatively, a numerical approach may be used to directly model the arrangements of particles via Monte-Carlo simulations based on a computer model the particle deposition. The numerical model, has the advantage of increased flexibility in addressing a variety of physical methods of particle deposition and interaction.

We present here a set of six distinct pair distribution functions, each has been given a simple label (in parentheses) that will be used for reference in the remainder of the paper.

Hole Correction (HC). The hole correction formula is the simplest of the theoretical pair distribution functions and can be used to model an ideal gas consisting of mono-sized particles of diameter b.

$$g(\rho) = \begin{cases} 0 & \rho < b \\ 1 & \rho \geq b \end{cases} \tag{40}$$

HC has the effect of eliminating the $\overline{\overline{I}}_2$ term in (30) and thus it is possible to use QCA-HC as a measure to gauge the effect of the pair distribution function on the QCA formulation.

Classical fluid medium (PY). Of the theoretical pair distribution functions, the most common is given by Percus and Yevick [1958] which can be used to model particle positions in a classical fluid of hard spheres. Three-dimensional closed form solutions of PY can be found in Wertheim [1963] and have been shown to agree closely with numerical simulations of particle arrangements [Ding et al., 1992]. In two dimensions, the PY equations have been solved numerically by Lado [1968] (Fig. 2). The assumptions of hard-sphere PY are 1.) there are no external forces acting on the particles and 2.) the potential energy between particles is infinite when they overlap and zero when their centers are separated

10

by a distance greater than one particle diameter. The first assumption allows the system energy to be directly related to the particle arrangement and the second assumption creates a basis from which this energy may be calculated. These assumptions are the physical parallel of placing particles randomly within a confining volume until a given volume fraction or particle density has been reached.

In performing two-dimensional numerical simulations, it was found that volume fractions from 0 to approximately 48% were attainable without resorting to arrangement initialization techniques (such as given by Metropolis et al. [1953]). Initialization techniques allow high particle densities to be reached by initializing particle positions to a totally packed crystalline array. Individual realizations are performed by perturbing particles from their original positions by a random vector. It should be noted that by resorting to this method, we can no longer guarantee an axially symmetric pair distribution function and for this reason, only volume fractions below 45% are generally used for the analysis component of this paper. It may be however that it is possible to determine a mean pair distribution function which calculates probable particle locations based on radial distance only and ignores the angular dependence by averaging over all angles. While this violates the assumption made in determining (28), we can examine the effects of the approximation here.

Particle extraction method (extract). Particles are arranged together in a near crystalline fashion using a packing algorithm (PA) described in Siqueira et al. [1995]. Particles are removed one by one without disturbing the lattice until the desired volume fraction is achieved (Fig. 3). Because of the effect of gravity, the pair distribution function is not axially symmetric. The pair distribution function is shown in the vertical direction (o), the horizontal direction(×) and for the azimuthal average (solid line).

Snow-type medium (snow). This two-dimensional simulation utilizes PA to simulate the process of falling snow (Fig. 4). In this simulation, deposited par-

ticles are made to stick near their initial starting points after which the volume fraction is adjusted using the extraction method. Particles are not allowed to find their state of minimum potential energy. This stacking process is reflected in the pair distribution function which illustrates an ordered array in the vertical direction (o) and a disordered one in the horizontal direction(×).

Distributed particle size (shrink). This method of adjusting volume fraction is given to illustrate the dependence of the pair distribution function on the packing method (Fig. 5). To obtain a volume fraction of 30%, a Gaussian particle size distribution is used whose mean diameter is one and a half times larger than the target particle diameter. After the particles have been packed together (dotted lines), the radius is shrunk to a uniform diameter to achieve the correct volume fraction. While this pair distribution function is not physical, it illustrates how the pair distribution function is reflective of the packing method used.

Ellipse to disk method (ellipse). This method is the final example of how a pair distribution function may be achieved for a given volume fraction using an alternate method of particle arrangement (Fig. 6). In this case, for a volume fraction of 30%, uniform ellipses whose major axis was twice that of the minor axis were used to generate the initial particle arrangement (dotted lines). The ellipses were then changed to disks having uniform diameters equal to the minor axes, resulting in a particle arrangement that may appear outwardly to be very similar to that of the classical fluid simulation in Fig. 2. Note however, that statistically the two methods are very different, as can be seen by their pair distribution functions.

In this section, we have introduced six different methods of arranging particles in a volume or area. Each of the different methods were presented to illustrate the variety of pair distribution functions that can be achieved by altering the method of particle deposition in the simulations. The presentation accentuated the fact that the pair distribution functions are not necessarily axially symmetric

nor similar, effects that will be further explored in the paper. The resulting pair distribution functions can be used directly in the QCA theory developed in the previous section to analyze the sensitivity of QCA to the pair distribution function. $g(\bar{r})$. or we can extend our evaluation one step farther by using the particle position simulations to directly determine the effective constant of propagations for a random medium.

4   Independent Determination of ϵ_{eff}

This section provides a brief review of a numerical method (NUM) of determining the effective permittivity of a two-dimensional random medium [Sarabandi and Siqueira 1995]. Given a method of arranging particles in a volume, it is possible to directly determine ϵ_{eff} using a numerical solution to Maxwell's equations. In the paper describing this method, it has been shown that the technique agrees well with the low-frequency mixing formula of Polder and Van Santen [1956] when dielectric losses are more significant than scattering losses. This method has also been demonstrated to show appropriate behavior in the low frequency region as well as for both sparse and very dense concentrations of particles.

The numerical method compares the average scattered field from a random collection of particles confined within an imaginary boundary with that of a homogeneous dielectric body whose shape is the same as the imaginary boundary (Fig. 7). By varying the permittivity of the homogeneous body, we may minimize the difference between the scattered fields of the two bodies. One such example is given in Figs. 8 and 9 for both the TM and TE polarizations for three different particle sizes using the particle extraction method of adjusting volume fraction. Shown also in the figures is the two-dimensional Polder-Van Santen (PVS) mixing formula given by

$$\epsilon_{\text{eff}} = \epsilon_h + f(\epsilon_i - \epsilon_h) \tag{41}$$

$$\epsilon_{\text{eff}} = \epsilon_h + f(\epsilon_i - \epsilon_h)\frac{2}{\epsilon_i + \epsilon_h} \tag{42}$$

13

for the TM and TE polarizations respectively. It can be seen that for the small particle sizes that there is excellent agreement between the two methods at low volume fractions. Furthermore, the increased losses shown for larger particles is consistent with physical expectations. What remains to be done is to include results from the two-dimensional QCA theory developed in Section 2 and to compare those results with the results from this section for the six different methods of generating particle arrangements (HC, PY, extract, snow, shrink and ellipse).

5 Evaluation of the Two-Dimensional Quasi-Crystalline Approximation

In this section, the behavior of QCA as a function of particle size, polarization, volume fraction, scattering/dielectric losses and particle arrangement method is explored. To begin, we present three sets of six plots (Figs. 10, 11 and 12) which demonstrate the theoretical and numerical methods dependence on particle size, volume fraction, polarization and dielectric loss. Fig. 10 (TM polarization) and Fig. 11 (TE polarization) demonstrate real and imaginary ϵ_{eff} performance for particles with a modest amount of dielectric loss ($\epsilon_i = 3.6 + i0.1$) while Fig. 12 gives the imaginary component of ϵ_{eff} for particles with low dielectric loss ($\epsilon_i = 3.6 + i0.01$) for both TM and TE polarizations. The real component of ϵ_{eff} is not included in Fig. 12 because it was found that the behavior of Re(ϵ_{eff}) did not change appreciably from the examples given in Figs. 10 and 11. In all three figures, a classical fluid (PY) was used to model particle positions for both QCA and the numerical method. The particle diameters used in each of the demonstrations range from $\lambda_i/10(kd = 0.33)$, $2\lambda_i/10(kd = 0.67)$ to $3\lambda_i/10(kd = 1.0)$ as the plots go from left to right (k is the wavenumber of the included particles).

Referring to Figs. 10 through 12, the following observations are in order:

1.) *Re(ϵ_{eff}), TM polarization.* The real part of the effective permittivity is practi-

cally the same for the theoretical methods of PVS, EFA, QCA-PY, QCA-HC and NUM-PY for all volume fractions, particle size and both values of particle dielectric loss (Fig 10 (a) through (c)). The performance of EFA and PVS degrades as particle size increases, an effect of an increase in scattering by the larger particles. Both QCA-PY and QCA-HC track the behavior of the numerical method well in this aspect because of the inclusion of multiple scattering terms in the QCA formulation. Note that PVS may be used as a reference as particle size varies because particle size is in general not a factor in mixing formulae. We may notice therefore, via PVS, that QCA-PY, QCA-HC and NUM-PY agree that phase velocity decreases with increasing particle size. The similarities between the results of $Re(\epsilon_{eff})$ for both low loss and moderate loss inclusions indicate that dielectric loss in the particles does not appreciably effect the phase velocity. This may also highlight the effect that only near particle interactions effect the real part of ϵ_{eff}.

2.) *Im(ϵ_{eff}), TM polarization.* The imaginary part of the effective permittivity displays a more complex behavior than the real part as a function of volume fraction and particle size. The theoretical and numerical methods agree well at low volume fractions with the exception of small particle sizes for moderately lossy inclusions (Fig. 10, part (d)). In this respect, while it is known in the low frequency limit that all the methods agree, the losses indicated by NUM-PY are significantly larger than results given by the theoretical methods of QCA-HC and QCA-PY. We believe that these differences may be caused by an overestimation of absorption losses with respect to the multiple scattering losses for the methods of QCA-PY and QCA-HC. That is, numerically, we detect more multiple scattering than QCA does for moderately lossy particles with sizes that are relatively small with respect to wavelength.

We may also note that QCA-PY does an excellent job of tracking the losses predicted by NUM-PY for the larger particle sizes shown in parts (e) and (f) of Fig. 10. At a volume fraction of approximately 20% the methods of QCA-PY and QCA-HC diverge significantly with a trend reversal seen in QCA-PY due to

the contribution from the pair distribution function. In both cases for the larger particles we also see a significant difference between EFA. QCA-PY. QCA-HC. NUM-PY and that of PVS. an effect that is expected because of the scattering losses incurred by the larger particles are not accounted for by the mixing formula.

The change in $Im(\epsilon_{eff})$ is considerably more noticeable between Fig. 10 parts (d) through (f) and Fig. 12. parts (a) through (c). Proportional to the PVS mixing formula the losses are significantly larger for $\epsilon_i = 3.6 + i0.01$ than for $\epsilon_i = 3.6 + 0.1$, indicating that multiple scattering is a much more dominant factor in the low loss case. The multiple scattering however does not translate into greater losses overall as we can see that the numerical method predicts lower losses in general than the losses predicted for particles with higher dielectric loss. What this means is that although the field in the $\epsilon_i = 3.6 + i0.01$ case interacts with more particles, the field does not suffer enough additional absorption losses due to the multiple interactions to make up for the absorption losses incurred with the lossier $\epsilon_i = 3.6 + i0.1$ particles. We also make a final note that QCA does a comparably well job at predicting $Im(\epsilon_{eff})$ in this case as it did in the previous TM case when $\epsilon_i = 3.6 + i0.1$.

3.) *Re(ϵ_{eff}), TE polarization.* The real parts of ϵ_{eff} for all methods and particle sizes agree well at the low volume fractions but begin to deviate at a volume fraction of about 20% (Fig. 11, parts (a) through (c)). This effect is expected because of the necessary non-linear contribution from electrical dipoles to the total field for the TE polarization. The trends of EFA, QCA-PY, and QCA-HC all follow that of the PVS model relatively well despite an even poorer performance for the theoretical methods in the prediction of scattering losses (discussed below). We note that NUM displays the physically expected trend of ϵ_{eff} approaching ϵ_i as volume fraction increases towards unity.

4.) *Im(ϵ_{eff}), TE polarization.* We may first note that all methods agree well with respect to losses at very low volume fractions irrespective of particle size. In the zero to twenty percent volume fraction range it is evident that QCA-PY and

QCA-HC reflect the correct trend of increased scattering loss for increased particle size. However, for this polarization, the dominant term in (30) is $\overline{\overline{I}}_e$ (the particle exclusion integral) and not $\overline{\overline{I}}_2$ (the integral dependent on the pair distribution function). Thus $\text{Im}(\epsilon_{\text{eff}})$ becomes unphysically negative be seen through the effect of QCA-PY following QCA-HC into the non-physical domain of negative $\text{Im}(\epsilon_{\text{eff}})$. QCA-PY and QCA-HC do not adequately describe the multiple scattering losses at fractional volumes greater than 5% and in fact the scattering losses under-predicted by QCA-PY and QCA-HC significantly fall below the lower limit given by the PVS mixing formula.

In Fig. 12, parts (d) through (f) we illustrate the behavior of $\text{Im}(\epsilon_{\text{eff}})$ for low-loss particles whose permittivity is $\epsilon_i = 3.6 + i0.01$. Without the additional support of dielectric losses, QCA gives realistic values for $\text{Im}(\epsilon_{\text{eff}})$ for only the smallest of volume fractions. As with the TM case, the losses predicted by NUM-PY are larger in proportion to the losses predicted by PVS but are smaller overall than the losses shown in Fig. 11 (d) through (f).

It may be disturbing to see the poor performance of QCA in its ability to predict losses for TE polarized fields (Figs. 11 and 12). To answer questions related to this effect, it is useful to examine the low frequency behavior of QCA (or more specifically QCA-HC) for both the TM and TE polarizations (Fig. 13). Only the hole correction formula with QCA is used in this demonstration to examine the effect of the exclusion integral, $\overline{\overline{I}}_e$, term in (30). The results of QCA-HC are compared with the PVS mixing formula (which is essentially the low frequency limit of EFA) so that a single curve can be used as a reference for different particle sizes. The real component of ϵ_{eff} for both polarizations follows that of PVS very closely for all particle sizes and therefore is not shown. Only for particle diameters of $\lambda_i/20$ and larger does $\text{Im}(\epsilon_{\text{eff}})$ deviate significantly from PVS for the two polarizations, but the deviation for the TM polarization is much milder than that shown for a TE polarized field in which ϵ_{eff} actually becomes negative. We attribute these differences to the higher order singularity found in the Green's

function for a TE polarized field (i.e. dipole interactions instead of mono-pole interactions as is the case for TM polarization). The negative trend seen for the TE polarized field is much more difficult for the $\overline{\overline{I}}_2$ term in (30) to overcome and it is for this reason that we see the degraded performance of the TE polarization results shown in Figs. 11 and 12.

Given the extensive analysis presented so far with respect to the performance of QCA. EFA. PVS and NUM. it is convenient to present the results in a more compact form. To this end, we present Figs. 14 and 15 which graphically illustrate the differences between the three theoretical method's (QCA, EFA and PVS) and the numerical method's (NUM) estimation of ϵ_{eff} in terms of validity regions. The differences used to determine the validity regions were computed in terms of errors with respect to the numerical method given by

$$ err = \frac{theory - NUM}{NUM} \times 100\%. \tag{43} $$

The numerical method is used as a reference because there are no current exact formulations to determine ϵ_{eff} in the regions under consideration and the numerical method is the only method presented thus far that displays the expected behavior of ϵ_{eff} as a function of volume fraction, particle size and polarization. The validity regions were drawn to enclose areas where differences between the numerical and theoretical methods were less than 20%. The validity regions shown are based on a grid of numerical simulations that varied the volume fraction from 5% to 45% in 5% steps and varied particle sizes from $kd = 0.33$ to $kd = 1.0$ in steps of one third. It should be noted that because NUM is used as a reference, errors in NUM will manifest themselves as a systematic offset in the presented validity regions of QCA, EFA and PVS. Additional regions of validity have also been drawn for the limiting cases of low frequency and low fractional volume where all of the different methods employed are known to converge. Because of computational limitations, it was not possible to test the high frequency limits of the theoretical methods.

Figs. 14 and 15 illustrate well the behavior of the theoretical methods as a

18

function of volume fraction, particle size and polarization. QCA-PY for the TM polarization does well with the exception of $kd = 0.33$ sized particles (a region which was discussed earlier) and the region of volume fractions extending between 30% and 40%. In this latter region, the reduced performance of QCA is most likely due to an enhanced component of multiple scattering with respect to the other volume fractions. This behavior has been observed both numerically and experimentally [Nashashibi and Sarabandi, 1995].

As a final analysis of QCA, we compare the numerical method's evaluation of ϵ_{eff} with that of QCA for the array of different particle arrangement methods presented earlier (Figs. 16 and 17). To simplify the treatment, only the angular averaged pair distribution functions were used. At a volume fraction of 30% and $\epsilon_i = 3.6 + 0.01$ we expect multiple scattering to play an important role in determining ϵ_{eff}. It can be noticed that the exact form of the pair distribution function has little effect on the performance of QCA or NUM for $Re(\epsilon_{eff})$ for both the TM and TE polarizations, with the possible exception of the snow simulation. More interesting however is the behavior of the $Im(\epsilon_{eff})$ to the different methods of particle arrangement. Both QCA and NUM agree in the increasing trend of scattering losses going from left to right (note that the estimate of $Im(\epsilon_{eff})$ can vary by as much as a factor of two based on the particle arrangement method alone). The particle arrangement methods in these examples were arranged in such a way so that in going from left to right we increase the likelihood of two particles being in contact with one another. Essentially, when two particles are in contact, we may consider them as being a single, larger particle, thus explaining the increase in scattering loss. This result argues strongly against the use of the Percus-Yevick pair distribution function (which models a classic fluid) in the determination of extinction for granular media such as snow, sand or soils.

19

6 Conclusions

In this paper we have made a complete analysis of the subject of determining effective permittivity for dense random media in two dimensions. The popular method of the quasi-crystalline approximation was derived and associated results for the effective field approximation and the mixing formula for both TM and TE polarizations were presented. Because QCA depends on the form of pair distribution function used, a variety of different particle arrangement methods were presented. We then discussed a numerical method based on the method of moments which may also be used to determine effective permittivity and has been shown to follow expected trends from low to high density and from low to high frequency. The behavior of the methods and the general behavior of effective permittivity were then studied for a variety of different situations, from which it was possible to determine regions of validity for the theoretical methods based on the presented numerical method. Finally, a comparison was made between the effective permittivities found by the numerical method and the quasi-crystalline approximation as a function of particle arrangement method. From this analysis, we have made the following conclusions:

1.) The real component of effective permittivity is essentially the same for all methods up to a value of $kd \approx 1$. The TM polarization in this respect is valid for all volume fractions and the TE polarization is valid up to a volume fraction of 20%.

2.) Given 20% error bounds, the losses predicted by QCA for the TM polarization agree quite well with the numerical method (Fig. 14). It is important however to use the correct form of pair distribution function (Fig. 16).

3.) The losses predicted by QCA for the TE polarization agree very poorly with the numerical method (Fig. 15). At volume fractions greater than 15% it is not uncommon for $\text{Im}(\epsilon_{\text{eff}})$ to become unphysically negative. We believe this poor behavior is due to the strong singularity found in the Green's function for this

20

polarization.

4.) The effect of decreasing absorption losses of the inclusions has the expected effect of increasing multiple scattering but this does not translate into higher total losses.

5.) The pair distribution function (or similarly, the particle arrangement method) does play an important role in determining extinction (Figs 14 and 15). It is believed that this is due to the effect of two neighboring particles acting together as a single larger particle. Thus it is inappropriate to use the Percus-Yevick pair distribution when analyzing a random medium whose particle locations do not resemble a classical fluid.

The work presented in the paper opens up a number of avenues for future work. In two dimensions the effect of the angular asymmetry in the pair distribution function on QCA can be explored by carrying out the two-dimensional integration in (27). It would also be informative to analyze the effect of varying $Re(\epsilon_i)$ on ϵ_{eff} and to determine an empirical method of determining the effective permittivity based on a combination of QCA and generalized results found by NUM. The most important and useful future work however, will be to bring the presented analysis and methods into three dimensions. In this sense, the study presented here offers an important set of methods and background that can be used to conduct that investigation.

References

[1] Chew, W.C., Wang, Y.M., and Gurel, L., "Recursive Algorithm for Wave-Scattering Solutions Using Windowed Addition Theorem," Journal of Electromagnetic Waves and Applications, v.6 n.11, pp 1537-1560, November 1992.

[2] Ding, K.H., Mandt, C.E., Tsang, L., and Kong, J.A., "Monte Carlo Simulations of Pair Distribution Functions of Dense Discrete Random Media with Multiple Sizes of Particles," Journal of Electromagnetic Waves and Applications, v.6 n.8, pp 1015-1030, August 1992.

[3] Mandt, C.E., Kuga, Y., Tsang, L. and Ishimaru, A., "Microwave propagation and scattering in a dense distribution of non-tenuous spheres: experiment and theory," Waves in Random Media, v.2, pp 225-234, 1992.

[4] Metropolis, N. Rosenbluth, A.W., Rosenbluth, M.N. Teller, A.H., "Equation of State Calculations by Fast Computing Machines,", Journal of Chemical Physics, v.21 n.6, pp 1087-1092, June 1953.

[5] Nashashibi, A. and Sarabandi, K., "A Technique for Measuring the Effective Propagation Constant of Dense Random Media," 1995 IEEE AP-S International Symposium, Newport Beach, CA. June, 1995.

[6] Polder, D. and VanSanten, J.H.,"The Effective Permeability of Mixtures of Solids," Physica, v.12 n.5, pp 1257-271. August, 1946.

[7] Ruck, G.T., Barrick, D.E., Stuart, W.D., Krichbaum, C.K. *Radar Cross-Section Handbook*. McGraw-Hill, New York, 1970.

[8] Sarabandi, K. and Siqueira, P.R., "Numerical Scattering Analysis for Two-Dimensional Dense Random Media: Characterization of Effective Permittivity," Submitted to IEEE-AP, February 1995.

[9] Siqueira, P.R., Sarabandi, K., and Ulaby, F.T., "Numerical Simulation of Scatterer Positions in a Very Dense Media with an Application to the Two-Dimensional Born Approximation," submitted to Radio Science, June 1994.

[10] Stark, H., and Woods, J.W. *Probability, Random Processes, and Estimation Theory for Engineers*. Prentice-Hall, Englewood Cliffs, New Jersey, 1986.

[11] Tsang, L., Kong, J., and Shin, R. *Theory of Microwave Remote Sensing*. John Wiley & Sons, New York, 1985.

List of Figures

Figure 1: Domain of integration. Shown are the three surfaces $(S_d, S_e, \text{and} S_\infty)$ and their inward pointing surface normals for the integral in (18).
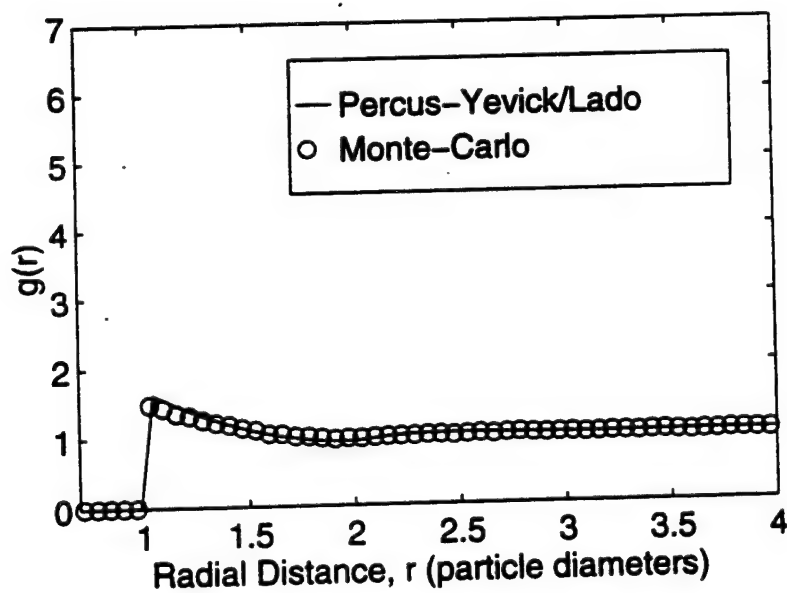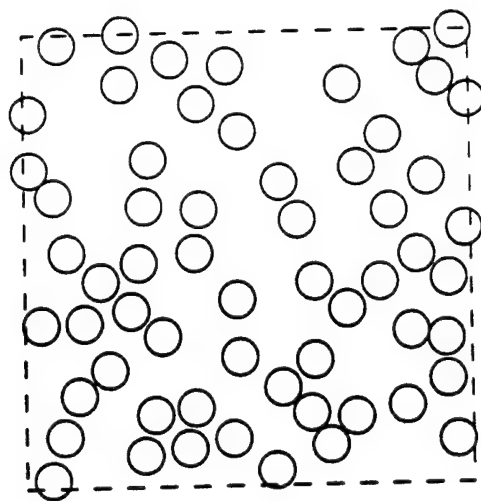
Figure 2: Simulation of a classical fluid for a volume fraction of 30%. Shown are results from Monte-Carlo numerical simulations and the PY equation in two dimensions solved by Lado.

24
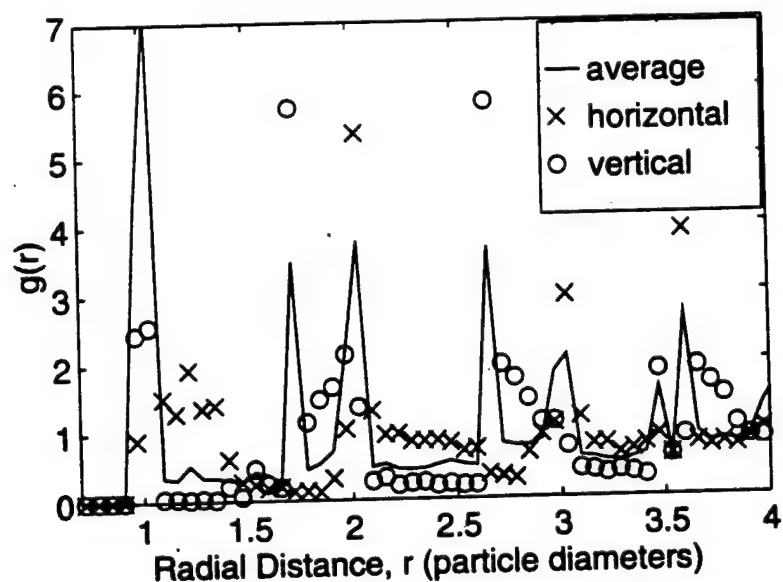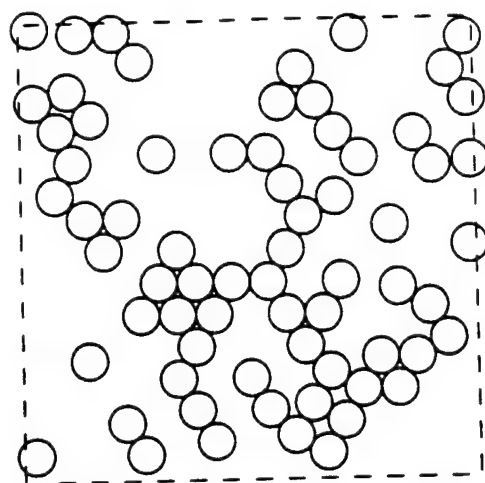
Figure 3: Particle arrangement simulation using particle extraction from a near perfect lattice for a volume fraction of 30%. Shown is the average pair distribution function over all angles and the pair distribution function from the vertical and horizontal directions which accentuate the azimuthal asymmetry. Because the basic structure of the lattice remains unchanged for different volume fractions, the pair distribution function does not change with particle number density.
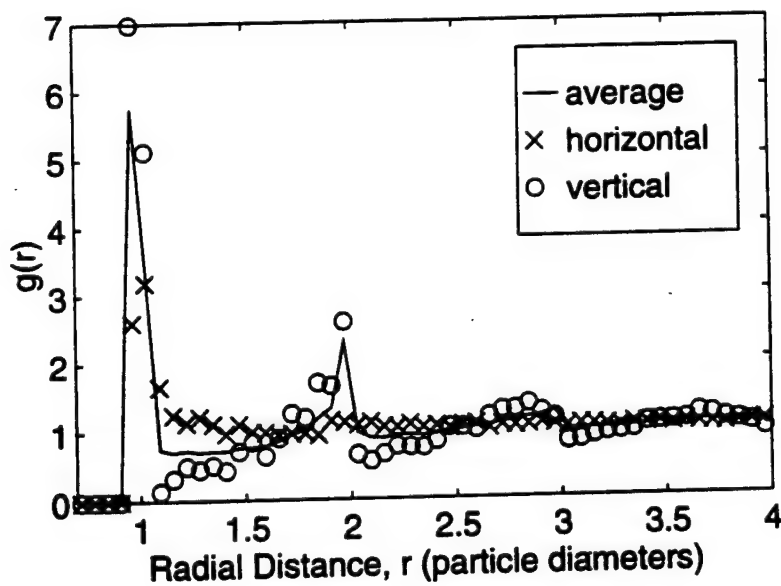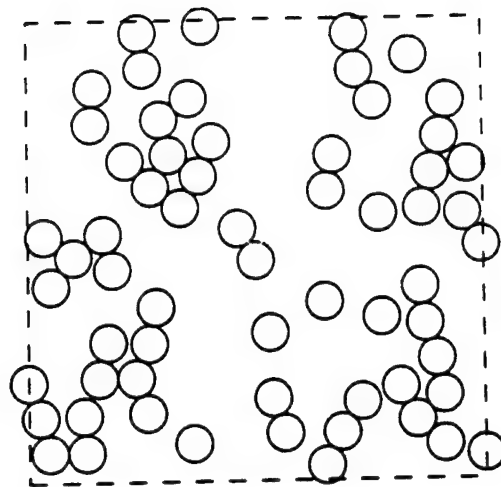
Figure 4: Simulation of a two-dimensional snow-type medium for a volume fraction of 30%. Shown is the average pair distribution function over all angles and the pair distribution function from the vertical and horizontal directions which accentuate the azimuthal asymmetry.
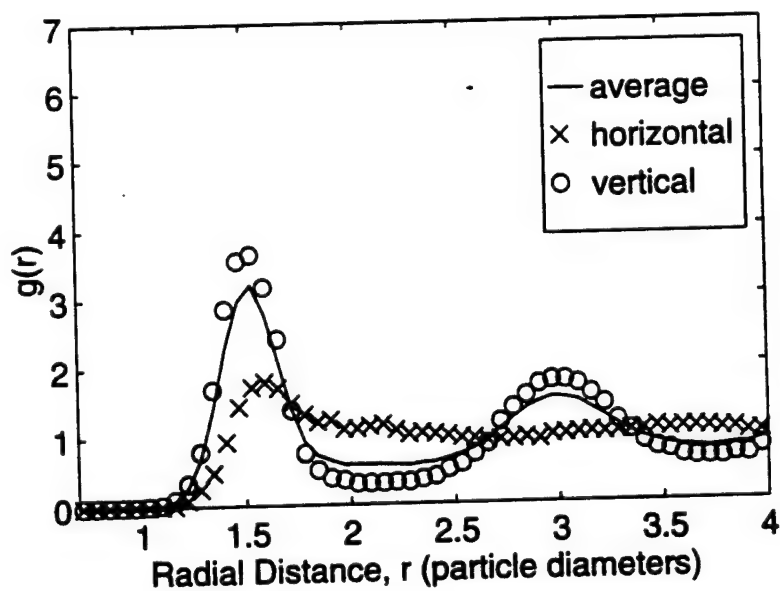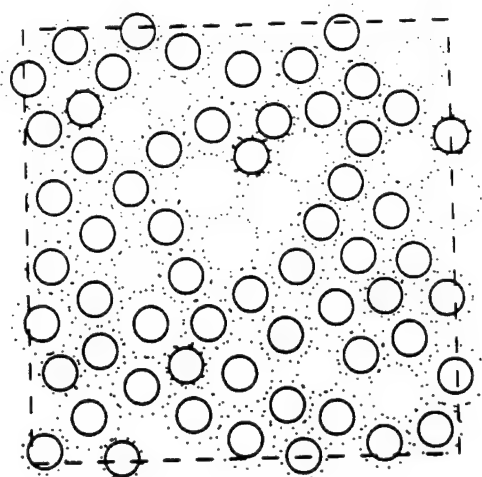
Figure 5: Particle arrangement simulation using a distribution of disks shrunk down to a uniform size for a volume fraction of 30%. Shown is the average pair distribution function over all angles and the pair distribution function from the vertical and horizontal directions which accentuate the azimuthal asymmetry. This example is given to demonstrate one method of obtaining different particle arrangements and different pair distribution functions.
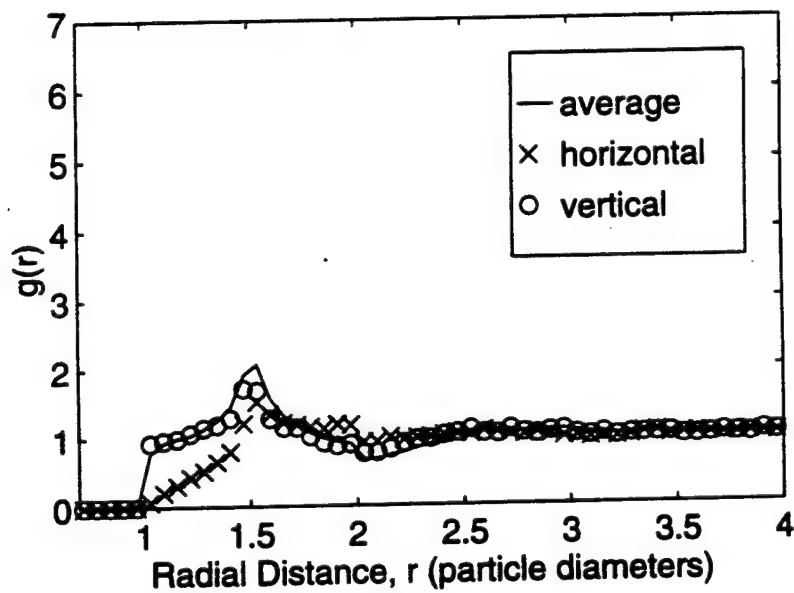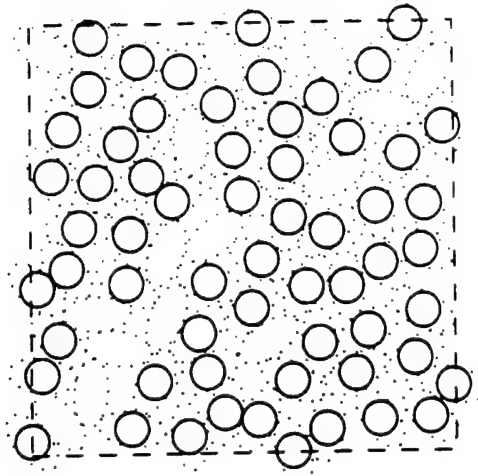
Figure 6: Particle arrangement simulation using ellipses for a volume fraction of 30%. Shown is the average pair distribution function over all angles and the pair distribution function from the vertical and horizontal directions which accentuate the azimuthal asymmetry. This example is given to demonstrate one method of obtaining different particle arrangements and different pair distribution functions.
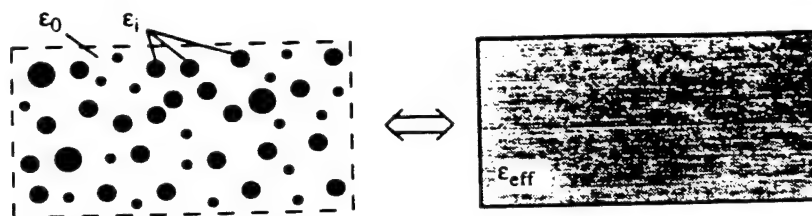
Figure 7: Model for numerical determining ϵ_{eff} for a random medium.
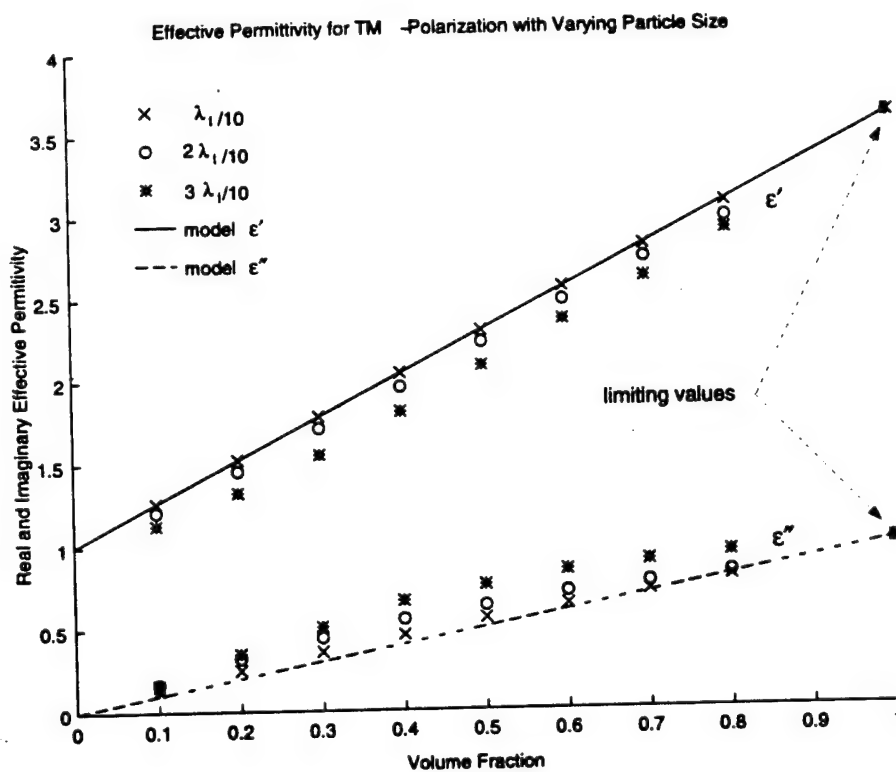
Figure 8: Effective permittivity, ϵ_{eff}, vs. volume fraction for a TM polarized field incident upon a random medium. Shown are results from the numerical method for different particle sizes along with those obtained by the Polder-Van Santen mixing formula. The volume fraction was adjusted by particle extraction.
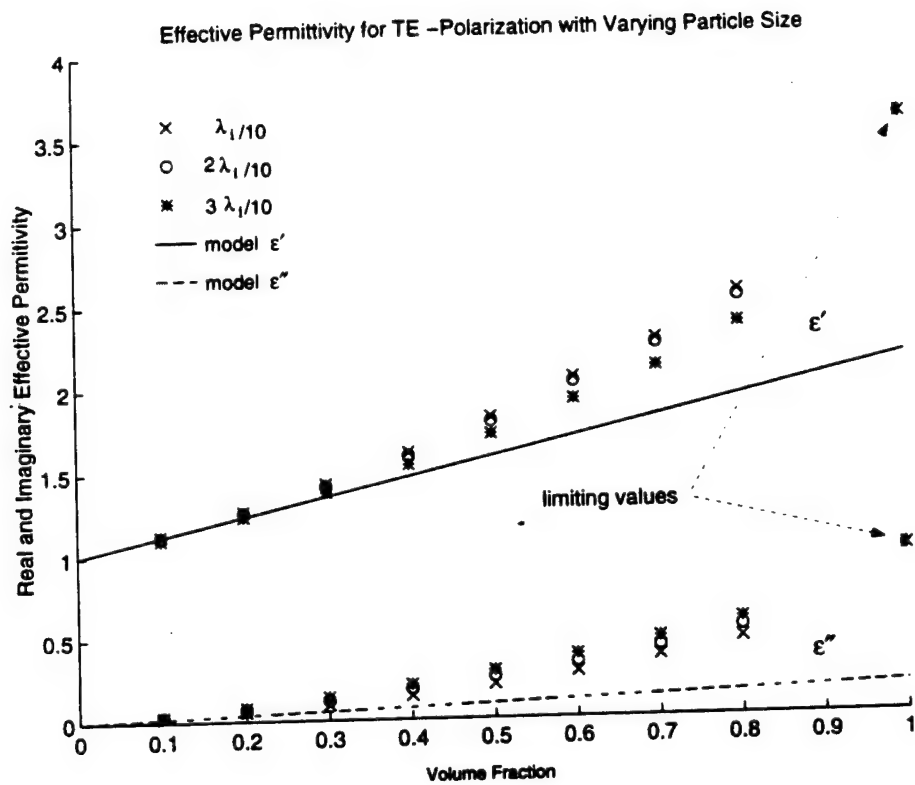
Figure 9: Effective permittivity, ϵ_{eff} vs. volume fraction for a TE polarized field. See Fig. 7 for details.
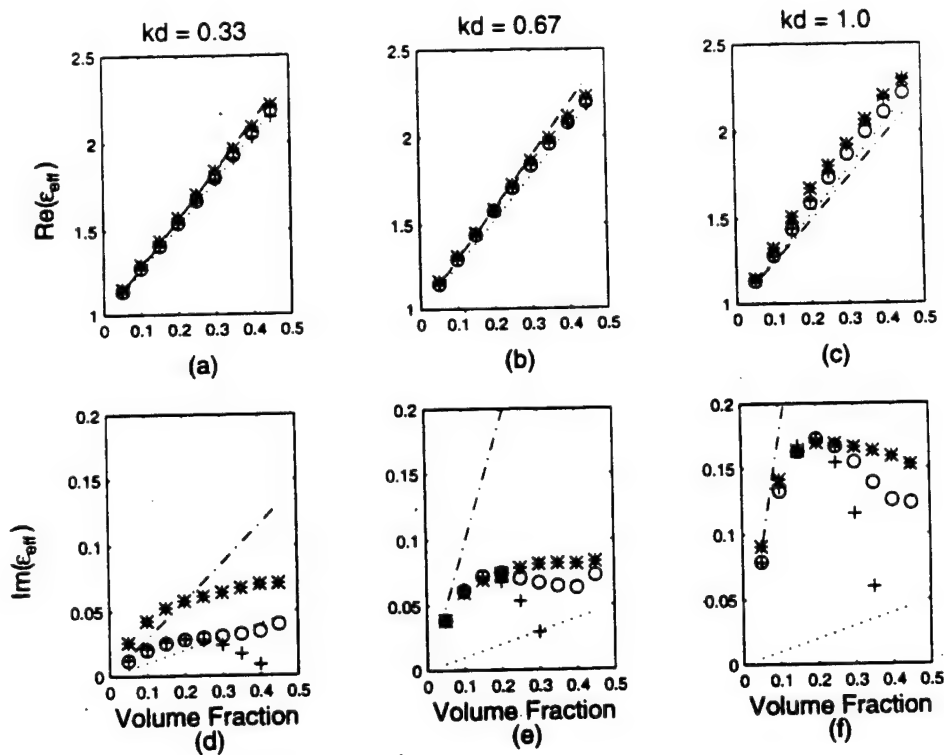
Figure 10: Comparison between five methods of determining effective permittivity for a TM polarized field: EFA (-.), PVS (...), QCA-PY (o), QCA-HC (+) and NUM-PY (*). Plots (a) through (c) illustrate $\text{Re}(\epsilon_{\text{eff}})$ and (d) through (e) illustrate $\text{Im}(\epsilon_{\text{eff}})$ as a function of volume fraction using a model of particles ($\epsilon_i = 3.6 + i0.1$) suspended in a classical fluid. Particle diameter ranges from $\lambda_i/10(kd = 0.33)$ (a and d), $2\lambda_i/10(kd = 0.67)$ (b and e), to $3\lambda_i/10(kd = 1.0)$ (c and f).

31
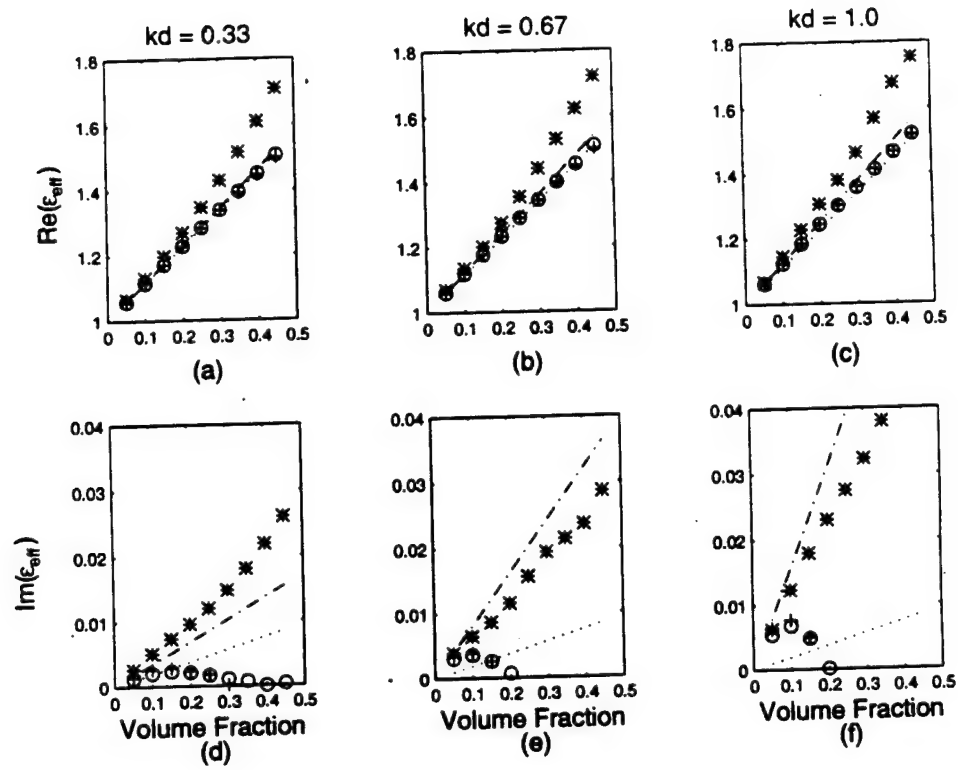
Figure 11: Comparison between five methods (QCA-PY, QCA-HC, EFA, PVS and NUM-PY) of determining effective permittivity for a TE polarized field. See the caption of Fig. 10 for details.
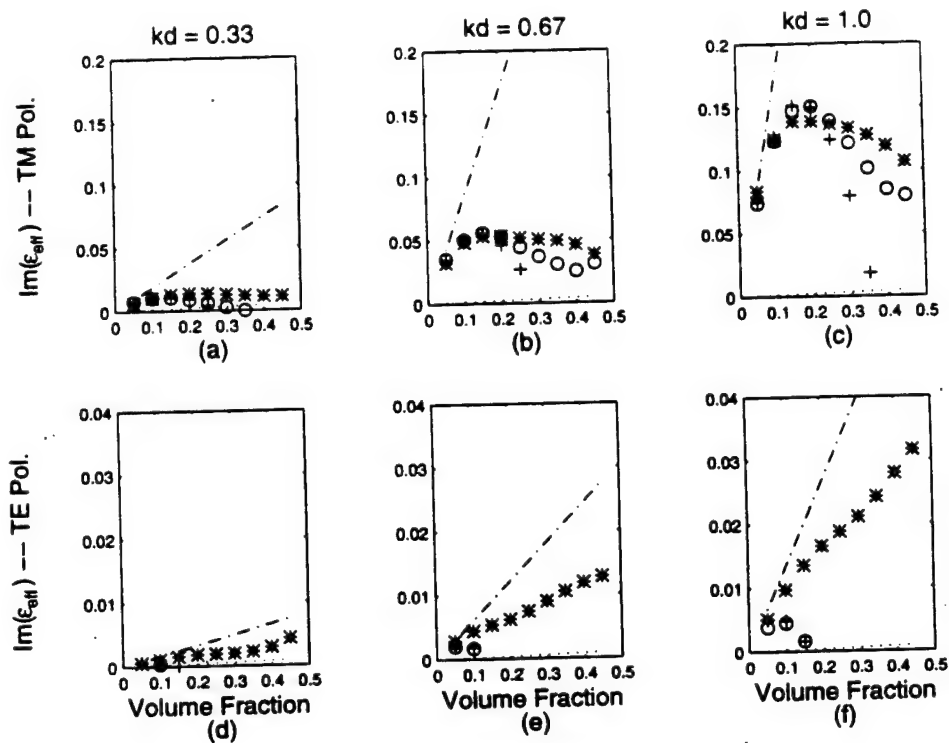
Figure 12: Comparison between five methods (QCA-PY, QCA-HC, EFA, PVS and NUM-PY) of determining the effective permittivity for TM and TE polarized fields. The permittivity of the included particles is $\epsilon_i = 3.6 + i0.01$. The real component (not shown) is essentially unchanged from the previous example when $\epsilon_i = 3.6 + i0.1$. See the caption in Fig. 10 for details.

33
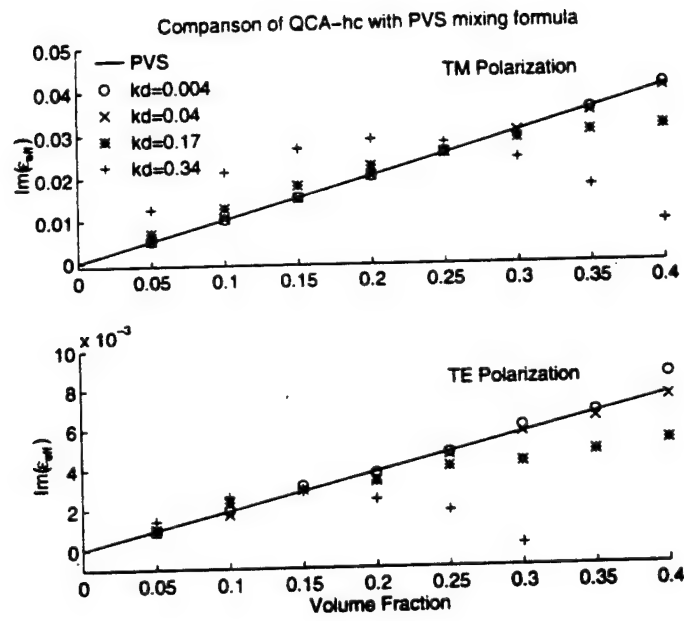
Figure 13: Performance of QCA-HC at very low frequencies. Shown. is $\mathrm{Im}(\epsilon_{\mathrm{eff}})$ for particles with diameter $\lambda_i/800$, $\lambda_i/80$, $\lambda_i/20$, and $\lambda_i/10$ for both TM and TE polarizations ($\epsilon_i = 3.6 + i0.1$).
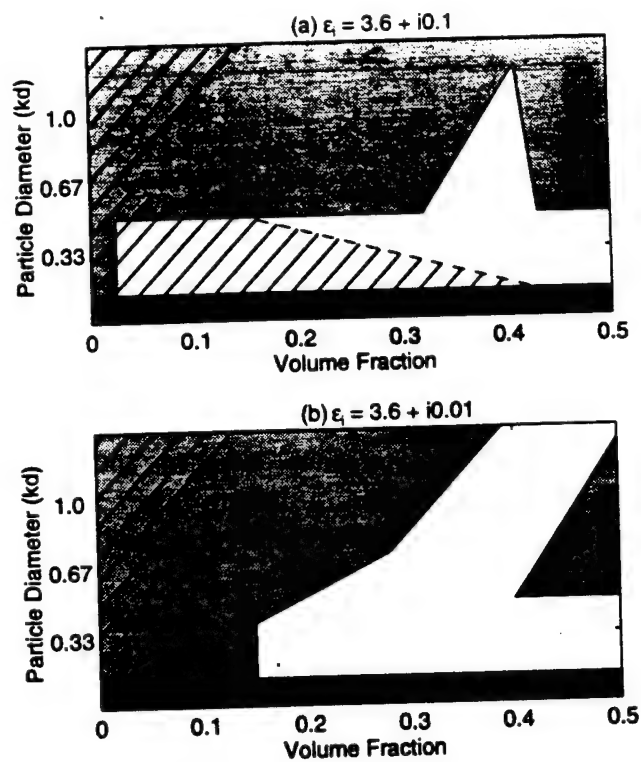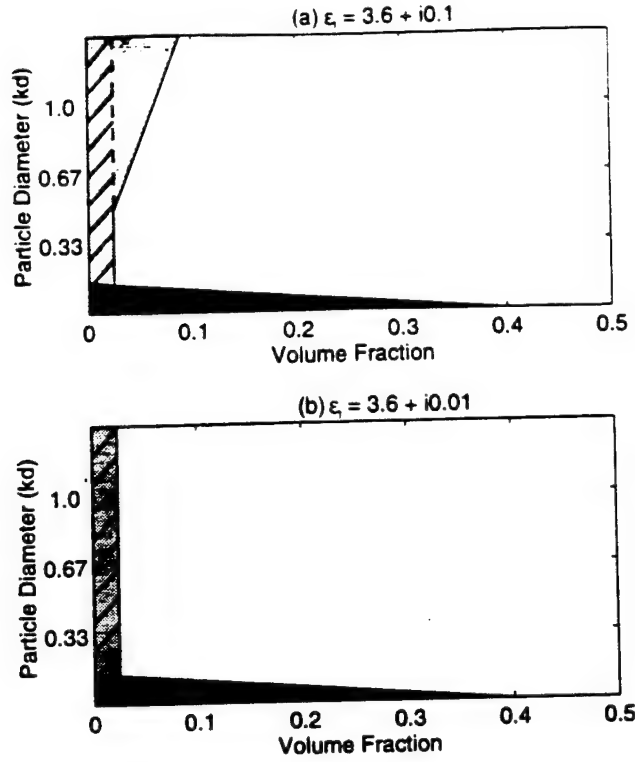
Figure 14: TM polarization validity regions based on 20% differences between imaginary ϵ_{eff} for the numerical method of determining ϵ_{eff} (NUM-PY) and the theoretical methods of QCA-PY (light gray), EFA (hatched) and PVS (dark gray) for (a) $\epsilon_i = 3.6 + i0.1$ and (b) $\epsilon_i = 3.6 + i0.01$.
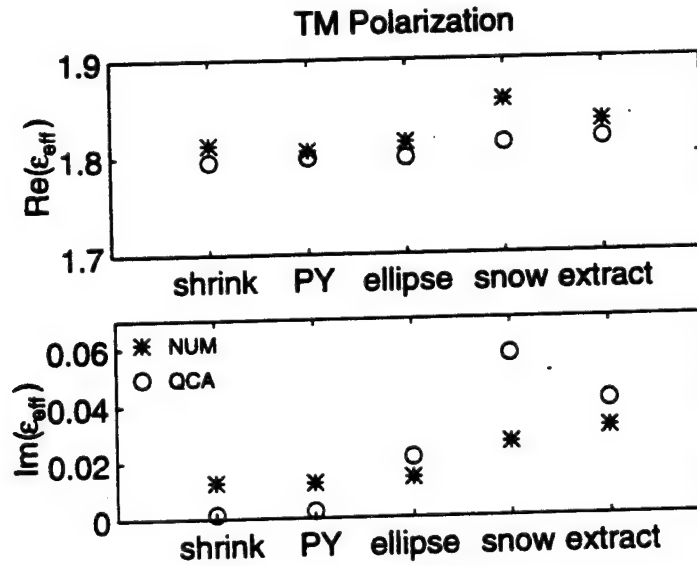
Figure 15: TE polarization validity regions based on 20% differences between imaginary ϵ_{eff} for the numerical method of determining ϵ_{eff} (NUM-PY) and the theoretical methods of QCA-PY (light gray), EFA (hatched) and PVS (dark gray) for (a) $\epsilon_i = 3.6 + i0.1$ and (b) $\epsilon_i = 3.6 + i0.01$.

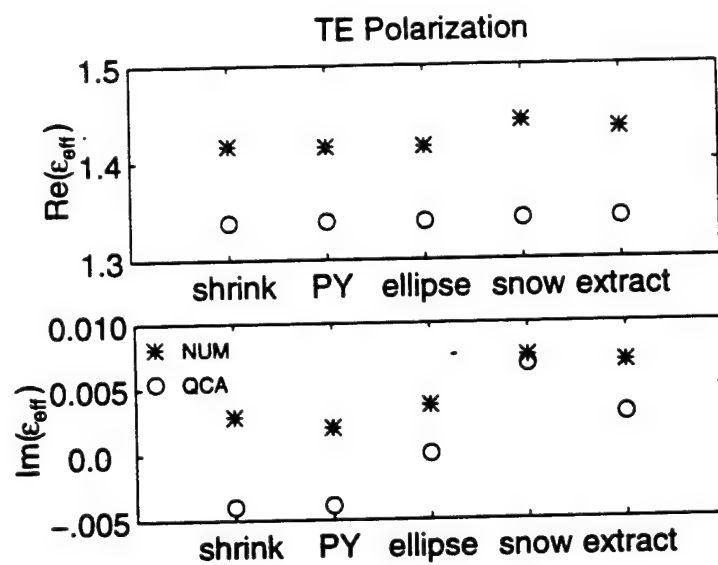Figure 16: Effective permittivity comparison between particle arrangement methods. Volume fraction = 30%, $\epsilon_i = 3.6 + i0.01$, TM Polarization.

Figure 17: Effective permittivity comparison between particle arrangement methods. Volume fraction = 30%, $\epsilon_i = 3.6 + i0.01$, TE Polarization.

Derivation of phase statistics from the Mueller matrix

K. Sarabandi

Radiation Laboratory, Department of Electrical Engineering and Computer Science,
University of Michigan, Ann Arbor

To answer the question of what radar polarimetry has to offer to the remote sensing of random media, statistics of the phase difference of the scattering matrix elements must be studied. Recent polarimetric measurements of rough surfaces have indicated that the statistical parameters of the phase difference (mean, standard deviation, etc.) are very sensitive to some of the physical parameters. In this paper the probability density function of the phase differences is derived from the Mueller matrix, assuming that the elements of the scattering matrix are jointly Gaussian. It is shown that the probability density functions of the copolarized and cross-polarized phase differences are similar in form, and each can be determined by two parameters (α and ζ) completely. The expressions for the probability density functions are verified by comparing the histograms, the mean, and the standard deviations of phase differences derived directly from polarimetric measurements of a variety of rough surfaces to the probability density function, its mean, and standard deviation derived from the Mueller matrices of the same data. The expressions for the probability density functions are of special interest for noncoherent polarimetric radars and noncoherent polarimetric models for random media such as vector radiative transfer.

1. INTRODUCTION

In the past decade, substantial effort within the microwave remote sensing community has been devoted to the development and improvement of polarimetry science. Polarimetric radars are capable of synthesizing the radar response of a target to any combination of the receive and transmit polarizations from coherent measurements of the target with two orthogonal channels. Polarimetric radars have demonstrated their abilities in improving point target detection and classification [Ioannidis and Hammers, 1979]. That is, for a point target in a clutter background the transmit and receive polarizations can be chosen such that the target to clutter response is maximum. Also, different point targets in the radar scene can be classified according to their optimum polarization. Although radar polarimeters have shown a great potential in point target detection and classification, their capabilities in remote sensing of distributed targets are not completely understood yet.

Considering the complexity involved in designing, manufacturing, and processing the data of an imaging polarimeter as opposed to a conventional imaging radar, it is necessary to examine the advantages that the imaging polarimeter provides with the targets of interest. For example, in retrieving the biophysical parameters from the polarimetric radar data, one should ask whether there exists a dependency between the parameters and the measured phase of the scattering matrix components. If the answer is negative, obviously gathering polarimetric data for inversion of that parameter is a waste of effort. One way of confirming this question is by collecting data over a range of the desired parameter while keeping other influential parameters constant. This procedure, if not impossible, is very difficult to conduct because of problems in repeatability of the experiment and difficulties in controlling the environmental conditions. Moreover, at high frequencies (millimeter wave frequencies and higher), coherent measurement of the scattering matrix is impossible because of instabilities of local oscillators and relative movements of the target and the radar platform [Meads and McIntosh, 1991]. At these frequencies, noncoherent radars are employed which provide the Mueller matrix of the target.

Another approach to examine the dependency of the

radar response to the desired parameters of the targets is the application of theoretical models. One of the most successful polarimetric models for random media is the vector radiative transfer theory [Tsang et al., 1985]. This model is based on conservation of energy and the single scattering properties of the constituent particles. The solution of the radiative transfer equation relates the scattered wave Stokes vector to the incident wave Stokes vector via the Mueller matrix. The Mueller matrix, as computed by this method, is an ensemble- averaged quantity because of the inherent nature of the radiative transfer theory. Since the Mueller matrix is related to the scattering matrix through a nonlinear process and the components of the scattering matrix are statistically dependent, the information about the phase difference of the scattering matrix components cannot be obtained from the Mueller matrix directly. To achieve information about the phase statistics, one may resort to the Monte Carlo type models which are computationally inefficient and, in general, inaccurate.

Experimental observations of phase difference statistics from a polarimetric synthetic aperture radar at L-band [Ulaby et al., 1987; Zebker et al., 1987] over agricultural terrain and bare soil surfaces indicate that the statistics of the copolarized phase difference depends on the target type and its conditions. Recent measurements of bare soil surfaces by polarimetric scatterometers show that the variance of the copolarized phase difference is a function of the roughness parameters and incidence angle but is less sensitive to moisture content [Sarabandi et al., 1991].

In view of difficulties in measuring the scattering matrix at high frequencies and performing controlled experiments, it is necessary to establish a relationship between the Mueller matrix and the statistics of the phase differences of the scattering matrix elements. In the next section we derive the probability density function of the copolarized and cross-polarized phase difference in terms of the Mueller matrix elements assuming that the scattering matrix elements are jointly Gaussian. Then the assumptions and final results are compared with the experimental data acquired by polarimetric scatterometers in section 3.

2. THEORETICAL DERIVATION OF PHASE DIFFERENCE STATISTICS

The polarimetric response of a point or distributed target can be obtained by simultaneously measuring both the amplitude and phase of the scattered field using two orthogonal channels. If the incident and scattered field vectors are decomposed into their horizontal and vertical components, the polarimetric response can be represented by the scattering matrix S, which for plane wave illumination we can write

$$\mathbf{E}^s = \frac{e^{ikr}}{r} \left[\begin{array}{cc} S_{vv} & S_{vh} \\ S_{hv} & S_{hh} \end{array} \right] \mathbf{E}^i \qquad (1)$$

where r is the distance from the radar to the center of

the distributed target. It should be noted that in the backscattering case, reciprocity implies that $S_{vh} = S_{hv}$. Each element of the scattering matrix, in general, is a complex quantity characterized by an amplitude and a phase. When the radar illuminates a volume of a random medium or an area of a random surface, many point scatterers contribute to the total scattered energy received by the radar, and therefore each element of the scattering matrix may be represented by

$$S_{pq} = |S_{pq}|e^{i\phi_{pq}} = \sum_{n=1}^{N} |s_{pq}^n|e^{i\phi_{pq}^n} \qquad p,q = v,h \quad . \quad (2)$$

Here N is the total number of scatterers each having scattering amplitude $|s_{pq}^n|$ and phase ϕ_{pq}^n. It should be mentioned that the phase of each scatterer, as given in (2), includes a phase delay according to the location of the scatterer with respect to the center of the distributed target. Without loss of generality all multiple scattering over the surface or in the medium can be included in (2). Since the location of the scatterers within the illuminated area (volume) is random, the process describing the phasor s_{pq} is a Wiener process (random walk) [Davenport, 1970]. If N is large enough, application of the central limit theorem shows that the real and imaginary parts of the scattering matrix element S_{pq} are independent identically distributed zero mean Gaussian random variables. Equivalently, it can also be shown that $|S_{pq}|$ and ϕ_{pq} are Rayleigh and uniform independent random variables, respectively. The three elements of the scattering matrix, in general, can be viewed as a six-element random vector, and it is again reasonable to assume that the six components are jointly Gaussian.

Observation of polarimetric data for a variety of distributed targets such as bare soil surfaces and different kinds of vegetation-covered terrain all indicates that the cross-polarized component of the scattering matrix (S_{hv}) is statistically independent of the copolarized terms (S_{vv} and S_{hh}). Therefore the statistical behavior of S_{hv} can be obtained from a single parameter, namely, the variance (σ_c^2) of the real or imaginary part of $S_{hv} = X_5 + iX_6$; that is,

$$f_{X_5,X_6}(x_5,x_6) = \frac{1}{2\pi\sigma_c^2}\exp[-\frac{x_5^2 + x_6^2}{2\sigma_c^2}]$$

or equivalently the joint density function $|S_{vh}|$ and ϕ_{vh} is

$$f_{|S_{vh}|,\phi_{vh}}(|s_{vh}|,\phi_{vh}) = \frac{1}{2\pi\sigma_c^2}|s_{hv}|\exp[-\frac{|s_{hv}|^2}{2\sigma_c^2}] \quad , \quad (3)$$

which indicates that ϕ_{vh} is uniformly distributed between $(-\pi, +\pi)$.

Since measurement of the absolute phase of the scattering matrix elements is very difficult, it is customary to factor out the phase of one of the copolarized terms, for example S_{vv}, and therefore the phase difference statistics are of concern as opposed to the absolute phases. Since S_{hv} is assumed to be independent of S_{vv} (not a necessary assumption) and both ϕ_{hv} and ϕ_{vv} are uniformly distributed,

it can be easily shown that the cross-polarized phase difference $\phi_c = \phi_{vh} - \phi_{vv}$ is also uniformly distributed between $(-\pi, +\pi)$.

The copolarized elements of the scattering matrix, however, are dependent random variables which can be denoted by a four-component jointly Gaussian random vector $\mathbf{X}$. Let us define

$$S_{vv} = X_1 + iX_2, \qquad S_{hh} = X_3 + iX_4$$

and since $X_1, \cdots, X_4$ are Gaussian, their joint probability density function (pdf) can be fully determined by a 4 × 4 symmetric positive definite matrix known as covariance matrix Λ whose entries are given by [Davenport, 1979]

$$\lambda_{ij} = \lambda_{ji} = <X_i X_j> \qquad i,j \in \{1, \cdots, 4\} \quad .$$

The joint probability density function in terms of the covariance matrix takes the following form:

$$f_{\mathbf{X}}(x_1, \cdots, x_4) = \frac{1}{4\pi^2 |\Lambda|^{\frac{1}{2}}} \exp\left[-\frac{1}{2}\bar{\mathbf{X}}\Lambda^{-1}\mathbf{X}\right] \quad , \quad (4)$$

where $\bar{\mathbf{X}}$ is a transpose of the column vector $\mathbf{X}$. To characterize the covariance matrix, the following observations are in order. First, it was shown that the real and imaginary parts of the scattering matrix elements are mutually independent and identically distributed zero mean random variables; therefore

$$\lambda_{11} = \lambda_{22} = <X_1^2> = <X_2^2> \quad , \quad (5)$$

$$\lambda_{12} = <X_1 X_2> = 0 \quad , \quad (6)$$

$$\lambda_{33} = \lambda_{44} = <X_3^2> = <X_4^2> \quad , \quad (7)$$

$$\lambda_{34} = <X_3 X_4> = 0 \quad . \quad (8)$$

Second, it was shown that the absolute phase ϕ_{pp} is uniformly distributed and is independent of $|S_{pp}|$. Thus the random variable $\phi_{vv} + \phi_{hh}$ is also uniformly distributed and is independent of $|S_{vv}||S_{hh}|$ from which it can be concluded that

$$\begin{aligned} <|S_{vv}||S_{hh}|\cos(\phi_{vv} + \phi_{hh})> &= 0 \quad , \\ <|S_{vv}||S_{hh}|\sin(\phi_{vv} + \phi_{hh})> &= 0 \quad . \end{aligned} \quad (9)$$

In fact, the complex random variable $S_{vv}S_{hh}$ is obtained from a similar Wiener process which led to the random variables S_{vv} and S_{hh}. On the other hand

$$\begin{aligned} X_1 X_3 - X_2 X_4 &= |S_{vv}||S_{hh}|\cos(\phi_{vv} + \phi_{hh}) \quad , \\ X_1 X_4 + X_2 X_3 &= |S_{vv}||S_{hh}|\sin(\phi_{vv} + \phi_{hh}) \quad . \end{aligned} \quad (10)$$

In view of (9) and (10) it can easily be seen that

$$\lambda_{13} = \lambda_{24} \quad , \quad (11)$$

$$\lambda_{14} = -\lambda_{23} \quad . \quad (12)$$

The properties derived for the entries of the covariance matrix, as given by (5)-(8), (11), and (12), indicate that there are only four unknowns left in the covariance matrix,

namely λ_{11}, λ_{13}, λ_{14}, and λ_{33}, which can be obtained directly from the Mueller matrix of the target as will be shown next. The Mueller matrix relates the scattered wave Stokes vector to the incident wave Stokes vector by [van Zyl and Ulaby, 1990]

$$\mathbf{F}^s = \frac{1}{r^2}\mathbf{MF}^i \quad ,$$

where $\mathbf{F}^{i,s}$ are the modified incident and scattered wave Stokes vector defined by

$$\mathbf{F} = \begin{bmatrix} |E_v|^2 \\ |E_h|^2 \\ 2\Re[E_v E_h^*] \\ 2\Im[E_v E_h^*] \end{bmatrix} \quad .$$

The Mueller matrix can be expressed in terms of the elements of the scattering matrix as follows [Ulaby et al., 1987]

$$\mathbf{M} = \begin{bmatrix} |S_{vv}|^2 & |S_{vh}|^2 & \Re[S_{vh}^* S_{vv}] \\ |S_{hv}|^2 & |S_{hh}|^2 & \Re[S_{hh}^* S_{hv}] \\ 2\Re[S_{vv}S_{hv}^*] & 2\Re[S_{hv}S_{hh}^*] & \Re[S_{vv}S_{hh}^* + S_{hv}S_{vh}^*] \\ 2\Im[S_{vv}S_{hv}^*] & 2\Im[S_{hv}S_{hh}^*] & \Im[S_{vv}S_{hh}^* + S_{hv}S_{vh}^*] \end{bmatrix}$$

$$\bullet\bullet\bullet \begin{bmatrix} -\Im[S_{vh}^* S_{vv}] \\ -\Im[S_{hh}^* S_{hv}] \\ -\Im[S_{vv}S_{hh}^* - S_{hv}S_{vh}^*] \\ \Re[S_{vv}S_{hh}^* - S_{hv}S_{vh}^*] \end{bmatrix}$$

In the case of a random medium we are dealing with a partially polarized scattered wave, and the quantity of interest is the ensemble-averaged Mueller matrix. Using the assumption that the copolarized and cross-polarized terms of the scattering matrix are independent and employing the properties given by (5)-(8), (11), and (12), the Mueller matrix in terms of the entries of the covariance matrix is given by

$$\mathcal{M} = <\mathbf{M}> = \begin{bmatrix} 2\lambda_{11} & 2\sigma_c^2 & 0 & 0 \\ 2\sigma_c^2 & 2\lambda_{33} & 0 & 0 \\ 0 & 0 & 2\lambda_{13} + 2\sigma_c^2 & 2\lambda_{14} \\ 0 & 0 & -2\lambda_{14} & 2\lambda_{13} - 2\sigma_c^2 \end{bmatrix} \quad . \quad (13)$$

Equation (13) provides enough equations to determine the unknown elements of the covariance matrix and variance of the cross-polarized component, i.e.,

$$\begin{aligned} \sigma_c^2 &= \frac{\mathcal{M}_{12}}{2} \quad , \\ \lambda_{11} &= \frac{\mathcal{M}_{11}}{2} \quad , & \lambda_{33} &= \frac{\mathcal{M}_{22}}{2} \\ \lambda_{13} &= \frac{\mathcal{M}_{33} + \mathcal{M}_{44}}{4} \quad , & \lambda_{14} &= \frac{\mathcal{M}_{34} - \mathcal{M}_{43}}{4} \quad . \end{aligned}$$

With the covariance matrix the joint pdf of $X_1, \cdots, X_4$ can be obtained as given by (4). Using a rectangular to polar transformation, i.e.,

$$\begin{aligned} x_1 &= \rho_1 \cos\phi_{vv} \quad , & x_2 &= \rho_1 \sin\phi_{vv} \quad , \\ x_3 &= \rho_2 \cos\phi_{hh} \quad , & x_4 &= \rho_2 \sin\phi_{hh} \quad , \end{aligned}$$

the joint pdf of the amplitudes and phases takes the following form

$$f_{\rho_1,\rho_2,\Phi_{vv},\Phi_{hh}}(\rho_1,\rho_2,\phi_{vv},\phi_{hh}) = \frac{1}{4\pi^2\sqrt{\Delta}}\rho_1\rho_2$$

$$\cdot \exp\left\{-\frac{1}{2}[a_1\rho_1^2 + a_2\rho_2^2 - 2a_3\rho_1\rho_2]\right\} , \qquad (14)$$

where

$$\Delta = |\Lambda| = \left(\lambda_{11}\lambda_{33} - \lambda_{13}^2 - \lambda_{14}^2\right)^2 ,$$
$$a_1 = \lambda_{33}/\sqrt{\Delta} , \qquad a_2 = \lambda_{11}/\sqrt{\Delta} ,$$
$$a_3 = [\lambda_{13}\cos(\phi_{hh} - \phi_{vv}) + \lambda_{14}\sin(\phi_{hh} - \phi_{vv})]/\sqrt{\Delta}.$$

To obtain the copolarized phase difference statistics, the joint density function of ϕ_{vv} and ϕ_{hh} is needed which can be obtained from

$$f_{\Phi_{vv},\Phi_{hh}}(\phi_{vv},\phi_{hh}) = \int_0^\infty\int_0^\infty f_{\rho_1,\rho_2,\Phi_{vv},\Phi_{hh}}(\rho_1,\rho_2,\phi_{vv},\phi_{hh})$$

$$d\rho_1 d\rho_2. \qquad (15)$$

Noting that a_1 is a positive real number, the integration with respect to ρ_1 can be carried out which results in

$$f_{\Phi_{vv},\Phi_{hh}}(\phi_{vv},\phi_{hh}) = \frac{1}{4\pi^2\sqrt{\Delta}}\left\{\frac{1}{a_1}\int_0^\infty \rho_2 e^{-\frac{a_2}{2}\rho_2^2}d\rho_2 + \right.$$

$$\sqrt{\frac{\pi}{8a_1^3}}a_3\int_0^\infty \rho_2^2\left[1 \pm \text{erf}(\frac{|a_3|}{\sqrt{8a_1}}\rho_2)\right]$$

$$\left. e^{-\frac{1}{2a_1}(a_1a_2-a_3^2)\rho_2^2}d\rho_2\right\} , \qquad (16)$$

where erf( ) is the error function and the plus or minus sign is used according to the sign of a_3. To evaluate the integrals in (16), we need to show that both a_2 and $a_1a_2 - a_3^2$ are positive numbers. By definition, a_2 is positive, and to show $a_1a_2 - a_3^2$ is positive, we note that Λ is a symmetric positive definite matrix, therefore its eigenvalues must be positive. It can be shown that Λ has two distinct eigenvalues, γ_1 and γ_2, each with multiplicity 2, and their product is given by

$$\gamma_1\gamma_2 = \lambda_{11}\lambda_{33} - \lambda_{13}^2 - \lambda_{14}^2 > 0.$$

Thus

$$a_1a_2 - a_3^2 = \gamma_1\gamma_2 + [\lambda_{13}\cos(\phi_{hh} - \phi_{vv}) \\ -\lambda_{14}\sin(\phi_{hh} - \phi_{vv})]^2$$

is positive. After integrating the first integral and the first term of the second integral in (16) directly and using integration by parts on the second term of the second integral, (16) becomes

$$f_{\Phi_{vv},\Phi_{hh}}(\phi_{vv},\phi_{hh}) = \frac{1}{4\pi^2\sqrt{\Delta}}\left\{\frac{1}{a_1a_2} + \frac{a_3^2}{a_1a_2(a_1a_2 - a_3^2)}\right.$$

$$+\frac{\sqrt{\pi}|a_3|}{\sqrt{8a_1}(a_1a_2 - a_3^2)}\int_0^\infty \text{erf}(\frac{|a_3|}{\sqrt{8a_1}}\rho_2)$$

$$\left. e^{-\frac{1}{2a_1}(a_1a_2-a_3^2)\rho_2^2}d\rho_2\right\} .$$

By expanding the error function in terms of its Taylor series, interchanging the order of summation and integration, and then using the definition of the gamma function, it can be shown that

$$\int_0^\infty \text{erf}(\frac{|a_3|}{\sqrt{8a_1}}\rho_2)e^{-\frac{1}{2a_1}(a_1a_2-a_3^2)\rho_2^2}d\rho_2 = \sqrt{\frac{2a_1}{\pi(a_1a_2 - a_3^2)}}$$

$$\tan^{-1}\left(\frac{|a_3|}{2\sqrt{a_1a_2 - a_3^2}}\right) .$$

The joint density function of ϕ_{vv} and ϕ_{hh} is a periodic function of $\phi = \phi_{hh} - \phi_{vv}$, and therefore the random variable ϕ, after some algebraic manipulation, can be shown to have the following pdf over the interval $(-\pi, +\pi)$

$$f_\Phi(\phi) = \frac{\lambda_{11}\lambda_{33} - \lambda_{13}^2 - \lambda_{14}^2}{2\pi(\lambda_{11}\lambda_{33} - D^2)}\left\{1 + \frac{D}{\sqrt{\lambda_{11}\lambda_{33} - D^2}}\right.$$

$$\left.\left[\frac{\pi}{2} + \tan^{-1}\frac{D}{\sqrt{\lambda_{11}\lambda_{33} - D^2}}\right]\right\} , \qquad (17)$$

where we recall that

$$D = \lambda_{13}\cos\phi + \lambda_{14}\sin\phi$$

and the elements of the covariance matrix in terms of the Mueller matrix elements are given by

$$\lambda_{11} = \frac{\mathcal{M}_{11}}{2} , \qquad \lambda_{33} = \frac{\mathcal{M}_{22}}{2} ,$$
$$\lambda_{13} = \frac{\mathcal{M}_{33} + \mathcal{M}_{44}}{4} , \qquad \lambda_{14} = \frac{\mathcal{M}_{34} - \mathcal{M}_{43}}{4} .$$

Some limiting cases can be considered in order to check the validity of (17). For example, when S_{vv} and S_{hh} are uncorrelated, then both λ_{13} and λ_{14} are zero for which $f_\Phi(\phi) = 1/(2\pi)$, as expected. Also, for the case of completely polarized scattered wave where S_{vv} and S_{hh} are completely correlated, the determinant of Λ is zero, and so $f_\Phi(\phi)$ is a delta function.

It is interesting to note that the pdf of the phase difference is only a function of two parameters defined by

$$\alpha = \sqrt{\frac{\lambda_{13}^2 + \lambda_{14}^2}{\lambda_{11}\lambda_{33}}} , \qquad \zeta = \tan^{-1}\frac{\lambda_{14}}{\lambda_{13}}$$

where α and ζ can vary from 0 to 1 and $-\pi$ to π, respectively. In fact, if the wave were completely polarized, ζ

would have been the phase difference between the copolarized terms. The parameter ζ will henceforth be referred to as the polarized phase difference. In terms of these parameters, (17) can be written as

$$f_\phi(\phi) = \frac{1-\alpha^2}{2\pi[1-\alpha^2\cos^2(\phi-\zeta)]}\left\{1+\frac{\alpha\cos(\phi-\zeta)}{\sqrt{1-\alpha^2\cos^2(\phi-\zeta)}}\right.$$

$$\left.\left[\frac{\pi}{2}+\tan^{-1}\frac{\alpha\cos(\phi-\zeta)}{\sqrt{1-\alpha^2\cos^2(\phi-\zeta)}}\right]\right\}. \quad (18)$$

It can be shown that the maximum of the pdf occurs at $\phi = \zeta$ independent of α. However, the width of the pdf (e.g., the 3-dB angular width) is only a function of α which will be referred to as the degree of correlation. The probability distribution function given by (18) is the analog of Gaussian distribution for periodic random variables where ζ and α are the counterparts of the mean and variance for Gaussian random variables, respectively. Figure 1 shows the pdf for different values of ζ while keeping α constant, and Figure 2 shows the pdf for a fixed value of ζ while changing α as a parameter. The calculated mean and standard deviation of the phase difference as a function of both the polarized phase difference and the degree of correlation are depicted in Figures 3 and 4, respectively.

Last, it is necessary to point out that the formulation

Fig. 2. The probability density function of the copolarized phase difference for a fixed value of ζ (coherent phase difference) and four values of α (degree of correlation).

of the copolarized phase difference pdf, as given in (17), is not restricted to the backscattering case or to the copolarized and cross-polarized components being uncorrelated. In fact, we can derive the cross-polarized phase difference statistics in a similar manner, and the pdf in this case for the backscattering case can be obtained from (17) upon the following substitution for the elements of the cross-polarized covariance matrix

$$\lambda_{11} = \frac{\mathcal{M}_{11}}{2}, \qquad \lambda_{33} = \frac{\mathcal{M}_{12}}{2},$$
$$\lambda_{13} = \frac{\mathcal{M}_{13}}{2}, \qquad \lambda_{14} = \frac{\mathcal{M}_{14}}{2}.$$

3. COMPARISON WITH MEASUREMENTS

Using the polarimetric data gathered by scatterometers from a variety of natural targets, the assumptions leading to the pdf of phase differences as derived in the previous section are examined. Also, by generating the histograms, means, and standard deviations of the phase differences from the data and comparing them with the results based on the pdf derived from the measured Mueller matrices, validity of the model is also examined. The polarimetric radar measurements of bare soil surfaces were performed at L-, C-, and X-band frequencies for a total of eight different soil surface conditions (four roughness and two moisture conditions). For this experiment we tried to preserve the absolute phase of the measured scattering matrix by calibrating the surface data with a metallic sphere located
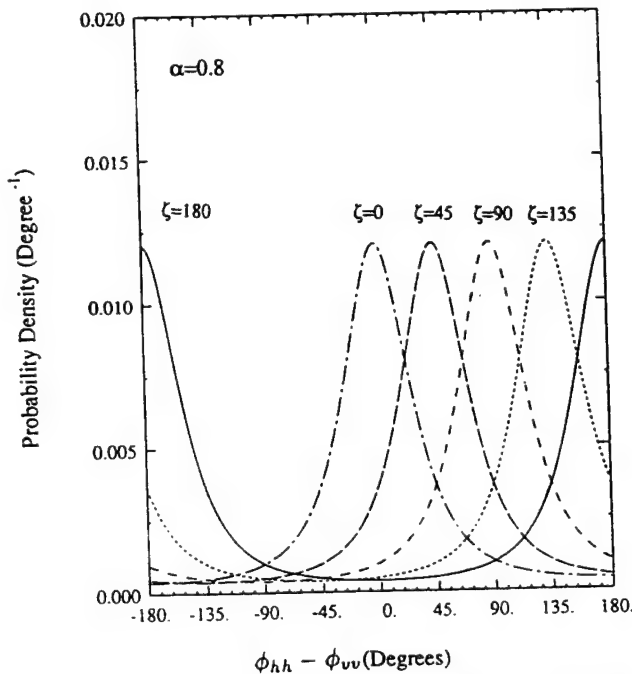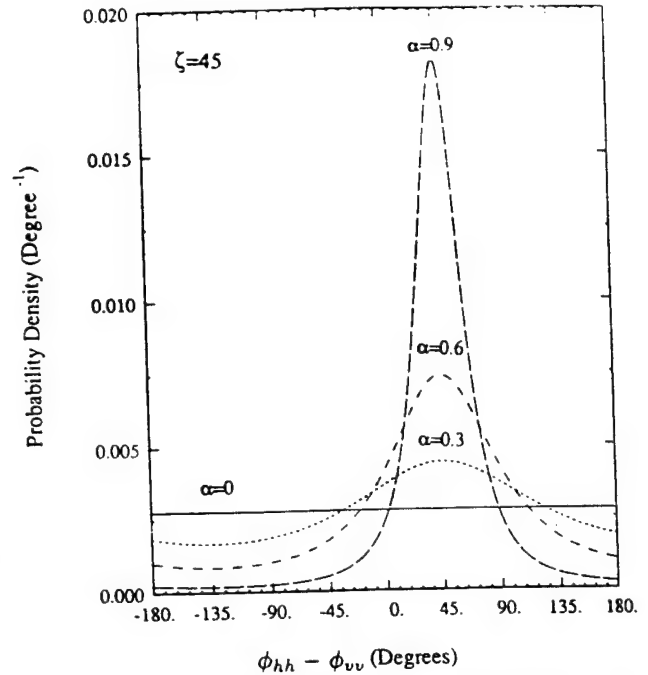

Fig. 1. The probability density function of the copolarized phase difference for a fixed value of α (degree of correlation) and five values of ζ (coherent phase difference).
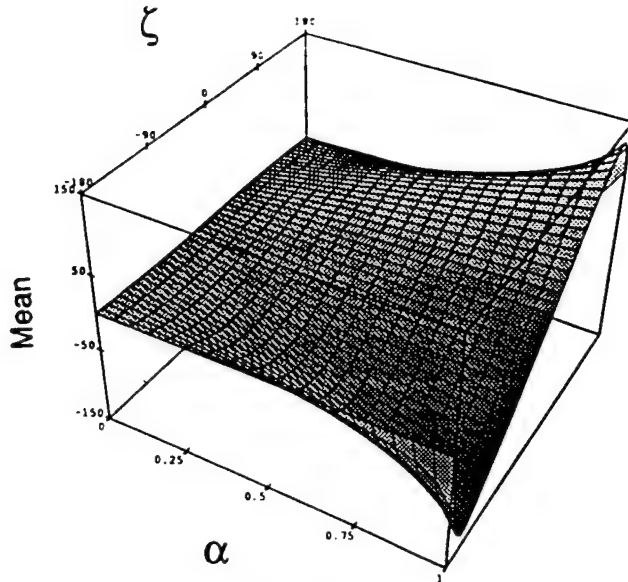
Fig. 3. The mean value of the copolarized phase difference as a function of α (degree of correlation) and ζ (coherent phase difference).

at the same distance from the radar as the center of the surface target. For each frequency, surface condition, and incidence angle a minimum of 700 independent samples were collected. The detailed procedure of the data collection and calibration is given by Sarabandi et al. [1991].

By generating the histograms of the real and imaginary
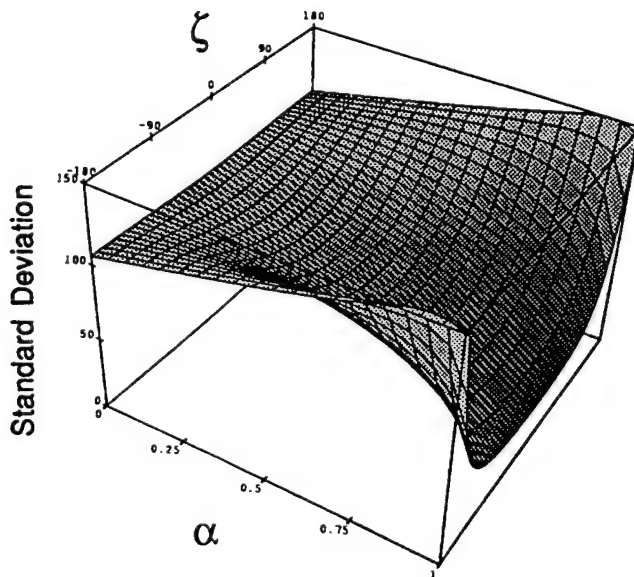
Fig. 4. The standard deviation of the copolarized phase difference as a function of α (degree of correlation) and ζ (coherent phase difference).
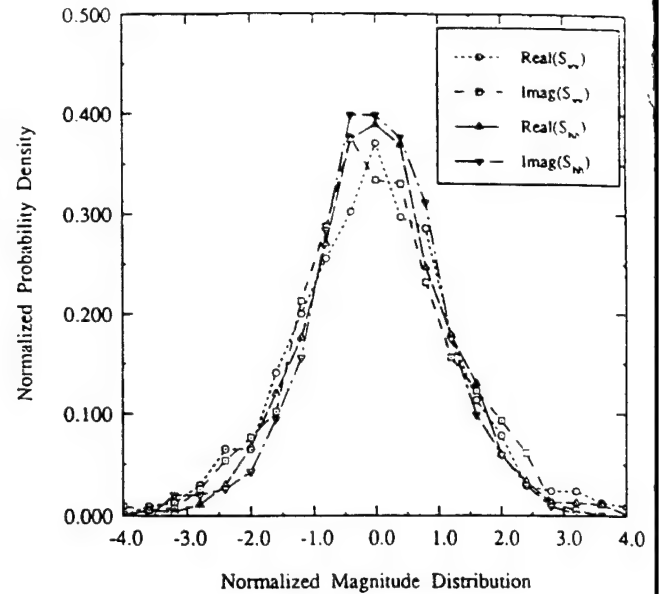
Fig. 5. The histogram of the real and imaginary parts of S_{vv} and S_{hh} for a rough surface with a rms height of 0.32 cm and a correlation length of 9.9 cm at C-band and at a 30° incidence angle.

parts of the elements of the scattering matrix for all surfaces, it was found that they have a zero mean Gaussian distribution as we assumed. Figure 5 represents a typical case where the histogram of the real and imaginary
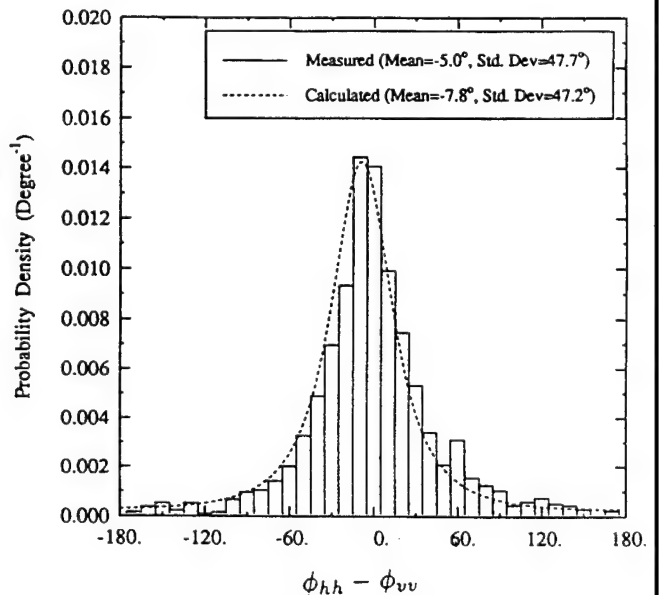

Fig. 6. The histogram and pdf of the copolarized phase difference for a rough surface with a rms height of 0.32 cm and a correlation length of 9.9 cm at C-band and at a 30° incidence angle.
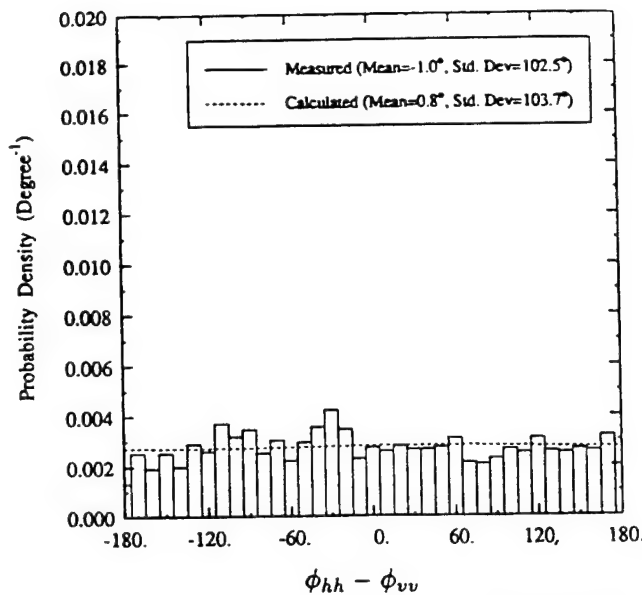
Fig. 7. The histogram and pdf of the cross-polarized phase difference for a rough surface with rms height of 0.32 cm and correlation length of 9.9 cm at C-band and at a 30° incidence angle.
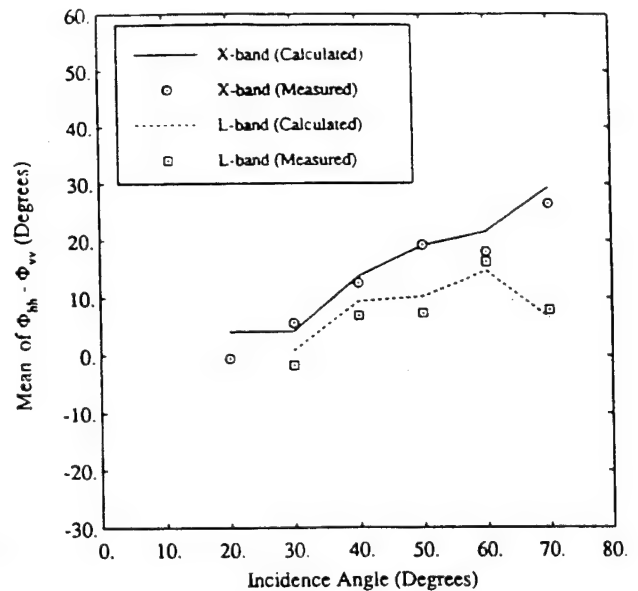

Fig. 8. Angular dependency of the mean of the copolarized phase difference for a dry rough surface with a rms height of 0.4 cm and a correlation length of 8.4 cm at L- and X-band.

parts of S_{vv} and S_{hh} of a dry surface with a rms height of 0.32 cm and correlation length of 9.9 cm at C-band has a bell-shaped distribution. The properties of the covariance matrix as given by (5)-(8) and (11)-(12), are verified by calculating the covariance matrices of the data for all cases. The normalized vocariance matrix of the surface with rms height .3 cm and correlation length 9 cm at C-band is given by

$$\Lambda = \begin{bmatrix} 1.00 & 0.03 & 0.75 & -0.12 \\ 0.03 & 0.90 & 0.08 & 0.68 \\ 0.75 & 0.08 & 0.77 & 0.05 \\ -0.12 & 0.68 & 0.05 & 0.69 \end{bmatrix}$$

where it possesses the mentioned properties approximately; that is, $\lambda_{11} \approx \lambda_{22}$, $\lambda_{12} \approx \lambda_{34} \approx 0$, $\lambda_{33} \approx \lambda_{44}$, $\lambda_{13} \approx \lambda_{24}$, and $\lambda_{14} \approx -\lambda_{23}$. The small discrepancies are due to the fact that the measurement of the scattering matrix with absolute phase has an uncertainty of $\pm 30°$.

The Mueller matrix of the typical surface at C-band is given by

$$\mathcal{M} = \begin{bmatrix} 1.000 & 0.030 & 0.000 & 0.000 \\ 0.028 & 0.767 & 0.000 & 0.000 \\ 0.000 & 0.000 & 0.770 & -0.11 \\ 0.000 & 0.000 & 0.110 & 0.711 \end{bmatrix}$$

from which the copolarized and cross-polarized phase difference pdfs are calculated using (17) and are compared with the measured phase histograms in Figures 6 and 7, respectively. Similar comparisons were also made for the rest

of surfaces, frequencies, and incidence angles, and it was found that the expression (17) predicts the density functions very accurately. Some examples of these comparisons are shown in Figures 8 and 9. Figures 8 and 9 compare
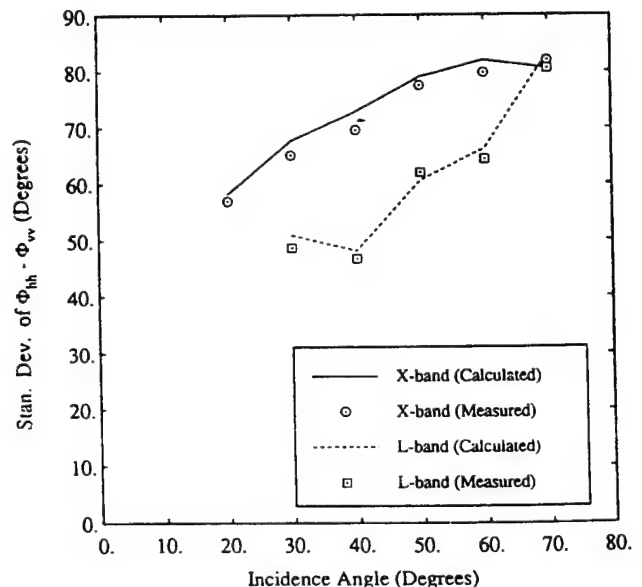

Fig. 9. Angular dependency of the standard deviation of the copolarized phase difference for a dry rough surface with a rms height of 0.4 cm and a correlation length of 8.4 cm at L- and X-band.

the mean and standard deviation of the copolarized phase difference versus incidence angle at L- and X-band for a surface with rms height of 0.4 cm and correlation length of 8.4 cm in dry conditions using the results based on the direct calculation and the results derived from (17).

4. CONCLUSIONS

Prompted by the experimental observations which show strong dependence of phase differences of the scattering matrix elements on the physical parameters of random media, the statistical behavior of the phase differences for distributed targets is studied. The pdfs of the phase differences are derived from the Mueller matrix of the target. In derivation of the density functions it is assumed that the real and imaginary parts of the copolarized and cross-polarized terms of the scattering matrix are jointly Gaussian and their covariance matrices are found in terms of the Mueller matrix elements. The functional forms of the copolarized and cross-polarized density functions are similar and are obtained independently. It is shown that the density function of the phase difference is completely determined in terms of only two parameters. The assumptions and final expressions are verified by using a set of polarimetric data acquired by scatterometers from rough surfaces.

REFERENCES

Davenport, W. B., *Probability and Random Processes*, McGraw-Hill, New York, 1970.

Ioannidis, G. A. and D. E. Hammers, Optimum antenna polarization for target discrimination in clutter,' *IEEE Trans. Antennas Propag.*, AP- 27(3), 357-363, 1979.

Meads, J. B., and R. E. McIntosh, Polarimetric backscatter measurements of deciduous and coniferous trees at 225 GHz,' *IEEE Trans. Geosci. Remote Sens.*, 29(1), 21-28, 1991.

Sarabandi, K., Y. Oh, and F. T. Ulaby, Polarimetric radar measurement of bare soil surfaces at microwave frequencies, paper presented at IEEE Geoscience and Remote Sensing Symposium, Institute of Electrical and Electronic Engineering, Espoo, June 1991.

Tsang, L., J. A. Kong, and R. T. Shin, *Theory of Microwave Remote Sensing*, John Wiley, New York, 1985.

Ulaby, F. T., D. Held, M. C. Dobson, K. C. McDonald, and T. B. A. Senior, Relating polarization phase difference of SAR signals to scene properties, *IEEE Trans. Geosci. Remote Sens.*, 25(1), 83-92, 1987.

van Zyl, J. J., and F. T. Ulaby, *Radar Polarimetry for Geoscience Applications*, edited by F. T. Ulaby and C. Elachi, Chap. 2, Artech House, Norwood, Mass. 1990.

Zebker, H. A., J. J. van Zyl, and D. N. Held, Imaging radar polarimetry from wave synthesis, *J. Geophys. Res.*, 92(B1), 683-701, 1987.

K. Sarabandi, Radiation Laboratory, 3225 EECS Bldg., University of Michigan, Ann Arbor, MI 48109-2111.

WILLIAM M. POLIVKA
IBM Federal Systems Company
Owego, NY

REFERENCES

[1] Vorperian, V. (1990)
       Simplified analysis of PWM converters using the model of
       the PWM switch: Parts I and II.
       IEEE Transactions on Aerospace and Electronic Systems,
       26, 3 (May 1990), 490–505.

[2] Maksimovic', D., and C'uk, S. (1991)
       A unified analysis of PWM converters in discontinuous
       modes.
       IEEE Transaction on Power Electronics, 6, 3 (July 1991).

[3] C'uk, S., and Middlebrook, R. D. (1977)
       A general unified approach to modelling switching dc-to-dc
       converters in discontinuous conduction mode.
       IEEE Power Electronics Specialists Conference Record,
       1977, pp. 36–57; IEEE Publication 77 CH 12-13-8AES.

[4] Chetty, P. R. K. (1982)
       Current injected equivalent circuit approach to modeling
       of switching dc-dc converters in discontinuous inductor
       conduction mode.
       IEEE Transactions on Industrial Electronics, IE-29, 3 (Aug.
       1982), 230–234.

[5] Smedley, K. S., and C'uk, S. (1990)
       One cycle control of switching converters.
       IEEE Power Electronics Specialists Conference Record,
       1990, pp. 888–896; IEEE Publication 91CH3008-0.

[6] C'uk, S. (1976)
       Modelling, analysis, and design of switching converters.
       Ph.D. dissertation, California Institute of Technology,
       Pasadena, Nov. 1976.

[7] Middlebrook, R. D., and C'uk, S. (1976)
       A general unified approach to modelling switching
       converter power stages.
       IEEE Power Electronics Specialists Conference Record,
       1976, pp.18–34; IEEE Publication 76 CHO 1084-3AES.

[8] Krien, P. T., Bentsman, J., Bass, R. M., and Lesieutre, B. C.
       (1990)
       On the use of averaging for the analysis of power
       electronic systems.
       IEEE Transactions on Power Electronics, 5, 2 (Apr. 1990),
       182–190.

[9] Sanders, S. R., Noworolski, J. M., Liu, X. Z., and Verghese,
       G. C. (1991)
       Generalized averaging method for power conversion
       circuits.
       IEEE Transactions on Power Electronics, 6, 2 (Apr. 1991).

Power Lines: Radar Measurements and Detection Algorithm for Polarimetric SAR Images

Polarimetric radar backscattering measurements of a variety
of powerline cables are presented. The objective of the first part
of the investigation was to study the effect of braiding of the
cables on the backscattering at skew incidence. The measurements
were performed for four different actual size powerline samples
at C-, X-, and Ka-band over a wide range of incidence angles.
The data were collected over a 500 MHz bandwidth at C- and
X- band with a 1.25 MHz increment and a 1 GHz bandwidth at
Ka-band with a 2.5 MHz increment. Also the effect of nonuniform
illumination and measurement in the near field of the cables were
studied. Experimental data shows a significant radar backscatter
for VV-polarization (σ_{vv}) at angles away from normal incidence.
This backscatter is proportional to the number and diameter of
the strands on the surface of the cables. There is also noticeable
backscatter for the HH and VH components of the scattering
matrices. Their magnitudes, relative to that of the VV component,
are proportional to the pitch angle of the helix.

Since detection of these cables is an important safety issue
for low-flying airplanes a detection algorithm using polarimetric
synthetic aperture radar (SAR) images was developed using the
knowledge gleaned from the measurements.

The detection algorithm was tested on a simulated image and
worked well, detecting a power line whose backscatter power was 6
dB below the average background power.

I. INTRODUCTION

Detection and collision avoidance of obstacles
of small physical cross section has always been
an important problem for low-flying aircrafts.
High voltage powerlines and powerline towers are
particularly hazardous in this respect.

Many collision warning techniques have been
suggested in the past. Among the most promising
techniques are laser radar [Savan and Barr, 1988]
and millimeter wave radar [Rembold et al., 1982],
particularly the latter when used in the synthetic
aperture imaging mode. Available methods, however,
suffer from a number of shortcomings. A major
limitation of laser systems is atmospheric attenuation
under fog and cloudy conditions, which would hamper

target detection considerably. The problem with microwave and millimeter wave radars lies in the fact that current models used for characterizing the scatter by powerlines are inadequate. The radar uses a linearly polarized wave and transmission lines are modeled as long perfectly conducting circular cylinders [Rembold, 1984]. The description imposes a significant restriction on the ability of radar to detect powerlines. The choice of frequency and polarization have not been examined in previous measurements and models in order to optimize the detection of powerlines by radars. The fact that a high voltage powerline is made up of strands of wires in a helical arrangement can be exploited with regard to backscattering detection of the ,powerlines. At high frequencies the helical geometry of powerlines becomes an important factor influencing the scattering behavior of electromagnetic waves which can be taken advantage of in detecting powerlines at off-specular directions. The surface of the cables is periodic along the axis of the cables and usually the period is only a fraction of the helical pitch. The effect of the helicity and the periodicity of the surface in backscatter at incidence angles away from normal incidence is investigated in this report.

Here we present the polarimetric backscatter response of four different types of powerline cables at C-, X-, and Ka-band. Experimental data are collected over a wide range of incidence angles and for two different cable lengths. In one case the cable length is chosen such that the illumination is uniform, and in the other case the cable is long and the illumination is nonuniform. In the case of nonuniform illumination on a cable, the scattering matrix of a smooth cylinder of identical length and diameter is also measured for comparison. First the measurement setup and the radar configurations are discussed briefly and then a polarimetric calibration procedure used in support of these measurements is mentioned. Next, the radar cross section measurements and significant results are given. Finally, an algorithm is presented to detect power lines in polarimetric synthetic aperture radar (SAR) images and it is tested on a simulated image.

II. MEASUREMENT

A. System Configuration and Setup

The polarimetric measurements of the powerline cables were performed by C-, X-, and Ka-band scatterometers. The scatterometers are HP 8753-based (8753A for C- and X-band and 8753C for Ka-band) systems with both phase and amplitude measurement capability and 100 dB dynamic range. The ability of the network analyzer to generate the time domain response of the frequency measurements allows the removal of the unwanted short-range signals from the desired target response (known as software gating). It also allows the separation of the contributions from

different scattering points within the target under investigation. The C- and X-band scatterometers are slightly different from the Ka-band system. The C- and X-band system are single antenna radars while the Ka-band is a dual antenna system. The sequence of polarization selection, data collection, and target orientation is performed via an HP 9000 series computer. A relay actuator energizes frequency and polarization switches. An amplifier and pulsing network eliminate the short-range returns from the antenna and circulators helps to increase the dynamic range for the radar cross section (RCS) measurements [Liepa et al., 1989]. The pulsing network is not used for the Ka-band system since there is enough isolation between the transmitter and the receiver. In this scheme, the receiver is switched off during transmission and then reconnected when the target return is expected to arrive at the receiver. Since the switching is done at a much higher rate than the bandwidth of the receiver, the network analyzer does not sense that the incoming signal is pulsed and it is measured as if it were a continuous wave signal.

The synthesized source of the network analyzer spans the frequency range 300 KHz to 3 GHz and therefore up- and down-convertors are used to transmit and receive the desired frequencies. The up-convertors for the C- and X-band units are very stable microwave sources operating at 6.5 and 8 GHz, respectively. The frequency range of the network analyzer is set to 1.5–2 GHz and 1.25–1.75 GHz, respectively, in order to operate the C- and X-band scatterometer at 4.5–5 and 9.25–9.75 GHz. The antenna for each system is comprised of an orthomode transducer (OMT) and a dual-polarized square horn with an overall cross-polarization isolation of 20 dB.

The Ka-band scatterometer can operate in both the coherent and coherent-on-receive modes [Kuga et al., 1991]. In the coherent mode the scattering matrix of the target can be measured and in the coherent-on-receive mode the scatterometer measures the Mueller matrix of the target directly. In this study the coherent mode of the scatterometer is used. The dual channel capability of the HP 8753C allows simultaneous measurements of V and H channels in coupled/chop mode. Point by point external triggering is used for transmitting V and H sequentially and for synchronizing a polarization control circuit to create different polarizations. This scatterometer is a two-antenna system with at least 70 dB isolation between the transmitter and the receiver. The polarization selection in the transmitter is accomplished by a Faraday rotator and in the receiver by an OMT. The antennas in both the transmit and receive channels are lens-corrected corrugated circular horns. The local oscillator is a 32 GHz Gunn diode which is stabilized by an injection locking technique. Table I gives the important specifications of the scatterometer systems.

TABLE I
System Specifications of Scatterometers

	C-band	X-band	Ka-band
Center Frequency (GHz)	4.75	9.5	34.5
Bandwidth (MHz)	500	500	1000
Antenna Gain (dB)	25.3	29.5	32.5
Beamwidth (deg.)	9	6	5
Far field distance (m)	5.8	10.5	5.5
Cross-pol isolation (dB)	25	20	25
Output power (mW)	100	100	100
Minimum detectable target at 15 m (dBsm)	-35 (co-pol.) -60 (cross-pol.)	-45 (co-pol) -65 (cross-pol.)	-45 (co-pol.) -65 (cross-pol.)
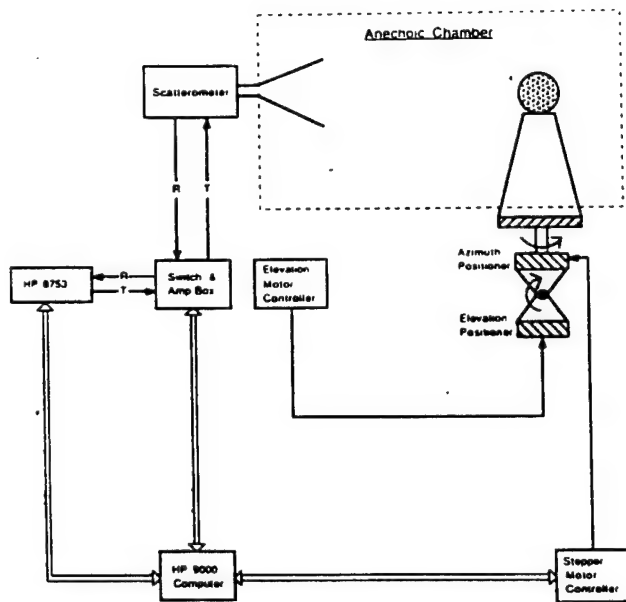
Fig. 1. Automatic radar cross section measurement setup.

To measure the backscatter of the cables with a very good signal to background ratio for all incidence angles, the cables were mounted on a styrofoam pedestal in an anechoic chamber. Positioning of the cables with respect to the antenna coordinate system was accomplished by an azimuth-over- elevation positioner as depicted in Fig. 1. The azimuth turntable is a computer controlled stepper motor with an accuracy of a fraction of a tenth of a degree and the elevation controller is a precise analog positioner.

B. Calibration Procedure

To obtain accurate measurements of the scattering matrices of the cables, the measured data must be calibrated. In this study the scatterometers are calibrated using the single-target calibration technique (STCT) [Sarabandi and Ulaby, 1990]. The error in measurement of the scattering matrix using this technique is less than 0.5 dB in magnitude and less than 5° in phase. With STCT the antenna cross-talk contamination and channel imbalances are obtained by measuring only a single calibration target, namely a metallic sphere. This technique is immune to errors caused by target alignment with respect to the antenna coordinate system.

STCT was developed for single antenna radars, thus its application in the Ka-band scatterometer is questionable. However, measurements of targets with known scattering matrices with the Ka-band system show that STCT is capable of improving the cross-polarization isolation of the antenna system.

C. Experimental Results

High voltage transmission line cables are usually constructed from a number of aluminum strands twisted around a central core of one or more steel strands in a helical fashion. The number of layers and diameter of aluminum strands determines the current capacity of the cable. In a distribution network, however, low tension and high current cables are used which are made of either copper or aluminum strands. Four different types of powerline cables were acquired for this experiment and their electrical and geometrical specifications are listed in Table II. Also the geometry of the cross section of the powerline samples are depicted in Fig. 2. The important parameters of the cables, as far as electromagnetic scattering is concerned, are the outer surface geometry such as the cable diameter, diameter of each strand, the pitch of the helices, and the surface period along the axis of the cable as shown in Fig. 3.

The powerline cables are targets of extended length, that is the length of the cables, in all practical situations, extends beyond the footprint of the illumination area. Thus in reality the cables are illuminated with a tapered wave and the radar may be in the near field of the target. In this case the radar echo is a function of not only the geometry but also the radiation pattern and the distance. In contrast, the far field measurement reveals both the main scattering features and a unique quantitative value for the radar echo independent of the radiation pattern. In this study we use cables with two different lengths, short and long. For short cables uniform

No	Circular Mils (MCM)	Copper # St	Copper d (cm)	D (cm)	Current Capacity (Amps)	P (cm)	L (cm)
1	167.8	7	0.400	1.20	420	11.60	1.95

No	Circular Mils (MCM)	Aluminum # St	Aluminum d (cm)	Steel # St	Steel d (cm)	D (cm)	Current Capacity (Amps)	P (cm)	(cm)
2	556.5	19	0.446	.	.	2.22	730	23.5	1.52
3	954	54	0.337	7	0.337	3.01	1010	35.56	2.00
4	1431	45	0.446	7	0.301	3.52	1300	40.65	2.40

Note: See Fig. 3 for definitions of some of the symbols.

167.8 MCM (Copper)

954 MCM (Aluminum & Steel)

1431 MCM (Aluminum & Steel)

556.5 MCM (Aluminum)
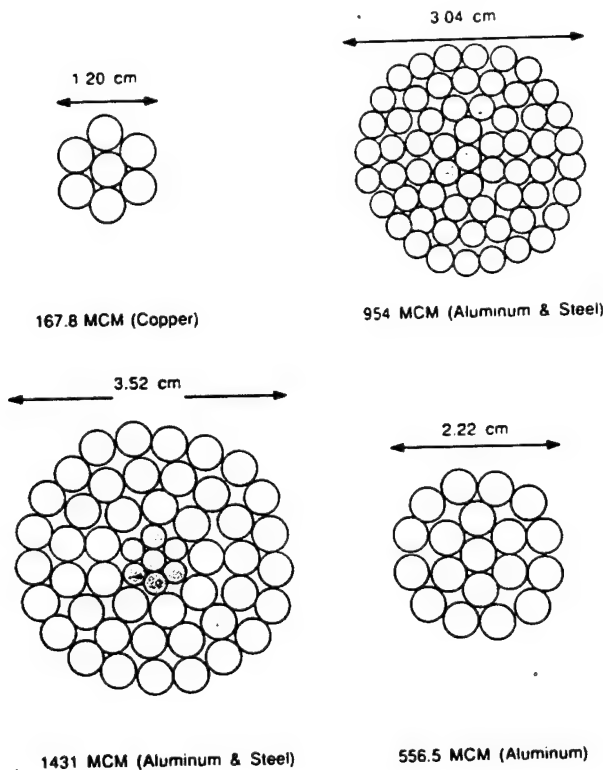
Fig. 2. Cross section of powerline samples.

d: Stranded conductor diameter
D: Overall outside diameter
L: Spacing between surfaces
P: Spacing between turns
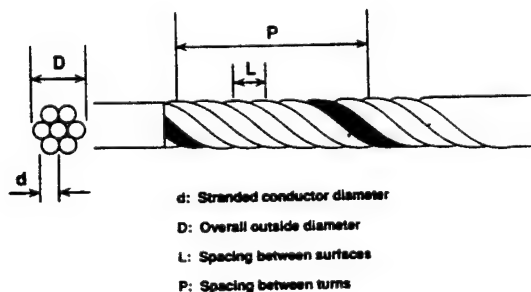
Fig. 3. Geometry of powerline cable.

Fig. 4. Geometry of radar system above powerline cable.

cylinders of similar lengths and diameters to study the effect of braiding on the cables. A series of scattering matrix measurements of powerline cables and smooth cylinders is performed at C-, X-, and Ka-band over the frequency ranges 4.5–5 GHz, 9.25–9.75 GHz, and 34–35 GHz, respectively. All the data presented in this report are measurements at the center frequencies, namely 4.75 GHz for C-band, 9.5 GHz for the X-band, and 34.5 GHz for Ka-band.

The scattering matrix measurements were performed in an 18 m long anechoic chamber at a distance of 13 m. The targets are mounted on a styrofoam pedestal to get a minimal background contribution. The styrofoam pedestal is practically invisible at C- and X-band but at Ka-band its radar cross section is considerable (about −30 dBsm). To remove the contribution of the background and the effects of multiple reflection within the radar system, the chamber and pedestal are measured in the absence of targets and then subtracted from the target response. A 30.5 cm and a 4.45 cm metallic spheres are used for C-, X-band and the Ka-band system as calibration targets, respectively. The signal to noise ratio was better than 30 dB in all cases.

The cables are positioned in the horizontal plane (H-plane) of the antenna system and the radiation

illumination and far field criteria are satisfied and for long cables the illumination is nonuniform and the radar is in the near field of the cables. The measured radiation pattern and radar cross section of the long cable are compared with those measured for smooth
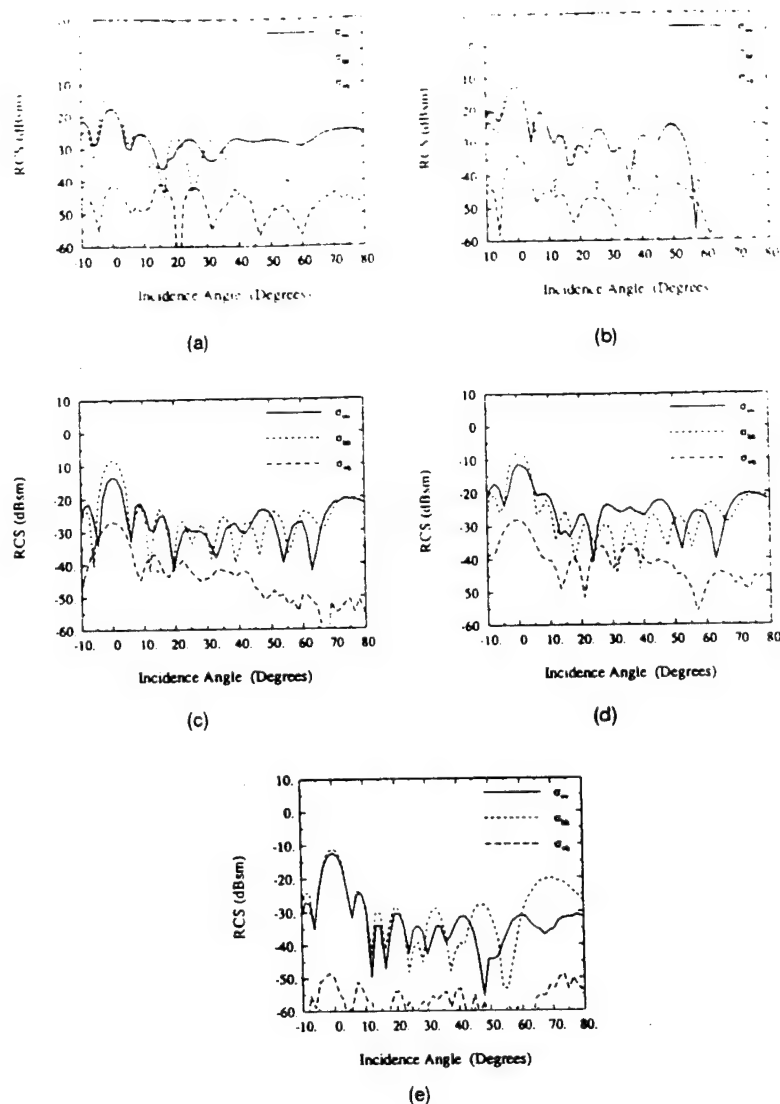
CORRESPONDENCE

Fig. 5. Radar backscatter cross section for 30 cm long cable. (a) Cable 1. (b) Cable 2. (c) Cable 3. (d) Cable 4. (e) Smooth cylinder of diameter 1.27 cm, at 4.75 GHz.

patterns are measured in the principal plane, that is the axis of rotation is perpendicular to the horizontal plane. Accurate orientation of the cables with respect to the antenna system is achieved by a stepper motor positioner with an accuracy of a fraction of a tenth of a degree. This cable orientation is similar to that of radar systems mounted on low-flying aircraft where the powerlines are in the horizontal plane. In the detection of powerlines using SARs, however, the results of this experiment must be transformed to account for the different viewing geometry. When a powerline cable is not in the principal plane of the radar antenna, the circular symmetry of the powerline cables can be used to obtain its scattering matrix from the scattering matrix of the cable in the principal plane. Fig. 4 shows the relative positions of a radar system and a powerline. The plane of incidence, which includes the cable axis and the direction of incidence, intersects the antenna polarization plane, which includes the vertical and horizontal directions of the antenna, along a unit

vector $\hat{h}'$. If the antenna coordinate frame is rotated by an angle ψ such that $\hat{h}$ and $\hat{h}'$ coincide, then the horizontal principal plane and the plane of incidence would also coincide for the case in which the scattering matrix is known. For known values of polar direction of the cable axis (ϕ) and incidence angle (θ), the coordinate frame rotation angle (ψ) can be obtained from

$$\psi = \tan^{-1}[\cos\theta\tan\phi]. \tag{1}$$

The scattering matrix of the cable in this situation S, in terms of the scattering matrix of the cable in the principal plane S_P, can be obtained from

$$\mathbf{S} = \begin{bmatrix} S_{vv} & S_{vh} \\ S_{hv} & S_{hh} \end{bmatrix}$$

$$= \begin{bmatrix} \cos\psi & -\sin\psi \\ \sin\psi & \cos\psi \end{bmatrix} \mathbf{S}_P \begin{bmatrix} \cos\psi & \sin\psi \\ -\sin\psi & \cos\psi \end{bmatrix}. \tag{2}$$

We are now in a position to present the measured data. Fig. 5(a)–(d) shows the C-band radar cross

TABLE III
Radar Cross Section (dBsm) of Smooth Cylinders 1 m Long

Diam (cm)	4 75 GHz		9.5 GHz		34.5 GHz	
	vv	hh	vv	hh	vv	hh
1 27	-2 08	-0 68	0 73	1 73	6.75	6.72
2 22	0.08	1 27	3.66	3 77	9.17	9.08
3 15	-0 03	2 45	5.25	5.15	10.57	10.58
3 49	1.73	2.81	5.38	5.57	11.03	11.02
7 62	5.05	5 92	8.61	8.84	14.4	14.4

(a)

(b)

Fig. 6. Near field radar backscatter cross section for 20 cm long cable. (a) Cable 4. (b) Smooth cylinder of diameter 3.49 cm at 4.75 GHz.

section for the 30 cm long cables 1 through 4. The measured RCS of a 30 cm long smooth cylinder with a diameter similar to that of cable 1 is shown in Fig. 5(e) for comparison. The co-polarized components (VV, HH) of the scattering matrix are more or less similar to those of the smooth cylinders except for cable 4 where σ_{vv} is slightly higher than σ_{hh}. At incidence angles beyond 50 degrees scattering is dominated by the end cap of the cables. There is also a rather significant decrease in the ratio σ_{vv}/σ_{hh} for the cables, when compared with the same ratio for smooth cylinders at normal incidence (see Table III for RCS of the smooth cylinders). The reason for this phenomena is that the surface of the cables shows two different surface impedances due to the corrugations and the surface impedance is higher for vertical polarization (TE case) than for horizontal polarization (TM case) [Sarabandi and Ulaby, 1991]. The decrease in the ratio of the copolarized terms is inversely proportional to the diameter of the cables. It is also important to note the differences between the levels of the braided cables and the smooth cylinder. Braided co-pol responses are about 10 dB higher for nonnormal incidence angles. Braided cross-pol responses are about 30 dB higher for all angles. These two differences are critical to the performance of our cable detection algorithm for all incidence angles.

Fig. 6 gives the near field measurements of cable 4 and its smooth cylinder counterpart. The near field effect reduces the RCS at normal incidence, widens the RCS pattern, and enhances the increase in σ_{vv} and σ_{hh}.

Fig. 7(a)–(d) gives the backscattering cross section of 30 cm long cables at X-band and Fig. 7(e) shows the measurement of the cylinder counterpart of cable 1. The near field measurements of cable 4 and its reference cylinder are shown in Fig. 8. Similar scattering features, but more pronounced than those observed for C-band, exist in the X-band data. The most important scattering feature is the increase in σ_{vv} at angles away from normal incidence. This increase in σ_{vv} can be interpreted as follows. The surface of a cable can be viewed as a cylinder with a number of parallel slanted narrow grooves on the surface. The inclination angle of the grooves is equal to the pitch angle of the helices which is around 15°. The backscatter from a metallic groove for the TE case (electric field perpendicular to the groove axis) is much
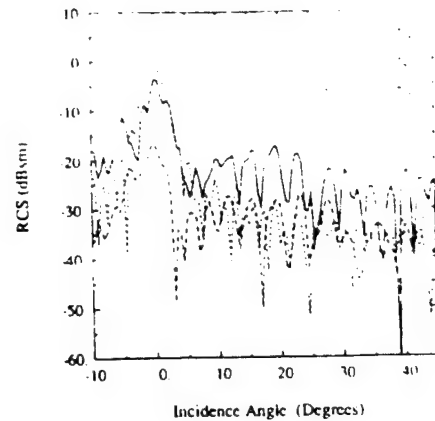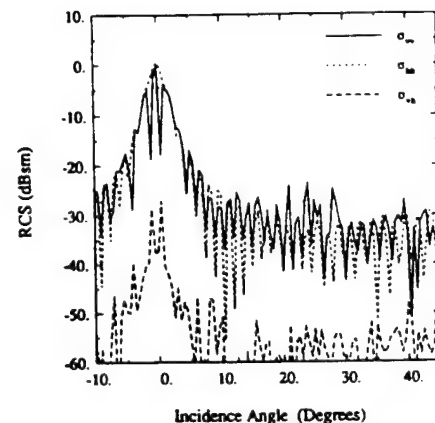
stronger than for the TM case (electric field parallel to the groove axis) [Senior, et al., 1990], because in the TE case the groove is capable of supporting a transverse electromagnetic (TEM) wave and in the TM case the groove is incapable of supporting any waveguide mode. Since the grooves are almost parallel to the axis of the cylinder the backscatter for VV-polarization is much stronger.

Fig. 9 shows the RCS of the 30 cm long cables at Ka-band. The RCS response of the cables at all polarizations has peaks at approximately 10°–15° from the backscatter direction (see Fig. 9). These peaks are due to the Bragg modes in backscatter. For a periodic target the Bragg backscatter occurs for incidence angles according to

$$\theta_n = \sin^{-1}\left(\frac{n\lambda}{2L}\right) \qquad (3)$$

where λ is the wavelength and L is the period (Fig. 3). Since most of the scattered energy is in the specular direction, the higher order Bragg modes are very weak at angles away from normal incidence.

In these cables only one of the Bragg modes is observable, and, as in the lower frequencies, the
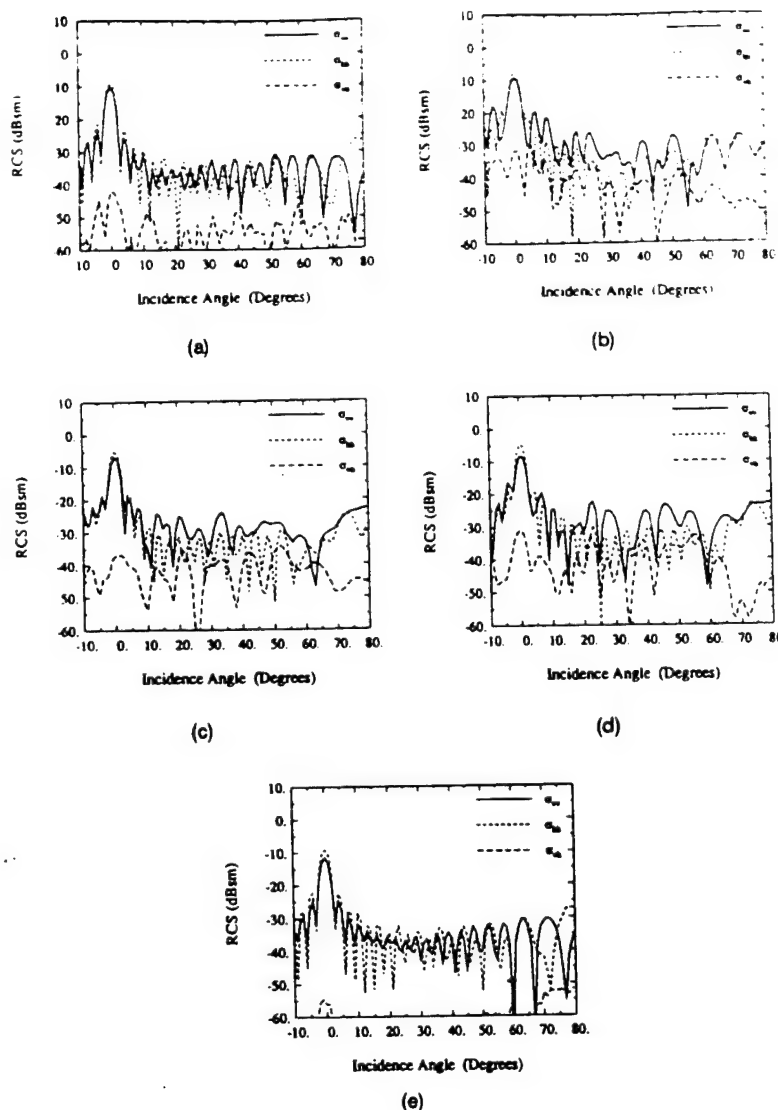
Fig. 7. Radar backscatter cross section for 30 cm long cable. (a) Cable 1. (b) Cable 2. (c) Cable 3. (d) Cable 4. (e) Smooth cylinder of diameter 1.27 cm, at 9.5 GHz.

backscatter for VV-polarization is significantly higher than the other components. The effect of curvature on cable 2 has also been tested and the result is shown in Fig. 11 for a curved cable with radius of curvature of about 10 m. The curvature lowers the RCS of the cable at normal incidence and the Bragg directions and widens the scattering patterns. Also the near field measurement of cable 4 and its cylinder counterpart are shown in Fig. 10.

The backscattering measurements are performed polarimetrically so that the target response to any desired transmit and receive polarization configuration can be synthesized [van Zyl and Ulaby, 1990]. Obviously for detection purposes the desired polarization is the one which maximizes the target response. It turns out that all the polarization signatures closely resemble the polarization signature of a vertical dipole. Thus the optimum polarization for detection, as expected, is VV-polarization when the cable is in the H-plane of the antenna system. If

the cable were not in the H-plane, then the optimum polarization would still be a linear polarization with rotation angle ψ as given by (1).

D. Summary of Experimental Results

Near field and far field polarimetric backscattering measurements of four powerline cable samples have been presented at C-, X-, and Ka-band over a wide range of incidence angles. The near field measurements of smooth cylinders with a length and diameter similar to those of the cables were also performed for comparison. The experimental results from the backscatter measurements of cables and cylinders indicate the following.

1) At normal incidence there is a significant decrease in σ_{vv}/σ_{hh} of the cables in comparison with the ratio for the smooth cylinders. This decrease is inversely proportional to the diameter of the cables.
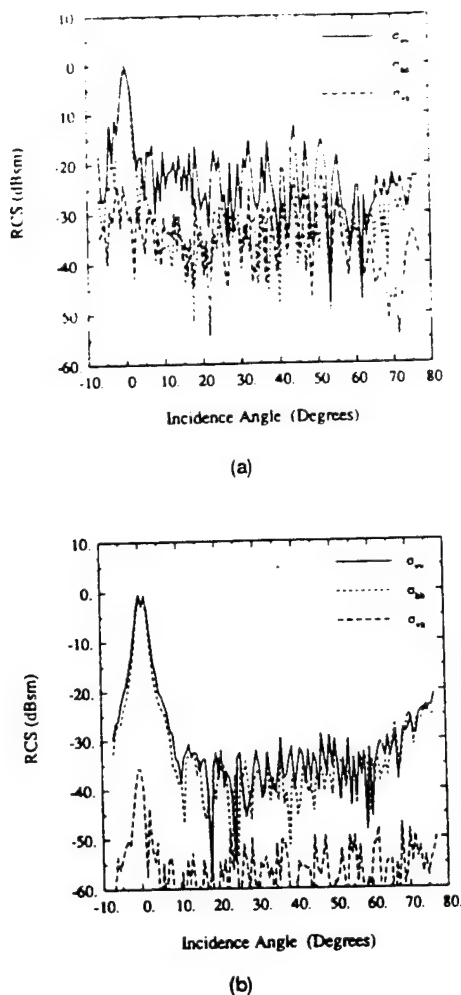
Fig. 8. Near field radar backscatter cross section for 120 cm long cable (a) Cable 4. (b) Smooth cylinder of diameter 3.49 cm at 9.5 GHz.

2) At low frequencies and for small diameter cables ($D/\lambda \ll 1$) there is no significant backscatter at angles away from normal incidence.

3) The cross-polarized component of the cable backscatter is very high over the entire range of incidence angles. The cross-polarized RCS level is directly proportional to the cable and the cable strand diameters.

4) When the cable diameter is comparable to the wavelength there is a considerable increase in σ_{vv} in off-specular directions and this increase depends on the diameter of the cable strands.

5) At millimeter wavelengths the Bragg modes are observable at angles close to normal incidence ($\theta^i < 15°$). The VV-polarized backscatter for the Bragg modes is much higher than the other polarizations.

III. DETECTION

A. Introduction

For imaging radars the powerline is not necessarily in the H-plane of the antenna system, however the circular symmetry of the cables can be used to derive the scattering matrix of the cable (S), with an arbitrary orientation with respect to the antenna system, in terms of the scattering matrix of the cable in the principal plane (S_p).

The scattering matrix of the cable in this situation S, in terms of the scattering matrix of the cable in the principal plane S_p, can be obtained from (2), and the scattering matrix in the principal plane away from normal incidence can be approximated by

$$S_p = \sqrt{\sigma/4\pi} \begin{bmatrix} 1 & 0 \\ 0 & 0 \end{bmatrix} \qquad (4)$$

where σ is the radar cross section of the cable.

Knowing the optimum polarization for detection of powerlines, we attempted to extract the location of powerlines by applying standard techniques such as 1) Polarization Synthesis and Optimization [van Zyl and Ulaby, 1990], and 2) Speckle Reduction Through Application of the Polarimetric Whitening Filter, [Novak et al., 1991]. Unfortunately we were not successful in extracting the powerline features by applying the mentioned methods. One reason for this failure was perhaps the limited polarimetric images and the associated ground-truth available to us. But the main reason is that the signal to clutter ratio, for most practical purposes, is usually very low which makes the detection very difficult if not impossible.

B. Detection Algorithm

A major difficulty in extraction of powerlines positions from a polarimetric radar image is the lack of enough signal-to-clutter ratio. Here signal refers to the radar backscatter from a powerline cable alone and clutter is referred to the backscattering coefficient of the terrain beneath the powerline. Depending on the type of the terrain the average signal-to-clutter ratio may vary from 0 to −15 dB at higher microwave and millimeter wave frequencies. Obviously any detection method using single pixels would fail when faced with poor signal-to-clutter ratios from a 20 dB variation in clutter due to speckle. Any successful algorithm must be based on the statistics of the clutter, which can be obtained from the image itself, to reduce not only the speckle but also the energy in the clutter signal.

To demonstrate how the statistics of the clutter can be exploited in the detection of a signal contaminated by noise, suppose $\mathcal{L}$ is an operator on the elements of the scattering matrix which satisfies the following

$$\langle \mathcal{L}(S_c) \rangle = 0 \qquad (5)$$

where S_c is the measured scattering matrix of the clutter and $\langle \cdot \rangle$ represents ensemble averaging. If $\mathcal{L}$ is applied to a number of pixels which include the powerline cable all with scattering matrix S_s, then the measured scattering matrix is $S = S_c + S_s$. Since $\mathcal{L}$ may
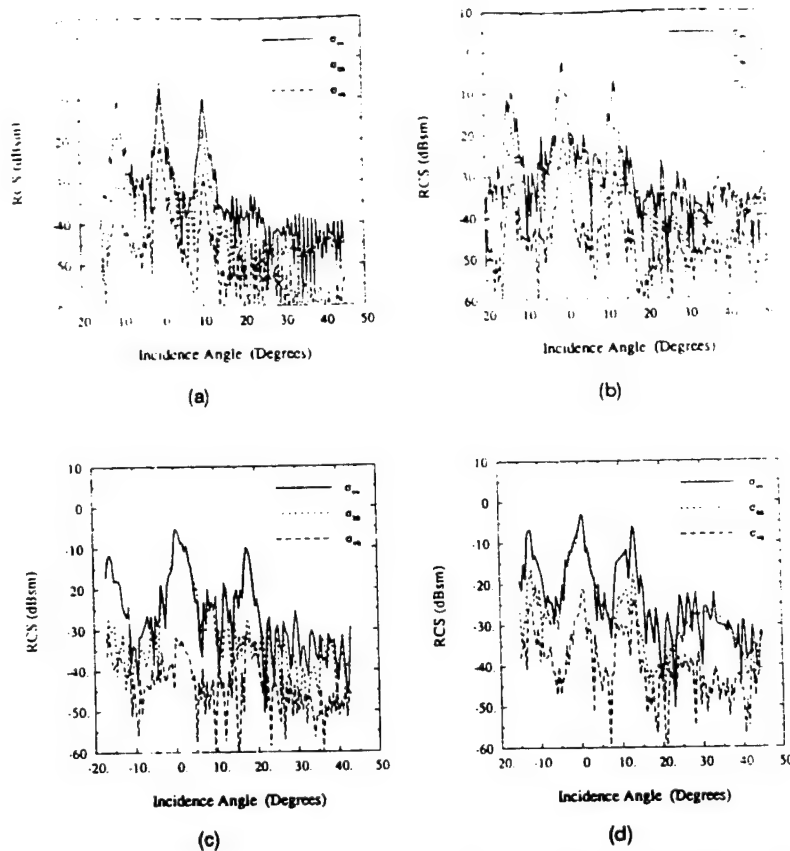
Fig. 9. Radar backscatter cross section for 30 cm long cable. (a) Cable 1. (b) Cable 2. (c) Cable 3. (d) Cable 4 at 34.5 GHz.

need to be a nonlinear operator let us further assume that

$$\mathcal{L}(S) = \mathcal{L}(S_c) + \mathcal{L}(S_s) + \mathcal{G}(S_s)\mathcal{H}(S_c) \qquad (6)$$

with $\langle \mathcal{H}(S_c) \rangle = 0$. If such an operator exists, then $\langle \mathcal{L}(S) \rangle \approx 0$ along every line in the image which does not include the powerline.

In the electromagnetic modeling of a layer of randomly oriented small particles above a ground layer, it is shown that for azimuthally symmetric particle orientation the co- and cross-polarized components of the scattering matrix are uncorrelated [Borgeaud et al., 1987; Tsang et al., 1991; Nghiem et al., 1992]. In other words $\langle S_{hh} S_{vh}^* \rangle = \langle S_{vv} S_{vh}^* \rangle = 0$ which satisfies the conditions required for $\mathcal{L}$, noticing that for distributed targets $\langle S_{hh} \rangle = \langle S_{vv} \rangle = \langle S_{vh} \rangle = 0$. Based on our recent polarimetric measurements of rough surfaces at microwave frequencies, we may postulate that the co- and cross-polarized components of the scattering matrix are uncorrelated for a general random medium with azimuthal symmetry [Sarabandi, 1992]. In fact this assumption is used in a calibration routine for polarimetric imaging SARs to remove the antenna cross-talk factors [van Zyl, 1989].

C. Results of Simulation

To verify the applicability of this operator, we used a portion of an L-band polarimetric SAR image to simulate extraction of a powerline with -6 dB signal-to-clutter ratio. The L-band image is from JPL AIRSAR of northern Michigan and is fully polarimetric. The resolution of each pixel is approximately $12m \times 6.66m/\sin\theta$ where θ is the incidence angle. A random number generator picked a point with a distance ρ from the center of the image and the direction of the powerline ($\hat{\phi}$) was chosen to be normal to the line connecting the point and the center. The scattering matrix of the cable for each pixel was then calculated according to (2). The calculated scattering matrix for the powerline was then added to the clutter signal along the chosen direction. Fig. 12 shows a portion of the L-band SAR image without a powerline and Fig. 13 shows the same image after the powerline is added. These images display the total power for each pixel which is defined as

$$p = |S_{hh}|^2 + |S_{vv}|^2 + (|S_{hv}|^2 + |S_{vh}|^2)/2.$$

No discernible feature of the power line can be observed by comparing the two figures.

Next we need an automated algorithm to detect the powerline and find its location in the image. This can be accomplished by noting that every line in the $x - y$ plane can be mapped into a point in $\rho - \phi$ plane where ρ is the distance of the origin to the line and ϕ is the angle specifying the direction as shown in Fig. 14. The
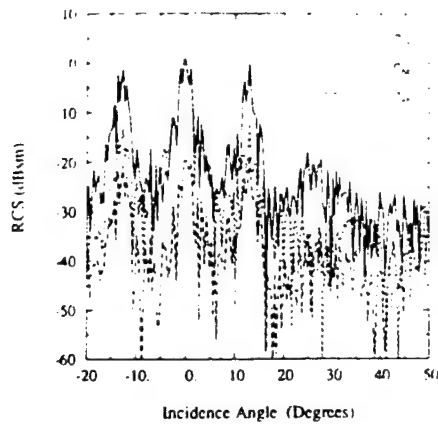
(a)
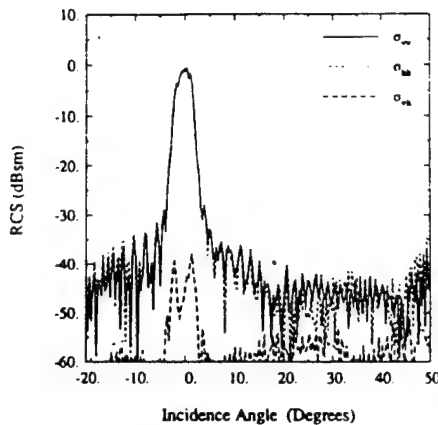
(b)

Fig. 10. Near field radar backscatter cross section for 120 cm long cable. (a) Cable 4. (b) Smooth cylinder of diameter 3.49 cm at 34.5 GHz.
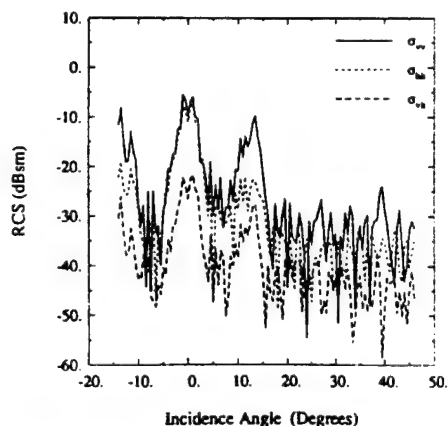

Fig. 11. Radar backscatter cross section of curved 30 cm long cable 2 at 34.5 GHz versus incidence angle (radius of curvature $\approx$ 10 cm).

operator $\mathcal{L}$ can be chosen as given by

$$\mathcal{L}(S) = \text{Re}[S_{hh}S_{vh}^*] + \text{Im}[S_{hh}S_{vh}^*] \qquad (7)$$

and averaging should be performed along each line. The real quantity $\mathcal{L}(S)$ was computed for the image
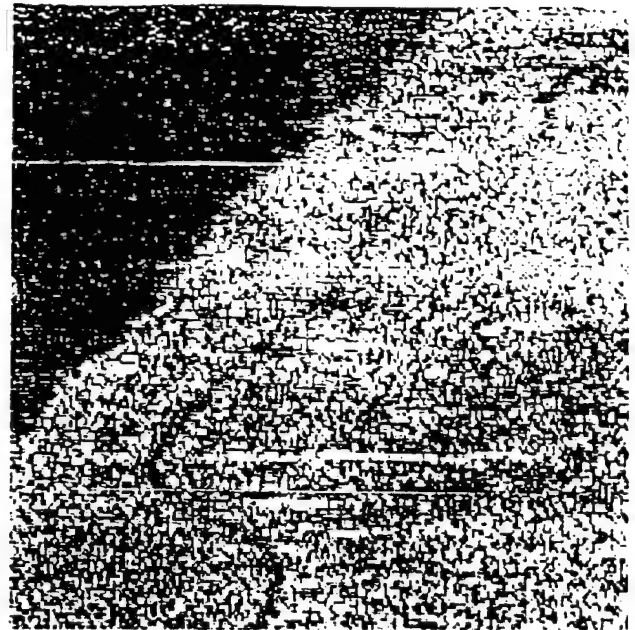
Fig. 12. Portion of L-band polarimetric SAR image in northern Michigan. Figure shows total power image.
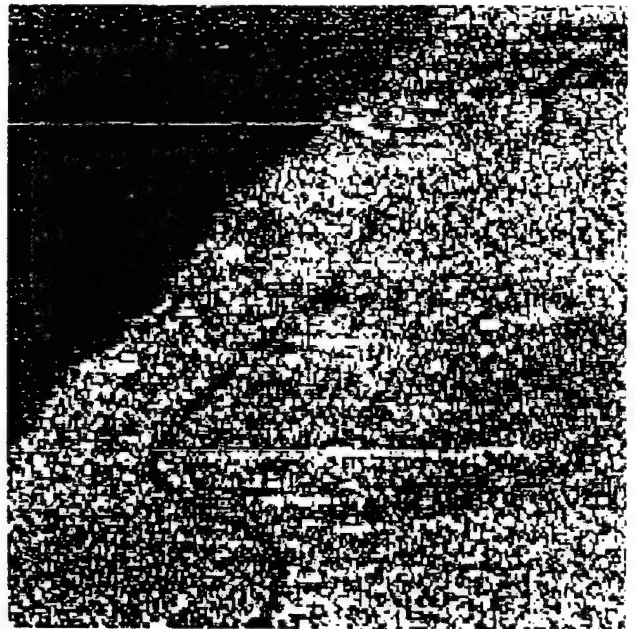
Fig. 13. Portion of L-band polarimetric SAR image in northern Michigan with inserted powerline whose RCS is 6 dB lower than average clutter power.

with inserted powerline for all values of ρ and ϕ and the result is shown in Fig. 15 in the transformed $\rho - \phi$ plane. The brightest spot represents the direction and position of the powerline. Fig. 16 shows the powerline in the image after detection. The bright spot in the $\rho - \phi$ plane is about 5 dB higher than all other points.

IV. CONCLUSIONS AND FUTURE WORK

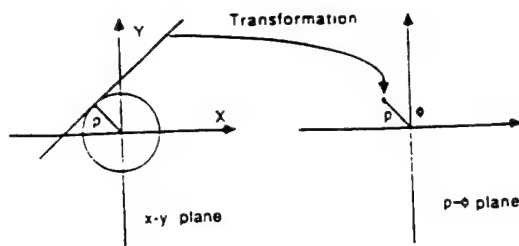This simulation encourages further investigations in the statistical properties of distributed targets

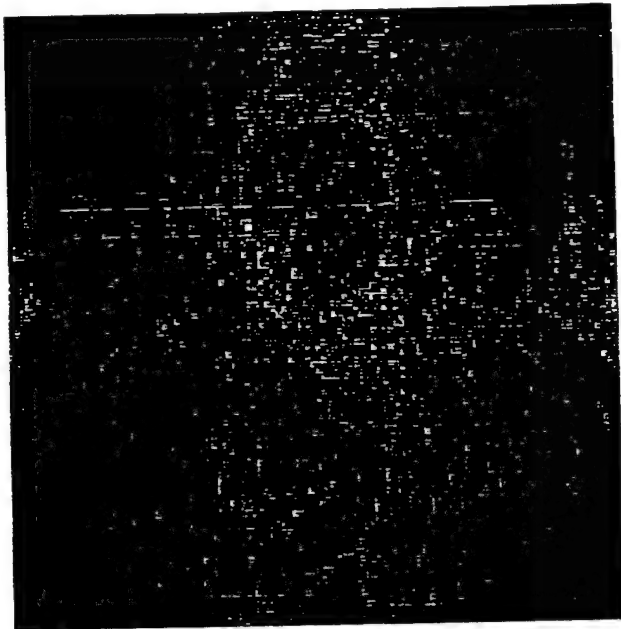Fig. 14. Transformation of line in the $x - y$ plane to a point in $\rho - \phi$ plane.

at different frequencies which can guide us in choosing the best operator according to the clutter type. What is needed in the future is polarimetric scattering measurements of distributed targets such as bare surfaces, grass land, and surfaces covered with shrubs in order to characterize the statistical properties of clutter background for powerlines. These measurements would enable us to find the best operator, $\mathcal{L}$, and after completion of this stage we can apply our algorithm to real cases. For the final step we would require polarimetric SAR images at millimeter wavelengths which include powerlines. Of particular interest is the MIT Lincoln Laboratory 35 GHz SAR system. The images should be acquired at different incidence angles and look directions and ground-truth data should also be collected immediately after the flights.

KAMAL SARABANDI
LELAND PIERCE
YISOK OH
FAWWAZ T. ULABY
Radiation Laboratory
Department of Electrical Engineering and Computer Science
University of Michigan
Ann Arbor, MI 48109-2122

Fig. 15. $\langle \mathcal{L}(S) \rangle$ of L-band image in $\rho - \phi$ plane.

REFERENCES

[1]   Borgeaud, M., Shin, R. T., and Kong, J. A. (1987)
      Theoretical models for radar clutter.
      Journal of Electromagnetic Waves and Application, 1, 1 (1987), 73–89.

[2]   Ioannidis, G. A., and Hammers, D. E. (1979)
      Optimum antenna polarization for target discrimination in clutter.
      IEEE Transactions on Antennas Propagation, 27, 5 (May 1979).

[3]   Kuga, Y., Sarabandi, K., Nashashibi, A., Ulaby, F. T., and Austin, R. (1991)
      Millimeter wave polarimetric scatterometer systems: Measurement and calibration techniques.
      In *Proceedings of AGARD, Electromagnetic Wave Propagation Panel 48 Symposium*, Montreal, May 1991.

[4]   Liepa, V. V., Sarabandi, K., and Tassoudji, M. A. (1989)
      A pulsed network analyzer based scatterometer.
      In *Proceedings of IEEE Geoscience Remote Sensing Symposium*, Vancouver, July 1989.

[5]   Novak, L. M., Burl, M. C., Irving, W. W., and Owirka, G. J. (1991)
      Optimal polarimetric processing for enhanced target detection.
      In *Proceedings of National Telesystems Conference*, Mar. 26–27, 1991.

[6]   Nghiem, S. V., Yueh, S. H., Kwok, R., and Li, F. K. (1992)
      Symmetry properties in polarimetric remote sensing.
      Radio Science, 27, 5 (Sept. 1992), 693–711.

[7]   Rembold, B., Wippich, H. G., Bischoff, M., and Frank, W. F. X. (1982)
      A MM-wave collision warning sensor for helicopters.
      Proceedings of Military Microwave., (1982), London, 344–351.

Fig. 16. L-band polarimetric SAR image after powerline detection algorithm.

[8]   Rembold, B. (1984)
       Radar cross section of long wires.
       IEEE Transactions on Antennas Propagation, 32, 10 (Oct 1984).

[9]   Senior, T. B. A., Sarabandi, K., and Natzke, J. (1990)
       Scattering by a narrow gap.
       IEEE Transactions on Antennas Propagation, 38, 7 (July 1990), 1102–1110.

[10] Sarabandi, K. (1992)
       Derivation of phase statistics of distributed targets from the Mueller matrix.
       Radio Science, 27, 5 (Sept.–Oct., 1992), 553–560.

[11] Sarabandi, K., and Ulaby, F. T. (1991)
       High frequency scattering from corrugated stratified cylinders.
       IEEE Transactions on Antennas Propagation, 39, 4 (Apr. 1991), 512–520.

[12] Sarabandi, K., and Ulaby, F. T. (1990)
       A convenient technique for polarimetric calibration of radar systems.
       IEEE Transactions on Geoscience and Remote Sensing, 28, 6 (Nov. 1990).

[13] Savan, M., and Barr, D. N. (1988)
       Reflectance of wires and cables at 10.6 micrometer.
       MSEL-NV-TR-0063, Center for Night Vision and Electro-Optics, Jan. 1988.

[14] Tassoudji, M. A., Sarabandi, K., and Ulaby, F. T. (1989)
       Design consideration and implementation of the LCX polarimetric scatterometer (POLARSCAT).
       Radiation Laboratory Report No. 022486-T-2, The University of Michigan, Ann Arbor, June 1989.

[15] Tsang, L., and Ding, K. H. (1991)
       Polarimetric signatures of a layer of random nonspherical discrete scatterers overlaying a homogeneous half-space based on first- and second-order radiative transfer theory.
       IEEE Transactions on Geoscience and Remote Sensing, 29 (Mar. 1991), 242–253.

[16] van Zyl, J. J., and Ulaby, F. T. (1990)
       In Ulaby, F. T., and Elachi, C. (Eds.), *Radar Polarimetry for Geoscience*.
       Dedham, MA: Artech House, ch. 2, 1990.

[17] van Zyl, J. J. (1990)
       Calibration of polarimetric radar images using only image parameters and trihedral corner reflector responses.
       IEEE Transactions on Geoscience and Remote Sensing, 28 (May 1990), 337–348.

Multiple Target Angle Tracking Algorithm Using Predicted Angles

We modify a multiple target angle tracking algorithm presented by Sword, et al. The predicted estimates, instead of the existing estimates, of the target angles are updated by the most recent output of the sensor array to improve the tracking performance of the algorithm for crossing targets. Also, the least square solution is modified to avoid abnormally large angular innovations when the target angles are very close. The improved performance of the proposed algorithm is demonstrated by computer simulations.

I.   INTRODUCTION

Multiple target tracking problem has received considerable interest recently, owing to its various applications in sonar, radar, remote sensing, communications, air traffic control, and others [1–2]. In target state model approach, a dynamic model of target state is established and tracking is performed by estimating the state vector using measurements [3–4]. In target angle tracking approach, tracking is performed by estimating the time delay of the target signals with respect to sensors in the array [5]. These approaches have the data association problem in tracking multiple targets.

An alternative approach of tracking multiple target angles has been proposed by Sword, et al. [6]. A signal subspace algorithm such as the MUSIC (multiple signal classification) algorithm [7] is first applied to yield the initial estimates of the number of targets, sensor noise power, target signal power, and the target angles. The angular displacements of the targets during a sampling period are estimated in the least square sense using the most recent estimate of the sensor output covariance matrix. The target angles are then tracked recursively by adding the estimated angular displacements to the existing estimates of the target angles. This algorithm has attractive features of simple structure and avoidance of data association problem. However, it has some drawbacks. The approximation errors in estimating the angular displacements are relatively large, which are propagated into the next step. More seriously, it's poor performance for multiple targets with crossing angles prohibits the general use of the algorithm.

Sword's algorithm has been modified by Lo and Li [8]. Lo's algorithm reduces the propagation errors by

Numerical Simulation of Scatterer Positions in a Very Dense Medium with an Application to the Two-Dimensional Born Approximation

Paul R. Siqueira, Kamal Sarabandi and Fawwaz T. Ulaby
Radiation Laboratory
Electrical Engineering and Computer Science Department
University of Michigan, Ann Arbor, MI 48109-2122

Abstract

Electromagnetic volume-scattering theories for random media using a coherent field approach require some understanding of the statistical behavior of the locations of individual scatterers within the random medium. This knowledge manifests itself as the correlation function or pair distribution function, which is used to characterize the medium. This article presents a method for simulating the arrangements of particles of arbitrary shape within a very dense random medium, thus allowing for these functions to be calculated numerically. To demonstrate the significance of the Monte-Carlo simulation, the problem of scattering from a two-dimensional dense random medium is considered. Using a first-order solution based on the Born approximation, it is shown that the approximate theoretically derived correlation function may lead to significant errors in the prediction of the backscatter response.

1 Introduction

Study of electromagnetic wave interaction with a collection of random particles (volume-scattering) is of importance because of its application to a variety of radar remote sensing problems. Volume-scattering theories are developed to determine basic electromagnetic properties of the medium such as the effective propagation constant, the attenuation constant and the incoherent scattered power. Modelling efforts for volume-scattering can be categorized into two groups: (1) incoherent approaches, and (2) coherent approaches. In incoherent volume-scattering theories, such as radiative

1

transfer [Chandrasekhar, 1960], the effect of the phases of the fields scattered between neighboring particles is ignored. These methods are usually applied to sparse media where single scattering properties of constituent particles are used to formulate the volume-scattering problem. Intensity approaches implicitly make the sparse-medium assumption that individual scatterers are randomly positioned with respect to one another. As the scatterer density increases, multiple scattering between particles becomes significant and the scattering solution based on the incoherent approach becomes prohibitively complex [Tsang and Ishimaru, 1987]. Coherent approaches, on the other hand, such as the Born approximation and the Quasi-crystalline Approximation (QCA) [Tsang, et al., 1985], account for the interaction between particles through the inclusion of a permittivity fluctuation correlation function or a scatterer center pair distribution function which provide statistical descriptions of the location of scatterers with respect to each other. The need for the correlation or pair distribution functions adds another complexity to volume-scattering theories, namely that associated with how to determine these functions for the medium under consideration. These functions play an important role in determining the scattering behavior of the random medium and thus must be characterized accurately. The importance of this characterization has been somewhat overlooked in the literature. Simple Gaussian and exponential functions are usually used as an approximation for the correlation function since they are amenable for algebraic manipulation, but there is little evidence in support of the hypothesis that these are accurate representations of natural media. It is the purpose of this paper to (1) present a numerical technique to determine the correlation and pair distribution functions accurately and efficiently based on physical modelling of particle arrangements in a random medium, (2) demonstrate the application of the correlation function to the 2D Born approximation and make a comparison with theoretically derived results, (3) use the derived correlation function to demonstrate limitations in the use of the exponential correlation function, (4) highlight the use of packing algorithms as a method of scattering analysis that can be used to analyze or enhance existing scattering theories.

The methods of determining the correlation function or the pair distribution

function can be categorized into: (1) experimental, (2) theoretical and (3) numerical approaches. Experimental determination involves capturing an undisturbed sample of the volume under study and analyzing it for the desired information. This approach is quite difficult, very time consuming, and its accuracy depends on the particle size and measurement method. A classical example of such a process is given by Vallese and Kong [1981] where a layer of snow was infused with liquid plastic. The final result was the two-dimensional correlation function of the permittivity fluctuations due to the two dissimilar dielectrics of air and ice. The observed correlation function for one sample was then fit to a theoretical model (exponential) from which further calculations could be carried out. Further assumptions, such as azimuthal symmetry and validity of the theoretical model, were required to estimate the three-dimensional correlation function.

Theoretical methods of determining the correlation and pair distribution functions, while benefiting from a greater generality must use simplifying assumptions to make the theories tractable and easy to handle. For the correlation function, it is common to use an exponential function [Debye et al., 1957] which is derived by assuming that individual particles are positioned completely random with respect to one another. Such an assumption is valid in the limit when particle sizes are distributed over a wide range and/or when the particle density is low. This function will be the used as a basis of comparison further in the paper.

The pair distribution function of Percus and Yevick [Percus and Yevick, 1958] is another such theoretically derived function commonly used in conjunction with QCA and dense media radiative transfer [Tsang and Ishimaru, 1987]. This particular distribution is tailored for a medium consisting of discrete sized spherical particles which there are no inter-particle forces except exclusion, as in a classical fluid; external forces, such as gravity, are not taken into account. For macroscopic media such as snow, soils and sand, the Percus-Yevick distribution may not be applicable because particle positions are dominated by forces such as friction, gravity and inertia. It is not difficult to come up with examples where the Percus-Yevick pair distribution func-

tion would give considerably different results than would be expected for macroscopic particles under the influence of these conditions. For instance, if we were to create a dense assembly of uniform spheres in their lowest energy state, a crystal, and then randomly remove 10-20% of them, we would not expect the pair distribution function to change because the basic structure of the crystal still remains. In a classical fluid however, particles are allowed to rearrange themselves to reach the lowest energy state, which is dependent on their relation to one another. Thus, the pair distribution function in a classical fluid would change as the Percus-Yevick distribution predicts, but there is no reason to expect that the pair distribution functions of macroscopic particles under a different set of forces would be similar. Thus it is important to explore other avenues of determining these functions to either verify the validity of employing these theoretical techniques to specific applications or to generate the functions themselves.

Numerical methods refer to algorithms for determining the correlation function and pair distribution functions through the use of a computer to simulate the scatterer positions in a given space. Some of these methods are used to validate already existing theoretical distributions [Ding et al., 1992; Broyles et al., 1962] while others are used to determine the desired correlation or pair distribution functions directly [Buchalter and Bradley, 1992]. *Packing algorithms are basically split into two groups, those that physically model the deposition of particles and those that generate possible particle arrangements. The first group is capable of investigating properties such as local particle ordering and the effects of shaking packed sets of particles. The algorithm of Buchalter and Bradley is the most elaborate of these methods, it models collisions and rotations of uniform two-dimensional ellipsoids as they "pour" downward into a two-dimensional volume and is the only method developed thus far that uses elliptical particles. The methods of this set of algorithms are heuristic and can become time consuming as the complexity of the modeling more closely tries to match that of physical reality. Thus this direction may not be appropriate for use in Monte-Carlo simulations.*

4

For the scattering problem, we may be more interested in computational effi-ciency in determining possible arrangements of particles rather than physically mod-elling their deposition. In this set of algorithms, some methods simply find open spaces for particles to fit within a confined area, such as in the sequential addition method [Ding et al., 1992], or incorporate an external force such as gravity, from which po-tential energy can be minimized and particle stability can be maximized [Visscher and Bolsterli, 1972]. While the existing algorithms of this type can be considered to be much more computationally efficient than the physical deposition models, up until now they have been lacking in flexibility to model arrangements of particles of differ-ent shapes, particularly when it comes to the three dimensional problem (this is also a considerable challenge for the physical deposition models).

The method described here takes into account the three important factors of determining particle arrangements: non-penetration of neighboring particles, gravity and particle shape. This presented method is a particle arrangement method that is capable of determining particle distributions in both two and three dimensions and is computationally efficient enough to provide a large sample size for Monte-Carlo sim-ulations. The new method is not restricted to spherical/elliptically shaped particles and as will be described, may be used in conjunction with coherent volume-scattering theories to explore the scattering from dense random media . In what follows, first the packing algorithm is described in Section 2 and examples for both two- and three-dimensional particles are given. Methods describing accurate calculation of the correlation function and pair distribution function from the computer generated par-ticle positions are given in Section 3. In order to demonstrate the importance of the packing algorithm to the problem of volume-scattering from a very dense medium, scattering solutions based on the Born approximation using the correlation function computed from the packing algorithm and an exponential function having the same correlation length are compared as a function of incidence angle and frequency. *Be-cause the angular backscatter response is proportional to the two-dimensional Fourier transform of the correlation function, it is possible to introduce the concept of a "vis-ible region" where we can gain insight of how the choice of observation frequency*

samples the fourier space of the correlation function. This is done in second half of section 3 where the angular dependence of the backscatter response is demonstrated for a particular example at two different frequencies, one below and one above the resonance of the mean particle size.

2 Packing Algorithm

We begin by introducing a user-defined distribution of particle states, P_p, where the state of a particle is a vector representing the particle size, shape, orientation and dielectric constant. For the purposes of demonstration, elliptically shaped particles will be used, however, this packing algorithm is not restricted to the simplified elliptical shapes. In two dimensions the state of such a particle is represented by

$$P_p = (a_p, b_p, \theta_p, \epsilon_p) \tag{1}$$

where a_p, b_p are the lengths of the two principle axes, θ_p describes the orientation, and ϵ_p is the dielectric constant of the particle. To simulate the particle positions in two dimensions, a rectangular region with j being the discrete horizontal coordinate and z being the vertical coordinate is considered (Fig. 1). Coordinates of the intersection of the principal axes of the particle p denotes the position of the particle, which, together with the particle state, completely specifies the particle in the medium. The vector state of a particle is chosen by a random number generator with a prescribed distribution for the different states a_p, b_p, θ_p, and ϵ_p. In this paper, it is assumed that the principal axes of the particle have a normal distribution ($N(\overline{a}, \sigma_a)$) and the orientation angle of particles has a uniform distribution ($U(-\pi, \pi)$). The exact distributions of the particle states may be chosen according to physical measurements or an empirical model. The particle is then laid down via the packing algorithm individually into the region to be filled. By making the limits of the region large compared to the sizes of the individual particles and by using the periodic boundary conditions, a semi-infinite layer of particles can be simulated. Periodic boundary conditions refer to making the spillover of a particle on one boundary appear on the opposite boundary of the region.

6

The packing algorithm starts by setting down an initial layer on the bottom of the rectangular region such that the lower surface is covered by a single layer of particles. This set of particles creates a bumpy solid surface, S_p. Particles are then sequentially added to the region in the following manner:

1. A particle state P_p is selected from the distribution.

2. The surface of the particle is discretized and then categorized into a set of lower and upper surface points as shown in Fig. 2. The points of the lower surface will be used in matching the surface of the particle to the current surface, S_p.

3. A fitting method is used to find the lowest height, z_p, that the particle will fit to the surface. This is equivalent to minimizing the potential energy of the particle.

4. The particle's position, $\bar{r}_p$, and state, P_p are stored in a file and the surface is updated to S_{p+1} using the upper surface points determined in step two.

5. Return to the first step until the desired layer thickness is reached.

The fitting method described in step three is one of the key components that makes this algorithm computationally efficient. While any fitting method will be sufficient in this treatment, the one used here borrows a concept from the image processing technique of gray-scale morphology [Serra, 1982; Giardina and Dougherty, 1988; Appleton et al., 1993]. In this packing algorithm, a gray scale dilation is used to find the minimum height that a given shape fits to the surface. To describe this procedure, consider a particle as shown in Fig. 2. The surface of a particle is represented by an upper (M^{upper}) and a lower surface (M^{lower}). The lower part of the surface determines how the particle will fit the the current surface, S_p, and the upper part determines how the particle will contribute to the new surface, S_{p+1}, once the particle has been deposited. Given a parametric equation for the surface of a particle, $z_p(i)$, these surfaces can be described by

$$M_p^{\text{upper}}(i) = \{\max_z z_p(i) : -m \leq i \leq m\} \tag{2}$$

7

$$M_p^{\text{lower}}(i) = \{\min_z z_p(i) : -m \leq i \leq m\} \qquad (3)$$

where for a normally oriented ellipse, $z_p(i) = \pm b_p \sqrt{(1 - \frac{i^2}{a_p^2})}$ with a_p and b_p given in (1) and m being the horizontal limit of the extent of the ellipse ($m \geq \max(a_p, b_p) \; \forall p$). Note that the form of $z_p(i)$ is used here only for demonstration purposes and does not constrain the process once (2) and (3) have been determined.

The height of where a particle will rest for a given horizontal position, j, along the surface S_p is given by the morphological dilation (Fig. 3)

$$\text{height}(j) = \{\max_i \left(S_p(j + i) - M_p^{\text{lower}}(i)\right) : -m \leq i \leq +m\}. \qquad (4)$$

The minimum height attainable used by step three in the procedure is

$$z_p = \min_j \left(\text{height}(j)\right). \qquad (5)$$

Successful algorithms have been implemented for both two- and three-dimensional elliptical particle distributions and examples are shown in Figs. 4 and 5 (to make the three-dimensional problem more efficient, a local minimization over an area of several particle diameters was performed rather than global minimization indicated by Eq. 5). The two-dimensional example clearly shows the algorithm's ability to generate very dense arrangements of particles in a short amount of computer time, two characteristics that make the algorithm amenable to Monte-Carlo dense media volume scattering analysis. Furthermore, an analogous dense medium three-dimensional example is given for non-spherical particles using twenty four processors of a parallel computer, a result that has heretofore not been available or realistic to perform at all. Because the algorithm lends itself to parallelization, as the number of available processors increase in the future, the problem of solving arrangements of arbitrarily shaped particles in three-dimensions can be scaled down in time proportionally.

Results from the packing algorithm can be used to determine physical characteristics of a volume under study such as volume fraction, correlation length and function, pair distribution function, etc. Future work in this area may be to include impurities such as water and determine the coating of individual grains through the

8

implementation of simple physical processes such as surface tension and entropy maximization. Other natural substances, such as snow, may also be simulated by reducing the minimization of potential energy constraint, which can be accomplished by making individual particles stick once they reach the surface of the packed layer. The simplicity with which the algorithm can be changed for particles with general cross section is demonstrated in Fig. 6 where packing of two-dimensional rocks is simulated. In this figure the standard packing algorithm is used with a random walk modification of the individual particle surfaces.

3 Permittivity Correlation and Pair Distribution Functions

One of the principal uses of the packing algorithm is in the calculation of the permittivity correlation and pair distribution functions which can be used in conjunction with coherent theoretical approaches to compute scattering in inhomogeneous random media. One such classical approach is the Born approximation (Fig. 7) [Tsang et al., 1985] where the permittivity fluctuations act as distributed sources in an effective homogeneous medium. The scattering solution is then determined using a perturbation series. It is shown that for a random medium where the variation of the fluctuating permittivity is relatively small, the scattering coefficient from the medium can be directly calculated from the Fourier transform of the correlation function given by

$$C(\overline{r} - \overline{r}') = \langle \epsilon_f(\overline{r})\epsilon_f(\overline{r}') \rangle \tag{6}$$

where $\epsilon_f(\overline{r})$ is the fluctuating part of the permittivity function. The most commonly accepted form for the correlation function is the exponential function which was derived originally by Debye et al. [1957] for a sparse random collection of spherical particles and is given by

$$C(\overline{r}) = e^{-|\overline{r}|/r_0}. \tag{7}$$

The corresponding two-dimensional power spectral density is given by

$$\phi(\overline{k}) = \frac{r_0^2}{(1 + r_0^2|\overline{k}|^2)^{3/2}}. \tag{8}$$

Here, the parameter $\bar{r}_0$ is related to the mean diameter of particles in the random medium. For dense random media, experimental and numerical methods have been attempted to determine $C(\bar{r} - \bar{r}')$ from the recorded samples of the medium under study. For most practical cases, the behavior of the correlation function when $\bar{r}'$ is in the near vicinity of $\bar{r}$ does indeed resemble that of an exponential or Gaussian function. Because of the ease with which these functions can be manipulated algebraically, their use has become widely prevalent in the literature. A difficulty that arises however, is that the power spectral density is proportional to the integral of the correlation function over all space and thus estimation of the correlation function for only small values of $\bar{r} - \bar{r}'$ may not be sufficient for accurate estimation of the power spectral density for different ranges of observing frequencies.

The packing algorithm described in the previous section is an ideal tool for determining the validity and range of applicability of assumptions made in the determination of this correlation function. Furthermore, since the packing algorithm is capable of making a full Monte-Carlo realization of a random medium, it may be used to enhance the understanding of the physics behind the scattering mechanisms in a very dense medium. Computationally, it is much faster to perform simulations in two dimensions to first develop an understanding and then in the future to extend the results to three dimensions. In two dimensions, it can be shown that the radar cross section using the Born approximation is given by

$$
\begin{aligned}
\sigma^o_{vv}(\theta_i) &= |X_{01i}|^4 \mathcal{K} \\
\sigma^o_{hh}(\theta_i) &= \frac{k_0^4}{k_1^4} |Y_{01i}|^4 \mathcal{K} \\
\mathcal{K} &= \frac{2\pi^2 k_0^3 \phi(2k_{xi}, -2k_{1zi})}{\cos(\theta_i)(2k''_{1zi})} \left| \frac{k_{zi}}{k_{1zi}} \right|^2 \\
k_{xi} &= k_0 \sin(\theta_i) \\
k_{1zi} &= k_{1m} \cos(\theta_i)
\end{aligned}
\tag{9}
$$

where θ_i is the angle of incidence, X_{01i} and $\frac{k_0}{k_1} Y_{01i}$ are the transmission coefficients from medium 1 to medium 0, k_{1m} is the mean field propagation constant due to the average dielectric, $\langle \epsilon \rangle$, k''_{1zi} is the imaginary part of the propagation constant in the

10

scattering medium and the power spectral density ϕ is

$$\phi(k_x, k_z) = \frac{1}{(2\pi)^2} \int C(\bar{r} - \bar{r}') e^{i\bar{k}\cdot\bar{r}} d^2r. \tag{10}$$

The unknowns in this formulation are the propagation constant and the correlation function for the random medium. The propagation constant can be either the spatial average of the dielectric constant within the random medium (Born approximation) or derived from a mixing formula (distorted Born approximation). In what follows, the Born approximation will be developed for a prototypical example in which the described packing algorithm will be used to provide the correlation function. After illustrating the two-dimensional correlation function with the associated power spectral density, a comparison will be made with similar results obtained by using an exponential correlation function (7) having the same correlation length. In the calculation of the permittivity fluctuation correlation function from the collected samples of the medium, it is common to generate the auto-correlation function of each sample and then average the resultant auto-correlation functions. However, a difficulty may arise from this procedure in that the Fourier transform of the correlation function may become negative over some partial frequency range. This is a result of poor estimation of the tail of the correlation function and possible asymmetry in the sample cross section, both of which are a consequence of the finite size of the sampled medium. To circumvent this difficulty while keeping the size of the sampled medium within realistic dimensions, the power spectral density should be computed directly from the Fourier transform of a profiled sample of the random medium. Since the correlation function of the permittivity fluctuation process is continuous, it implies that the process is continuous in the root mean squared sense, which in turn implies that the power spectral density can be directly computed from

$$\phi(k_x, k_z) = \lim_{\substack{X \to \infty \\ Z \to \infty}} \frac{1}{XZ} E \left| \int_0^X \int_0^Z \epsilon_f(x, z) e^{i(k_x x + k_z z)} dx dz \right|^2. \tag{11}$$

The example considered here simulates the observation of a two-dimensional layer of sand particles with permittivity $\epsilon_s = 3.15 + j0.005$, $\langle\epsilon\rangle = 2.54 + j0.004$, $\langle\epsilon_f^2\rangle = 0.56$ and volume fraction $f = 0.8$. Individual realizations of Gaussian dis-

11

tributed packed particles were created using a mean radius $r = 2$ mm with a standard deviation of 0.4 mm for the two principal axes and a uniform distribution for the orientation angle of the ellipses. Observation frequencies used for this discussion will be at a below-resonance frequency of 10 GHz ($\lambda_s/2 = 8.5$mm) and an above-resonance frequency of 35 GHz ($\lambda_s/2 = 2.4$mm), where resonance refers to the average half wavelength ($\lambda_s/2$) dimension of the scattering particles. Over three hundred packing realizations of dimension 0.2 x 0.2 m were used to determine the power spectral density directly from the Fourier transform of the packed profiles given by the packing algorithm. The correlation function and the power spectral density are shown in Figs. 8 and 9, respectively, where the non-axial symmetry patterns are clearly displayed. The strongest peak in the power spectral density lies along the diagonal as would be expected in a tightly packed array of two-dimensional spheres with a narrow size distribution. A wider distribution would give a more axially symmetric two-dimensional spectrum.

This can be demonstrated by using a Rayleigh distribution to determine particle radius rather than a Gaussian distribution. Because the packing algorithm has a limited resolution due to the discretization of the particle (Eqs. 2 and 3), the Rayleigh distribution is truncated at the very small scale. Furthermore, for the sake of comparison with previous theoretical and experimental work, particle shapes used with the Rayleigh distribution were made circular rather than elliptical, this has the effect of reducing the randomness of particle locations, but this is an effect that is ameliorated by the wider particle size distribution.

The probability density functions of both distributions are shown in Fig 10, where it can be seen that the Rayleigh distribution is wider by about a factor of three. Thus for the wider particle size distribution we would expect that the correlation function and spectral density to more closely approximate that of the exponential function (which would be correct for completely random particle placement) and this is indeed shown to be the case. Plots in Fig. 11-a through 11-c illustrate the correlation function and its power spectral density along three principal axes of the

two-dimensional volume for both particle distributions and the exponential correlation function. It can be seen that at both short and long distances, the correlation function of both particle distributions and the theoretical exponential function agree very well, but it is at the mid-range distances where the functions can be seen to differ. These differences become more apparent in the low frequency region of the power spectral density for the derived correlation functions. Note again a better agreement of the Rayleigh distributed particle result to the theoretical exponential function but still an appreciable error at the low frequency region.

Referring to the Gaussian distribution function, the effect of the strong peaks in the power spectral density function along the XZ axis in Fig. 11-b can be clearly seen in the extended periodicity of the correlation function along this axis. Again, this is indicative of the natural ordering of the system for tightly packed arrays of particles with a narrow particle size distribution and we note that it is less of a feature when the particle sizes follow a Rayleigh distribution. An important consequence of this lack of symmetry, however, is that it would be inappropriate to calculate the correlation function along one axis of the distribution (such as the function in Fig. 10-a) and to enforce axial symmetry. The effect of such an action would be that the resulting power calculated through (10) would not be positive for all frequencies because the chosen correlation function along the one axis is not, and can not be, the correlation function for an axially symmetric medium. In effect then, if an exponential or Gaussian function is not to be used, the only appropriate way to calculate the correlation function is to completely sample the fluctuations in two- or three-dimensional space. Furthermore, and more importantly, as is shown by Figs. 11-a through 11-c, the deviation of the numerically derived power spectral density from the exponential power spectral density is as high as an order of magnitude at the lower frequencies, which is precisely the region of validity for the Born approximation.

As indicated by (9), only a portion of $\phi(k_x, k_z)$ is "visible" at a particular frequency. The loci of the spatial frequencies as the incidence angle varies from $0°$ to $90°$ is an ellipse with semi-axes of $2k_0$ and $2k_{1m}$ as illustrated in Fig. 12. In this figure

it can be seen that while the spectral density is not axially symmetric, the visible regions at each of the observing frequencies are nearly so. The effects of the asymmetry are most strongly observed at frequencies near the resonance of the particles within the medium. This figure can be used to understand the relationship between observing frequency and physical structure of a random medium. Decreasing particle sizes would have the effect of moving features radially outward in the figure, the same effect as decreasing frequency. Narrowing the particle distribution would have the effect of increasing the magnitude of the peaks shown in the figure and further disturb the high frequency agreement of the observed backscatter with the backscatter response expected for a medium whose particles follow an exponential function. Another interpretation of the figure shows that the particle size distribution of a random medium may be explored by frequency sweeping near the particle resonance at angles slightly greater than forty five degrees.

Given the derived correlation function for a specific particle size distribution we can carry out the remaining mathematical operations in (9) to get the observed backscattering cross section, which is shown in Figs. 13 and 14. In Fig. 13 the backscattering coefficients of the medium for both the vertical and horizontal polarizations at 10 GHz and 35 GHz are shown and compared with those derived based on an exponential correlation function for a Gaussian particle size distribution. Fig. 14 is the same as Fig. 13 for an observation frequency at particle resonsance (21 GHz), where differences between observed and predicted backscatter response are expected to be the greatest.

Referring to Figs. 8 through 14, the following observations are in order: (1) differences between the backscattering coefficients estimated from the correlation function derived from the Monte-Carlo simulation and the exponential function can be as high as 10 dB, (2) angular variation may depend strongly on the observation frequency and particle size distribution (see Fig. 14), and (3) the correlation function and the respective power spectral density are not likely to be radially symmetric, but this may not have a strong effect on the observation with the exception of frequencies

14

near resonance.

Another statistical function relating to particle positions that is commonly used in the study of random media is that of the pair distribution function, $p(\bar{r}_j | \bar{r}_i)$, which is the probability of finding a particle located at a position $\bar{r}_j$, given a particle located at position $\bar{r}_i$. The knowledge of the pair distribution function becomes necessary where the effective propagation constant of a dense random media is to be determined [Tsang et al., 1985; Lax 1952]. As the packing algorithm can be used to determine the correlation function, it can also be used to determine the pair distribution function. This has been done for the previous example and the result is illustrated in Fig. 15. In this figure the function is shown as a gray scale image in two dimensions where the brightness is directly proportional to the probability. As expected, a dark area covers the central region indicating the zero probability of having two particles intersecting one another. More remarkable is the ringing effect along the diagonals of the image, indicating periods of high and low probability which is reflective of the results obtained by the correlation function. Again, this is a result of the dense packing with a narrow size distribution. In comparison, the Percus-Yevick pair distribution function predicts an axially symmetric function for single sized spherical particles. The example given here clearly is not so and cannot be so for mono-sized particles under the influence of gravity. This does not disprove the Percus-Yevick pair distribution function but it does call into question its application to macroscopic granular media under the influence of external forces.

4 Conclusions

In this paper we have introduced a new approach to determining particle arrangements. The approach is computationally efficient, flexible and was demonstrated to work in two dimensions as well as three for non-spherical particles. A two-dimensional "rocks" example was also given that demonstrated the ability of the algorithm to work with particles of arbitrary shape. The algorithm was then used to compute the correlation function for two different size distributions of particles, one Gaussian and the

15

other Rayleigh and it was highlighted that the proper way to calculate the correlation function was through an averaged periodogram in the spectral domain rather than averaging individual correlation functions or assuming radial symmetry from the outset. The correlation functions of the two particle size distributions were compared with a theoretical exponential correlation function where it was shown that the derived functions deviated from the theoretical at low frequencies but agreed well at high frequencies. It was also shown that the wider Rayleigh distribution gave a better fit overall to an exponential function as is expected.

Derived correlation functions from the packing algorithm was used to compute radar backscatter via the Born approximation. Finally, another application of the packing algorithm is given as it applies to the determination of the particle pair distribution function which is a key unknown in the quasi-crystalline approximation and an argument is presented as to why the more common Percus-Yevick pair distribution function is not appropriate for use with granular media.

Acknowledgements

References

[1] Appleton, P.N., P.R. Siqueira, and J.P. Basart, A Morphological Filter for Removing 'Cirrus-Like' Emission from Far-Infrared Extragalactic IRAS Fields, The Astronomical Journal, 106(4), 1664-1678, 1993.

[2] Broyles, A.A., S.U. Chung, and H.L. Sahlin, Comparison of Radial Distribution Functions from Integral Equations and Monte-Carlo, Journal of Chemical Physics, 37(10), 2462-2469, 1962.

[3] Buchalter, B.J. and R.M. Bradley, Orientational Order in Random Packings of Ellipses, Physical Review A, 46(6), 3046-3056, 1992.

[4] Chandrasekhar, S., *Radiative Transfer*, 393 pp., Dover Publications, New York, 1960.

[5] Debye, P., H.R. Anderson, and H. Brumberger, Scattering by an Inhomogeneous Solid. II. The Correlation Function and Its Applications, Journal of Applied Physics, 28(6), 679-683, 1957.

[6] Ding, K.H., C.E. Mandt, L. Tsang, and J.A. Kong, Monte-Carlo Simulations of Pair Distribution Functions of Dense Discrete Random Media With Multiple Sizes of Particles, Journal of Electromagnetic Waves and Applications, 6(8), 1015-1030, 1992.

[7] Giardina, C.R. and E.R. Dougherty, *Morphological Methods in Signal and Image Processing*, 321 pp., Prentice Hall, Englewood Cliffs, N.J., 1988.

[8] Lax, M., Multiple Scattering of Waves. II. The Effective Field in Dense Systems, Physical Review, 85(4), 621-629, 1952.

[9] Percus, J. and G. Yevick, Analysis of Classical Statistical Mechanics by Means of Collective Coordinates, Physical Review, 110, 1-13, 1958.

[10] Serra, J.P. *Image Analysis and Mathematical Morphology*, 601 pp., Academic Press, New York, 1982.

[11] Tsang, L. and A. Ishimaru, Radiative Wave Equations for Vector Electromagnetic Propagation in Dense Non-tenuous Media, Journal of Electromagnetic Waves and Applications, 1(1), 59-72. January 1987.

[12] Tsang, L., J.A. Kong, and R. Shin, *Theory of Microwave Remote Sensing*, 613 pp., John Wiley & Sons, New York, 1985.

[13] Vallese, F. and J.A. Kong, Correlation Function Studies for Snow and Ice, Journal of Applied Physics, 52(8), 4921-4925, 1981.

[14] Visscher, W.M. and Bolsterli, M. Random Packing of Equal and Unequal Spheres in Two and Three Dimensions. Nature, 239, 504-507, October 27, 1972.

[15] Wen, B., L. Tsang, D. Winebrenner, and A. Ishimaru, Dense Media Radiative Transfer Theory: Comparison with Experiment and Application to Microwave Remote Sensing Polarimetry, IEEE Transactions on Geoscience and Remote Sensing, 28(1), 46-59, 1990.
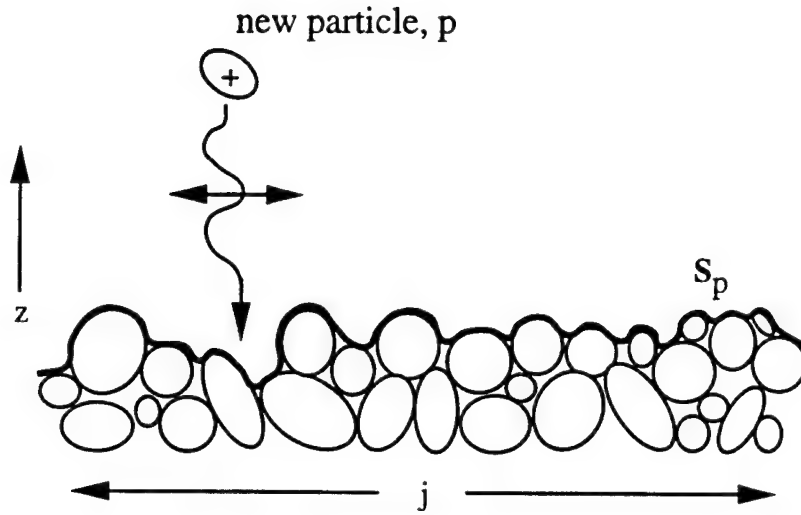
Figure 1: Illustration of the two-dimensional packing algorithm. Particles are fit to the surface S_p to find the minimum height, z. Once a particle has been fit to the surface, it becomes part of the surface for the next iteration of the process.
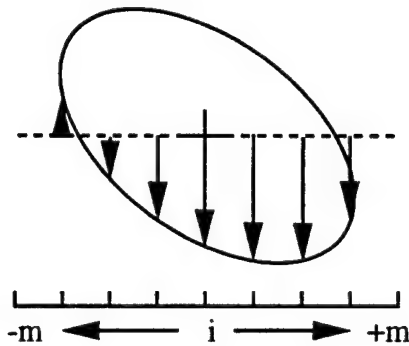
Figure 2: Illustration of the lower surface of a particle, M_p^{lower}. The particle is discretized into a horizontal grid and the maximum and minimum heights of the particle at points on the grid define the upper and lower surfaces.

S(j_1 + i) - M(i) lower

S(j_2 + i) - M(i) lower

max

max

min

j = j_1

j = j_2
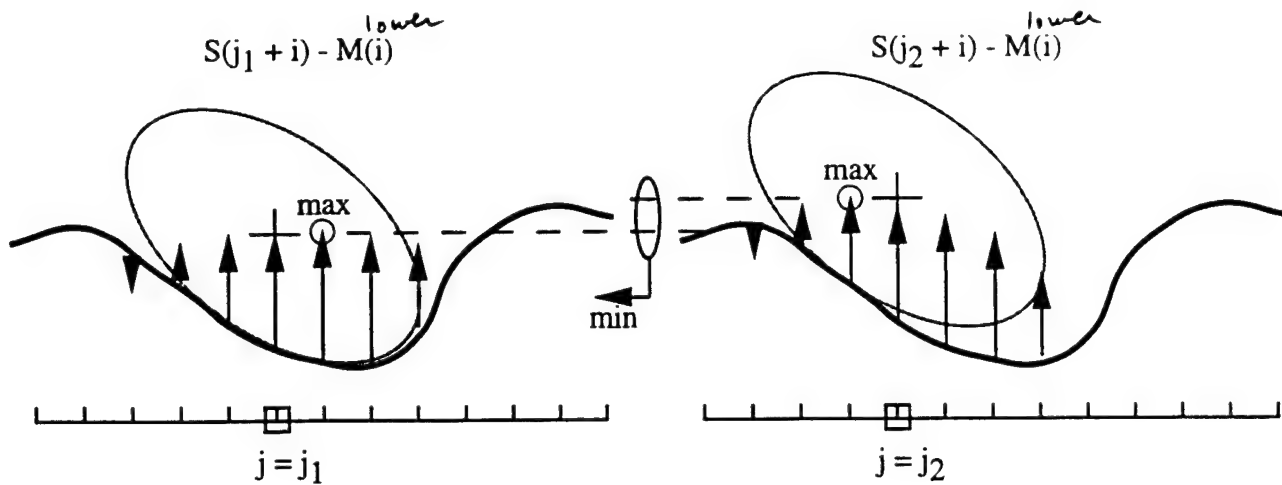
Figure 3: Illustration of equation (4) for two different points (j_1, j_2) on the surface $S(j)$. The dilation of the surface is shown for each point on the surface where the maximum is highlighted by a circle. This is the height of where the center of the ellipse would lie for a given horizontal location, j. The minimum of these heights defines the point of minimum potential energy.
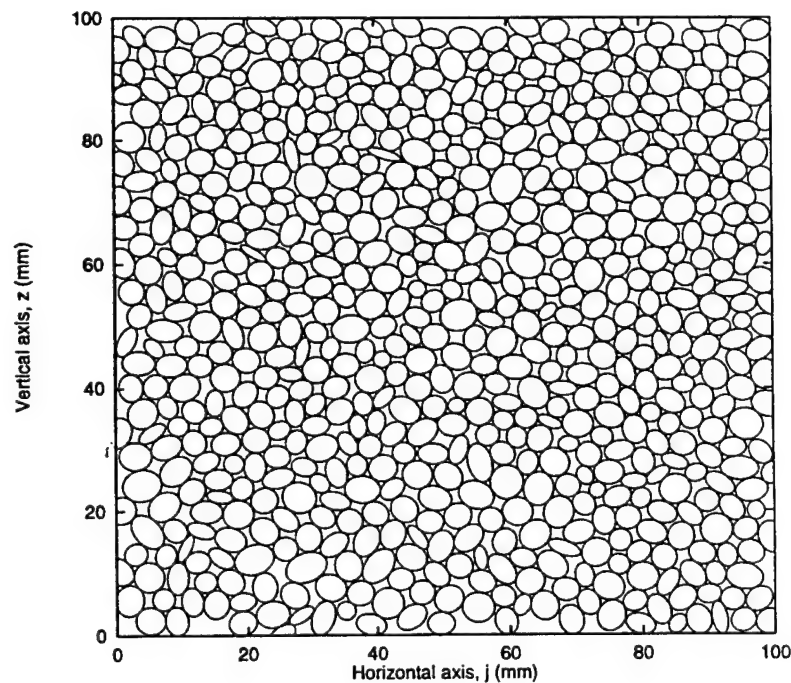
Figure 4: Demonstration of the two-dimensional packing algorithm. Particle radius is 2mm ± 0.4mm. In this case the volume fraction is 0.8. This particular simulation took 23 seconds on a Sun 10 workstation.
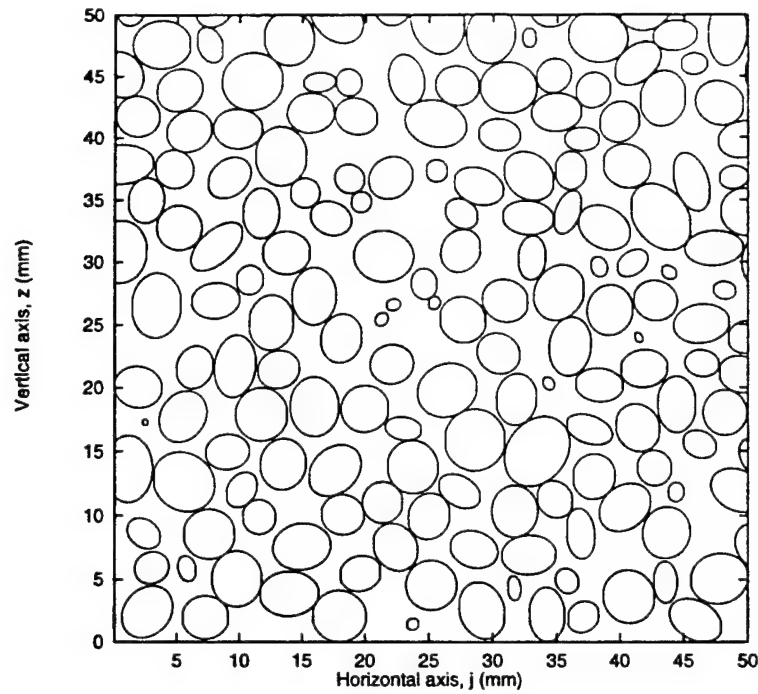
Figure 5: Demonstration of the three-dimensional packing algorithm. Shown is one slice taken out of a 50mm^3 cube filled with ellipsoidal particles with radii of 2mm $\pm$ 0.4 mm. This simulation using 3300 particles took approximately 3 hours using 24 processors of an IBM SP Parallel computer.
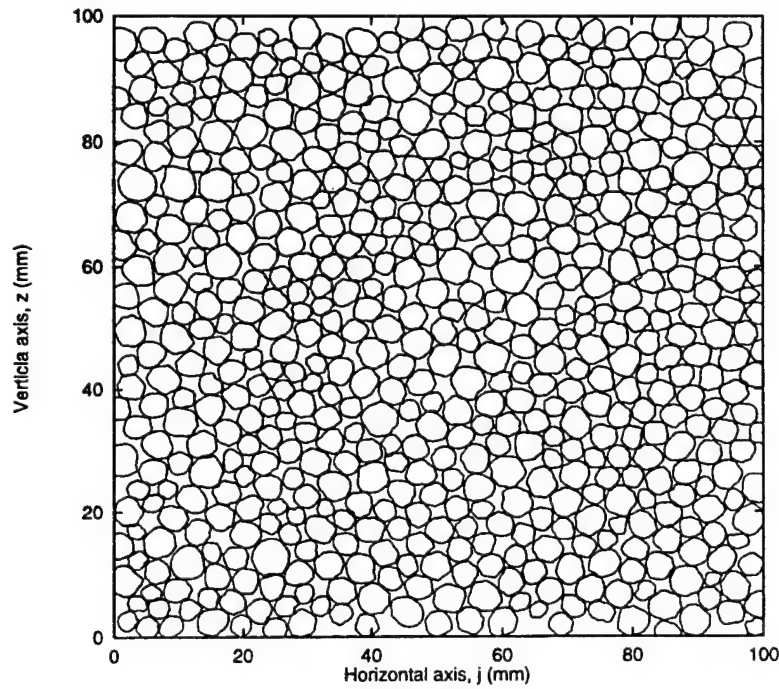
Figure 6: Demonstration of the packing algorithm for two-dimensional rocks. Rock surfaces are generated by a random walk about a uniform radius 2mm $\pm$ 0.4mm. This particular simulation took approximately 30 seconds on a Sun 10 Workstation.
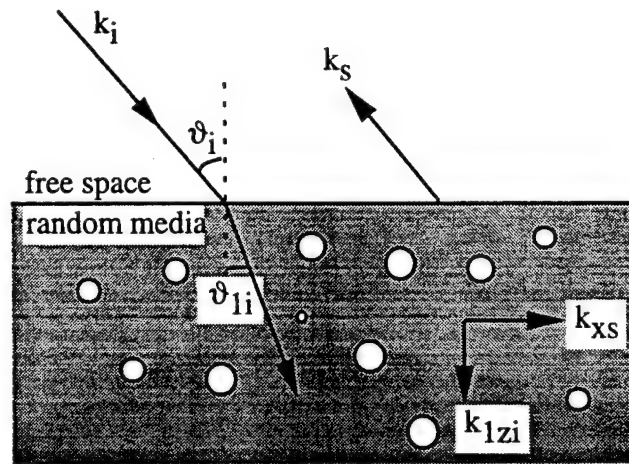
Figure 7: Geometry for a two-dimensional random medium. Medium 0 is considered free space and medium 1 is a random media consisting of particles as described in Fig. 4.
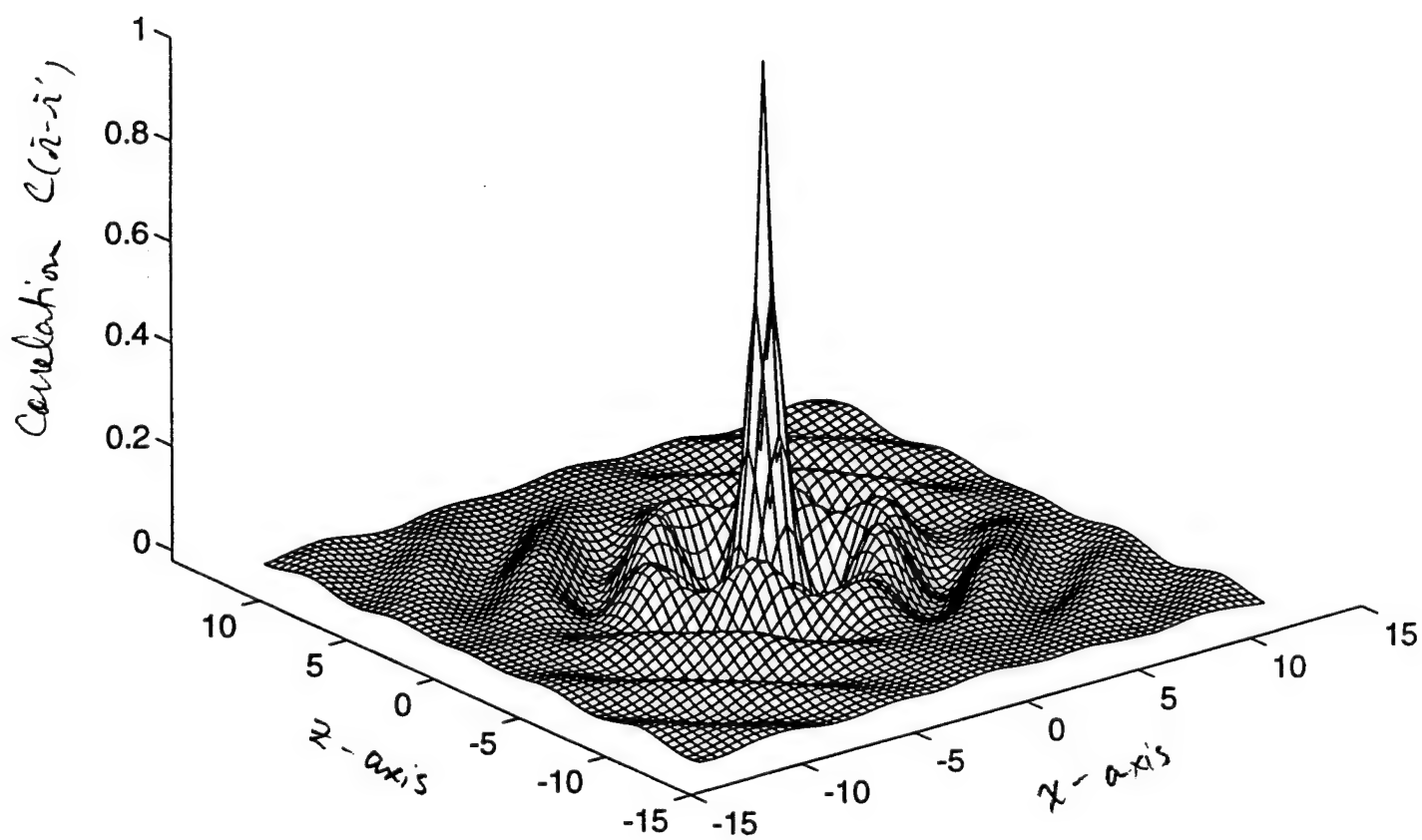
Figure 8: Two-dimensional correlation function for the particles in Fig 4. The correlation function is not axially symmetric.
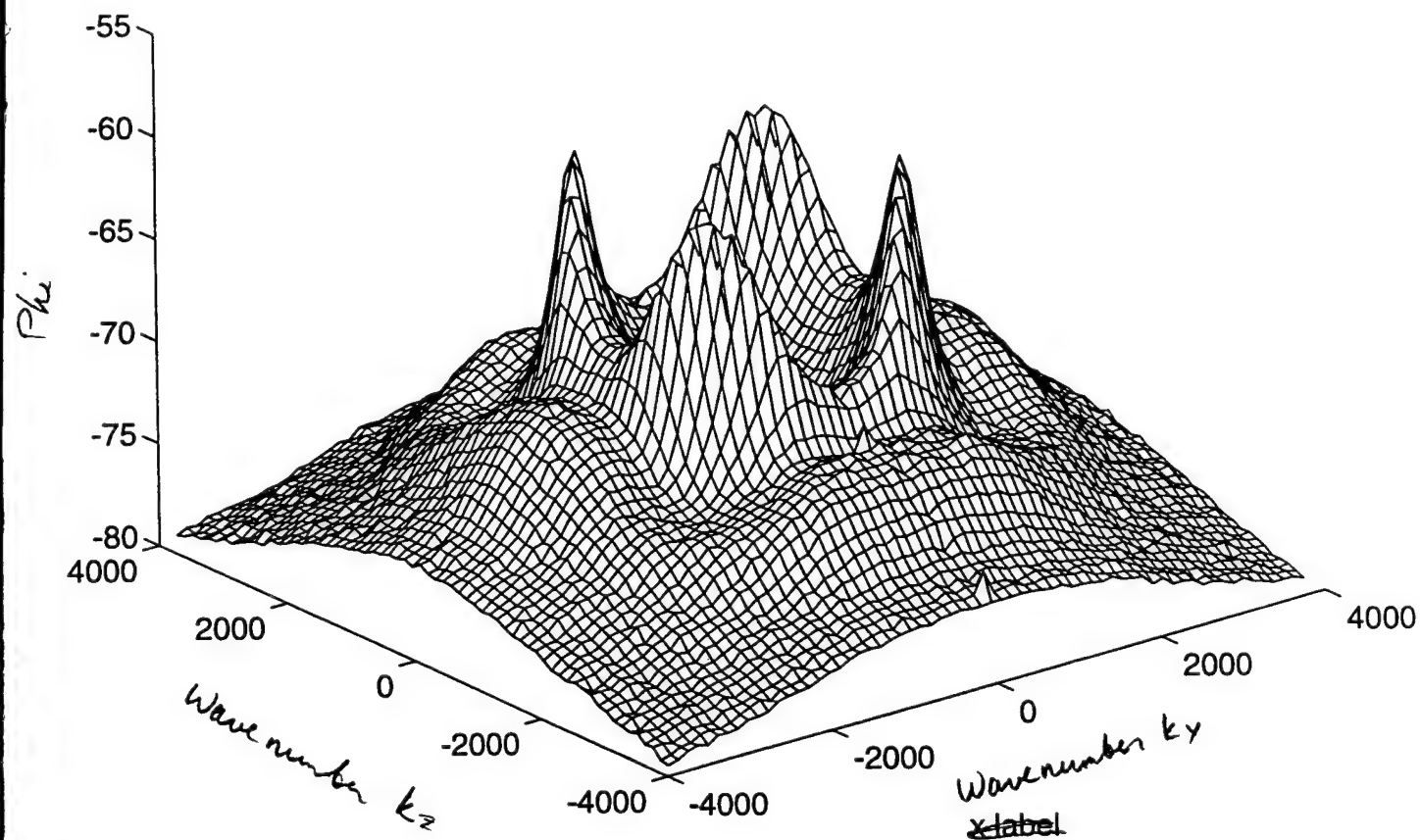
Figure 9: The power spectral density derived from data shown in Fig. 4. Strong peaks along the diagonal highlight the periodicity in the correlation function seen along this axis. Arcs drawn along a constant radius are proportional to the backscatter intensity as a function of incidence angle.
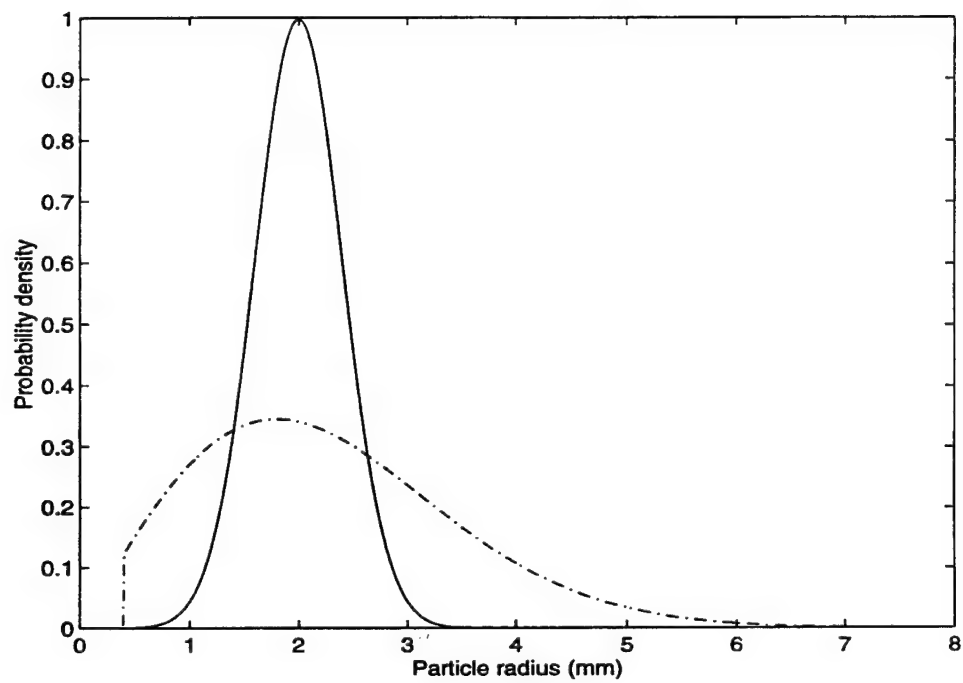
Figure 10: Gaussian (solid line, --) and truncated Rayleigh (dot dashed line, .--) Probability distribution functions of particle radii used in the packing algorithm. Both distributions have the same mean.
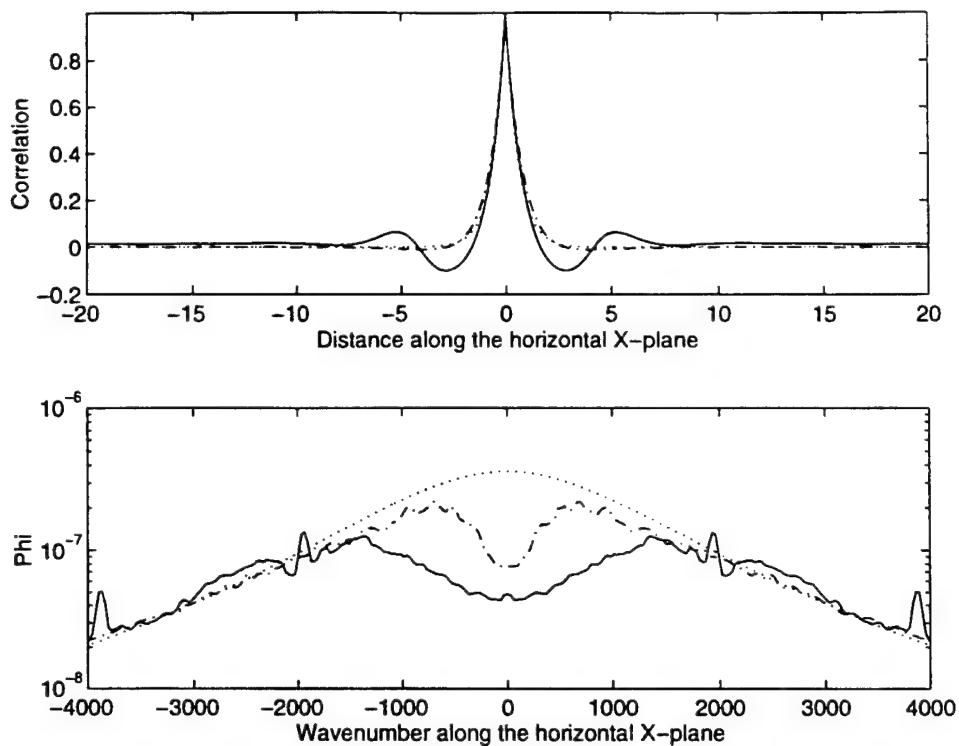
(a)
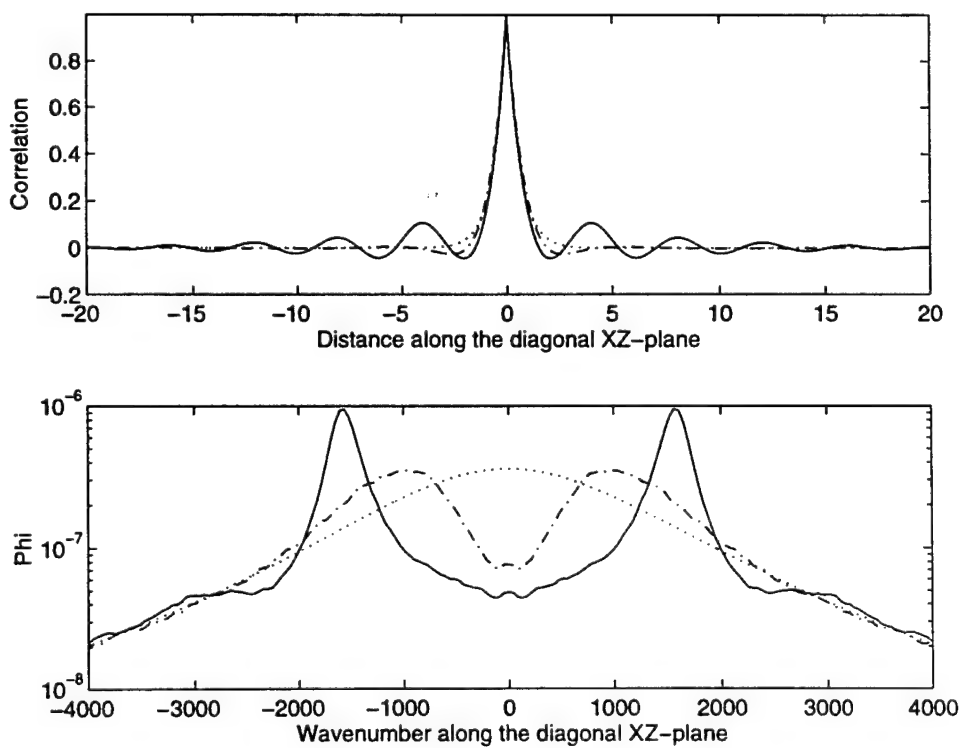
(b)
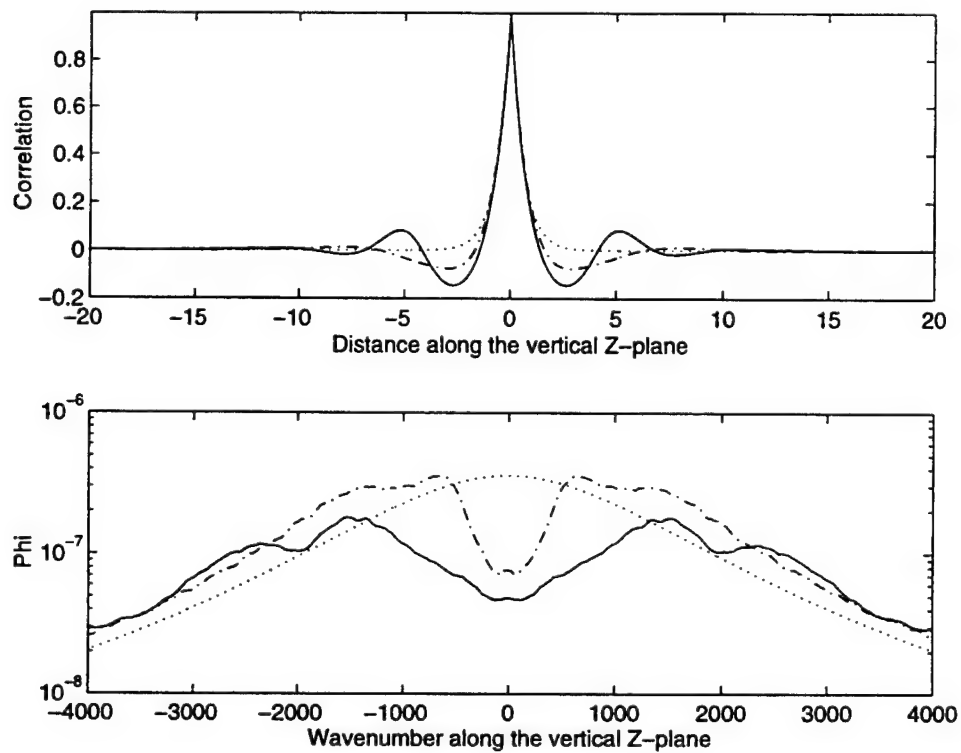
(c)

Figure 11: Slices of Figs. 8 and 9 taken along the principal axes of (a) $\theta = 0°$, (b) $\theta = 45°$, and (c) $\theta = 90°$. The solid lines (–) and the dot-dashed lines (.–) show the numerically derived values for the Gaussian and Rayleigh particle size distributions respectively. The dotted lines (⋯) show the equivalent correlation function and spectrum for the best fit exponential.
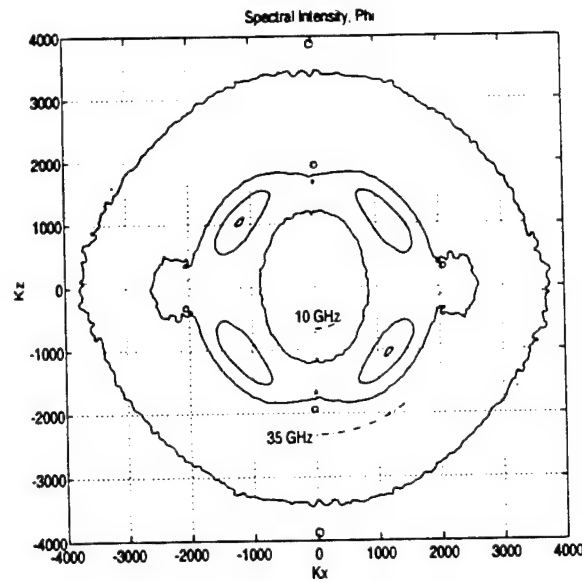
Figure 12: Illustration of the visible region of the Born approximation at two different frequencies shown overlaid on a contour map of the power spectral density (Fig. 9) for the Gaussian particle size distribution. Note that the greatest angular variation due to the packing structure occurs near resonance at $f = 21\text{GHz}$.
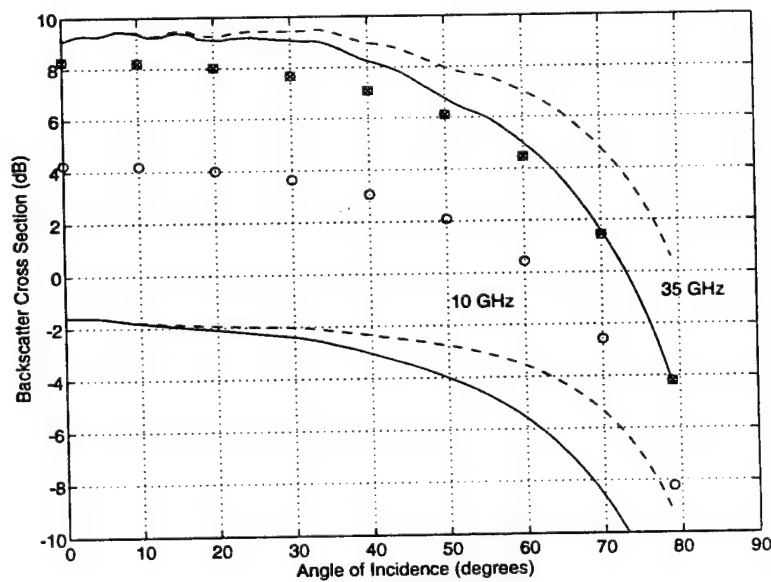
Figure 13: Results of the two-dimensional Born approximation for both 10 and 35 GHz for the Gaussian particle size distribution. Solid lines (–) are for vertical polarization, dashed (- -) are for horizontal polarization and the symbols (o and ⌗) indicate vertically polarized results of the Born approximation using the best fit exponential (Fig. 10).
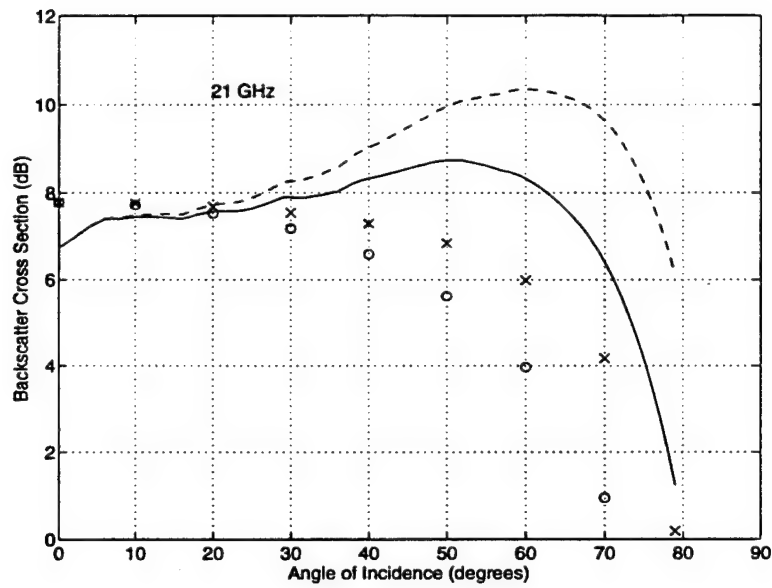
Figure 14: Results of the two-dimensional Born approximation at particle resonance ($f = 21\,\text{GHz}$) for both numerically derived (Gaussian particle size distribution) and exponential correlation functions. Solid lines (–) and circles (o) indicate vertical and dashed lines (- -) and crosses (×) indicate horizontal polarizations. The symbols represent the theoretical exponential curves in both cases.
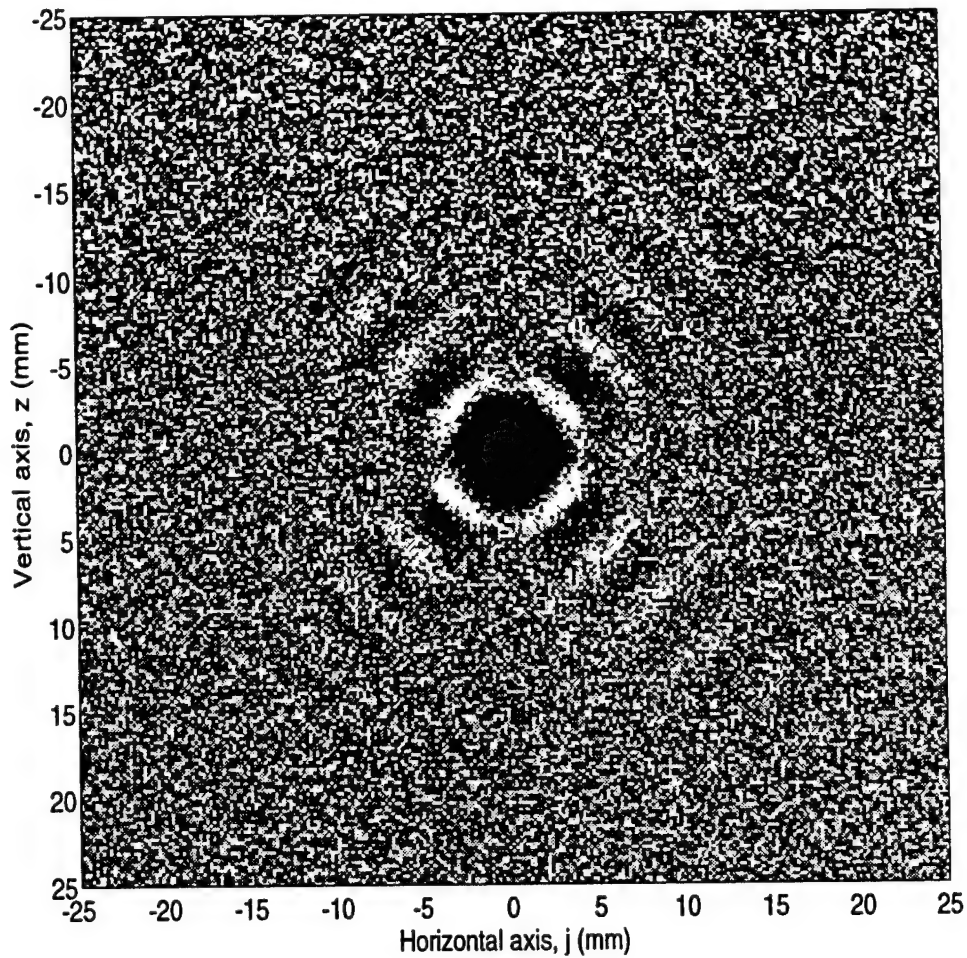
Figure 15: The pair distribution function, $p(\bar{r}_j|\bar{r}_i)$ for the packed array shown in Fig. 4 (Gaussian size distribution). Dark areas indicate low probability and bright areas indicate high probability of finding another particle at $\bar{r}_j$ given a particle at $\bar{r}_i$.

Numerical Scattering Analysis for Two Dimensional Dense Random Media: Characterization of Effective Permittivity

Kamal Sarabandi and Paul R. Siqueira
Radiation Laboratory
Electrical Engineering and Computer Science Department
University of Michigan, Ann Arbor, MI 48109-2122

Abstract

In this paper a new numerical method for determining effective permittivity of dense random media in two dimensions is presented. The core of the method is to compare the average scattered field of a random collection of scatterers confined within an imaginary boundary with the scattered field from a homogeneous dielectric of the same shape as the imaginary boundary. The two-dimensional problem is aggressively studied here to provide insight into the dependence of the method's convergence on particle size, boundary shape and boundary dimension. A novel inverse scattering method is introduced based on the method of moments which greatly reduces the computation time and increases the flexibility of the procedure to analyze a variety of geometries. Results from this two-dimensional method may be used directly to compare with theoretical methods for determining effective permittivity such as the Polder-Van Santen mixing formula or field techniques such as the quasi-crystalline approximation.

1   Introduction

A fundamental electromagnetic characteristic of a radar target is its permittivity or equivalently its propagation constant for a non-magnetic material. Most natural targets at certain scales can be considered to be inhomogeneous, consisting of discrete components (or inhomogeneities) that are separate from a uniform background material. A uniform layer of snow for instance at low frequencies may appear to be a homogeneous medium, variations of interest being differences in snow depth or changes in the snow wetness on a scale similar to the observing wavelength. As the wavelength decreases there will come a point where it is necessary to consider the interaction of electromagnetic fields with individual crystals of ice that make up the snow layer. In such a case the background

1

medium may be considered the host and the ice crystals the inclusions. In both of these cases, it is of interest to theoretically predict the effective permittivity of the random medium. At low frequencies, this is accomplished through the use of a mixing formula that directly models the interaction of electromagnetic fields with individual scattering particles through the polarizability tensor of isolated particles.

The most commonly used mixing formula is given by Polder and Van Santen [3]. The Polder-Van Santen mixing formula relates the combined, effective dielectric constant of a collection of particles, to that of its constituents. The Polder-Van Santen model, as with many mixing formulas, relies on the observing wavelength to be much larger than the scale of the inhomogeneities within the material under study.

Approaches where the field interaction with the individual discontinuities are taken into account are termed field models, popular forms of which are Foldy's approximation, strong fluctuation theory, the quasi-crystalline approximation (QCA) and the quasi-crystalline approximation with coherent potential (QCA-CP) [1, 10]. With the exception of Foldy's approximation, these theories include additional interaction terms that occur because of the scattering of fields between individual particles and thereby are considered to be more accurate than mixing formulas when scattering from individual particles becomes a factor. Theoretical field approaches however must truncate this interaction at some given order to make the theory tractable, through which an approximation is introduced. The validity of this approximation for different situations is often difficult to assess, particularly when the variety of situations that need to be considered is large.

Validation of the mixing formula and field models is commonly accomplished through a comparison with physical experiment. Several drawbacks of experimental methods are that it is difficult to reduce natural variabilities in the sample under study and often it is not possible to gather sufficient and accurate

2

ground truth to fully characterize the experiment. One such example is with the implementation of the quasi-crystalline approximation, where knowledge of the pair distribution function of particle positions is required, a parameter that is nearly impossible to measure for a naturally occurring random medium. These variabilities can be reduced by performing a controlled experiment in the lab, one notable experiment performed by Mandt [2], where individual glass spheres where placed at computer generated positions in Styrofoam. While experiments such as the one described here are an important component in analyzing the validity of field models or mixing formulas, errors still may be introduced due to insufficient sample sizes or possible systematic errors made in the measurement. It is of course also useful to analyze similar problems through alternate approaches so as to provide a measure of validity of those measurements.

An alternative to the physical measurement process is to perform Monte-Carlo numerical simulations, where through the use of computers, physical variations can be eliminated. Such a numerical method requires the use of a packing algorithm to simulate particle arrangements in a medium and an electromagnetics code such as the method of moments or the T-matrix method to solve for the fields within the medium under study. These methods are capable of accounting for all multiple scattering terms within the medium and therefore can be considered an exact solution for the problem. One such method uses a truncated T-matrix approach to estimate the extinction from a collection of up to 4000 spheres confined in a cubic volume [11]. Extinction for the non-absorptive scatterers is calculated by integrating the incoherent power scattered by the cubic volume over all observation angles (i.e. the amount of coherent power attenuated due to scattering). In effect, this method calculates the imaginary component of the effective permittivity due to multiple scattering. Difficulties with this method may arise however due to the fact that the volume is isolated in free space, thereby enhancing the contrast of the scattering volume being analyzed from its surroundings; ideally, the volume under study would be immersed in a homogeneous medium with a permittivity equal to that of the effective permit-

tivity of the volume. Furthermore, because of this contrast problem, it is likely that the calculated extinction would be dependent on the shape and size of the boundary walls, an effect not thoroughly explored in the paper.

In this light, we present a new method of determining the complex effective permittivity for two-dimensional dense random media. The core idea of the method is to confine a random distribution of particles within an imaginary boundary from which the coherent field may be determined over many realizations. Using a homogeneous material whose dimensions are the same as the imaginary boundary used for the random distribution of particles, we adjust the permittivity of the material so that the homogeneous medium coherent field is identical to the random medium coherent field. Thus, rather than ignoring the effect of the boundary shape and size, it is directly taken into account.

The two-dimensional problem is rigorously implemented here to provide insight and guidance for future work in analyzing the more general problem in three-dimensions. This is accomplished by exploring the convergence effect as it depends on boundary shape and size and particle size. The two-dimensional problem does have direct application in modeling field interaction with fibrous material such as muscle tissue or dense prairie grasses. Results from this study can also provide a very important contribution to the study of dense media, that is, an "exact" solution for the effective permittivity that may be used as a benchmark for testing theoretical formulations such as the Polder-Van Santen mixing formula and the quasi-crystalline approximation.

2   Formulation

In this section the numerical procedure for characterizing the effective permittivity of a random medium containing discrete scatterers is outlined. The procedure for determining the effective permittivity is a four step process: (1) the first step is to generate a collection of particles with a specified volume fraction and particle arrangement contained within an imaginary boundary, (2) given an incident field, the method of moments [4,5] is then used to solve for the scattered field,

4

(3) scattered fields for each realization of the collection of particles are averaged over all observation angles to determine the coherent scattered field which is related to the shape and size of the imaginary boundary, as well as the effective permittivity and (4) the effective permittivity of the medium is then found by finding the best fit between the coherent field from the Monte-Carlo simulations and the field scattered from a homogeneous medium with permittivity, ϵ_{eff} having the same boundary as the imaginary boundary. This step is an inverse scattering problem for which a novel technique based on the eigen-analysis in conjunction with the method of moments is developed.

The packing algorithm used here [8] simulates the arrangements of particles with arbitrary shape, size and orientation for "natural", dense media. From this arrangement of particles, a method of moments solution for the scattered fields is obtained and the process is repeated many times in order to generate the statistics of the scattered field. This Monte-Carlo simulation determines the average (coherent) scattered field as a function of observation angle, θ, for a random dense medium, $\langle \overline{E}^s_{\text{random}}(\theta) \rangle$. At this stage it is possible to retrieve the incoherent scattered power which can be used directly to provide insight into the phase function used by radiative transfer. By taking the coherent scattered field one step farther, it is possible to determine the effective propagation constant which can in turn be used to compare with QCA or even to create an empirical mixing formula for the simulated media.

To characterize the propagation constant of the mean field, we search for the dielectric constant of a uniform, homogeneous dielectric whose shape and size are the same as that used to bound the collection of random scatterers and exhibits the same scattering pattern. It has been found that a unique effective permittivity does exist such that the scattering patterns from both the homogeneous and random media are very closely matched and thus the basic concept of the approach is validated. In the first case, a rectangular dielectric slab is used (Fig. 1). The method of moments is used to determine the scattered field from

5

this uniform dielectric as a function of observation angle and dielectric constant, $\overline{E}^s_{\text{uniform}}(\epsilon, \theta)$. A minimization technique can then be used to find the best fit permittivity for observed scattered field of the uniform slab to the average field from the random scatterers:

$$\epsilon_{\text{eff}} = \frac{\min}{\epsilon} \left[|\overline{E}^s_{\text{uniform}}(\epsilon, \theta) - \langle \overline{E}^s_{\text{random}}(\theta) \rangle | \right]. \tag{1}$$

To find the minimum of (1) by iteration requires calculation of the volume currents and the scattered field for each new trial. While performing these calculations for each trial entails a straightforward electromagnetic numerical solution, since the dimensions of the boundary may be electrically large, as required by convergence criteria, the procedure can become very time consuming. However a novel inversion solution is introduced in which using the method of moments, the problem may be solved essentially only once, additional trials entailing a simple matrix multiplication.

3 Dielectric Inversion, MoM – Eigen-analysis Procedure

The procedure of determining the scattered field from a dielectric body with inhomogeneous dielectric profile is a simple extension to the method of moments. In this procedure, the dielectric dependence of the impedance matrix is explicitly separated from the equation where it is highlighted that only the diagonal elements of the impedance matrix depend on the permittivity. By computing the eigenvectors and eigenvalues of the impedance matrix, it is possible to perform an inversion of the matrix prior to the inclusion of the permittivity term. Thus, calculation of the scattered field requires only a multiplication of the inverted eigenvector matrix and the dielectric term.

Consider a two-dimensional dielectric body illuminated by a plane wave. The incident wave induces a polarization current which becomes the source of the scattered field. The induced current is proportional to the total electric field

inside the scatterer and is given by

$$\overline{J} = -ik_0 Y_0(\epsilon - 1)(\overline{E}^s + \overline{E}^i) \qquad (2)$$

where $\overline{E}^i$ represents the incident wave and $\overline{E}^s$ is the scattered field given by

$$\overline{E}^s = \int_s \overline{J}(x', y') \cdot \overline{\overline{G}}(x, y; x', y') dx' dy'. \qquad (3)$$

Here $\overline{\overline{G}}(x, y; x', y')$ is the dyadic Green's function for two-dimensional problems and k_0 and Y_0 are, respectively, the free space propagation constant and characteristic admittance. Substitution of (3) in (2) results in the desired integral equation for the polarization current.

Solution to this integral equation must be obtained numerically. Using the method of moments, the integral equation is cast into a matrix equation of the following form

$$\overline{\overline{Z}}\,\overline{J} = \overline{E} \qquad (4)$$

where $\overline{\overline{Z}}$ is the impedance matrix, $\overline{J}$ is the polarization current, and $\overline{E}$ is the excitation vector. The polarization current can be obtained by inverting (4) and is given by

$$\overline{J} = \overline{\overline{Z}}^{-1}(\epsilon) \cdot \overline{E}, \qquad (5)$$

where $\overline{\overline{Z}}^{-1}$ is an implicit function of ϵ. The minimization algorithm, depending on the initial guess, usually requires the calculation of $\overline{\overline{Z}}^{-1}$ many times, a numerical procedure which makes the inversion algorithm numerically very inefficient for large scatterers.

In what follows, a procedure for the calculation of the polarization current is presented which does not require repetitive evaluation of $\overline{\overline{Z}}^{-1}$ for different values of ϵ. The minimization routine can be made efficient by noticing that the permittivity appears only in the diagonal elements of the impedance matrix. By splitting the impedance matrix into a diagonal term, $\beta(\epsilon)\overline{\overline{I}}$, and a modified impedance matrix term, $\overline{\overline{W}}$, we have

$$\overline{\overline{Z}} = \overline{\overline{W}} + \beta(\epsilon)\overline{\overline{I}} \qquad (6)$$

7

where $\overline{\overline{I}}$ is the identity matrix and $\beta = 1/(\epsilon - 1)$. Note that the $\overline{\overline{W}}$ matrix is dependent only on the scatterer geometry and is not dependent on the permittivity of the scatterer. By computing the eigenvalues, $\overline{\overline{\Lambda}}$, and the eigenvector matrix, $\overline{\overline{Q}}$ of the $\overline{\overline{W}}$ matrix, it is known that

$$\overline{\overline{W}} = \overline{\overline{Q}}\, \overline{\overline{\Lambda}}\, \overline{\overline{Q}}^{-1}. \tag{7}$$

Also noting that the identity matrix can be expressed by

$$\overline{\overline{I}} = \overline{\overline{Q}}\, \overline{\overline{I}}\, \overline{\overline{Q}}^{-1}, \tag{8}$$

(5) can be written as

$$\overline{J} = \overline{\overline{Q}}\, [\, \overline{\overline{\Lambda}} + \beta\overline{\overline{I}}\,]^{-1}\, \overline{\overline{Q}}^{-1}\, \overline{E} \tag{9}$$

where the dependency of the polarization current on the permittivity has been made explicit. The calculation of the eigenvalues and eigenvector matrix is performed only once for a particular scattering geometry. The determination of the scattered field as a function of dielectric constant has then been converted from one of matrix inversion to matrix multiplication. Convergence of the minimization takes place after approximately twenty seconds (15 iterations) on a Sun 10 workstation for a $3\lambda_i \times 1\lambda_i$ dielectric slab where λ_i is the wavelength in a dielectric slab with permittivity ϵ_i. Equivalently this is 300 unknowns for the TM polarization and 600 unknowns for TE polarization. The speed-up factor encountered is roughly two orders of magnitude.

4   2-D Mixing Formula

It is important to compare the numerical results from this analysis to theoretical models. At low frequencies, theories that relate the effective permittivity of a mixture to the permittivity of its components are termed mixing formulae, the most common of which is given by Polder and Van Santen [3]. The derivation given here parallels this work as it is applied to the two dimensional problem.

We begin by examining the interaction of one particle of a mixture with the surrounding mean field, $\langle \overline{E} \rangle$. We wish to find the effective permittivity, ϵ_{eff}

which is related to $\langle \overline{E} \rangle$ by

$$\langle \overline{D} \rangle = \epsilon_{\text{eff}} \langle \overline{E} \rangle \tag{10}$$

The electric flux density, $\overline{D}$ in the medium may be written as

$$A \langle \overline{D} \rangle = \int_{A_h} \epsilon_h \overline{E} ds + \sum_j \int_{A_j} \epsilon_i \overline{E} ds \tag{11}$$

where A is the area, ϵ_h and ϵ_i are the permittivity of the host and included materials, and the summation is taken over all of the particles, p_j in the medium. After some manipulation we arrive at

$$\epsilon_{\text{eff}} \langle \overline{E} \rangle = \epsilon_h \langle \overline{E} \rangle + \sum_j f_j \frac{1}{A_j} \int_{A_j} \overline{E}_j ds \tag{12}$$

with the volume fraction $f_j = A_j / A$. If we assume that the mean induced field in the particles may be expressed as the scalar product between a mean normalized polarizability tensor, $(\epsilon_i - \epsilon_h) \langle \overline{\overline{\alpha}} \rangle$, and the mean field in the medium, we find that the summation in (12) may be written as

$$\sum_j f_j \frac{1}{A_j} \int_{A_j} \overline{E} ds = f \langle \overline{\overline{\alpha}} \rangle \cdot \langle \overline{E} \rangle. \tag{13}$$

This substitution would be correct for a sparse, tenuous medium where individual particles do not perturb the field appreciably. The mean polarizability tensor in two dimensions is split into the TM and TE polarization. For the TM polarization, this tensor is unity, independent of particle shape and size. For TE polarization, the polarizability tensor can easily be obtained for arbitrary particle shapes as outlined by Sarabandi and Senior [6]. For a circular cylinder, the normalized polarizability tensor can be obtained analytically and is given by

$$\overline{\overline{\alpha}} = (\epsilon_i - \epsilon_h) \begin{bmatrix} \frac{2}{\epsilon_i + \epsilon_h} & 0 \\ 0 & \frac{2}{\epsilon_i + \epsilon_h} \end{bmatrix} \tag{14}$$

For radially symmetric particles or assuming random orientation we find the average polarizability as the average of the diagonal terms of the polarizability tensor. Thus for the two polarizations we arrive at the mixing formulae for circular cylinders as

$$\epsilon_{\text{eff}} = \epsilon_h + f(\epsilon_i - \epsilon_h) \tag{15}$$

$$\epsilon_{\text{eff}} = \epsilon_h + f(\epsilon_i - \epsilon_h) \frac{2}{\epsilon_i + \epsilon_h} \tag{16}$$

9

for the TM and TE polarizations respectively.

5   Results for a Simple Boundary Shape

Multiple trials of the presented method have been shown to provide values of effective permittivity independent of the boundary shape and independent of the boundary size once the size has passed some critical limit. This section describes the analysis of one such shape for varying particle size. The following section will address more completely the problem of algorithm convergence and shape independence.

The shape considered in this example is a rectangular $3\lambda_i \times 1\lambda_i$ dielectric slab where λ_i is the wavelength in a dielectric slab with permittivity $\epsilon_i = 3.6 + i1.0$ which reflects the real part of the inclusion permitivities. The size is chosen in this example so that at a volume fraction of 100%, the discretization of the homogeneous slab of 10 samples per wavelength will still be valid. The mean particle diameter is chosen to be one of $\lambda_i/10, 2\lambda_i/10,$ or $3\lambda_i/10$. A minimum of 100 realizations was performed for each volume fraction and the mean scattered field determined. From this mean scattered field, the forward and backscatter directions were used as sample points in the minimization algorithm given by (1). Other points might have been used, but empirical testing showed that this was not necessary, convergence to a unique solution occurred for all volume fractions and all particles sizes used for both TM and TE polarizations of the incident and scattered fields.

Demonstration of the ability of the method to find a true effective permittivity is given in Figs. 2 and 3 for volume fractions of 10% and 80% respectively. It can be seen in both extreme cases that the bistatic scattered field from the homogeneous dielectric gives an excellent fit to the entire average bistatic scattered field from the random medium even though only two points in the forward and backscatter direction are used in determining the effective permittivity. This is

particularly remarkable in Fig. 2 (10% volume fraction) where the locations of the scatterers for any particular realization is not reflective of the shape and size of the imaginary boundary.

Results from the simulations with varying volume fraction and particle size can be compiled onto a single plot that details the dependence of effective permittivity (real and imaginary components) on these parameters. Comparison can then be made with the theoretically derived mixing formula of Polder and Van Santen given in the previous section. This comparison is shown in Figures 4 and 5 for the TM and TE polarizations.

For the TM polarization it is interesting to note the exact agreement with the mixing formula model for small particle size for real permittivity. This behavior indicates that the mean field approach taken by the mixing formula is indeed effective for small particles illuminated by an E-polarized field. As particle size increases, we note a deviation from the mixing formula model. The imaginary component of the effective permittivity is especially illuminating as we note a measured loss term greater than the one predicted by the mixing formula, a result that indicates that the larger particles are contributing to the scattering process, a factor not accounted for in the mixing formula model.

For the TE polarization we see a significant deviation from the mixing formula results. The deviation of the numerical model however is an improvement over the mixing formula in that it follows the expected trend towards the limiting case of unity volume fraction. Similar to the case of TM polarization, the loss term for the H-polarized field demonstrates increased scattering losses due to the larger particle sizes as is expected.

This section has demonstrated how the presented method can be used to determine the effective permittivity for a random medium. The behavior of the effective permittivity was shown to behave in a manner consistent with what would be expected for changing volume fraction and particle size. An important question is whether or not the permittivity calculated is dependent on the shape

11

and size of the bounding area used. The next section addresses this problem and offers answers as to how small the imaginary boundary may be to still reflect the large scale behavior of the material parameters.

6 Convergence Considerations

This section seeks to offer evidence for the convergence of the solution for effective permittivity and to test independence of the method from the shape of the imaginary boundary used. To begin this controlled study, small particles of uniform diameter $\lambda_i/10$ are used, where, as before, λ_i is the field wavelength within the included material whose permittivity is chosen to be $\epsilon_i = 3.6 + i0.1$, the background material being free space.

There are some important differences between the results shown in this section and those given in the previous section. In this section, the imaginary part of the scatterer permittivity is chosen to be ten times smaller than that used in the previous section to assure that multiple scattering is allowed to take place more significantly. As a consequence however, since the imaginary component of the effective permittivity is a factor of approximately thirty-six times less than the real component, numerical errors in the estimate of the imaginary component may be much more evident than those for the real component. Another difference of concern between this and the previous section is that scatterers of uniform diameter are used here. Thus for high volume fractions in the range of 50% to the limit of 91%, the resulting collection of scatterer positions will be nearly crystalline and therefore anisotropic. To avoid this additional complexity, only volume fractions ranging from ten to fifty percent are shown here.

Already we have seen the ability of the method to achieve an excellent fit between the average scattered field from the random medium and the scattered field of a homogeneous dielectric. There are two questions that will be addressed in this section: 1.) How large should the scattering boundary be? and 2.) How many realizations are required to determine the forward and backscatter field accurately? As it happens, the answer to these two questions are related; the

larger the confining boundary gets, the larger is the variation of the electric field in the forward and backscatter directions. Thus as the bounded area increases, so does the uncertainty of the calculated field.

To determine the convergence of the method for changing boundary size, we refer to Figure 6 which displays the real part of the effective permittivity for the TM and TE polarizations as a function of boundary size for differing volume fractions of particles. We note in the figure that the solution is stable for a wide range of boundary sizes (i.e. horizontal lines). As boundary size decreases farther from the displayed range, it is expected that errors will increase due to an insufficient number of scatterers located within the boundary. At the other extreme of a large boundary size, it is expected that the numbers will become error prone due to the increased uncertainty in measuring the forward and backscattered field.

Individual realizations of the forward and backscatter field magnitude accurately follow a Rice-Nakagami distribution (Fig. 7) [9, pg. 94] where the mean value and standard deviation are dependent on the boundary shape and size. To explore the size dependence of the standard deviation, Figure 8 shows the standard deviation of backscatter magnitude for changing boundary size and volume fraction for both the TM and TE polarization. It can be seen from the graphs that the variation in observed field is not strongly dependent on volume fraction, but does increase steadily as the boundary size increases. If we make the observation that the standard deviation increases by a factor of two between the boundary sizes of $1.5\lambda_i$ and $2.0\lambda_i$, to achieve a given accuracy of field magnitude, the larger boundary would require four times as many simulations. The ideal boundary size would then appear to fall somewhere between $1.0\lambda_i$ and $1.5\lambda_i$. The increase of variance as a function of boundary size also highlights theoretical considerations for determining the incoherent scattered power, which should increase quadratically, proportional to the area. In the range of $1.5\lambda_i$ to $2\lambda_i$ this is not yet the case and therefore, based on these results, the boundary is not yet large enough

13

to determine the incoherent scattered field.

There are three basic geometries that have been tested here, a circular disk, a rectangular slab and a square. Real and imaginary effective permitivities for these shapes are shown in Figure 9 (note that the imaginary component is multiplied by a factor of ten) as a function of volume fraction for both TM and TE polarizations. Given also for comparison are the mixing formula results obtained from (15) and (16). From this figure it can be seen that there is essentially an exact match between the real permitivities for all three shapes with some small deviation being noticed for the imaginary part of the effective permittivity. These differences are likely due to difficulties in estimating an imaginary component that is much smaller than the real component of the permittivity with a relatively small number of realizations.

So far, in this section it has been demonstrated that the proposed technique yields stable results independent of boundary shape and size. It was also shown that the forward and backscattered field magnitudes accurately follow a Rice-Nakagami distribution whose variance increases as a function of boundary dimension. One final test is to show the dependence of minimum boundary size on particle size. As particle size increases, it is expected that increased scattering and reduction in the number scatterers for a given volume fraction will increase the minimum boundary dimension for which the algorithm will converge. Fig. 10 demonstrates this behavior by plotting the effective permittivity as a function of boundary dimension for three different particle sizes ($\lambda_i/10, 2\lambda_i/10$, and $3\lambda_i/10$) at a volume fraction of 40%, for a TM polarized field. From this figure it is evident that the $\lambda_i/10$ particles converge to a stable value even at the smallest of boundary sizes used. As particle size increases, so does the required boundary size. Particles of diameter $3\lambda_i/10$ require a boundary equal to or larger than two wavelengths before reaching convergence. Thus, care must be taken to insure that 1.) boundary size is large enough to insure convergence and 2.) a sufficient number of realizations is used to sufficiently calculate the coherent field.

7   Conclusion

This paper has put forward a new technique for numerically determining the effective permittivity of a random medium in two dimensions. A key component of the technique is a method of moments/eigen-analysis inversion technique that efficiently calculates the volume currents for a deterministic body with variable permittivity. This inversion technique was applied to a range of random media that varied particle size, volume fraction, boundary size and shape. Results from the inversion technique where compared with the two-dimensional Polder-Van Santen mixing formula and shown to agree in the small particle, low volume fraction limit. The last section then addressed the problem of boundary size, particle size and convergence of the solution. The extensive study performed in this section of the paper will provide insight as how to approach the three-dimensional problems. The strength of the method is to create multiple scattering numerical solutions for effective permittivity for a group of canonical situations. Such solutions can then be used to analyze theoretical methods such as the Polder-Van Santen mixing formula, the quasi-crystalline approximation or future models that address the dense random media problem.

References

[1] Lax, M., "Multiple Scattering of Waves. II. The Effective Field in Dense Systems," Physical Review, v.85 n.4, pp 621-629, February 15, 1952.

[2] Mandt, C.E., Kuga, Y., Tsang, L. and Ishimaru, A.. "Microwave propagation and scattering in a dense distribution of non-tenuous spheres: experiment and theory," Waves in Random Media, v.2, pp 225-234, 1992.

[3] Polder, D. and VanSanten, J.H.,"The Effective Permeability of Mixtures of Solids," Physica, v.12 n.5, pp 1257-271. August, 1946.

[4] Richmond, J.H., "Scattering by a dielectric cylinder of arbitrary cross-section shape," IEEE Transactions on Antennas and Propagation, v.AP-13, pp 334-341. May 1965.

[5] Richmond, J.H., "TE-Wave Scattering by a Dielectric Cylinder of Arbitrary Cross-Section Shape," IEEE Transactions on Antennas and Propagation, v.AP-14, pp 460-464. July, 1966.

[6] Sarabandi, K. and Senior, T.B.A., "Low-Frequency Scattering from Cylindrical Structures at Oblique Incidence," IEEE Transactions on Geoscience and Remote Sensing, v.28 n.5, pp 879-885. September 1990.

[7] Sarabandi, K., "A Technique for Dielectric Measurement of Cylindrical Objects in a Rectangular Waveguide", IEEE Transactions on Instrumentation and Measurement, v.43 n.6, pp 793-798, December 1994.

[8] Siqueira, P.R., Sarabandi, K., and Ulaby, F.T., "Numerical Simulation of Scatterer Positions in a Very Dense Media," IEEE Conference on Antennas and Propagation, 1994.

[9] Stark, H., and Woods, J.W., "Probability, Random Processes, and Estimation Theory for Engineers," Prentice-Hall, Englewood Cliffs, New Jersey, 1986.

[10] Tsang, L., Kong, J., and Shin, R. *Theory of Microwave Remote Sensing.* John Wiley & Sons, New York, 1985.

[11] Tsang, L., Mandt, C.E., and Ding, K.H., "Monte Carlo simulations of the extinction rate of dense media with randomly distributed dielectric spheres based on solution of Maxwell's equations," Optics Letters, v.17 n.5, pp 314-316, March 1, 1992.
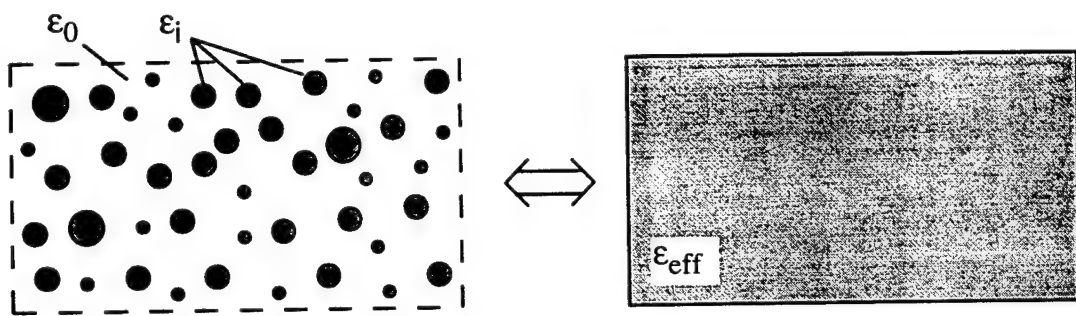
List of Figures

Figure 1: Model for determining the effective permittivity for a random collection of scatterers.
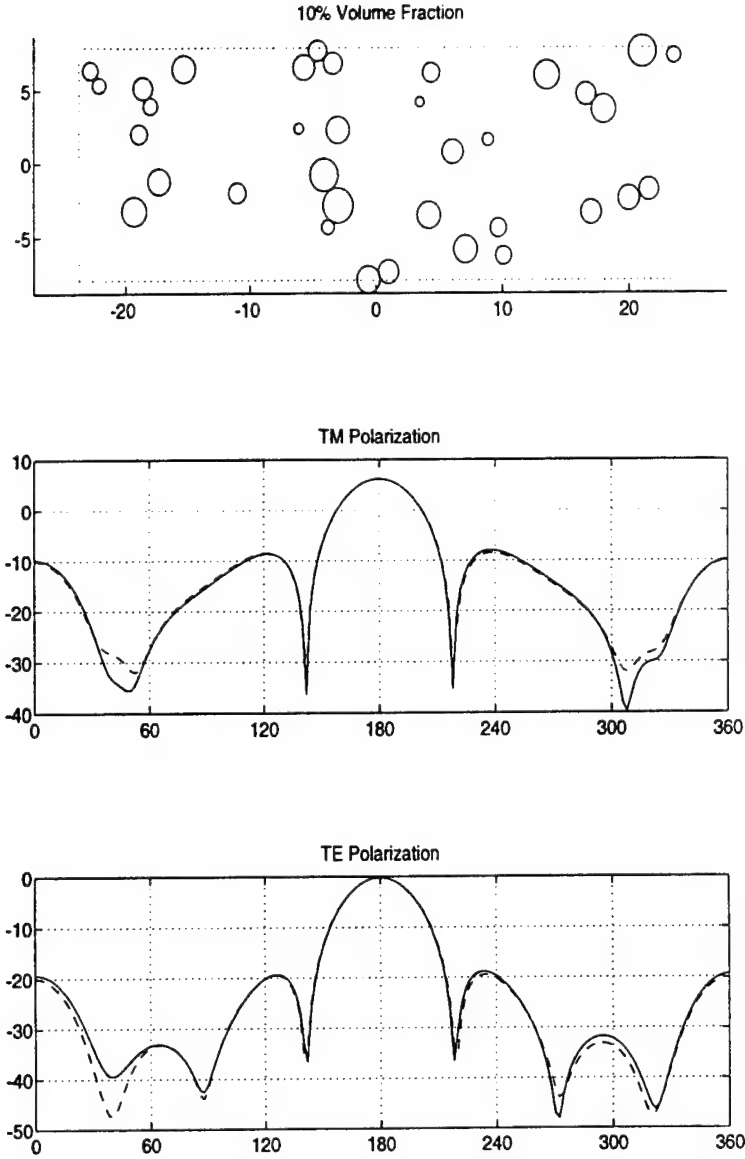
Figure 2: Algorithm results for 10% volume fraction. Shown here is a.) a sample collection of particles confined within an imaginary boundary, b.) average scattered TM field (solid line) and the scattered field from a homogeneous dielect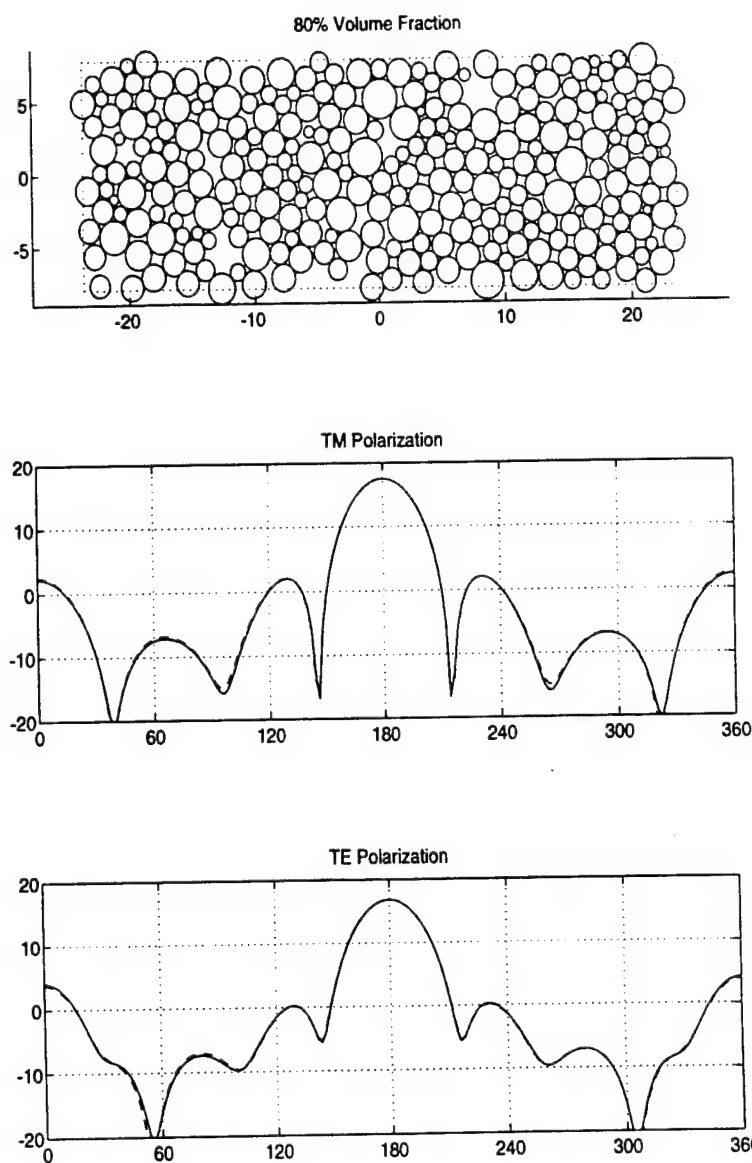ric with permittivity, ϵ_{eff} (dashed line), c.) average scattered TE field (solid line) and the scattered field from a homogeneous dielectric with permittivity, ϵ_{eff} (dashed line).

Figure 3: Algorithm results for 80% volume fraction. See Fig. 2 for description of individual sub-figures.
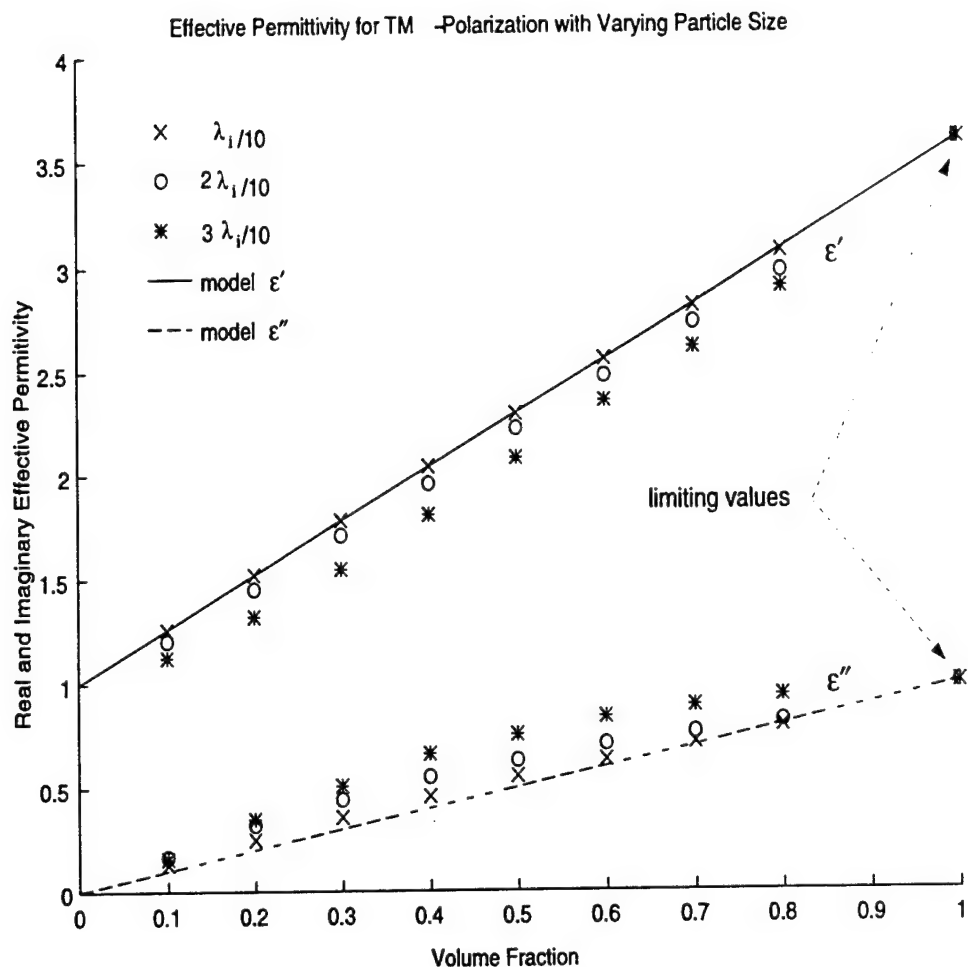
Figure 4: Simulation and mixing formula results for TM polarization. Real (solid line) and imaginary (dashed line) components of the effective permittivity derived from the Polder-Van Santen mixing formula compared with effective permittivity obtained by numerical simulation. Symbols indicate different particle diameters of $\lambda_i/10$ - x, $2\lambda_i/10$ - o, and $3\lambda_i/10$ - *. Inclusion permittivity is $\epsilon_i = 3.6 + i1.0$
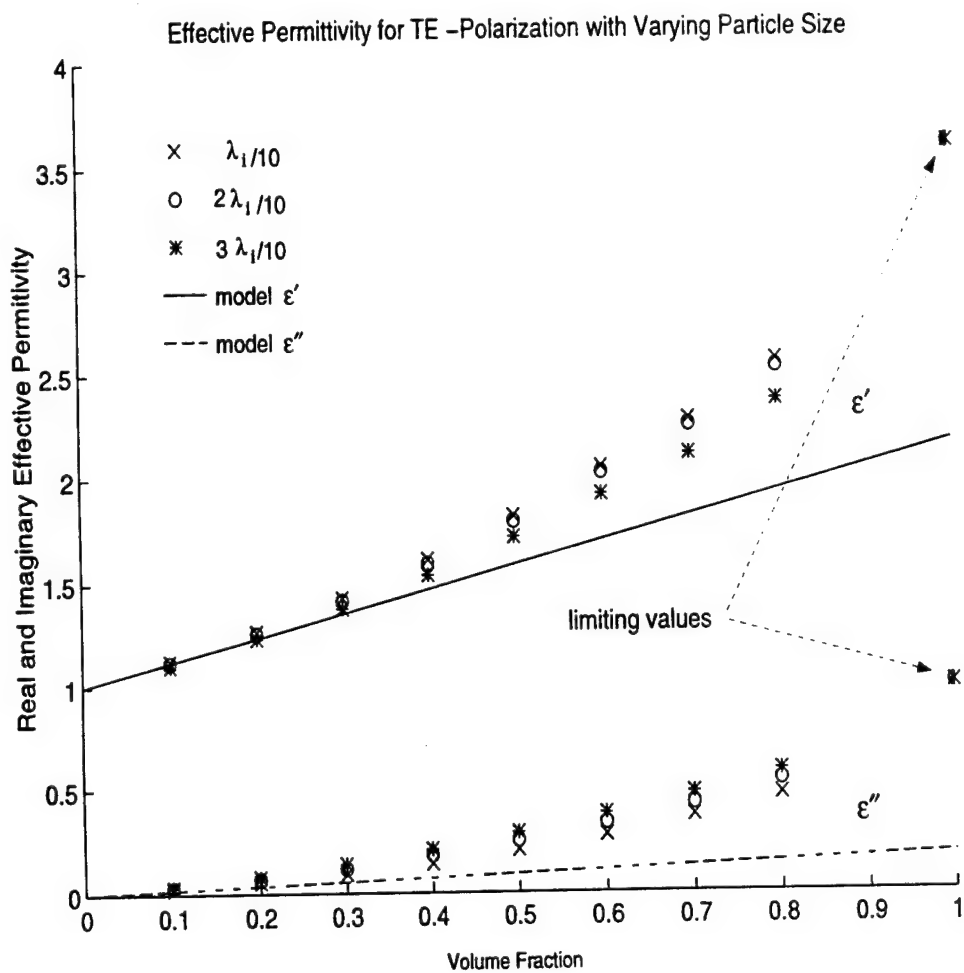
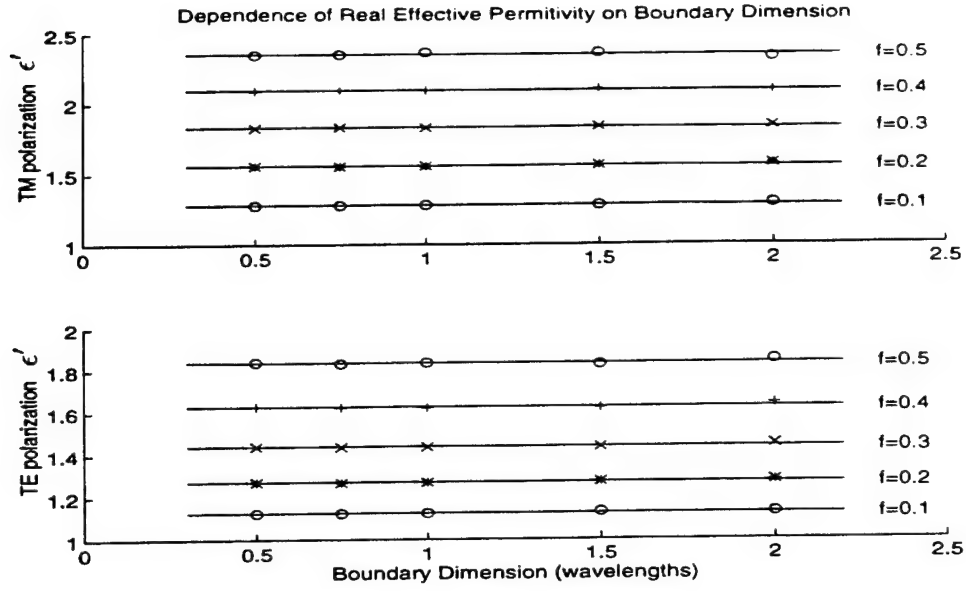Figure 5: Simulation and mixing formula results for TE polarization.

Figure 6: Solution dependence on boundary dimension for TM and TE polarizations. Different lines on the graph represent the average permittivity for a given volume fraction of f = 0.1, 0.2, 0.3, 0.4 or 0.5.
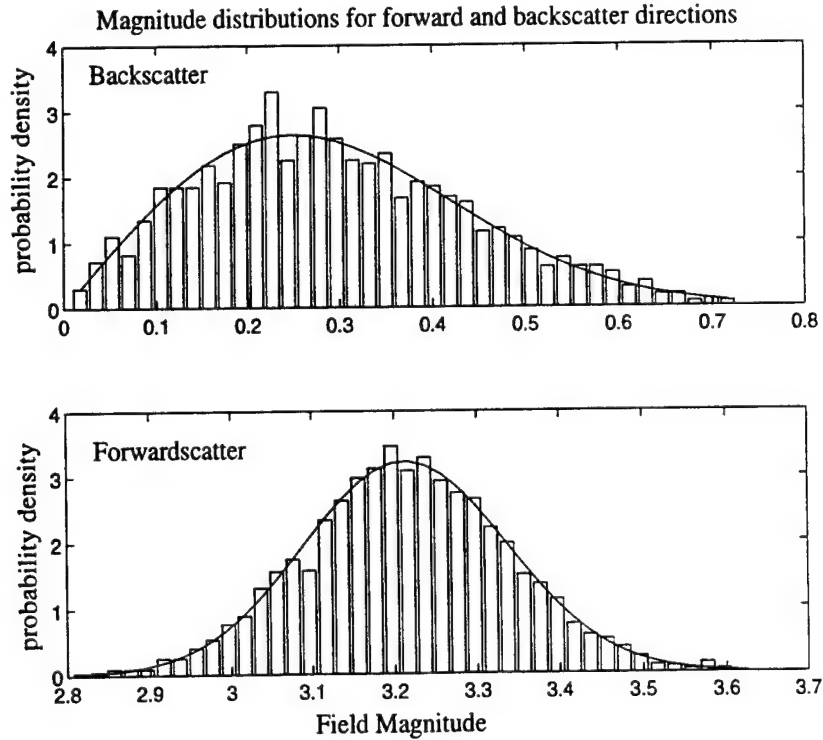

Figure 7: Forward and backscatter field magnitude distributions. Numerical simulations (bar graph) follow the Rice-Nakagami distribution (solid line). This example is for a square box of dimension $1.5\lambda \times 1.5\lambda$, 40% volume fraction, TE polarization.
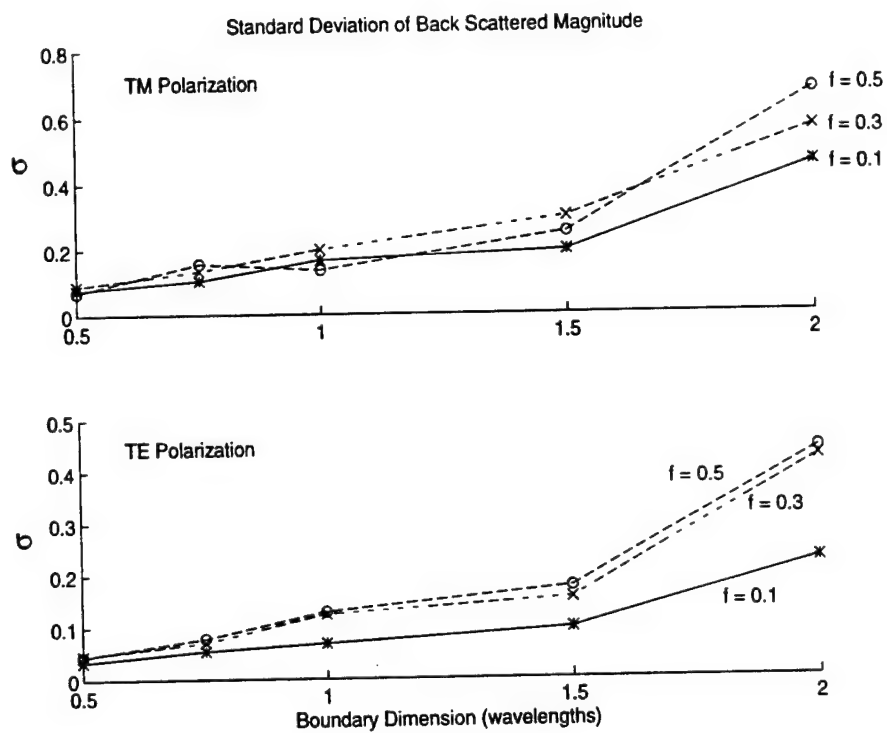
Figure 8: Standard deviation of backscattered field magnitude for three different volume fractions (0.1, 0.3 and 0.5), and both TM and TE polarizations. Similar behavior was observed for the forward scattered field as well.
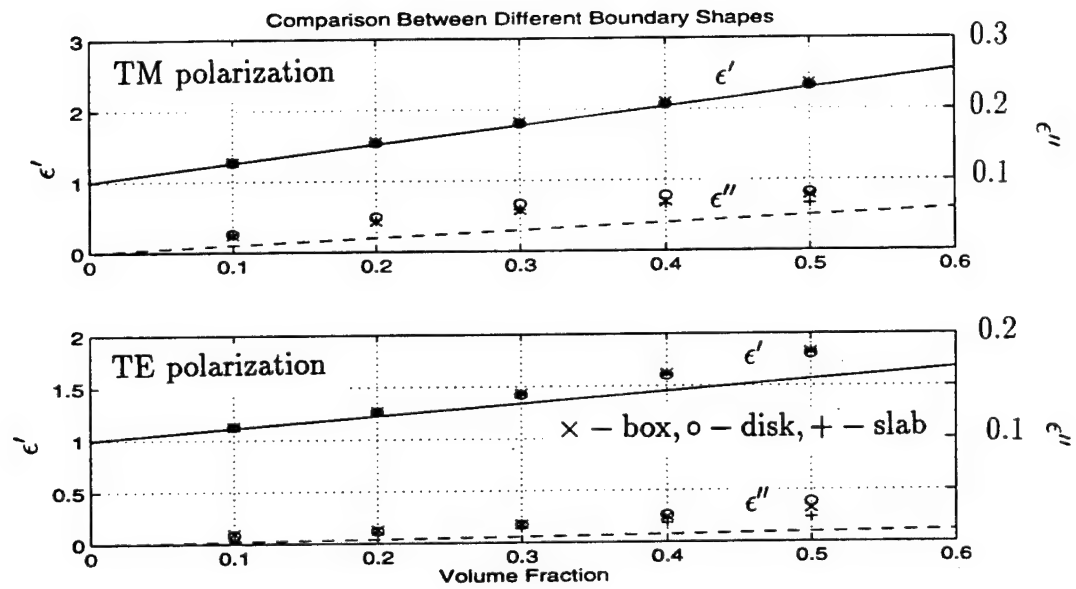
Figure 9: Effective permittivity comparison for differing boundary shapes. Shown are the real and imagary permitivities for three different boundary shapes: o − circular disk (diameter = $2\lambda_i$), + − rectangular slab ($3\lambda_i \times \lambda_i$) and and × − square box ($1.5\lambda_i \times 1.5\lambda_i$). The imaginary part of the effective permittivity is multiplied by ten so that both parts of the effective permittivity may be displayed on the same graph. Lines indicate results from the two-dimensional Polder-Van Santen mixing formula.
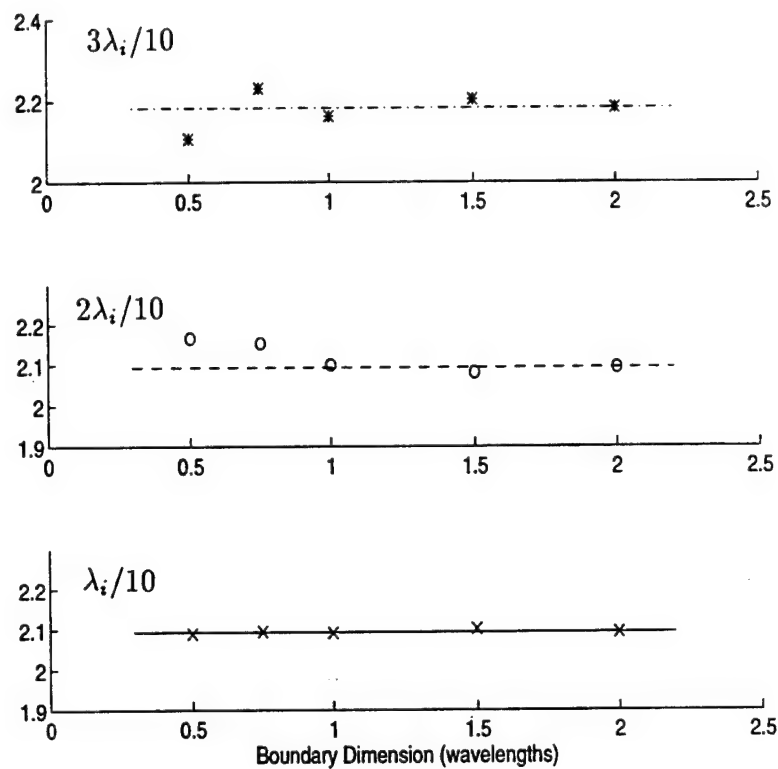
Figure 10: Real part of effective permittivity versus boundary dimension for three different particle sizes: $\lambda_i/10 - \times, 2\lambda_i/10 - \text{o}, 3\lambda_i/10 - *$ and a volume fraction of 40%, TM polarization.

A NUMERICAL SIMULATION OF SCATTERING FROM INHOMOGENEOUS DIELECTRIC RANDOM SURFACES

Kamal Sarabandi, Yisok Oh, and Fawwaz T. Ulaby

Radiation Laboratory
Department of Electrical Engineering and Computer Science
The University of Michigan, Ann Arbor, MI 48109-2122

Abstract

An exact solution for scattering by inhomogeneous, dielectric, random surfaces does not exist at the present time. This paper presents an efficient numerical technique for computing the scattering by inhomogeneous dielectric rough surfaces. The inhomogeneous dielectric random surface, which is intended to represents a bare soil surface, is considered to be comprised of a large number of randomly positioned dielectric humps of different sizes, shapes, and dielectric constants, lying on an impedance surface. Clods with non-uniform moisture content and rocks are modeled as inhomogeneous dielectric humps and the underlying smooth wet soil surface is modeled as an impedance surface. In this technique an efficient numerical solution for the constituent dielectric humps is obtained using the method of moments in conjunction with a new Green's function representation based on the exact image theory. The scattered field from a sample of the rough surface is obtained by summing the scattered fields from all the individual humps of the surface coherently, ignoring the effects of multiple scattering between the humps. The behavior of the scattering coefficient σ° is obtained from calculations of the scattered fields for many different surface samples of the same process. Numerical results are presented for several different roughnesses and dielectric constants of the random surface. The numerical technique is verified by comparing the numerical solution with the solution based

on the small-perturbation method and the physical-optics model for homogeneous rough surfaces. This technique can be used to study the behavior of the scattering coefficient of rough soil surfaces.

1 Introduction

Investigation of the radar scattering response of natural surfaces is an important problem in remote sensing because of its potential in retrieving desired physical parameters of the surface, namely its soil moisture content and surface roughness. Soil moisture is a key ingredient of the biochemical cycle and an important variable in hydrology and land processes. Although the problem of electromagnetic wave scattering from random surfaces has been investigated for many years, because of its complexity, theoretical solutions exist only for simple limiting cases. These include the small perturbation method (SPM) [1] and the Kirchhoff approximation (KA) [2], both of which are applicable for homogeneous surfaces over restricted regions of validity. Numerous techniques based on the basic assumptions of the SPM and KA have been developed in the past in an attempt to extend the regions of validity of these models; however, they all have the basic limitations of the original models [3]. Other theoretical models are available also, such as the full wave analysis technique [4], the phase perturbation technique [5], and the integral equation method [6], but they are not applicable for inhomogeneous surfaces and their regions of validity have not been fully determined yet. Several numerical solutions of the scattering problem have been proposed to identify the regions of validity and accuracies of these theoretical models. A scattering solution for a perfectly conducting random surface using the method of moments has been suggested by Axline and Fung [7] who used a tapered incident field as the excitation to eliminate the edge-effect contribution due to the boundaries of the illuminated area. A numerical solution for homogeneous dielectric random surfaces has

2

recently been reported [8] where again a tapered illumination is used to limit the size of the scattering area. The accuracy of the numerical solution with tapered illumination decreases with increasing incidence angle. To our knowledge, a solution for scattering from an inhomogeneous rough surfaces does not yet exist.

Analysis of microwave backscatter observations by Oh *et al.* [9] reveals that the existing theoretical models cannot adequately explain the scattering behavior of soil surfaces. The deviation between theoretical predictions and experimental data is attributed to three factors. First, the roughness parameters of some surfaces are often outside the region of validity of the theoretical models. Second, the autocorrelation functions associated with the measured height profiles of natural surfaces are very complicated and are not Gaussian or exponential functions. Finally, the most important reason is that in most cases natural surfaces are not homogeneous dielectric surfaces, *i.e.*, the moisture content is not uniform in depth. The top rough layer, which includes clods and rocks, is usually dry and the underlying soil layer is moist and smooth.

In this paper we model a soil surface as an inhomogeneous dielectric random surface comprised of a large number of randomly positioned two-dimensional dielectric humps of different sizes, shapes, and dielectric constants, all lying over an impedance surface. At microwave frequencies, the moist and smooth underlying soil layer can be modeled as an impedance surface, and the irregularities above it can be treated as dielectric humps of different dielectric constants and shapes. For the field scattered by a single dielectric hump over an impedance surface, we have an available efficient numerical solution that uses the exact image theory for the Green's function in conjunction with the method of moments [10]. In the solution of a single hump, it has been shown that the bistatic scattered field is very weak at points in close pproximity to the impedance surface; thus, the effects of multiple scattering between humps can be ignored. In this case the scattered field from a

3

collection of randomly positioned dielectric humps can easily be obtained by summing the scattered field of all the constituent humps coherently. The scattering coefficients (σ°) is obtained by a Monte Carlo simulation.

2 Monte Carlo Simulation of Rough Surface Scattering

Monte Carlo simulation of scattering by a rough surface comprised of a finite collection of dielectric humps involves the execution of five major steps, as shown in Fig. 1. The first step is to choose the type (size, shape, and dielectric constant) and number of constituent humps. The second step deals with generating a surface sample by positioning a large number of humps with a prescribed probability distribution function. The third step in this algorithm is to compute the inverse impedance matrices for all constituent humps using the numerical method explained in the previous section. Next, the scattered field from the surface is computed by coherent summation of the scattered fields from all of the humps in the surface sample. Finally, the scattering coefficient σ° is obtained by repeating the fourth step for a large number N of independently generated surface samples. For example, N is chosen to be around 100 to reduce the standard deviation associated with the estimation of mean backscattered power (σ°). The standard deviation of estimated σ^o is inversely proportional to $\sqrt{N}$ [11].

The types of constituent humps, in addition to their probability of occurrence, fully characterize the statistics of the random surface. Figure 2 shows the geometry and dielectric profiles of different types of dielectric humps that can be handled by this algorithm. For example, Fig. 2 (a) shows a typical hump arrangement for a dry clod above a moist and smooth underlying soil layer ($\epsilon_0 < \epsilon_1 < \epsilon_2$), and Fig. 2 (b) shows the same hump when the clod and underlying layer are both moist (a homogeneous surface). The hump

4

itself may be considered to be inhomogeneous as shown in Fig. 2 (c). Isolated irregularities such as rocks above a flat surface can be represented by the hump example shown in Fig. 2 (d) where the bump occupies only a part of the total width allocated to an individual hump. When the surface is very rough with a short correlation length, the geometry of the humps are more complicated. Two examples of such humps are shown in Figs. 2(e) and 2(f). The profiles of Figs. 2 (a)-(e) used in this paper are given by the following functionals; for (a)-(c)

$$y(x) = \frac{W}{A} \cos^2 \left(\frac{\pi x}{W} \right) , \quad -\frac{W}{2} \leq x \leq \frac{W}{2} , \tag{1}$$

for (d)

$$y(x) = A \left(1 - \frac{x^2}{B^2} \right) , \quad -B \leq x \leq B, \ B \leq W , \tag{2}$$

and for (e)

$$y(x) = A \, F_1(x) \, + \, B \, F_2(x) ,$$

with

$$\left. \begin{array}{l} F_1(x) = \cos^n \left(\frac{\pi x}{W} - \frac{\pi}{2} \right) \left(\frac{x}{W} \right)^m \\ F_2(x) = \cos^n \left(\frac{\pi x}{W} - \frac{\pi}{2} \right) \left(1 - \frac{x}{W} \right)^m \end{array} \right\} , \quad 0 \leq x \leq W , \tag{3}$$

where A and B are constants, n and m are integers, and W is the width of a hump. The set of constituent humps for a surface can be constructed by choosing a finite number of parameters and desired dielectric constants in the desired functionals. The profile of Fig. 2 (f) is very complicated and should be obtained numerically by the procedure outlined in [12]. In this procedure the hump profile is obtained from a sequence of independent Gaussian deviates with zero mean and unit variance which are correlated by a set of weighting factors derived from the desired correlation function.

5

Suppose the set of individual humps includes K different humps (including size, shape, and dielectric constant) and the profiles of the humps in the set are represented by $f_i(x)$, $i = 1, \cdots, K$. Then a sequence of random numbers ranging from 1 to K, which is generated by a random number generator with the prescribed probability distribution function, is used to position a large number of humps randomly to construct a surface sample. If the total number of humps (M) in the surface sample is much larger than the number of constituent humps (K) and the random number generator has a uniform distribution, the probability of occurrence of each hump in the surface will be about M/K. A functional form of the generated surface profile can be represented by

$$y(x) = \sum_{m=1}^{M} f_{i_m} \left(x - \sum_{l=1}^{m-1} W_{i_l} \right) \tag{4}$$

where $i_m, i_l \in \{1, \cdots, K\}$ and W_{i_l} represents the width of the hump of the i_lth type. The roughness parameters, rms height s, correlation length l, and rms slope m [13], can be computed either numerically or analytically from the surface profile given in (4). The analytical computation is possible for simple functional forms. The average height of the surface can be computed from

$$\overline{y}(x) = \frac{1}{L} \sum_{i=1}^{K} p_i \int_{0}^{W_i} f_i(x) dx , \tag{5}$$

where $L = \sum_{i=1}^{K} p_i W_i$ and p_i is the probability of occurrence of the hump of type i. The rms height s and the rms slope m, respectively, can be evaluated from

$$s = \left\langle (y(x) - \overline{y}(x))^2 \right\rangle^{\frac{1}{2}} = \left[\frac{1}{L} \sum_{i=1}^{K} \int_{0}^{W_i} (p_i f_i(x) - \overline{y}(x))^2 \, dx \right]^{\frac{1}{2}}, \tag{6}$$

and

$$m = \left\langle \left(\frac{d\,y(x)}{dx} - \left\langle \frac{d\,y(x)}{dx} \right\rangle \right)^2 \right\rangle^{\frac{1}{2}} = \left[\frac{1}{L} \sum_{i=1}^{K} p_i \int_{0}^{W_i} (f_i'(x))^2 \, dx \right]^{\frac{1}{2}}. \tag{7}$$

6

Assuming the surface has a Gaussian correlation function, the correlation length l is related to rms height and rms slope by,

$$l = \sqrt{2}\,\frac{s}{m}\,. \tag{8}$$

It is often required to generate a random surface of a specified rms height s and correlation length l. In that case, the required surface can be obtained by an iterative process where some initial values for the hump parameters are chosen. Then the roughness parameters are calculated and compared with the desired ones. Depending on the difference between the calculated s and l and the desired ones the hump parameters are modified and this process is repeated until the difference becomes smaller than a tolerable error.

Once the set of individual humps for a random surface with given s and l is formed, the impedance matrices, $[\mathcal{Z}_{pq}]_i$, $i = 1, \cdots, K$, can be computed using the method of moments. Since the scattered field of a hump near the impedance surface is very weak [10], the effect of multiple interaction between humps in a surface sample can be ignored. Therefore by inverting and storing the impedance matrices of the constituent humps, the scattered field of any surface sample comprised of M humps ($M \gg K$) can be computed very efficiently for any incidence and observation directions. For a given direction of incidence the polarization currents in the jth hump for the vertical and horizontal polarizations, respectively, are given by

$$\begin{bmatrix} [\mathcal{I}_x] \\ [\mathcal{I}_y] \end{bmatrix}_j = \begin{bmatrix} [\mathcal{Z}_{xx}] & [\mathcal{Z}_{xy}] \\ [\mathcal{Z}_{yx}] & [\mathcal{Z}_{yy}] \end{bmatrix}_{i_j}^{-1} \begin{bmatrix} [\mathcal{V}_x] \\ [\mathcal{V}_y] \end{bmatrix}_j \quad \text{and} \tag{9}$$

$$[\mathcal{I}_z]_j = [\mathcal{Z}_{zz}]_{i_j}^{-1}\,[\mathcal{V}_z]_j\,, \tag{10}$$

where $j \in \{1, \cdots, M\}$ and $i_j \in \{1, \cdots, K\}$ representing the hump of the ith type. The excitation vector $[\mathcal{V}]_j$ is computed from incident and reflected fields where the position

vector $\bar{p}$ is specified by the discretization procedure and the profile function (4). The electric polarization current induced inside the surface sample can be represented by

$$[\mathcal{J}_p] \;=\; \left[\, [\mathcal{I}_p]_1^T, \cdots, [\mathcal{I}_p]_i^T, \cdots, [\mathcal{I}_p]_M^T \,\right]^T \;,\quad p = x, y, z \tag{11}$$

where $[\mathcal{I}_p]_i$ is the p-polarized current inside the ith hump. The radiated far field can be evaluated from

$$E_{pp}^s \;=\; \sqrt{\frac{2}{\pi k_0 \rho}}\, e^{i(k_0\rho - \pi/4)}\, S_{pp}\,,\quad pp = hh \text{ or } vv \tag{12}$$

where S_{pp} is the far-field amplitude given by

$$S_{hh} = -\frac{k_0 Z_0}{4}\sum_{n=1}^{N_t} J_z(x_n, y_n)\,\Delta x_n \Delta y_n\, e^{-ik_0 \sin\theta_s x_n}\left[e^{-ik_0 \cos\theta_s y_n} + R_E(\theta_s)e^{ik_0 \cos\theta_s y_n}\right]\,, \tag{13}$$

$$S_{vv} = \frac{k_0 Z_0}{4}\sum_{n=1}^{N_t} \Delta x_n \Delta y_n\, e^{-ik_0 \sin\theta_s x_n}\left\{ J_x(x_n, y_n)\cos\theta_s \left([e^{-ik_0 \cos\theta_s y_n} - R_H(\theta_s)e^{ik_0 \cos\theta_s y_n}\right)\right.$$
$$\left. - J_y(x_n, y_n)\sin\theta_s \left(e^{-ik_0 \cos\theta_s y_n} + R_H(\theta_s)e^{ik_0 \cos\theta_s y_n}\right)\right\}. \tag{14}$$

Here N_t is the total number of cells in the surface sample.

The statistical behavior of the scattered field is obtained from evaluation of E_{pp}^s for many independent surface samples. For a sufficiently large number of surface samples (N_s), the incoherent scattering coefficient is computed from

$$\sigma_{pp}^o = \lim_{\rho\to\infty}\frac{2\pi\rho}{N_s L_{av}}\left[\sum_{j=1}^{N_s}\left|\mathbf{E}_{pp,j}^s\right|^2 - \frac{1}{N_s}\left|\sum_{j=1}^{N_s}\mathbf{E}_{pp,j}^s\right|^2\right]\,,\quad pp = hh,\ vv, \tag{15}$$

where $L_{av} = \frac{1}{N_s}\sum_{j=1}^{N_s} L_j$, and L_j is the total length of the jth random surface.

3 Numerical Results

To demonstrate the performance of the technique proposed in this paper, we shall use it to compute the scattering for some sample surfaces and then compare the results with those predicted by the available theoretical scattering models, when conditions apply.

First, we consider a surface with homogeneous dielectric humps as shown in Fig. 2(a). The functional form of the humps are given by (1) where the parameters A and W are varied to generate the set of the constituent humps. Keeping A as a constant controlling the height and varying W, a set of similar humps can be generated. A random number generator with output $i \in \{1, \cdots, K\}$ selects the parameter $W_i = B\lambda i$, where B is a constant controlling the width of the humps and λ is the wavelength. In this example the hump parameters were chosen according to Table 1 and the random number generator was given a uniform distribution with $K = 10$. Before presenting the statistical scattering behavior of the surface, it is useful to demonstrate the validity of the assumption regarding the significance of the effects of multiple scattering among the humps. Figures 3 (a) and (b) show the bistatic echo width of a squared-cosine hump with $W = 0.72\lambda$, $H = 0.07\lambda$, $\epsilon_1 = 15 + i3$ above a surface with $\eta = 0.254 - i0.025$ (which corresponds to $\epsilon_2 = 15 + i3$) at 5 GHz when the incidence angle $\theta_i = 0°$ and $\theta_i = 45°$, respectively. It is shown that the bistatic echo widths at the large scatter angles (near the surface) are very weak which implies that the effect of multiple scattering between humps can be ignored. In order to illustrate the effect of multiple scattering, a surface segment comprised of three squared-cosine humps with $\epsilon_1 = 15 + i3$ above an impedance surface with $\eta = 0.254 - i0.025$ was considered (see Fig. 4). Dimensions of three humps are, respectively, given by: $W_1 = 0.8\lambda$, $H_1 = 0.08\lambda$; $W_2 = 1.0\lambda$, $H_2 = 0.1\lambda$; and $W_3 = 0.6\lambda$, $H_3 = 0.06\lambda$. The backscatter echo widths of the surface segment were computed twice. In one case the scattered field was computed from the polarization current of isolated humps (ignoring the effect of mutual coupling) and in other case the polarization current of the three-hump structure was obtained directly from the method of moments solution (including the effect of mutual coupling). Figures 4(a) and 4(b) show that the effect of multiple scattering is negligible for both polarizations. As long as the ratio of rms height to correlation length of

9

the surface (s/l) is small, this approximation provides accurate results. For most natural surfaces $s/l < 0.3$ which satisfies this condition [9]. However if the ratio (s/l) is relatively large, the hump type of Fig. 2 (f) must be used to include the effect of multiple scattering at the expense of computation time.

The rms surface height s and the rms surface slope m for this surface can be computed from (6) and (7) respectively and are given by

$$ s = \left[\frac{1}{Lw} \sum_{i=1}^{K} \left(\frac{3}{8} \frac{W_i^3}{A^2} - \frac{W_i^2}{A} \bar{y} + W_i \bar{y}^2 \right) \right]^{\frac{1}{2}}, \tag{16} $$

$$ m = \frac{\pi}{\sqrt{2}\, A}. \tag{17} $$

where

$$ \bar{y} = \frac{1}{2\, A\, Lw} \sum_{i=1}^{K} W_i^2, \quad \text{and} \quad Lw = \sum_{i=1}^{K} W_i, $$

It should be noted that the rms surface slope m of this surface depends only on the constant A. Therefore for a fixed value of A, both the rms height and the correlation length increase at the same rate with increasing B. Table 1 shows several values of roughness parameters, s and l, corresponding to different values of A and B.

A random number generator was used to select and position 4000 squared-cosine humps over the impedance surface ($\eta = 0.254 - i0.025$). Then this surface was divided into 100 segments to obtain 100 independent surface samples each having 40 humps. The length of the surface segment was chosen to be about 44λ to 154λ depending on the correlation length of the surface which corresponds to the size of individual humps. In the method of moments solution of individual hump, the size of a discretized cell was chosen such that $\Delta x = \Delta y = \lambda/15$ (where $\lambda = \lambda_0/\sqrt{\epsilon_{r1}}$). Table 2 summarizes the characteristics of the surfaces and their constituent humps used in the examples considered in this study.

The backscattering coefficients for the surface at 5 GHz with $ks = 0.12$ and $kl = 2.13$ (Case 1 in Tables 1 and 2) are computed by the Monte Carlo simulation technique for

a homogeneous surface with $\epsilon_1 = \epsilon_2 = 15 + i3$ (Fig. 2(b)), and compared with the analytical results based on the SPM as shown in Figs. 5(a) and 5(b). For the SPM solution, the scattering coefficient σ° is proportional to the roughness spectrum (Fourier transform of the correlation function). Both the actual and Gaussian correlation functions are used in the calculation of the backscattering coefficients using the SPM. It is shown that the Monte Carlo simulation agrees very well with the SPM prediction when the actual correlation function is used. The discrepancies between the Monte Carlo simulation and the SPM with Gaussian correlation function indicate the importance of the tail section of the correlation function in the estimation of σ°.

The numerical simulation was also performed for a surface at 5 GHz with $ks = 0.42$, $kl = 7.49$ (Case 3 in Tables 1 and 2), and $\epsilon_1 = \epsilon_2 = 15 + i3$. The roughness parameters of this surface fall within the validity region of the physical optics (PO) model; therefore the numerical solution can be compared with the PO solution. The scattering coefficient σ°_{hh} predicted by the PO model using the actual correlation function agrees very well with the results computed by the numerical technique, as shown in Fig. 6. In this figure the PO solution using a Gaussian correlation function with the same correlation length as the actual correlation function is also compared with the numerical simulation. It is shown that the agreement is good only for low incidence angles ($\theta_i \leq 20°$) and the discrepancy between the two solutions becomes very significant for higher incidence angles. In this case, similar to the previous case (SPM), it is shown that the tail of the correlation function plays an important role in determining the angular patterns of the backscattering coefficients.

With the success of the Monte Carlo simulation in predicting the scattering behavior of rough surfaces in the small perturbation and physical optics regions, the numerical model can be used to study complex surfaces with intermediate roughness parameters

11

(Case 2 in Tables 1 and 2 for example) and inhomogeneous dielectric profiles.

4   Conclusions

In this paper an efficient Monte Carlo simulation technique is proposed for computing electromagnetic scattering by inhomogeneous one-dimensional rough surfaces. The surface irregularities are represented by inhomogeneous dielectric humps of different shapes and the underlying layer is represented by an impedance surface. A moment-method procedure, in conjunction with the exact image theory, is used for calculation of the field scattered by the dielectric humps. It was shown that the scattered field near the impedance surface is weak , and hence the effect of multiple scattering between humps can be ignored.

To check the validity of the Monte Carlo simulation, the numerical results were compared with the existing analytical solutions for surfaces at extreme roughness conditions. A smooth surface that satisfies the validity region of the SPM and a surface that satisfies the validity region of the PO model were considered, and in both cases excellent agreement was obtained between the analytical results and those computed using the proposed technique. It was found that away from normal incidence the tail of the correlation function plays an important role in the determination of the backscattering coefficients.

The analysis presented in this paper is only for one-dimensional surfaces and therefore is incapable of predicting the cross-polarized scattering coefficients. A numerical simulation for a two-dimensional rough surface using a similar method is computationally tractable.

Acknowledgment

12

References

[1] Rice, S. O., "Reflection of electromagnetic waves by slightly rough surfaces", *Communication in Pure and Applied Mathematics*, vol. 4, pp. 351-378, 1951.

[2] Beckmann, P. and A. Spizzichino, **The Scattering of Electromagnetic Waves from Rough Surfaces**, Artech House, MA, 1987.

[3] Brown, G. S. "Backscattering from a Gaussian distributed perfectly conducting rough surface", *IEEE Trans. Antennas Propagat.*, vol. AP-26, pp. 472-482, May 1978.

[4] Bahar, E., "Full-wave solutions for the depolarization of the scattered radiation fields by rough surfaces of arbitrary slope," *IEEE Trans. Antennas Propagat.*, vol. AP-29, pp. 443-454, May 1981.

[5] Wineberner, D. and A. Ishimaru, "Investigation of a Surface Field Phase Perturbation Technique for Scattering from Rough Surfaces", *Radio Science*, vol. 20, pp. 161-170, Mar. 1985.

[6] Fung, A.K., and G. W. Pan, "A scattering model for perfectly conducting random surfaces: I. Model development. II. Range of validity", *Int. J. Remote Sensing*, vol. 8, no. 11, pp. 1579-1605, 1987.

[7] Axline, R. M. and A. K. Fung, "Numerical computation of scattering from a perfectly conducting random surface," *IEEE Trans. Antennas Propagat.*, vol. AP-26, pp. 482-488, May 1978.

[8] Sanchez-Gil, J. A. and M. Nieto-Vesperinas, "Light scattering from random rough dielectric surfaces", *J. Opt. Soc. Am. A*, vol. 8, pp. 1270-1286, Aug. 1991.

[9] Oh, Y., K. Sarabandi, and F.T. Ulaby, "An empirical model and an inversion technique for radar scattering from bare soil surfaces", *IEEE Trans. Geosci. Remote Sensing*, vol. 30, pp. 370-382, Mar. 1992.

[10] Sarabandi, K., "Scattering from dielectric structures above impedance surfaces and resistive sheets", *IEEE Trans. Antennas Propagat.*, vol. 40, pp. 67-78, Jan. 1992.

[11] Ulaby, F. T. and M. C. Dobson, **Handbook of radar scattering statistics for terrain** Artech House, Norwood, MA, 1989.

[12] Fung, A.K., and M. F. Chen, "Numerical Simulation of Scattering from Simple and Composite Random Surfaces", *J. Opt. Soc. Am. A*, vol. 2, no. 12, pp. 2274-2284, Dec. 1985.

[13] Ulaby, F. T., M. K. Moore, and A. K. Fung, **Microwave Remote Sensing, Active and Passive**, vol. 2 and 3, Artech House, Norwood, MA, 1986.

Table 1: Roughness parameters corresponding to constants A and B.

Case	A	B	Approx. † s	l	Exact ‡ s	l	At 5 GHz ks	kl	Remarks
			in cm		in cm				
1	30	0.20	0.115	2.21	0.115	2.03	0.12	2.13	SPM region
2	30	0.36	0.208	3.98	0.207	3.63	0.22	3.80	
3	30	0.70	0.405	7.74	0.405	7.15	0.42	7.49	PO region

† Approximation by equations (16-17) and (8),

‡ Numerical evaluation with 4000 humps,

s : rms surface height,

l : correlation length.

Table 2: Constants used in the numerical computations.

Case No.	Individual hump size Width min. (λ)	max. (λ)	Height min. (λ)	max. (λ)	No. of humps for each surface segment	Length of surface segment (λ)	No. of segments for a surface
1	0.2	2.0	0.0066	0.066	40	44	100
2	0.36	3.6	0.012	0.12	40	79	100
3	0.7	7.0	0.023	0.233	40	154	100
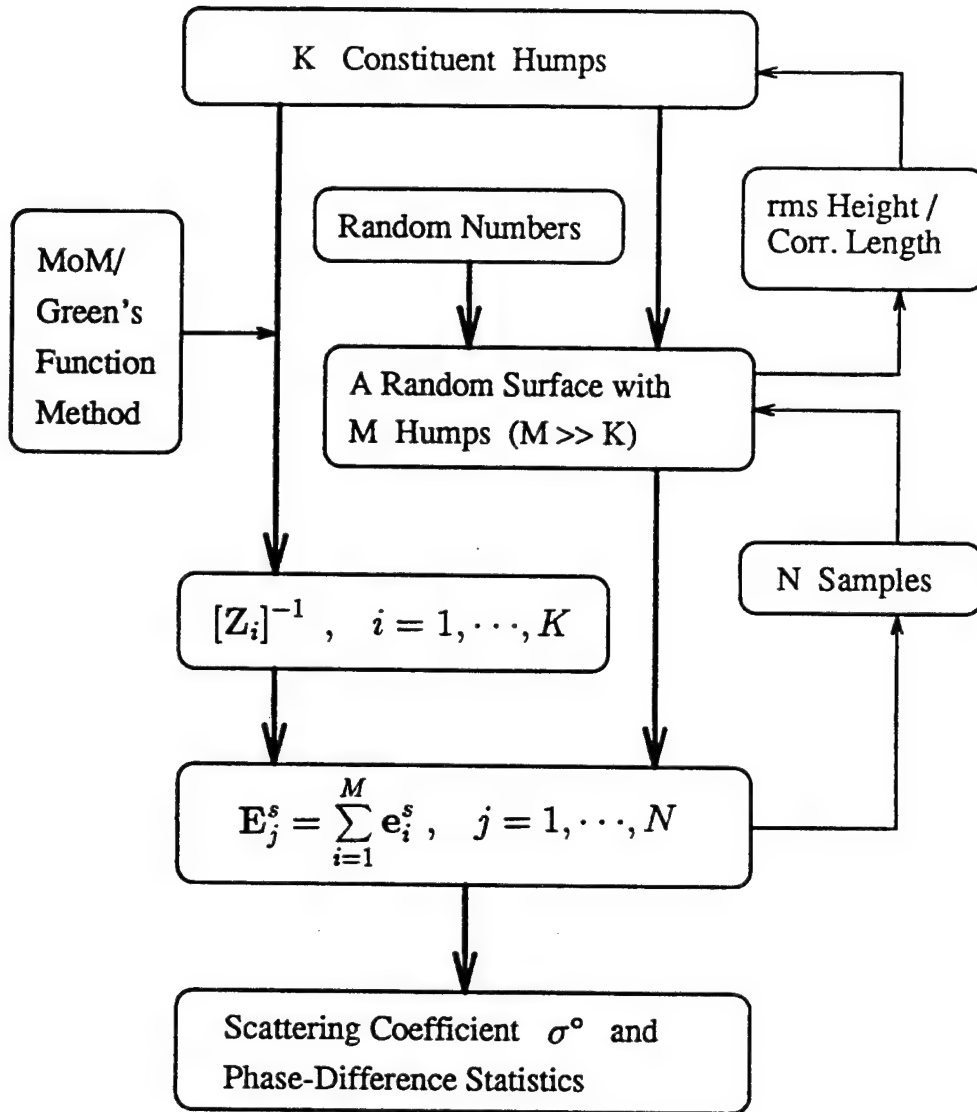
Figure 1: Flow chart of the Monte Carlo simulation for the rough surface problem.
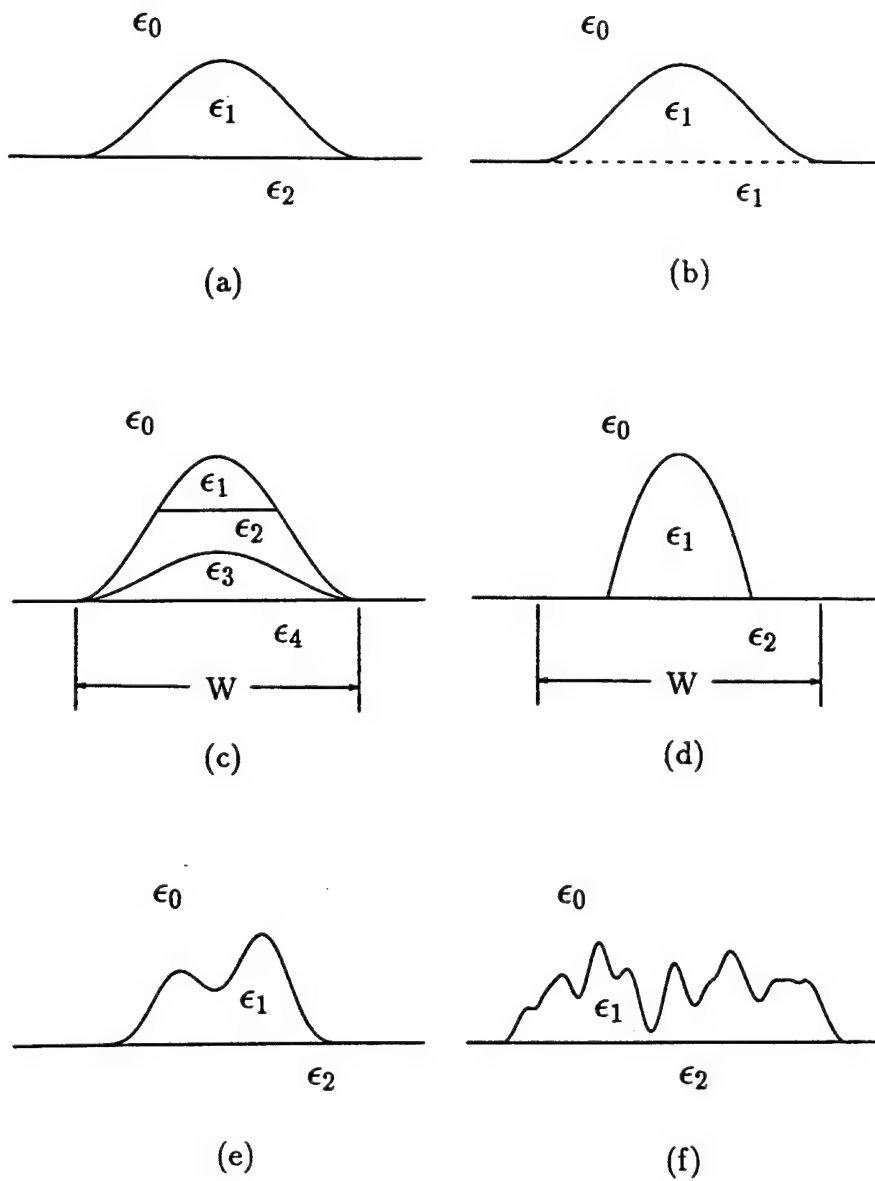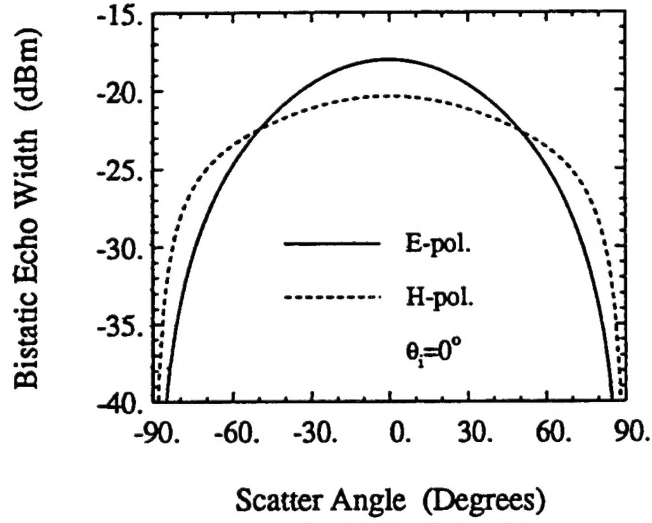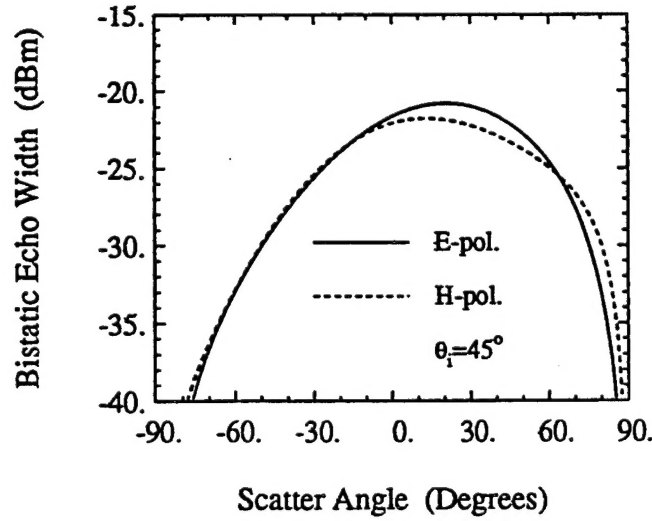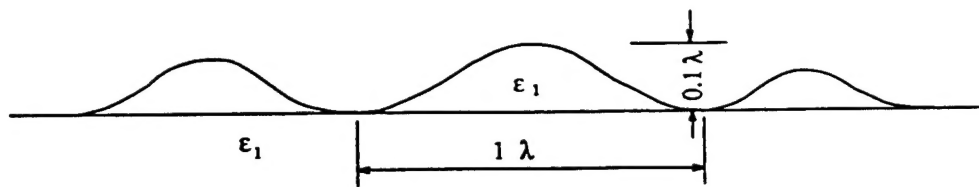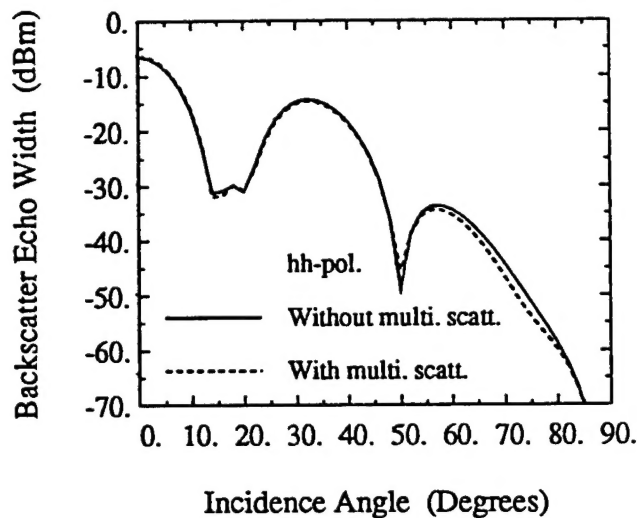
Figure 2: Hump types considered in this paper.
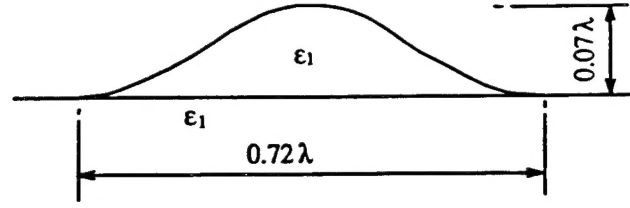
Figure 3: Bistatic echo width of a squared-cosine hump of $\epsilon_1 = 15 + i3$, $W = 0.72\lambda$, $H = 0.07\lambda$ over an impedance surface of $\eta = 0.254 - i0.025$ at (a) $\theta_i = 0°$ and (b) $\theta_i = 45°$ at $f = 5$ GHz for E- and H-polarizations.
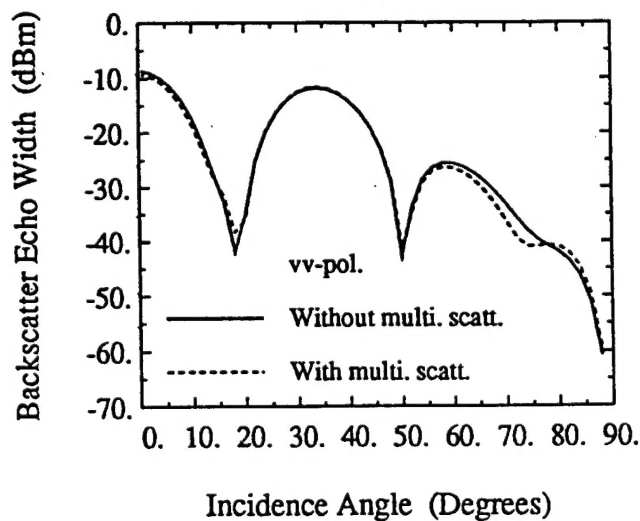
(a)

Incidence Angle (Degrees)

(b)

Incidence Angle (Degrees)

Figure 4: Multiple scattering effect on the backscatter echo width of a surface segment consisting of hump-4 , hump-5, and hump-3, corresponding to the roughness of $ks = 0.36$, $kl = 2.2$, with $\epsilon_1 = 15 + i3$ over an impedance surface of $\eta = 0.254 - i0.025$ at (a) hh-polarization and (b) vv-polarization at $f = 5$ GHz .
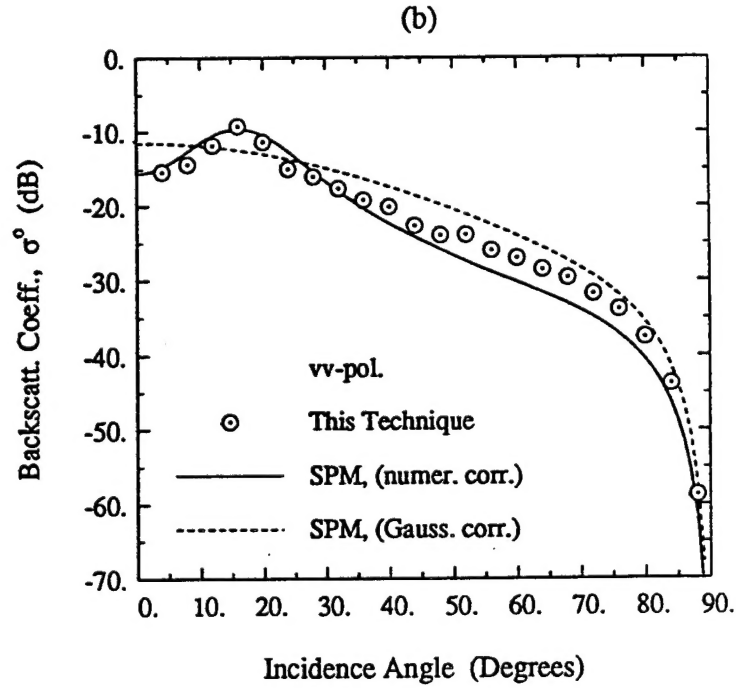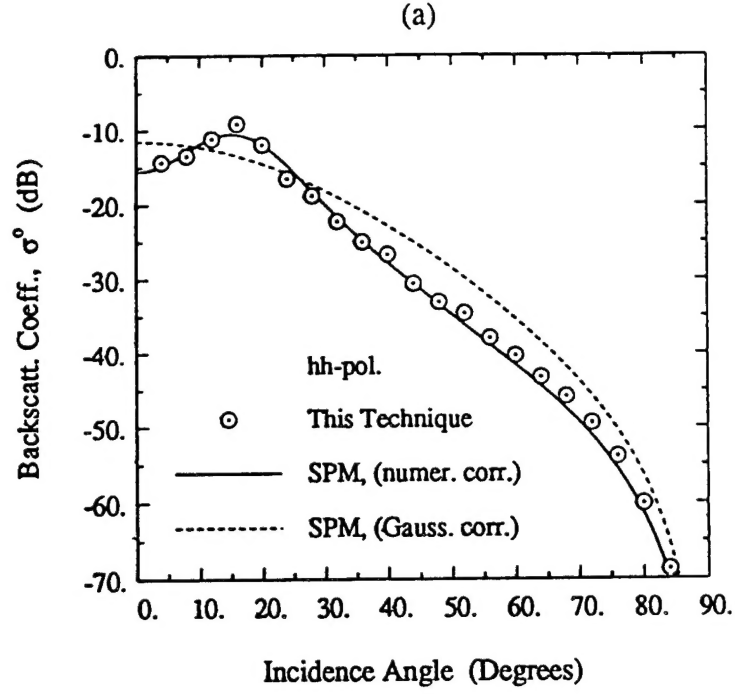
Figure 5: Backscattering coefficient σ° of the random surface with $ks = 0.12$, $kl = 2.13$, and $\epsilon_1 = \epsilon_2 = 15 + i3$ as computed by the SPM and the numerical technique; (a) hh-polarization and (b) vv-polarization.
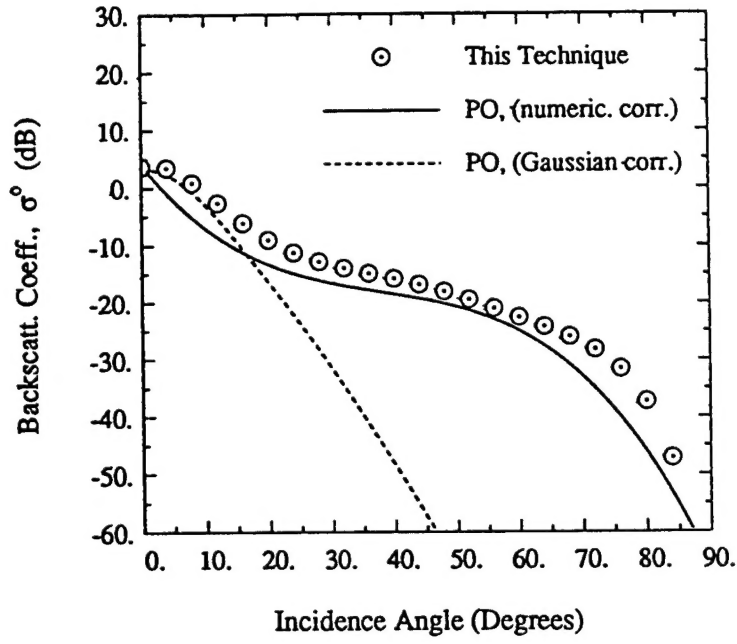
Figure 6: Backscattering coefficient σ° of the random surface with $ks = 0.42$, $kl = 7.49$, and $\epsilon_1 = \epsilon_2 = 15 + i3$ as computed by the PO model and the numerical technique for hh-polarization.